

# CYCLIC ANALYSIS OF POWER PLANT COMPONENTS AND MATERIALS

by

Michael Zimnoch

A dissertation submitted to the faculty of  
The University of North Carolina at Charlotte  
in partial fulfillment of the requirements  
for the degree of Doctor of Philosophy in  
Mechanical Engineering

Charlotte

2024

Approved by:

---

Dr. Alireza Tabarraei

---

Dr. Youxing Chen

---

Dr. Russell Keanini

---

Dr. David Weggel

---

Dr. Ian Perrin

©2024  
Michael Zimnoch  
ALL RIGHTS RESERVED

## ABSTRACT

MICHAEL ZIMNOCH. Cyclic Analysis of Power Plant Components and Materials.  
(Under the direction of DR. ALIREZA TABARRAEI)

This study conducts thermomechanical analyses of various steam headers to evaluate the cost-effectiveness of different material choices, demonstrate the influence prior service exposure may have, and model damage within these systems. Several headers designed in accordance with ASME BPVC were evaluated as potential replacements for an existing unit. The existing header, constructed from 2.25Cr-1Mo Grade 22 material located in Charlotte, NC, provided the basis for the operational specifications used in the proposed solutions. To achieve improved durability and cost-effectiveness, the study focused on identifying more robust alloys as potential replacements. In this context, P91 and IN740H were specifically considered due to their superior properties. Each header was subjected to thermo-mechanical loading, reflecting conditions experienced by the in-service header unit. The material's response to these conditions was captured using Abaqus finite element software. Among the various material models available, the analysis for each header was conducted using the elastic perfectly plastic material model. This particular approach was adopted in light of the constrained data pertaining to the IN740H alloy and to facilitate a homogeneous comparison across different alloys.

The low cycle fatigue, LCF, and response of each header were approximated by incorporating the Ostergren damage parameter. This methodology searched the region of the header to identify the region within the header exhibiting the highest damage coefficient, subsequently assessing its impact on the overall reduction in fatigue life. Intriguingly, the study's findings revealed a lack of correlation between the predicted damage under realistic loading conditions and the known issues observed in the P22 unit.

This observation led to the hypothesis that the strength of the ex-service unit had been altered by the prior service exposure. It is well documented that prolonged exposure to high temperatures can result in carbide coarsening and phase changes in 2.25Cr-1Mo steel. Test specimens were taken from the ex-service unit and subjected to uniaxial testing at various temperatures to substantiate this hypothesis. This data was used to calibrate a new material model for the P22 alloy. An identical header configuration was reviewed using two sets of material properties to elucidate the differences between the materials. The first header was modeled using properties characteristic of virgin material, while the second incorporated properties derived from the ex-service test specimens. In order to accurately capture and compare the behavior of these materials, a Non-Linear Kinematic Hardening, NLKH, model was selected. This choice was motivated by the NLKH model's capability of capturing cyclic behavior in metals and the relative simplicity of obtaining coefficients. The coefficients for the model were acquired by evaluating test and publicly available data. To aid the comparison of the material's response, simplified loading conditions were established to represent a common start-up and shut-down cycle, as well as a common and limit case transient within the tube header junction.

The concluding segment of the project focuses on evaluating damage mechanisms in the P22 header. This evaluation consists of iteratively propagating a theoretical crack using an algorithmic approach. The theoretical crack is incorporated into the header using Abaqus' seam crack capability. Then, by combining Paris law and an algorithmic approach, the crack is propagated through the material. The crack propagation phase of modeling incorporates the sub-modeling approach, which allows for high levels of accuracy to be obtained in an efficient manner. The results are then compared to those found using XFEM to propagate the crack. By applying these dual techniques, the study aims to provide a basic understanding of crack growth behavior in a P22 header using the techniques available in Abaqus. This study establishes a

comprehensive framework for evaluating headers and similar components subjected to thermomechanical fatigue. Our methodology, which integrates advanced material modeling with fatigue analysis, offers a replicable framework for other researchers.

## DEDICATION

To my wife and family for their unwavering encouragement and belief in me.

## ACKNOWLEDGEMENTS

I am thankful to all the faculty members and colleagues who have contributed to my academic journey.

I would like to extend my appreciation to the Electric Power Research Institute, the Department of Energy, and UNC Charlotte for their financial support, which has made this research possible.

## TABLE OF CONTENTS

LIST OF TABLES	xi
LIST OF FIGURES	xiii
LIST OF ABBREVIATIONS	xxii
CHAPTER 1: INTRODUCTION	1
1.1. Background and Motivation	1
1.2. Scope and Organization	3
CHAPTER 2: Literature Review	5
2.1. Introduction	5
2.2. Literature Review	6
2.3. Overview of metals and alloys	16
2.4. Material behavior modeling	22
2.4.1. Plastic deformation	22
2.4.2. Cyclic plasticity	24
2.4.3. Time-dependent plasticity	31
2.5. Fatigue	33
CHAPTER 3: Service life comparison of IN740 P22 P91 steam headers	41
3.1. Introduction	41
3.2. Geometric Design	42
3.3. Design loading conditions	46
3.4. Thermal-mechanical analysis	50
3.5. Fatigue life predictions	63

3.6. Conclusion	69
CHAPTER 4: Service exposure effects on 2.25Cr-1Mo steam header service life	71
4.1. Introduction	71
4.2. Experimental Characterization	74
4.2.1. Experimental results	74
4.2.2. Identification of Parameters	77
4.3. Fatigue life predictions	85
4.4. Boundary Conditions	86
4.5. Results and Discussion	92
4.6. Conclusion	105
CHAPTER 5: Comparison of Crack Propagation Methods in a 2.25Cr-1Mo steam header	107
5.1. Introduction	107
5.2. Material Properties and Boundary Conditions	107
5.2.1. Material Properties	107
5.2.2. Boundary Conditions	109
5.3. Automated Iterative Method	114
5.3.1. Theory	114
5.3.2. Automation Methodology	117
5.3.3. Calibration of finite element model	121
5.4. Crack growth analysis	132

5.5. XFEM Fatigue Analysis	145
5.5.1. Background	145
5.5.2. Modeling Approach	147
5.5.3. Fatigue Analysis	150
5.6. Method Comparison	154
5.7. Conclusion	156
CHAPTER 6: CONCLUSIONS AND FUTURE WORK	158
6.1. Research Goals	158
6.2. Conclusions	159
6.3. Future Work	162
REFERENCES	166

## LIST OF TABLES

TABLE 2.1: Element composition of virgin 2.25Cr-1Mo material in mass%. [1]	16
TABLE 2.2: Mechanical properties of ASTM-A335 2.25Cr-1Mo material. [2]	19
TABLE 2.3: Element composition of virgin 9Cr-1Mo-V P91 material in mass%. [2]	19
TABLE 2.4: Mechanical properties of ASTM-A335 9Cr-1Mo-V material. [2]	19
TABLE 2.5: Element composition of IN740H material in mass%.	20
TABLE 3.1: Minimum wall thickness in accordance with PG27.2.2	43
TABLE 3.2: Temperature dependent elastic perfectly plastic parameters for P22.	43
TABLE 3.3: Temperature dependent elastic perfectly plastic parameters for P91.	44
TABLE 3.4: Temperature dependent elastic perfectly plastic parameters for IN740H.	44
TABLE 3.5: Finalized Wall Thickness.	44
TABLE 3.6: Cost Estimate.	70
TABLE 4.1: Temperature dependent Chaboche NLKH parameters for service exposed P22.	79
TABLE 4.2: Temperature dependent parameters for both P22 models.	81
TABLE 4.3: Comparison of $k'$ and $n'$ values at different temperatures for virgin and service-exposed materials.	83
TABLE 4.4: Temperature dependent Chaboche NLKH parameters for virgin P22.	83
TABLE 4.5: Comparison of C and ( $\beta$ ) values at different temperatures.	86

TABLE 4.6: Predicted Lifetime of Header.	104
TABLE 5.1: Temperature dependent material properties models.	109
TABLE 5.2: Temperature-dependent Paris law parameters.	109

## LIST OF FIGURES

FIGURE 2.1: Micrograph of P22 after normalization and tempering. [3]	17
FIGURE 2.2: Micrograph of P22 after prolonged service exposure. [1]	18
FIGURE 2.3: Micrograph of P91 after normalization and tempering. [4]	20
FIGURE 2.4: Micrograph of IN740H after heat treatment. [5]	21
FIGURE 2.5: 2D Isotropic hardening representation. [6]	24
FIGURE 2.6: 2D Kinematic hardening representation. [6]	25
FIGURE 3.1: Finalized dimensions of the P22 header	45
FIGURE 3.2: Finalized dimensions of the P91 header	45
FIGURE 3.3: Finalized dimensions of the IN740 header	46
FIGURE 3.4: Sample of provided operating data. [6]	47
FIGURE 3.5: Representative transient cycle. [6]	48
FIGURE 3.6: P91 boundary conditions, representative of all of the models.	49
FIGURE 3.7: Final mesh for the P22 model 42,772 C3D20RT elements.	51
FIGURE 3.8: Final mesh for the P91 model 32,652 C3D20RT elements.	52
FIGURE 3.9: Final mesh for the IN740H model 15,232 C3D20RT elements.	53
FIGURE 3.10: Thermal convergence of interior surfaces in P22 header.	54
FIGURE 3.11: Thermal convergence of interior surfaces in P91 header.	54
FIGURE 3.12: Thermal convergence of interior surfaces in IN740H header.	55
FIGURE 3.13: von Mises distribution and location of critical point in P22.	56
FIGURE 3.14: von Mises distribution and location of critical point in P91.	56

FIGURE 3.15: von Mises distribution and location of critical point in IN740H.	57
FIGURE 3.16: Decomposed stress component response of the P22 header taken at the peak axial location.	58
FIGURE 3.17: Decomposed stress component response of the P22 header taken at the peak radial location.	58
FIGURE 3.18: Decomposed stress component response of the P91 header taken at the peak axial location.	59
FIGURE 3.19: Decomposed stress component response of the P91 header taken at the peak radial location.	59
FIGURE 3.20: Decomposed stress component response of the IN740H header taken at the peak radial location.	60
FIGURE 3.21: Decomposed stress component response of the IN740H header taken at the peak axial location.	60
FIGURE 3.22: Stress in comparison to temperature and time for the P22 header taken at the peak radial location.	61
FIGURE 3.23: Stress in comparison to temperature and time for the P91 header taken at the peak axial location.	62
FIGURE 3.24: Stress in comparison to temperature and time for the IN740H header taken at the peak axial location.	62
FIGURE 3.25: Stress-strain response of the P22 header taken at the peak radial location.	63
FIGURE 3.26: Stress-strain response of the P22 header taken at the peak axial location.	64
FIGURE 3.27: Stress-strain response of the P91 header taken at the peak radial location.	64
FIGURE 3.28: Stress-strain response of the P91 header taken at the peak axial location.	65
FIGURE 3.29: Stress-strain response of the IN740H header taken at the peak radial location.	65

FIGURE 3.30: Stress-strain response of the IN740H header taken at the peak axial location.	66
FIGURE 3.31: Plastic strain magnitude over time for each of the materials.	67
FIGURE 3.32: Plastic strain magnitude distribution in the P22 header.	68
FIGURE 3.33: Plastic strain magnitude distribution in each of the (a) P91 (b) IN740H headers.	69
FIGURE 4.1: Complete strain history of service exposed test sample at 20 °C. [6]	72
FIGURE 4.2: Complete hysteresis history of service exposed test sample at 20 °C. [6]	72
FIGURE 4.3: Complete hysteresis history of service exposed test sample at 300 °C. [6]	73
FIGURE 4.4: Complete hysteresis history of service exposed test sample at 500 °C. [6]	73
FIGURE 4.5: Stable hysteresis response of virgin and service exposed material at 20 °C. [6]	75
FIGURE 4.6: Stable hysteresis response of virgin and service exposed material at 300 °C. [6]	76
FIGURE 4.7: Stable hysteresis response of virgin and service exposed material at 500 °C. [6]	76
FIGURE 4.8: Stable hysteresis loop for service exposed material at 500 °C. [6]	77
FIGURE 4.9: Fitment of $k'$ and $n'$ coefficients for Service-Exposed material. [6]	79
FIGURE 4.10: Chaboche NLKH data vs. data for service exposed material. [6]	80
FIGURE 4.11: Chaboche NLKH data versus experimental data for service exposed material. [6]	80

FIGURE 4.12: Fitment of $k'$ and $n'$ coefficients for Virgin material. [6]	82
FIGURE 4.13: Chaboche NLKH data versus experimental data for virgin material. [6]	82
FIGURE 4.14: Correlation of virgin material data with damage function at 20 ° C.	86
FIGURE 4.15: Correlation of virgin material data with damage function at 300 ° C.	87
FIGURE 4.16: Correlation of virgin material data with damage function at 400 ° C.	87
FIGURE 4.17: Correlation of virgin material data with damage function at 500 ° C.	88
FIGURE 4.18: Correlation of virgin material data with damage function at 600 ° C.	88
FIGURE 4.19: Sample of provided operating data. [6]	90
FIGURE 4.20: Tube temperature comparison for the slow cycle. [6]	90
FIGURE 4.21: Representative slow transient cycle. [6]	91
FIGURE 4.22: Representative rapid-case transient cycle. [6]	91
FIGURE 4.23: Representative startup and shutdown cycle. [6]	92
FIGURE 4.24: Model boundary conditions. [6]	93
FIGURE 4.25: 3D meshed header with 48,736 C3D20RT elements. [6]	93
FIGURE 4.26: Temperature Profile Validation. [6]	94
FIGURE 4.27: Accumulated plastic strain vs. time for rapid-case transient. [6]	95
FIGURE 4.28: Virgin material peak von Mises response to the startup and shutdown transient loading profile. [6]	96
FIGURE 4.29: Virgin material peak von Mises response to the slow transient loading profile. [6]	96

FIGURE 4.30: Virgin material peak von Mises response to the rapid-case transient loading profile. [6]	97
FIGURE 4.31: Service exposed material peak von Mises response to the startup and shutdown transient loading profile. [6]	97
FIGURE 4.32: Service exposed material peak von Mises response to the slow transient loading profile. [6]	98
FIGURE 4.33: Service exposed material peak von Mises response to the rapid-case transient loading profile. [6]	98
FIGURE 4.34: Location of peak stress in response to (a) startup and shutdown (b) common/rapid transient loading profiles. [6]	99
FIGURE 4.35: Stress-strain response of the header to a startup and shutdown loading when virgin material is used. [6]	100
FIGURE 4.36: Stress-strain response of the header to a startup and shutdown loading when service exposed material is used. [6]	100
FIGURE 4.37: Stress-strain response of the header to slow transition loading when the virgin material model is used. [6]	101
FIGURE 4.38: Stress-strain response of the header to slow loading when the service exposed material is used. [6]	102
FIGURE 4.39: Stress-strain response of the header to rapid-case loading when virgin material is used. [6]	103
FIGURE 4.40: Stress-strain response of the header to rapid-case loading when service exposed material is used. [6]	103
FIGURE 5.1: Influence of temperature on crack growth rate and Paris Law fit.	108
FIGURE 5.2: Reference temperature and pressure data for a 24-hour cycle. [7]	110
FIGURE 5.3: Simplified temperature compared to reference data. [7]	111
FIGURE 5.4: Simplified temperature and pressure vs time. [7]	111

FIGURE 5.5: Applied temperature and pressure for crack growth vs time. [7]	112
FIGURE 5.6: Global model boundary conditions. [7]	112
FIGURE 5.7: Global model stress-strain response at the critical point. [7]	113
FIGURE 5.8: Nodes used in a stress contour around the crack front.	115
FIGURE 5.9: Sub-model boundary conditions. [7]	118
FIGURE 5.10: Automated cracked region sub-model tie constraints. [7]	119
FIGURE 5.11: Boundary describing the initial seam crack and the virtual extension directions. [7]	120
FIGURE 5.12: Summary of crack growth modeling procedure.	122
FIGURE 5.13: 3D meshed header with 30,960 C3D20R elements. [7]	123
FIGURE 5.14: Meshed sub-model with 3,564 C3D20R elements. [7]	123
FIGURE 5.15: Location of critical point. [7]	124
FIGURE 5.16: Stress-strain response of sub-model compared to global model at critical point. [7]	125
FIGURE 5.17: Stress-strain response of sub-models compared to global model at critical point. [7]	125
FIGURE 5.18: Meshed crack sub-model at (a) initial state (b) after cycling for thirty-five years. [7]	127
FIGURE 5.19: Stress intensity factor vs time for first five contours at crack header intersection. [7]	128
FIGURE 5.20: Stress intensity factor vs time for first five contours at crack tube intersection. [7]	128
FIGURE 5.21: Stress intensity factor $K_I$ vs angular position for the crack at five years response to pressure. [7]	129
FIGURE 5.22: Influence of pressure on $K_I$ at surface crack locations at five years. [7]	129

FIGURE 5.23: Thermal response of SIF at crack header intersection. [7]	131
FIGURE 5.24: Thermal response of SIF at crack tube intersection. [7]	131
FIGURE 5.25: Evolution of crack front over time. [7]	134
FIGURE 5.26: Incremental crack growth over time. [7]	135
FIGURE 5.27: Time-dependent response of $K_I$ , $K_{II}$ , and $K_{III}$ at the intersection of the crack and the (a) header (b) tube. [7]	135
FIGURE 5.28: Time-dependent response of $K_I$ , $K_{II}$ , and $K_{III}$ at year 5 at the intersection of the crack and the (a) header (b) tube. [7]	136
FIGURE 5.29: Time-dependent response of $K_I$ , $K_{II}$ , and $K_{III}$ at year 10 at the intersection of the crack and the (a) header (b) tube. [7]	136
FIGURE 5.30: Time-dependent response of $K_I$ , $K_{II}$ , and $K_{III}$ at year 15 at the intersection of the crack and the (a) header (b) tube. [7]	137
FIGURE 5.31: Time-dependent response of $K_I$ , $K_{II}$ , and $K_{III}$ at year 20 at the intersection of the crack and the (a) header (b) tube. [7]	137
FIGURE 5.32: Time-dependent response of $K_I$ , $K_{II}$ , and $K_{III}$ at year 25 at the intersection of the crack and the (a) header (b) tube. [7]	138
FIGURE 5.33: Time-dependent response of $K_I$ , $K_{II}$ , and $K_{III}$ at year 30 at the intersection of the crack and the (a) header (b) tube. [7]	138
FIGURE 5.34: Time-dependent response of $K_I$ , $K_{II}$ , and $K_{III}$ at year 35 at the intersection of the crack and the (a) header (b) tube. [7]	139
FIGURE 5.35: Time-dependent response of $K_I$ , $K_{II}$ , and $K_{III}$ at year 40 at the intersection of the crack and the (a) header (b) tube. [7]	139
FIGURE 5.36: $K_I$ along the crack front for the time representing the highest value for the location intersecting the header and tube for the initial crack. [7]	140
FIGURE 5.37: $K_I$ along the crack front for the time representing the highest value for the location intersecting the header and tube for the crack at five years. [7]	140

FIGURE 5.38: $K_I$ along the crack front for the time representing the highest value for the location intersecting the header and tube for the crack at ten years. [7]	141
FIGURE 5.39: $K_I$ along the crack front for the time representing the highest value for the location intersecting the header and tube for the crack at fifteen years. [7]	141
FIGURE 5.40: $K_I$ along the crack front for the time representing the highest value for the location intersecting the header and tube for the crack at twenty years. [7]	142
FIGURE 5.41: $K_I$ along the crack front for the time representing the highest value for the location intersecting the header and tube for the crack at twenty-five years. [7]	142
FIGURE 5.42: $K_I$ along the crack front for the time representing the highest value for the location intersecting the header and tube for the crack at thirty years. [7]	143
FIGURE 5.43: $K_I$ along the crack front for the time representing the highest value for the location intersecting the header and tube for the crack at thirty-five years. [7]	143
FIGURE 5.44: $K_I$ along the crack front for the time representing the highest value for the location intersecting the header and tube for the crack at forty years. [7]	144
FIGURE 5.45: Boundary conditions used in XFEM model. [7]	148
FIGURE 5.46: Surface used to define initial crack front in XFEM. [7]	149
FIGURE 5.47: Meshed crack sub-model for (a) complete cycle (b) validation. [7]	150
FIGURE 5.48: 3D meshed header for XFEM with 31,544 C3D8R elements. [7]	151
FIGURE 5.49: Crack front evolution with respect to mesh size. [7]	152
FIGURE 5.50: Crack propagation along tube at (a) initial (b) 5 years (c) 10 years. [7]	152

FIGURE 5.51: Crack propagation along header at (a) initial (b) 5 years (c) 10 years. [7] 153

FIGURE 5.52: Crack growth increments over time. [7] 153

FIGURE 5.53: Crack front evolution over time. [7] 154

## LIST OF ABBREVIATIONS

ASME	American Society for Mechanical Engineers
ASTM	American Society for Testing and Materials
BM	Base Metal
BPVC	Boiler and Pressure Vessel Code
CFD	Computational Fluid Dynamics
EPP	Elastic Perfectly Plastic
EPRI	Electric Power Research Institute
FEA	Finite Element Analysis
HAZ	Heat Affected Zone
HCF	High Cycle Fatigue
LCF	Low Cycle Fatigue
LEFM	Linear Elastic Fracture Mechanics
NIMS	National Institute for Material Science
NLKH	Non-linear Kinematic Hardening
SECC	Semi-Elliptic Corner Crack
SIF	Stress Intensity Factor
VCCT	Virtual Crack Closure Technique
WM	Weld Metal
XFEM	Extended Finite Element Method

## CHAPTER 1: INTRODUCTION

### 1.1 Background and Motivation

The endless pursuit for improved efficiency and performance in power generation has led to increased cyclic loading on many power generation components. These components, ranging from combustors to heat exchangers, are exposed to harsh environments subjected to high temperatures, pressures, and corrosive environments. Understanding the reliability and longevity of these components is critical to avoid premature failures and costly shutdowns. In this context, the present work focuses on steam headers as a primary example of high-temperature components subjected to fatigue. One of the most significant challenges limiting the longevity of steam headers is understanding the influence of fatigue damage. Fatigue is characterized by the accumulation of inelastic strains that result in the formation and propagation of cracks. Elevated temperatures can often accelerate the accumulation of fatigue damage, presenting a burdensome challenge in the design and maintenance of steam headers. The primary objective of this study is to assess the low cycle fatigue response of a steam header, demonstrating how finite element analysis, FEA, can be used to deliver accurate solutions in addressing this challenge.

The occurrence of fatigue is dependent on several factors, such as the material, temperature, and operating environment. Within the context of steam headers, several alloys are commonly found, such as 2.25Cr-1Mo, 9Cr-1Mo-V, and 304. However, it is noteworthy that many components designed prior to the prevalence of P91 were originally constructed using low alloy steels such as 1.25Cr0.5MoV, 0.5CrMoV, and 2.25Cr-1Mo [8]. During the time when first-generation units were designed, operational temperatures typically remained below 540 °C, and pressures were maintained

below 16 MPa [9]. However, throughout the 1970s and into the 1990s, the goal to improve efficiency resulted in increased temperatures and pressures [10]. These factors resulted in elevated levels of fatigue stress, particularly affecting the thick-walled section components. During this era, the limited number of energy-producing sources ensured relatively consistent operating conditions. However, with additional sources becoming available, there has been a decreased reliance on the energy found in combined cycle systems, resulting in increased cyclic operation. This added complexity exacerbates the challenges associated with fatigue in these components, leading to more frequent failures.

To address these challenges, engineers have explored various strategies. One approach involves transitioning to more creep-resistant alloys with higher strength at elevated temperatures. These advanced materials, such as 9Cr-1Mo-V, 304, and IN740H, allow for a reduction in the wall thickness of existing components. This reduction in wall thickness results in lower thermal stresses during thermal transients, ultimately leading to reduced fatigue damage. Furthermore, as designers continually aim to improve efficiency, it is possible that future operating temperatures may rise to levels unsuitable for low-alloy steels. Therefore, an alloy that exceeds current demands could prove more resilient to future operating conditions. However, it's essential to consider the point of diminishing returns, where the cost of transitioning to a high-performance alloy may not be justified by improved longevity. For that reason, the present work begins by evaluating a cost-benefit comparison of three alloys, 2.25Cr-1Mo, 9Cr-1Mo-V, and IN740H, seeking to strike a balance between enhanced resilience and economic feasibility.

In addition to consideration of the cost-benefit comparison of alloys, another critical aspect lies in how material properties are chosen for comparison. For instance, it is widely recognized that certain alloys, like 2.25Cr-1Mo and 9Cr-1Mo-V, exhibit changes in strength over time [11–13]. To assess the impact of these changes on

a 2.25Cr-1Mo header, the present work compares fatigue life predictions based on material properties derived from virgin material to those obtained from ex-service headers. After determining the influence that material selection may have on service life, our investigation concludes with an evaluation of fatigue crack propagation within the header.

## 1.2 Scope and Organization

The dissertation is structured into six chapters, each focusing on different aspects related to the design of an outlet header. Chapter 1 presents some of the basic background and motivations for the current work. Chapter 2 presents a literature review encompassing a broad review of the work done surrounding headers and the types of analyses that have been done. This is followed by an overview of the materials considered for the scope of this work and the mathematical foundations used in modeling the material's behavior. Chapter 3 presents the process to establish the geometric design of the headers considered for the experimental trials. This chapter outlines the process of utilizing the provided project information to finalize the design considerations for other materials. This chapter outlines the design parameters that serve as the basis of this study's trials, demonstrating how the information provided by EPRI is used with ASME BPVC to establish new designs. This is followed by the cost-benefit analysis completed to compare the implementation of P22, P91, and IN740. The material properties were taken from the literature. The designs are exposed to representative operational plant data. The life prediction for each design is presented based on the damage taken using the critical plane technique. An approximate cost-benefit analysis is also presented. Chapter 4 presents the experimental results found from the material samples and how they are used to establish the constants used in the material models. Material samples were taken from an ex-service header unit with over 100,000 hours of service exposure. These samples were then machined and tested at various temperatures using strain-controlled testing. The resulting information was

used to characterize the material and provide a comparison for the virgin alloy. The assumptions made during the parameter process are provided along with their justification. This is followed by the results of service exposure on the life expectancy of the P22 header. The influence of service exposure is extrapolated by applying the material properties identified from service-exposed material to the P22 header. The geometry is exposed to several transients to represent various loading conditions that could be applied. Comparisons are made by evaluating the same thermal transients in Chapter 5 presents the results of a postulated crack growing in an elastic P22 header. This section uses a sub-modeling approach to iteratively evaluate crack growth within a simplified P22 header. The results are compared to those found using XFEM and Abaqus's fatigue capability. The elastic material properties are taken from the literature and combined with linear elastic fracture mechanics, LEFM, and the seam crack approach. A representative thermo-mechanical cycle is applied to demonstrate the growth of a postulated crack over time. The results demonstrate that combining the algorithmic approach with the sub-modeling technique provides a methodology capable of evaluating planar crack growth without external programs. Chapter 6 presents the present work's key conclusions and possible avenues for future work.

## CHAPTER 2: Literature Review

### 2.1 Introduction

Understanding the significance of materials in component design is essential, specifically when parts are subjected to high temperatures and cyclic fatigue. In these conditions, details such as the composition and hardening mechanisms become very important to understand. Additionally, it is important to understand how these phenomena can be represented with computational models. With the incorporation of FEA, designers can predict a component's material behavior and fatigue. These topics are fundamental to understanding the performance of a header commonly found in combined cycle power plants. The harsh environment and cyclic loading often test the limits of the material. Therefore, the dissertation will initially introduce the necessary background related to evaluating components at high temperatures.

This section is followed by an outline of several prevalent methods to represent material plasticity. Given that there are distinct reasons a material accumulates plasticity, it is important to determine the specific cause responsible for the plastic deformation. The accuracy of the material model employed significantly influences the anticipated response. A misalignment between the selected material and model may result in overlooking certain aspects of plasticity. For instance, components enduring prolonged elevated temperatures and stresses may require the addition of time-dependent attributes to align with observed material behavior. Hence, the subsequent section introduces the fundamental principles of fatigue, outlining the underlying mechanisms and prevalent methodologies for failure prediction. Expanding upon this foundation, the following section introduces the theory of cracks, recognizing their pivotal role in initiating and propagating fatigue-induced failures. This

section will present an overview of various models, including Paris law and J-integral, aimed at characterizing crack behavior.

## 2.2 Literature Review

In the coming decades, the shift towards renewable energy sources is expected to significantly modify the landscape of power generation. Solar, geothermal, biomass, wind, hydro, and nuclear alternatives are projected to witness substantial growth. One report forecasts a future where, by 2050, wind energy becomes the predominant source of power in Texas, marking a significant departure from traditional energy sources [14]. This transition expects a shift in surge power generation from the current gas turbines to wind energy, while coal remains a primary energy source. Meanwhile, solar energy is anticipated to play a pivotal role in facilitating the move away from coal. Despite these shifts, natural gas systems are expected to maintain an essential role, particularly in meeting peak energy demands, albeit with a reduced contribution to overall energy production.

The dynamic future role nature of gas energy production following peak demand and consumption patterns introduces new challenges, especially in terms of the durability of power generation infrastructure. One study highlights the detrimental effects of increased cyclic operation in turbine generators, leading to accelerated wear on critical components, including rotors, casings, airfoils, and headers [15]. The findings highlight the significant impact that transitioning energy sources will have on the durability of existing systems.

Many have already begun exploring alternative materials for use in components that experience high stress and adverse environments, such as headers, is driven by several key factors. These include the need for improved oxidation resistance, enhanced creep performance, and greater fracture toughness. One component vital in natural gas power generation systems are headers. Headers are often evaluated for improved materials because they are routinely subjected to conditions that challenge

their longevity.

One of the primary concerns with headers is their exposure to harsh environments, which can lead to a variety of failure mechanisms. Thermal-mechanical fatigue, temper embrittlement, creep, and corrosion, compounded by the susceptibility of numerous welds to defects and residual stresses, are notable contributors to header failure. For instance, research conducted by Ahmadi et al. highlights that surface pitting from oxidation can create stress risers, facilitating crack initiation and propagation. As these cracks develop, ongoing oxidation exacerbates their growth, emphasizing the advantage of materials with reduced oxidation susceptibility [16].

Further complications stem from the system connections within headers, particularly between boreholes that link tubes. Stresses at these junctures, when combined with the deleterious effects of oxidation, have been shown to promote the development of radial cracks, presenting a significant risk to the component's structural integrity [17]. This issue is compounded by findings that fatigue, in environments that promote oxidation, can accelerate the expansion of minor cracks, a phenomenon supported by multiple studies [18–23]. The process known as oxide-notching, where the formation of oxides initiates crack formation, further emphasizes the role of selecting materials that can withstand operational demands while minimizing the risk of oxidation-induced damage.

Significant attention has been directed towards evaluating alternatives capable of offering enhanced creep resistance. One alternative, MarBN steel, has demonstrated its potential to surpass traditional materials like P91 in applications such as outlet headers by providing improved creep rupture strength over extended periods [24, 25].

In addition to MarBN steel, materials such as 316L have been considered for their superior corrosion resistance, an attribute critical for extending the lifespan of components exposed to corrosive environments [26, 27]. Meanwhile, comparative studies have established that P91 exhibits greater creep resistance than P22, suggesting that P91

may offer a balance of strength and durability favorable for use in high-temperature applications [28].

However, the selection of materials for high-performance applications must also take into account other factors, such as the behavior of welds under operational conditions. Some studies have indicated that welds in P91 systems exhibit a greater susceptibility to creep-fatigue interactions compared to those in P22 systems despite the superior base material characteristics of P91 [8]. This highlights the complexity of material selection, where focusing exclusively on a single property, such as oxidation resistance, might inadvertently overlook vulnerabilities in other areas. Continuing with the concept of evaluating material selection, the current work aims to conduct a comprehensive comparison of the viability of using P91, IN740H, and P22 materials. The process will evaluate the strengths and weaknesses of each material across a range of performance indicators, including fatigue resistance and cost. This analysis seeks to provide a deeper understanding of the most suitable materials for a replacement header, thereby contributing to the development of a more durable energy system.

The base material in consideration, P22, is widely known for its susceptibility to weakening from environmental factors. One mechanism identified as a cause is the transformation of  $M_2C$  to  $M_6C$  carbides within the ferrite matrix, significantly diminishing the material's strength [29]. Additionally, investigations have found that the fracture toughness of 2.25Cr-1Mo steels diminishes in hydrogen-rich environments, highlighting the impact of environmental conditions on material integrity [30]. Expanding on causes for material degradation, Ahn et al. explored the phenomenon of hydrogen-assisted crack growth. Through their modeling of voids in embrittled material, they demonstrated the reduction in material strength associated with environmental degradation, specifically highlighting the detrimental impact of hydrogen on the integrity of materials [31]. Whittaker et al. have also noted a substantial decrease in the creep strength of G22 steels, stemming from the transformation of

bainitic regions into ferrite and the formation of coarse molybdenum carbides [32].

These observations align with other studies focused on the examination of materials after service. The consensus among these studies is that the transformation processes occurring within ex-service materials significantly contribute to their degradation. These transformations encompass a range of structural changes that adversely affect the material's mechanical properties, including creep resistance and fracture toughness [12, 33–36].

Similar studies have been conducted on other materials, such as P91. Studies have indicated that G91 steels exhibit an enhanced stability of the lath structure compared to other low alloy steels, highlighting a potential advantage in terms of microstructural integrity [37]. Yet, the durability of these lath structures, and consequently their resistance to creep and fatigue, appears to be heavily influenced by the operational conditions they encounter, including temperature and strain range [38–41]. The influence that the properties representing the material behavior can have on the result is demonstrated in the work by Moslemi et al. Their work evaluated the sensitivity of 316L to the coefficients of the Chaboche NLKH in the prediction of ratcheting [42]. These examples highlight the need for a comprehensive understanding of material behavior to verify the reliability of the materials in practical applications.

The interaction between material properties and structural integrity, particularly in the context of welded joints in steam outlet headers, has garnered significant interest in recent engineering research. Welds within headers are frequently identified as critical points for failure due to various factors. One study by Ragab et al. focuses on understanding the impact of weld metal on the fatigue life of a tube-header intersection. Their findings indicate that creep crack initiation is most likely to occur at the boundary between the base metal, BM, weld metal, WM, and the heat-affected zone, HAZ, a conclusion that aligns with damage observed in specimens taken from operational settings [43].

The variation in hardness across the HAZ has been linked to the formation of coarsened carbides that form during welding procedures. This phenomenon contributes to the complexity of assessing weld integrity and performance under operational stresses [44]. To address these challenges, some researchers have advocated for a detailed analysis of the failure assessment properties for the HAZ, WM, and BM individually. This approach enables a more nuanced understanding of the material behavior across different sections of a welded joint, thereby enhancing the accuracy of failure predictions [45, 46].

Building on these insights, Zhou et al. explored the microstructural transitions within the HAZ, particularly noting the shift from coarse-grained to fine-grained structures. Their research underscores the critical role of this transition in damage initiation, pointing out that the change from fine grain HAZ to inter-critical HAZ marks a pronounced alteration in lath size and yield strength, which significantly influences the material's vulnerability to damage [47]. This phenomenon was further corroborated by Li et al., who examined the fatigue response of material in a T-joint configuration. Their work highlights how plastic strains accumulate at the onset of the HAZ, acting as a mediator between the more rigid weld metal and the base material, thereby indicating the HAZ's critical role in the structural integrity of welded assemblies [48].

Managing the effects of the HAZ presents considerable challenges due to the complexity of welding operations. Research has highlighted that variables such as heat input during welding significantly impact the material's toughness, emphasizing the need for precise control over welding parameters to ensure optimal material performance [49].

Studies have shown that the interaction between the fatigue history and subsequent creep fatigue within the weld zone can significantly compromise the integrity of the weld, adversely affecting its longevity and performance [50]. In line with this,

Segle et al. incorporated a method that integrated the HAZ, BM, and WM's distinct properties to evaluate a weld specimen's failure response. By incorporating the weld metal characteristics into an Abaqus model through a user-defined material subroutine, they were able to capture the failure mechanism within the welded structure [51]. Another study also found that stress concentration leads to ductile fractures in tubes welded to the headers [52]. Furthermore, an example of Holmstrom's use of Abaqus for modeling creep at welds demonstrates the potential of computational methods to improve our understanding of material responses under operational stresses [53].

Weld regions are also critical to evaluate when considering alternative materials to incorporate into an existing system. As previously indicated, the regions around welds in engineering structures are prone to creep-fatigue damage, a vulnerability exaggerated when the welds involve the joining of dissimilar metals. The inherent differences in material properties between these metals, compounded by the effects of the HAZ, cause variations in strength across the weld interface. This disparity often results in significant stress concentrations as the material undergoes transitions under operational loads [54].

Moreover, the resistance to oxidation ostensibly varies significantly across these junctions, adding another layer of complexity to the durability of welded regions. In a study conducted by Mittal and Sidhu, it was observed that the weld junction between T22 and P91 metals exhibited a higher rate of oxidation compared to the parent metals. This accumulation of oxides can further compromise the structural integrity of the weld area, highlighting the critical need for considering oxidation resistance in the selection of welding materials [55]. The complexity of material behavior under operational conditions is further exemplified by a case study involving specimens from a failed steam drum. The analysis indicated that in-process weld repairs on materials previously exposed to erosive environments could introduce additional contaminants into the weld area. Such contamination often accelerates the onset of cracking and

subsequent failure, underscoring the intricate interplay between material treatment, environmental exposure, and component longevity [56].

The creep-fatigue interaction at these weld junctions makes the regions more susceptible to accelerated damage and can lead to specific failure mechanisms, such as cavitation. Laha et al.'s investigation into the weld between 2.25Cr-1Mo and IN800 materials revealed that the transition zone is particularly susceptible to the formation of cavities under creep-fatigue conditions [57].

These studies collectively demonstrate the complex interplay between material properties, operational stresses, and environmental factors in determining the longevity and reliability of welds, especially those involving dissimilar metals. Understanding these dynamics is essential for optimizing material selection to mitigate the risks of creep-fatigue damage oxidation and improve the header's longevity.

The application of FEA in evaluating the service life of heat exchangers has garnered significant attention within the engineering community. A series of studies by Zhao et al., Patil et al., Okrajni et al., Kwon et al., Chen et al., and Ma et al. have collectively demonstrated the utility of FEA in predicting fatigue failure and aiding design improvements in heat exchangers across a variety of industries. These investigations highlight the critical role of FEA in improving the predictions of service life and identifying potential areas for improvement [58–64].

FEA can be used to aid in the design of components. For instance, Selvan et al. explored the impact of tube spacing on the fatigue response of a header component. Their findings shed light on the relationship between design parameters and the structural durability of outlet headers, emphasizing the significance of the design analysis in optimizing the longevity of the header [65]. Additionally, Rouse et al. examined the influence of tube spacing on thermal gradients and its subsequent impact on the fatigue life of an outlet header. Their investigation highlights the critical role of geometric factors in the design and maintenance of heat transfer systems [66].

In a similar vein, Farragher et al. assessed the fatigue life of an outlet header fabricated from P91 steel, applying the critical plane approach to evaluate the effects of cyclic loading [67]. The work on fatigue analysis critically relies on the ability to capture individual cycles. Azamfar et al., Chen et al., Zhu et al., and Wang et al. have made significant contributions to the field of cycle counting methods. Their research focuses on evaluating material responses under randomized loading conditions, helping advance the accuracy of fatigue life assessments. These methodologies are vital for the design and longevity of structures subjected to complex loading scenarios [68–71].

Moreover, the interplay between creep and fatigue in contributing to crack growth within headers has been the subject of detailed investigation. Moussavi et al.’s study on this topic revealed that creep, rather than fatigue, plays the dominant role in reducing the service life of headers. This finding highlights the necessity of focusing on creep resistance in the material selection and design process for components expected to operate under conditions conducive to creep [72]. Others have also demonstrated how creep can be detrimental [73].

Given these complexities, some researchers advocate for a multifaceted approach to assessing material durability. Specifically, the combination of the Palmgren-Miner rule with considerations for creep, fatigue, and environmental effects has been suggested as a comprehensive framework for evaluating material performance under varied operational stresses [74]. This methodological advancement proposes an integrated strategy for understanding and predicting the lifespan of materials in environments where multiple factors contribute to degradation, offering a path toward more reliable and accurate life predictions for critical components.

The presence of cracks can significantly influence the durability and operational reliability of headers. One self-evident finding is that the presence of cracks can lead to underestimations of fatigue life when relying solely on fatigue for assessments [75]. This highlights the need for a more nuanced understanding of material behavior

beyond what conventional guidelines can provide. Subsequently, the final portion of the present work demonstrates the ability to model crack growth within a header. It is widely noted that headers can remain operational even with visible cracking. For instance, a study examining headers with cracks up to 0.08 inch in depth determined that these components could still meet the criteria for continued service until the next inspection interval [76]. This finding, supported by similar research [77–81], demonstrates that potential defects can exist within operational tolerances. Similar to fatigue, the load history of a component influences the crack growth behavior. Gaur et al.’s investigation into the effect of the R-ratio on the fatigue response of materials enriches our understanding of how different stress ratios affect material fatigue life [82]. This knowledge can be applied to FEA models to help gain a clearer understanding of crack growth. For instance, Sun’s work uses Abaqus for an elastic crack analysis in pressure vessels subjected to thermal shock [83]. Additionally, the works of Zheng et al. and Lei et al. demonstrate the application of Abaqus in evaluating static crack behavior through the use of various constraint methodologies [84,85].

Building on the theme of computational analysis, Kumar et al. adopted Abaqus for the finite element analysis of bending beam cracks, applying LEFM. Their research offers a detailed understanding of crack behavior under bending loads, which plays a crucial role in designing structures that exhibit improved fracture resistance [86]. In a similar vein, Lee et al. leveraged the Seam Crack method in Abaqus to evaluate the SIF of theoretical corner cracks [87]. Focusing on the specifics of material composition, Li et al. explored how cladding influences the SIF of seam cracks [88]. Another common approach to modeling crack growth incorporates the concept of strain energy density. For instance, the work by Wang introduces the concept of strain energy to evaluate the fatigue life under variable loading [89]. The concept relies on the premise that a material will fail after a threshold of strain energy is met.

Therefore, the summation of multiple cycles allows for the calculation of fatigue life. Similarly, Nevcemer et al. have extended the application of energy-based methods to the study of fracture behavior in aluminum single-edge notched specimens and auxetic structures. Through a combination of experimental work and modeling studies utilizing the inelastic strain energy method in Abaqus, they were able to demonstrate the degradation of a material due to fatigue [90,91].

Further extending the scope of computational fracture mechanics, several studies have explored the application of the XFEM within Abaqus to delve into the fracture mechanics of pressure vessels under thermal transients [92–94]. Another example by Dominguez et al. demonstrates the use of XFEM within Abaqus to examine the growth of corner cracks in nozzles. Their work is particularly relevant to components found in pressure vessels such as headers [95].

Further advancing to the field of crack propagation, Shahani has proposed an innovative technique for simulating dynamic crack propagation using ANSYS. By incorporating an automated re-meshing strategy, this approach allows for precise modeling of crack evolution and its effects on the structural integrity of heat exchangers [96]. In parallel, Malekan et al. have focused on making crack growth propagation simulations more accessible to the engineering community. By developing a plug-in for Abaqus, they have provided a user-friendly interface for conducting detailed studies on crack behavior in various structures [97]. Further contributing to the body of knowledge on crack propagation, Liu et al. utilized FRANC3D software alongside ANSYS for iterative simulations of crack growth under diverse loading conditions [98]. These tools serve as inspiration for the final project, which incorporates an automated crack growth procedure into Abaqus for semi-elliptic corner cracks. Collectively, these studies represent the existing and emerging work in materials research, offering novel insights and methodologies for addressing the challenges posed by cyclic loading and high-temperature conditions.

### 2.3 Overview of metals and alloys

The oldest material being considered in the present work is 2.25Cr-1Mo P22. Originally developed in the 1950s, P22 had specific benefits against creep at temperatures up to 650°C [1]. This feature and its relatively low cost led to its widespread adoption in many components of early power plants. While 2.25Cr-1Mo is available in multiple heat treatments, the specification commonly found in power systems is identified as ASTM A335 [2,99]. This condition of the material is achieved through a heat process of tempering and normalizing. During this process, carbides are formed, providing strength to the material. Similarly, the material’s corrosion resistance stems from the addition of chromium. The composition of P22 is shown in table 2.1 [1].

Table 2.1: Element composition of virgin 2.25Cr-1Mo material in mass%. [1]

Material	C	Si	Mn	P	S	Cr	Mo	Fe
P22	0.08	0.24	0.46	0.007	0.002	2.26	1.00	Bal.

The microstructure of P22 steel is determined by its chemical composition and the specific heat treatment it undergoes. However, to achieve the desired mechanical properties and microstructure, P22 seamless pipes are normalized and tempered, a process standardized in accordance with ASTM-A335 [99]. The result is a microstructure with precipitates with the matrix reference [100]. The carbide precipitates within P22 steel play a significant role in its strength by inhibiting dislocation movement, with their size and spacing being key factors. Initially, smaller, closely spaced carbides effectively obstruct dislocations, enhancing the material’s strength. However, prolonged exposure to elevated temperatures increases the size and spacing of these carbides, which correspondingly diminishes the material’s strength. This reduction in strength is attributed to the transformation of the carbides from a high surface energy planar structure to a more stable spheroidal shape, driven by the material’s tendency to minimize energy [101]. Figure 2.1 illustrates the microstructure of P22 steel in

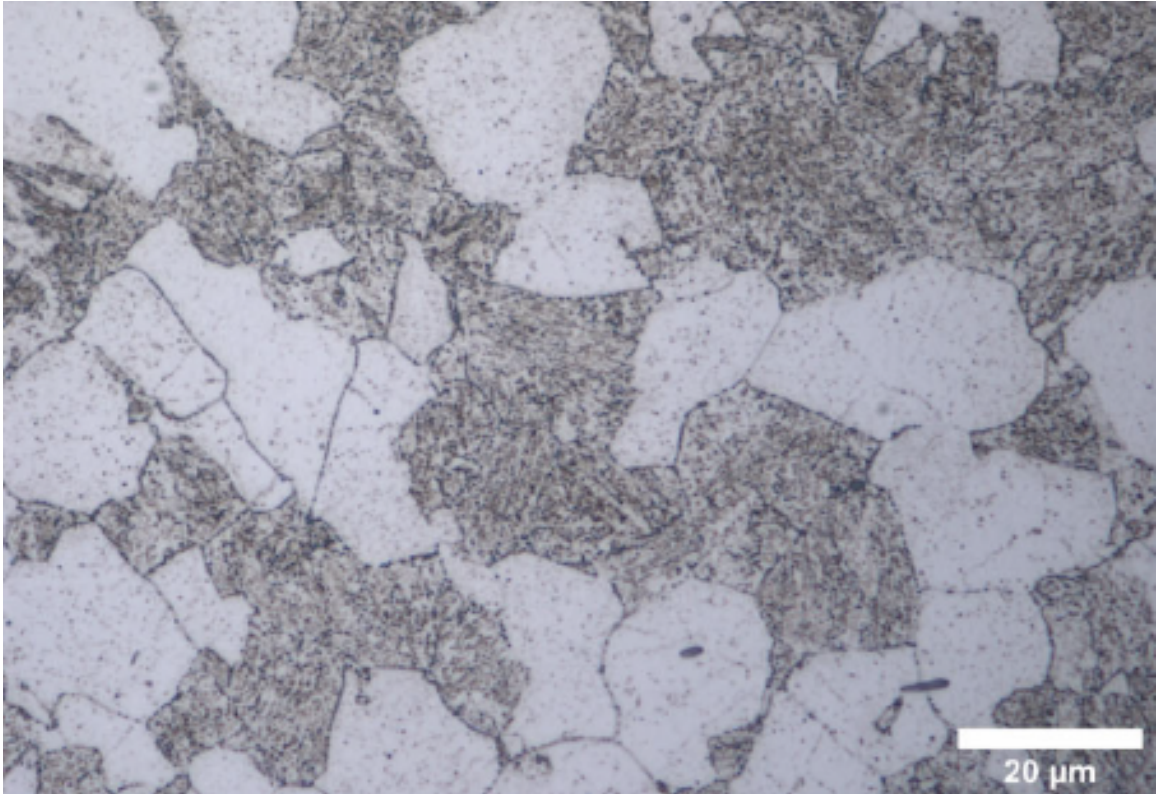


Figure 2.1: Micrograph of P22 after normalization and tempering. [3]

the normalized and tempered condition, while Figure 2.2 shows the same steel after long-term service at elevated temperatures [1, 3]. These micrographs highlight the evolution of P22 steel's structure, demonstrating the changes induced by prolonged exposure to high heat.

The base material properties used for P22 throughout this work are taken from ASME BPVC Section 2 Part D. The material properties used to represent 2.25Cr-1Mo, unless otherwise specified, are shown in Table 2.2 [2].

While P22 was widely used throughout plants early on, prolonged exposure to high temperatures would often lead to failures. Therefore, modern systems have switched higher temperature components to more resilient alloys such as P91. P91 steel offers improved creep in oxidation resistance at elevated temperatures. An example of the composition of P91 is shown in Table 2.3 [2].

The improved performance of P91 over P22 stems from the significant addition of

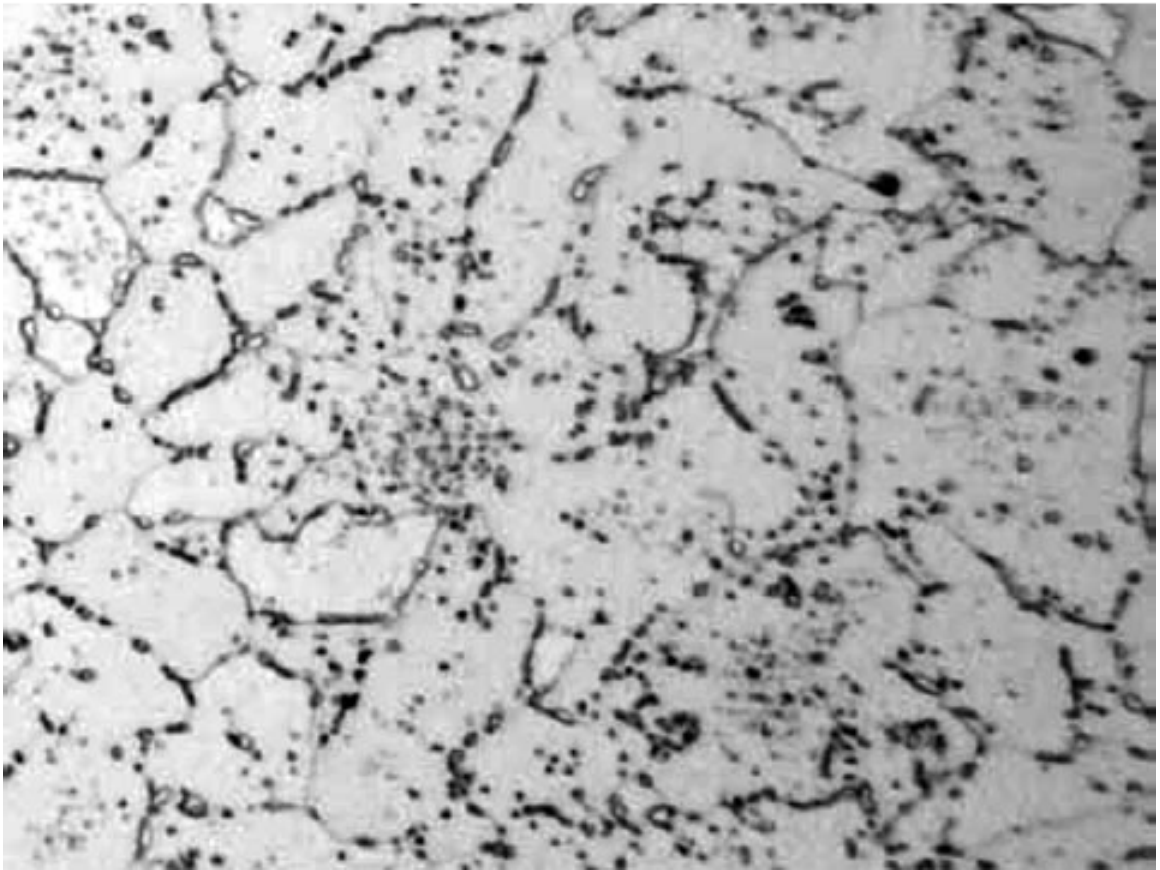


Figure 2.2: Micrograph of P22 after prolonged service exposure. [1]

Table 2.2: Mechanical properties of ASTM-A335 2.25Cr-1Mo material. [2]

T °C	0.2% Proof Stress MPa	Tensile Strength MPa	Elastic Modulus GPa
RT	433	589	208
300	391	510	195
400	387	501	189
500	354	438	178
600	283	329	162

Table 2.3: Element composition of virgin 9Cr-1Mo-V P91 material in mass%. [2]

Material	C	Mn	P	S	Si	Cr	Mo	V	N	Ni	Al	Nb	Fe
P91	0.08 0.12	0.30 0.60	0.02 Max	0.01 Max	0.20 0.50	8.00 9.50	0.85 1.05	0.18 0.25	0.03 0.07	0.40 Max	0.02 Max	0.06 0.10	Bal

chrome combined with traces of Vanadium and Niobium. This results in the normalized and tempered microstructure with a martensitic microstructure with dispersed carbides [100]. An example of the martensitic structure is shown in Figure 2.3 [4].

In a manner similar to P22, the carbide within the P91 steel evolves with time being held at elevated temperatures, eventually leading to a less robust material. The material properties used for P91 in the comparison were also taken from ASME BPVC II-D [2]. The material properties representing P91 are shown in table/reference [2].

Table 2.4: Mechanical properties of ASTM-A335 9Cr-1Mo-V material. [2]

T °C	0.2% Proof Stress MPa	Tensile Strength MPa	Elastic Modulus GPa
RT	414	589	213
300	377	510	195
400	358	501	187
500	306	438	179
600	218	329	168

As previously mentioned, both P91 and P22 soften with prolonged exposure to temperatures in excess of 550 ° C. Additionally, at these temperatures, both materials see significant reductions in their allowable stresses in comparison to room temperature.

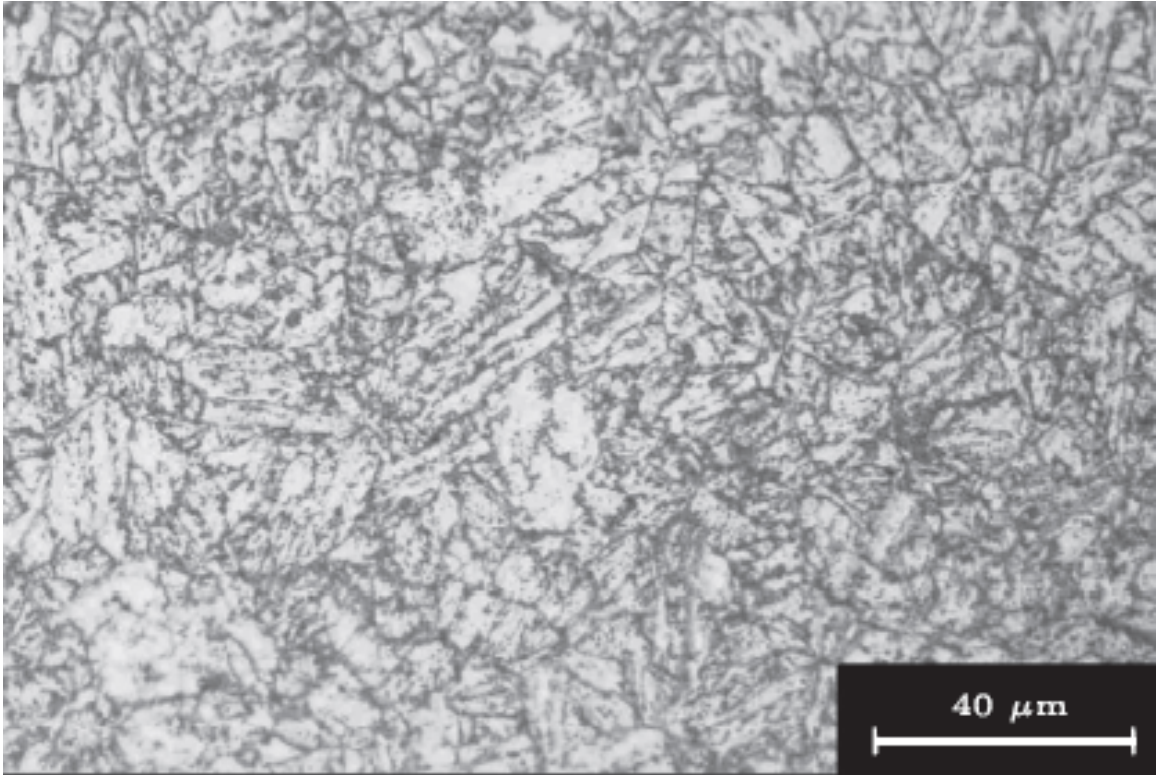


Figure 2.3: Micrograph of P91 after normalization and tempering. [4]

As such, there have been continuing efforts to develop stronger, more resilient materials. One example developed specifically for use in advanced ultra-supercritical power plants is IN740H [5, 102]. This nickel-based alternative is much stronger at elevated temperatures and has allowable stresses up to 800 °C [5]. The chemical composition of IN740H, as shown in table 2.5 [102].

Table 2.5: Element composition of IN740H material in mass%.

Material	Fe	Cr	Co	Mo	Al	Ti	Nb	Si	C	Ni
IN740H	3.0	23.5	15.0	2.0	0.2	0.5	0.5	1.0	0.01	Bal
	Max	25.5	22.0	Max	2.0	2.5	2.5	Max	0.08	

IN740H gains its strength during the hardening process in which various  $\gamma'$  nickel precipitates form within the austenitic structure [103]. Figure 2.4 provides a micrograph of the grain structure of IN740H at 200X magnification [5]. In addition to the high-temperature strength, IN740H is denser and retains a significant amount of

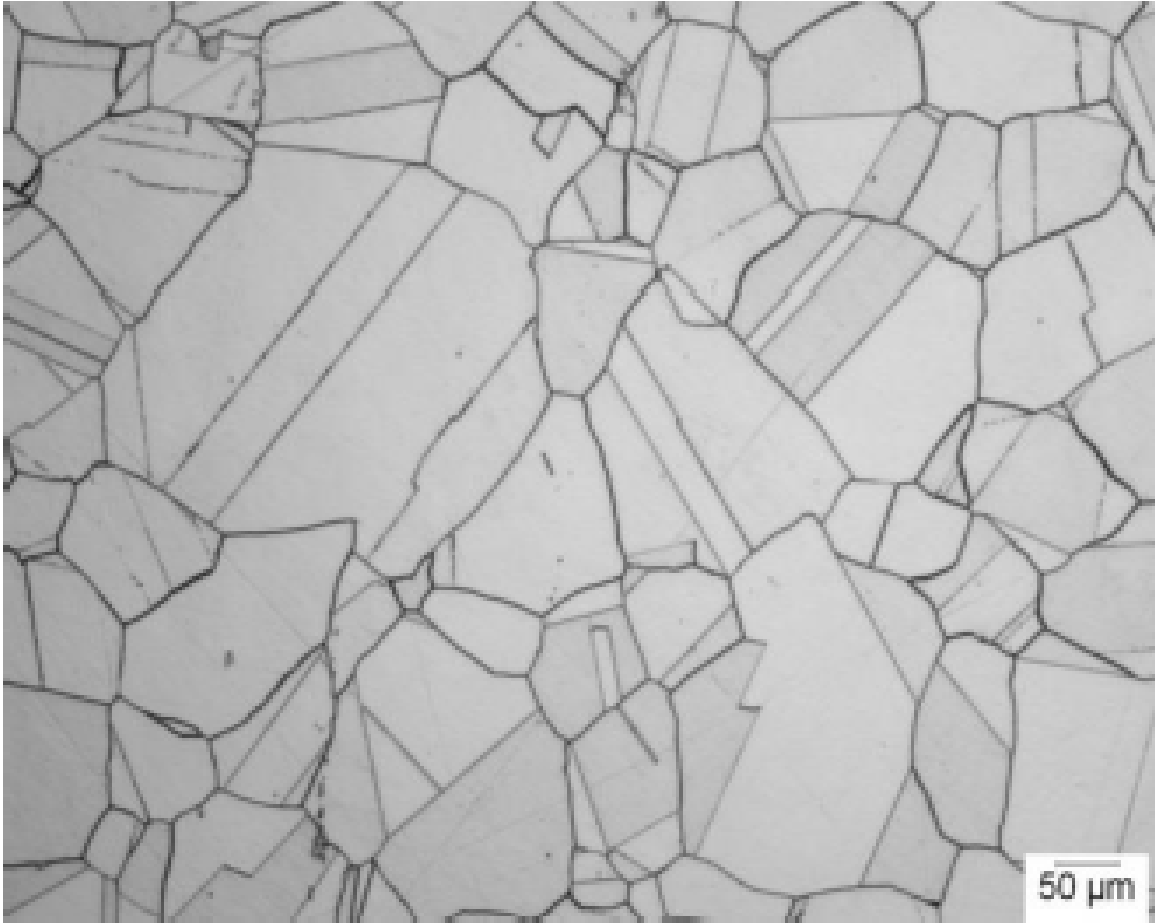


Figure 2.4: Micrograph of IN740H after heat treatment. [5]

strength at operating temperatures than the option of P22 and P91 [5].

The higher strength of IN740H allows for the same header to have significantly thinner wall thicknesses than options made from P91 or P22. This leads to material weight savings and minimizes thermal stress during transient conditions due to the thinner structure. While IN740H is relatively new with limited long-term operational data, its exceptional performance at high temperatures suggests it is unlikely to experience the same weakening as seen in traditional low alloy steels used in outlet headers.

## 2.4 Material behavior modeling

Selecting an accurate material model to represent the behavior of a component within an FEA program is critical to obtaining realistic results. Models such as those found in Abaqus have been developed to represent the behavior of different materials under a wide array of conditions. While several models are available, they are not universally applicable. The following section presents some of the common constituency models used when evaluating the material behavior of metals.

During operation, headers often experience stresses that exceed their elastic limit, resulting in plastic deformation. Additionally, headers experience numerous cycles, often consisting of rapid thermal transients separated by long periods held at high temperatures and pressures. Consequently, it is critical for the constitutive model to represent how the material hardens and softens with time. Several common methods can be found to represent a material response, including perfectly plastic, Isotropic hardening, and Kinematic hardening. However, as the following section will demonstrate, not all of these models accurately capture the changes and material yield behavior during the operational life of a header.

### 2.4.1 Plastic deformation

In solid mechanics, plasticity represents the permanent deformation of a material characterized by a translation or change in the size of the yield surface. The change in the size of the yield surface occurs after reaching a specified threshold. Depending on the hardening model being applied, the yield function can be modified with additional terms, for instance, in the case of combined kinematic and isotropic hardening as,

$$f = J(\boldsymbol{\sigma}_{eq} - \boldsymbol{\chi}) - k - R = 0 \quad (2.1)$$

where  $k$  is the initial size of the yield surface,  $\boldsymbol{\chi}$  is the back stress tensor,  $R$  is the isotropic hardening variable, and  $J(\boldsymbol{\sigma}_{eq} - \boldsymbol{\chi})$  represents the von Mises yield surface

defined as

$$J(\boldsymbol{\sigma}_{eq} - \boldsymbol{\chi}) = \sqrt{\frac{3}{2}(\boldsymbol{\sigma}' - \boldsymbol{\chi}') : (\boldsymbol{\sigma}' - \boldsymbol{\chi}')} \quad (2.2)$$

where  $\boldsymbol{\sigma}'$  is the deviatoric stress tensor,  $\boldsymbol{\chi}'$  is the deviatoric back stress tensor [104]. The present work concentrates on analyzing the behavior of metals, and therefore, the yield surfaces will be evaluated using the  $J_2$  von Mises plasticity criterion. This stems from the incompressibility theorem, where the metal's yield stress is not influenced by the hydrostatic stresses. This approach is selected for its robustness and widespread acceptance in predicting yielding and subsequent deformation in metallic materials.

Excluding the cases of time-dependent plasticity, the stress within the material can never exist outside of the yield surface. Therefore, the behavior within the yield surface is considered elastic, and when the stress is on the surface, plastic yielding takes place. After the yielding condition is reached, the yield surface begins to evolve normal to point that the stress is on the surface, which can be represented by one of many flow laws. The time-independent change in the yield surface is often characterized in one of two ways. The first is through isotropic hardening, which represents the increase in the overall size of the yield surface. the second is through kinematic hardening, which represents the translation of the yield surface in space. Figures 2.5, 2.6 represent a simplified interpretation of the yield surface behavior for both the isotropic and kinematic hardening, respectively. After a yield surface has evolved, in time-independent plasticity, the yield surface doesn't change until the stress state reaches a point where it evolves the surface further. While the transformation of the yield surface can be categorized as isotropic and kinematic, within each category there are numerous methods for defining the evolution of the surface. The following sections aim to elucidate the theoretical foundation of each model.

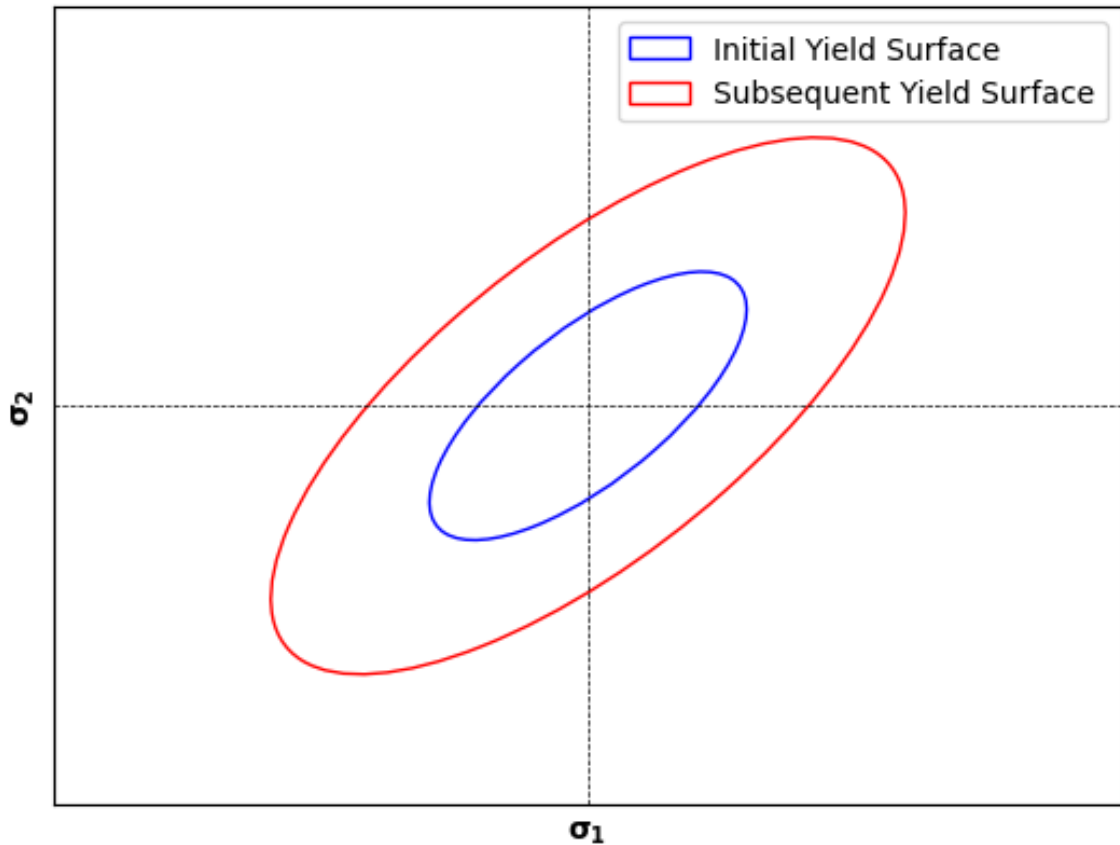


Figure 2.5: 2D Isotropic hardening representation. [6]

## 2.4.2 Cyclic plasticity

### 2.4.2.1 Isotropic hardening

Isotropic hardening represents a fundamental concept in material plasticity, characterizing the uniform expansion of a yield surface in stress space under plastic deformation, as shown in Figure 2.5. This effect is a result of the addition of a hardening variable to the yield equation in the form of,

$$f = J(\boldsymbol{\sigma}_{eq}) - k - R = 0 \quad (2.3)$$

where  $k$  is the initial size of the yield surface,  $R$  is isotropic hardening variable. Chaboche and Rousselier defined the flow rule defining the evolution of the isotropic

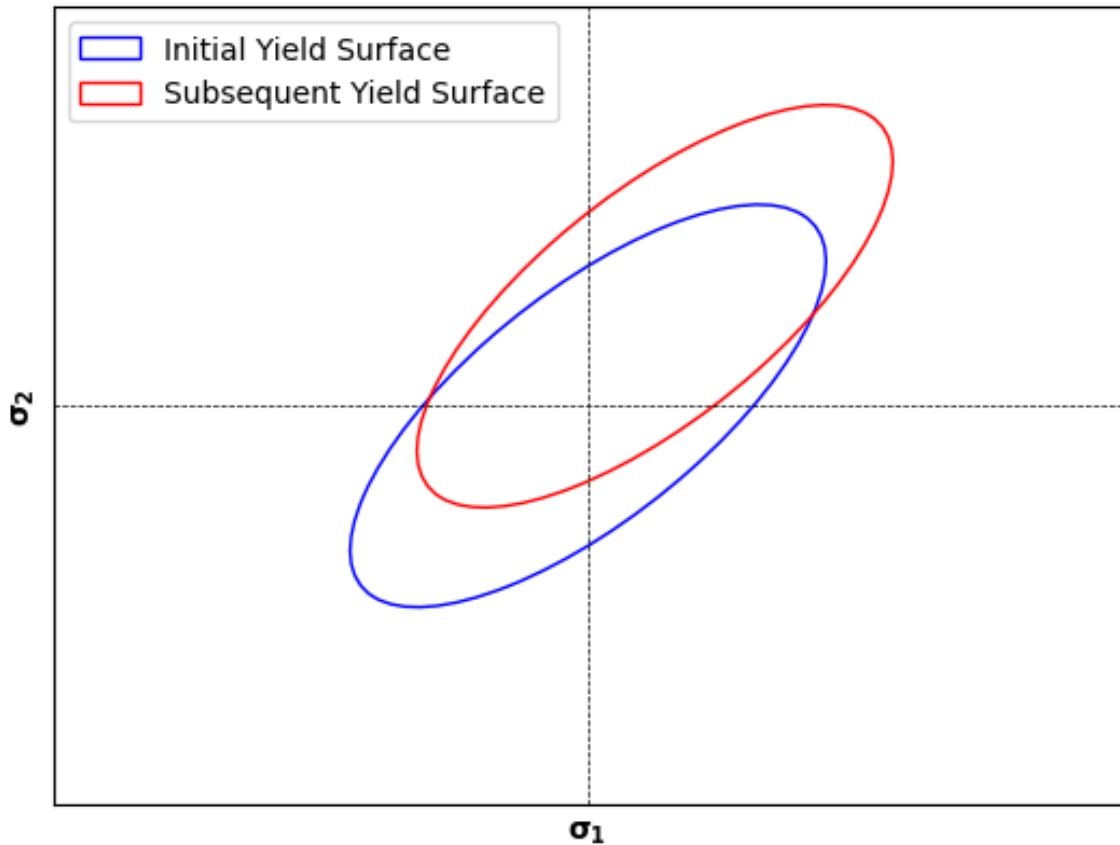


Figure 2.6: 2D Kinematic hardening representation. [6]

yield surface is defined as a function of the accumulated plastic strain as [105],

$$dR = b(Q - R)dp \quad (2.4)$$

where  $Q$  and  $b$  are material constants, and  $p$  represents the accumulated plastic strain. The integration of 2.4 yields

$$R(p) = Q(1 - e^{-bp}) \quad (2.5)$$

which demonstrates that the value of  $R$  asymptotically approaches its saturation value  $Q$ . Additionally, this law demonstrates that isotropic hardening is dependent upon the material's history. As such, a detailed understanding of the strain history is required to accurately identify the coefficients through material testing. As isotropic

hardening uniformly expands the yield surface, it inherently lacks the capability to account for the Bauschinger effect. This phenomenon is characterized by an asymmetry in the cyclic behavior of the material, originating from an increase in tensile strength that consequently reduces the compressive strength. Thus isotropic hardening by itself proves inadequate for cyclic loading applications. and all of the current isotropic analyses have been deliberately admitted for several reasons. First, all scenarios investigated involve cyclic loading, requiring a model that accurately reflects the Bauschinger effect. Additionally, this work focuses on low-cycle fatigue, which is typically represented by the stable hysteresis loops that occur after the influence of isotropic hardening has subsided. Furthermore, within the case of the material for the service exposed P22, the entire strain history was not available, preventing the establishment of isotopic hardening coefficients.

#### 2.4.2.2 Kinematic hardening

One of the simplest kinematic hardening models was proposed by Prager in 1956, which reflects a linear kinematic hardening of the yield surface [106].

$$\dot{\chi} = C d\epsilon_p \quad (2.6)$$

Consequently, the Prager model suggests that the loading and unloading curves, along with the hysteresis loop, would maintain a linear relationship. However, in situations where cyclic loading includes a mean stress, the Prager model is inadequate in capturing the differential behavior between the loading and unloading phases, leading to a response that does not accurately reflect the material's properties. Another limitation of the Prager model is its application of a uniform flow rule across all strain ranges, which oversimplifies material response. To address these shortcomings, early enhancements to this model were introduced by the Mroz model, which incorporates a multi-linear approach [107]. This modification allows for a more nuanced repre-

sentation of the material's response across different strain ranges by representing the linear behavior between multiple surfaces defined as  $f_l$ .

$$f_l = J(\sigma - \chi_l) - k_l = 0 \quad (2.7)$$

where  $\chi_l$  represents the position of the yield surface and  $k_l$  represents the size of the yield surface  $f_l$ . The movement between surfaces is guided by the relationships

$$d\epsilon_p = d\lambda_l \frac{\partial f_l}{\partial \sigma} = \sqrt{\frac{3}{2}} d\lambda_l n \quad (2.8)$$

$$d\chi_l - d\mu(\sigma_{l+1} - \sigma) \quad (2.9)$$

where  $\lambda_l$  is a scalar and  $\mu$  is a multiplier determined from the consistency condition of the yield surface. Further adjustments were implemented in the work by Ohno and Wang, who developed a piecewise model [108]. This advancement enables a more detailed and realistic simulation of material behavior under varied loading conditions through the relationship,

$$d\boldsymbol{\chi} = \gamma_i \left[ \frac{2}{3} r_i d\boldsymbol{\epsilon}_p - H(f_i) \left\langle d\boldsymbol{\epsilon}_p : \frac{\boldsymbol{\chi}_i}{\bar{\chi}_{ie}} \right\rangle \boldsymbol{\chi}_i \right] \quad (2.10)$$

where  $\bar{\chi}_i$  is the magnitude of the backstress,  $\gamma_i$ ,  $r_i$  are material constants,  $H$  represents the heavy side step function such that  $H(f_i) = 1$  if  $f_i \geq 0$ ; otherwise  $H(f_i) = 0$ , and the symbol  $\langle \rangle$  represents  $\langle x \rangle = 0$  if  $x < 0$  otherwise,  $\langle x \rangle = x$ . While these models improve the capability of the model by more accurately capturing the strain evolution, they suffer from the same restrictions of the Prager model. During cyclic loading, materials exhibit various complex behaviors, such as the Bauschinger effect, Ratcheting, and Masing behavior. The Bauschinger effect occurs during cyclic loading, where initially, the material experiences an increase in strength due to strain hardening when subjected to tension. However, when the loading direction reverses

to compression, the material exhibits a softening effect, reducing its resistance to deformation. This phenomenon reflects the material's asymmetrical response to the reversal of stress from tension to compression. In some cases, the shift in the yield locust can result in the material Ratcheting. Ratcheting refers to the progressive accumulation of plastic strain in a material, occurring in the direction of the mean stress during cyclic loading. This phenomenon can be transient, leading to what is known as shakedown. Shakedown is essentially the cessation of ratcheting and is characterized by the stabilization of plastic strain after a certain number of loading cycles. Another common behavior to consider is whether or not the material is a Masing material. Masing behavior describes a characteristic of a material's response to cyclic loading, specifically referring to the shape of the hysteresis loops under varying stress levels. When a material exhibits Masing behavior, the hysteresis loops at different stress amplitudes are similar and can be placed onto one another following the same path as the stress increases. This implies that the material's internal resistance mechanisms, like dislocation movements and strain hardening, respond uniformly across different stress levels. To improve the accuracy over linear models, Armstrong and Frederick added a drag stress term  $\chi$  to introduce nonlinearity, defined as [109, 110],

$$d\chi = \frac{2}{3}c d\epsilon_p - \gamma\chi dp \quad (2.11)$$

where  $d\epsilon_p$  is the plastic strain increment,  $c$  is the kinematic hardening modulus,  $\gamma$  is a material property, and  $dp$  is the change in equivalent plastic strain. The nonlinearity is made clear following an abridged summary of the derivation for the stress in response to uniaxial testing [110]. The equivalent plastic strain rate is defined as,

$$dp = \sqrt{\frac{2}{3}d\epsilon_p : d\epsilon_p} = d\lambda \quad (2.12)$$

which, when accounting for the consistency condition required for plastic flow,  $f =$

$df = 0$ ,  $dp$  can be rewritten as,

$$dp = d\lambda = \frac{1}{h} \left\langle \frac{\partial f}{\partial \boldsymbol{\sigma}} : d\boldsymbol{\sigma} \right\rangle = \frac{1}{h} \left\langle \frac{3 \boldsymbol{\sigma}' - \boldsymbol{\chi}'}{2 R + k} : d\boldsymbol{\sigma} \right\rangle \quad (2.13)$$

where  $h$  represents the hardening modulus, and the symbol  $\langle \rangle$  is an indicator function where  $\langle x \rangle = 0$  if  $x < 0$  otherwise,  $\langle x \rangle = x$ . In the equation 2.13,  $h$  constitutes the hardening modulus, defined as,

$$h = \frac{2}{3} c \frac{\partial f}{\partial \boldsymbol{\sigma}} : \frac{\partial f}{\partial \boldsymbol{\sigma}} - \gamma \boldsymbol{\chi} : \frac{\partial f}{\partial \boldsymbol{\sigma}} \left( \frac{2 \partial f}{3 \partial \boldsymbol{\sigma}} : \frac{\partial f}{\partial \boldsymbol{\sigma}} \right)^{0.5} \quad (2.14)$$

and when using the von Mises yielding conditions, reduces to,

$$h = c - \frac{3}{2} \gamma \boldsymbol{\chi} : \frac{\boldsymbol{\sigma}' - \boldsymbol{\chi}'}{R + k} = c - \sqrt{\frac{3}{2}} \gamma \boldsymbol{\chi} : \mathbf{n} \quad (2.15)$$

where  $\mathbf{n}$  represents the outward unit normal defined as,

$$\mathbf{n} = \frac{\partial f / \partial \boldsymbol{\sigma}}{\sqrt{\partial f / \partial \boldsymbol{\sigma} : \partial f / \partial \boldsymbol{\sigma}}} = \frac{3 \boldsymbol{\sigma}' - \boldsymbol{\chi}'}{2 R + k} \quad (2.16)$$

Therefore, it follows that the plastic strain rate can be written in the form,

$$d\boldsymbol{\epsilon}_p = \frac{3}{2} \frac{1}{h} \left\langle \frac{3 \boldsymbol{\sigma}' - \boldsymbol{\chi}'}{2 R + k} : d\boldsymbol{\sigma} \right\rangle \frac{\boldsymbol{\sigma}' - \boldsymbol{\chi}'}{R + k} = \frac{3}{2} \frac{1}{h} \langle \mathbf{n} : d\boldsymbol{\sigma} \rangle \mathbf{n} \quad (2.17)$$

Recall that with the assumption of an incompressible material with an initial state of  $\boldsymbol{\chi} = 0$ , the back stress can be defined as,

$$dTr(\boldsymbol{\chi}) = \frac{2}{3} c Tr(d\boldsymbol{\epsilon}_p) - \gamma Tr(\boldsymbol{\chi}) dp = -\gamma Tr(\boldsymbol{\chi}) dp \quad (2.18)$$

which can be integrated,

$$Tr(\boldsymbol{\chi}) = Tr(\boldsymbol{\chi}_0) e^{-\gamma p} = 0 \quad (2.19)$$

The relationships can be simplified in the case of uniaxial testing as,

$$f = |\sigma - \chi| - R - k = 0 \quad (2.20)$$

$$dp = |d\epsilon_p| = \frac{1}{h} \left\langle \pm (\sigma - \chi) d\sigma \right\rangle \quad (2.21)$$

$$h = c - \gamma\chi \pm (\sigma - \chi) \quad (2.22)$$

$$d\chi = cd\epsilon_p - \gamma\chi|d\epsilon_p| \quad (2.23)$$

Evaluating a complete cycle from  $\chi_0, \epsilon_{p0}$  yields the expression for the back stress as,

$$\chi(\epsilon_p) = \nu \frac{c}{\gamma} + \left( \chi_0 - \nu \frac{c}{\gamma} \right) e^{-\gamma(\epsilon_p - \epsilon_{p0})} \quad (2.24)$$

where  $\nu = \pm 1$  relates to the direction of the cycle. It follows that the stress response during loading can be represented as,

$$\sigma = \nu \frac{c}{\gamma} + \left( \chi_0 - \nu \frac{c}{\gamma} \right) e^{-\gamma(\epsilon_p - \epsilon_{p0})} + k + R \quad (2.25)$$

and when considering a complete cycle of the stable curve, the stress amplitude can be represented in the form of,

$$\frac{\Delta\sigma}{2} - k = \frac{C}{\gamma} \tanh\left(\gamma \frac{\Delta\epsilon_p}{2}\right) \quad (2.26)$$

This form of the Armstrong-Frederick model directly represents the non-linear relationship of material hardening. However, to improve the accuracy of the model over a larger range of strains, Chaboche introduced a summation term so that multiple terms could represent various portions of the hardening process. As a result, the

Armstrong-Frederick model is modified to the form of [104],

$$\frac{\Delta\sigma}{2} - k = \sum_{i=1}^2 \frac{C_i}{\gamma_i} \tanh\left(\gamma_i \frac{\Delta\epsilon_p}{2}\right) \quad (2.27)$$

where  $i$  represents the number of back stresses used to describe the material. This model, is commonly referred to as the Combined Chaboche NLKH model and is frequently used in combination with Isotropic hardening to simulate the hardening behavior of metals. Under strain-controlled behavior, this model leads to a relaxation of the mean stress, whereas it retains the ability to capture ratcheting effects under a cyclic load with a non-zero mean stress.

#### 2.4.3 Time-dependent plasticity

Creep can be characterized as the time-dependent plastic deformation experienced by a material at elevated temperatures under constant stress that is below its yield strength over a period. This phenomenon results from sustained stress at high temperatures, normally greater than half the melting temperature, leading to the accumulation of inelastic strains known as creep. Creep is delineated into three phases: primary, secondary, and tertiary. Many of the constitutive models developed are done to represent the behavior occurring at the microscopic scale. Dislocation movement within the material's structure is dependent on the load and the location of the dislocation. Dislocations can move within the material's structure, either through diffusion through the grain or along the boundary. Diffusive movement through the grain structure is often represented using the Nabarro-Herring model [111, 112],

$$\dot{\epsilon}_{NH}^c = \frac{AD\sigma\Omega_{SD}}{d^2kT} \quad (2.28)$$

where  $d$  is the grain size of the material,  $k$  is the Boltzmann constant,  $T$  is the absolute temperature,  $A$  is a material constant,  $D$  is the lattice diffusion coefficient,  $\sigma$  is the applied stress, and  $\Omega_{SD}$  is the activation enthalpy for movement through the

grain. The movement around the grain boundary can be represented using a similar relationship, referred to as Cobble creep represented as [113],

$$\dot{\epsilon}_{Coble}^c = \frac{AD\sigma\Omega_{GB}}{d^3kT} \quad (2.29)$$

where  $\Omega_{GB}$  is taken as the enthalpy for movement to occur along the grain boundary. These processes combine to form the three-stage creep behavior model. The first stage of creep behavior is marked by a decrease in the rate. During the initial stage, the rate of creep decelerates as dislocations accumulate, impeding further deformation. A constitutive model characterizing this stage of creep is presented by Andrade [114] as,

$$\dot{\epsilon}_{primary}^c = At^{\frac{1}{q}} \quad (2.30)$$

The rate within the first stage continues to decrease until it reaches a relatively constant rate, marking the start of the second stage of creep. The secondary stage, which is the most prolonged and steady phase of creep, is characterized by a balance between hardening and softening mechanisms, resulting in a constant rate of deformation. Given that the secondary stage accounts for the majority of creep deformation, it is frequently the focus of modeling efforts. A commonly employed model for secondary creep is represented by the Norton power law, which represents the creep rate as a function of stress [115].

$$\dot{\epsilon}_{secondary}^c = \sigma^n \exp\left(-\frac{Q}{kT}\right) = A\sigma_{eq}^n \quad (2.31)$$

Where  $Q$  and  $n$  are material constants. From this representation, it is clear that temperature and stress play critical roles in the accumulation of creep strain. The coefficient  $n$  is dependent on the dominant behavior responsible for the creep within the material. Depending on the activation energy and lattice of the material, dislocation

or diffusion may result in the dominant cause of creep strain. Therefore, the value of  $n$  represents the dominant dislocation method of the material. Therefore, using the power law representation is dependent on the stress and the dominant mechanism for damage. To try and bridge this, Garofalo [116] has developed a hyperbolic sign model to help represent the creep strain rate demonstrated as,

$$\dot{\epsilon}_{secondary}^c = (\sinh(\alpha\sigma))^n \exp\left(-\frac{Q}{RT}\right) = A\left(\sinh\left(\frac{\sigma}{\sigma_0}\right)^n\right) \quad (2.32)$$

Modifying the stress's relationship with the sign hyperbolic sine function makes the relationship more versatile for a larger range of stresses. The final stage, or tertiary phase, is marked by the emergence of voids that escalate stress within the material, accelerating until failure. As a result, models used to describe the tertiary region of creep often incorporate damage functions. First, an example without damage was developed by Prager [106],

$$\dot{\epsilon}_{tertiary}^c = \dot{\epsilon}_0 \exp(\Omega_p \epsilon) \quad (2.33)$$

where  $\Omega_p$  is the reciprocal of the Monkman-Grant constant. Another model that incorporates damage into the tertiary region of creep was developed by Kachanov-Rabotnov [117, 118]

$$\dot{\epsilon}_{tertiary}^c = A\left(\frac{\sigma_{eq}}{1-D}\right)^n \quad (2.34)$$

$$\dot{D} = \frac{M\sigma_{eq}^\chi}{1-D^\phi} \quad (2.35)$$

where  $D$  is damage and  $M$ ,  $\chi$ , and  $\phi$  are material constants.

## 2.5 Fatigue

Fatigue is a common phenomenon in materials, describing the failure of materials subjected to cyclic loading that, in many cases, does not exceed the material's yield stress. This process is characterized by the gradual emergence and propagation of

cracks over time, ultimately leading to material failure [119]. The fatigue process begins at the microscopic level, where cyclic loading induces dislocations that form extrusions and intrusions along the persistent slip bands on the material's surface [120–124]. Over time, these microscopic deformations accumulate, initiating cracks that grow and eventually propagate through the material, leading to its structural failure. It follows that surface finish plays a key role in influencing the fatigue life of a material. The formation of extrusions and intrusions contributes to the emergence of external cracks, which are significantly affected by the surface's finish [125–129]. Similarly, internal surfaces may also develop voids that transform into cracks.

The fatigue phenomenon can be divided into two stages: the initiation of cracks, known as high-cycle fatigue, and the subsequent propagation of these cracks, referred to as low-cycle fatigue. This distinction is typically made around the 10,000-cycle mark, with failure occurring below this threshold classified as low-cycle fatigue and above as high-cycle fatigue. Additionally, the onset of fatigue is contingent upon exceeding a certain threshold related to dislocation movement, referred to as the fatigue limit. This threshold delineates the conditions under which fatigue-induced damage begins to accumulate within the material. The relationship between the number of cycles to failure and the plastic strain range for low cycle fatigue can be found through the Coffin-Manson relation as,

$$C = \Delta\epsilon_{in} N_f^\beta \quad (2.36)$$

wheres,  $\Delta\epsilon_{in}$  is the plastic strain range,  $\beta$  is a material constants, and  $C$  represents the ductility intercept of  $\epsilon_{in}$  when  $N_f = 1$  [130]. In this context, the number of cycles until failure is represented as the diameter of several grains of the material, often between 0.1 - 0.3 mm in depth. [131–133]

Several methods have been established to calculate fatigue life, the most common is Palmgren Miner [134]. This method establishes a relationship between the total

work absorbed by a material, whereby a damage fraction can be calculated relating to the amount of work done to the material. The implication is that the damage from each cycle is cumulative and can be summed to establish the total damage to the material. This can be represented as,

$$\frac{n_i}{N_i} + \frac{n_j}{N_j} + \frac{n_k}{N_k} + \dots = 1 \quad (2.37)$$

where  $n_i, n_j, n_k$  are the number of cycles at a particular stress level and  $N_i, N_j, N_k$  are the number of cycles required for the material to fail at each level. Essentially, this method aggregates the damage from each cycle at various stress levels, predicting failure when the cumulative damage equals one. However, this threshold is not set with certainty. Variability with respect to the initiation of cracks correlates to variation with the lifespan until failure, and to account for this, some have suggested a lower threshold of 0.7 [135, 136].

Dislocation movement is dependent on the material, stress, and temperature. In low-temperature cases, the effects of fatigue can be characterized by the stress amplitude and mean stress. In higher temperature cases, the influence of time-dependent effects becomes influential, and the order and time at thresholds become relevant. One way to evaluate the damage influence of creep is through the Robinson rule. The Robinson rule estimates the time to fracture at a given time and stress threshold

$$\sum \frac{t}{t_r} = 1 \quad (2.38)$$

where  $t$  is the time at a threshold and  $t_r$  is the time to rupture at the threshold [137]. This method can also be adapted for continuously variable loads using an integrated form,

$$\int_0^{t_f} \frac{dt}{t_f} = 1 \quad (2.39)$$

This method can be combined with the Miner's rule to combine the damage that occurs from creep and fatigue using the following,

$$\sum \frac{t}{t_r} + \sum \frac{n}{N} = 1 \quad (2.40)$$

However, the method can often lead to non-conservative life estimates. As many have shown, fatigue followed by dwells under tension or compression can significantly alter the life of the part [23]. This is a result of the competing and connected mechanisms controlling the dislocation movement through the part. As a result, some load conditions may abet dislocation movement while others hinder, resulting in a dependence on load history. One approach to more accurately represent the interactions between creep and fatigue is through strain range partitioning. This approach separates the cycles depending on if it is purely cyclic, purely creep, or if it is a combined cycle that dwells either in compression or tension.

$$\frac{\Delta\epsilon_{in}}{N} = \frac{\Delta\epsilon_{cc}}{N_{cc}} + \frac{\Delta\epsilon_{pp}}{N_{pp}} + \frac{\Delta\epsilon_{pc}}{N_{pc}} + \frac{\Delta\epsilon_{cp}}{N_{cp}} \quad (2.41)$$

where the subscripts *cc* represent a pure creep cycle, *pp* represent a pure plastic cycle, *pc* represent a fatigue tensile cycle followed by a compressive creep cycle, and *cp* represent a tensile creep cycle followed by a fatigue compressive cycle. While these methods can more accurately represent the behavior of the material, they are seldom used due to the amount of testing required to establish the necessary relationships. Others have established a similar approach through the use of cumulative hysteresis energy absorbed until failure [138–143]. They have found that the number of cycles to failure correlates to the amount of plastic energy dissipated by the material. While elastic energy is dissipated during a hysteresis cycle, this factor is minimal in metals and neglected [142, 144].

The premise used to establish the multiaxial fatigue life throughout the present

work is based on the methodology outlined by Das and Sivakumar [145]. Their process of evaluating a set of trial planes is combined with the Ostergren damage parameter [146]. This parameter defined the number of cycles to failure as,

$$N_f = C(\Delta\epsilon_{in}\sigma_{max})^\beta \quad (2.42)$$

where  $C$  and  $\beta$  are material constants,  $\Delta\epsilon_{in}$  is the inelastic strain of the cycle being considered and  $\sigma_{max}$  is the maximum tensile stress along the critical plane. This process approximates the inelastic strain energy dissipated by the material. During this process, the damage parameter,  $\Delta\epsilon_{in}\sigma_{max}$ , is calculated and iterated on a set of trial planes to determine the most critical orientation. The process is easily implemented using the following procedure.

1. Establish the critical location and define an outward normal to establish  $\theta, \theta_r$
2. Calculate the direction cosines of the normal as
  - (a)  $n_x = \sin\theta\sin\theta_r$
  - (b)  $n_y = -\sin\theta\cos\theta_r$
  - (c)  $n_z = \cos\theta$
3. Calculate the normal stress and strain for the current plane
  - (a)  $\sigma_n = \sigma_x n_x^2 + \sigma_y n_y^2 + \sigma_z n_z^2 + 2\tau_{xy} n_x n_y + 2\tau_{yz} n_y n_z + 2\tau_{xz} n_x n_z$
  - (b)  $\epsilon_n = \epsilon_x n_x^2 + \epsilon_y n_y^2 + \epsilon_z n_z^2 + \gamma_{xy} n_x n_y + \gamma_{yz} n_y n_z + \gamma_{xz} n_x n_z$
4. Calculate the maximum value of  $\Delta\epsilon_{in}\sigma_{max}$
5. Iterate through all trial planes to identify the maximum Ostergren damage coefficient

There are multiple ways to represent cracks and damage within finite elements [147–152]. These techniques broadly fall into two principal categories, linear elastic and elastic-plastic. These methods are incorporated into programs such as Abaqus through one of several methods, such as the extended finite element, XFEM, and virtual crack closure technique, VCCT. Another method introduces a seam into the model and relies on a set of wedge elements around the crack tip to produce the required stress field. By modifying Another method modified the nodal spacing of elements to produce a stress field commonly found around a crack tip through seam cracks. The seam crack method adjusts the nodes of the elements around the crack tip so that the stress field is defined using a  $1/\sqrt{r}$  relationship. The crack methods measure the strength of the stress field around the crack tip using the stress intensity factor, SIF, represented in LEFM as  $K$ . The stress field around the crack tip in an elastic material can be represented as,

$$\sigma_{xx} = \frac{K}{\sqrt{2\pi r}} \cos \frac{\theta}{2} \left( 1 - \sin \frac{\theta}{2} \sin \frac{3\theta}{2} \right) + T + o(r^{0.5}) \quad (2.43)$$

$$\sigma_{yy} = \frac{K}{\sqrt{2\pi r}} \cos \frac{\theta}{2} \left( 1 + \sin \frac{\theta}{2} \sin \frac{3\theta}{2} \right) + o(r^{0.5}) \quad (2.44)$$

$$\sigma_{xy} = \frac{K}{\sqrt{2\pi r}} \cos \frac{\theta}{2} \left( \sin \frac{\theta}{2} \cos \frac{3\theta}{2} \right) + o(r^{0.5}) \quad (2.45)$$

where  $T$  represents the T-Stress stress represents the stress acting parallel to the crack tip in the direction of extension. This term was introduced to eliminate the transverse component of stress along the boundary edges of the crack [153]. However, in the single parameter description including  $K$ , the stress relationship can be represented by [154]

$$\sigma_{ij} = \frac{K}{\sqrt{r}} f_{ij}(\theta) \quad (2.46)$$

Through this relationship, it is clear to see that the SIF is related to the stress field away from the crack and the singularity relationship  $1/\sqrt{r}$  in an elastic body. As a result, the SIF can be related to the Griffith theory, defining the energy required to grow the crack by creating new surfaces as,

$$\mathcal{G} = -\frac{dU}{Bda} \quad (2.47)$$

where  $B$  represents the width of the material that the crack is growing through,  $da$  represents the crack growth increment, and  $dU$  represents the change in surface energy resulting from the creation of new surfaces. In LEFM, this energy can be related to the SIF through the modulus as,

$$\bar{E} = \begin{cases} E, & \text{for plane stress} \\ \frac{E}{1-\nu^2}, & \text{for plane strain} \end{cases} \quad (2.48)$$

However, when plasticity is considered, it becomes necessary to take into consideration strain energy that occurs from plastic deformation, and thus the parameter  $J$  is used [155],

$$J = \frac{dU}{Bda} \quad (2.49)$$

$J$  is related to the integral of a path taken around the crack front represented as [155],

$$J = \int_{\Gamma} \left( W_s dy - \sigma_{ij} \frac{\partial u_i}{\partial x_1} \right) ds \quad (2.50)$$

where  $\Gamma$  represents the surface of the material,  $T_i$  and  $u_i$  are components of the traction and displacement vectors,  $s$  is the path length along the surface  $\Gamma$ , and  $W_s$

is the strain energy density defined as,

$$W_s = \int_0^{\epsilon_{ij}} \sigma_{ij} d\epsilon_{ij} \quad (2.51)$$

Under mixed mode elastic conditions, the Griffith and J integral are related to the SIF through the relationship,

$$\mathcal{G} = J = \frac{1}{E}(K_I^2 + K_{II}^2) + \frac{1}{2G}K_{III}^2 \quad (2.52)$$

Under cyclic loading, the range of SIF becomes critical as demonstrated by the Paris law, which relates the change in crack growth per cycle to the range of SIF as [156],

$$\frac{da}{dN} = C(\Delta K)^m \quad (2.53)$$

This equation represents the linear region of crack growth between a threshold value  $K_{th}$  and a critical value  $K_{IC}$ . These values represent the limits of SIF where the crack growth is notably stable. Therefore, the linear relationship can be established by fitting the crack growth per cycle in comparison to  $\Delta K$ . To incorporate multiaxial effects, others have developed a  $K_{eff}$  to describe the stress state around the crack tip. One example of this is represented by Rhee represents the mixed-mode fracture as [157],

$$\Delta K_{eff} = \sqrt{\Delta K_I^2 + \Delta K_{II}^2} \quad (2.54)$$

## CHAPTER 3: Service life comparison of IN740 P22 P91 steam headers

### 3.1 Introduction

The first portion of the study aims to determine the cost-effectiveness of using P22, P91, or IN740H alloys for a steam header application. The approach involves evaluating the performance of the materials by leveraging data taken from an ex-service unit; this data includes temperature and pressure information, ensuring the relevance of the findings. Using the operational parameters of an existing P22 header as the benchmark, we aim to extend the investigation to headers fabricated from other materials. To ensure the integrity and applicability of the designs, all headers will be developed in alignment with the guidelines provided by the ASME BPVC Sections I, II, and VIII. This method promises to yield insights into the material-specific advantages and provides an understanding of the economics associated with each choice for steam header construction.

The first step in performing the cost-effectiveness study is to determine the geometrical designs relevant to each of the materials under consideration. This step takes into account the differences in material properties of each alloy. The alloys under consideration have significantly different material properties across the range of considered temperatures. These differences result in significant variations between the finalized designs.

Given the range of material properties considered, a uniform elastic perfectly plastic material model is chosen to compare the materials on the same basis. This approach maintains consistency across the analysis, allowing for a direct comparison of the materials despite their significant differences. The viability of each material is assessed through finite element modeling within Abaqus to apply real-world representative

conditions that each header would encounter. This step provides an understanding of how each material will perform in actual applications.

The operational data used to evaluate each header is taken from an ex-service unit. The data is simplified to ensure that the analysis remains precise and applicable while avoiding the complications that can arise from using an overly complex data set. This process helps to apply a focused and effective evaluation of each material in representative loading scenarios. This section concludes by presenting the findings demonstrating the cost-benefit considerations between P91, P22, and IN740H.

### 3.2 Geometric Design

The initial process considers the geometry of an existing unit, in order to serve as a viable alternative, the ID of the materials is fixed match the existing unit. Additionally, to aid in installation, the wall thickness of the tubes is held constant. This provides a viable option to weld the replacement unit to the tubes needed to incorporate it into the system. The geometry design is found through the use of the ASME BPVC I code requirements for the header are found using ASME PBVC Section I PG-27.2.2

$$t_{min} = \frac{PD_o}{2SE + 2yP} + C \quad (3.1)$$

where  $t$  is the thickness of the header,  $D_o$  is the outside diameter,  $P$  is the maximum allowable operating pressure,  $S$  is the maximum allowable stress at the design temperature of 1005 °f ( 540.6 °C),  $y$  is a temperature coefficient,  $C$  is a correction for the allowance of threads, and  $E$  is the efficiency relating to the size and spacing of the tubes defined as,

$$E = \frac{p - d}{p} \quad (3.2)$$

Table 3.1: Minimum wall thickness in accordance with PG27.2.2

<b>Material</b>	<b>Minimum Wall Thickness (Inch)</b>
P22	3.47
P91	1.37
IN740H	0.58

where  $p$  is the pitch of the spacing, and  $d$  is the diameter of the opening in the shell. Each header section incorporates 34 rows of tubes with  $30^\circ$  spacing across from one another, resulting in an efficiency of 0.797. The diameter of the opening is 1.219 inches (30.96 mm) and is held constant for all of the materials. The  $D_i$  is also held constant for all materials with a diameter of 15.25 inches (387.35 mm); the maximum allowable working pressure is 2450 psi (16.9 MPa). None of the materials include allowance for threading, and it is assumed that the tubes will be welded in. The minimum wall thicknesses found are shown in Table

Due to the thickness of the IN740H header, the tube manufacturing will be simplified, representing the tube welded to the exterior of the header. Each of the materials is represented as an elastic perfectly-plastic material with the yield strength values reported by ASME BPVC and Specialty Metals [2, 5]. The properties used for the comparison are shown in Table 3.2, 3.2, 3.2.

Table 3.2: Temperature dependent elastic perfectly plastic parameters for P22.

T °C	Conductivity mmTonne/s <sup>3</sup> K	Youngs Modulus MPa	Yield Stress MPa	Coefficient of thermal expansion K <sup>-1</sup>	Specific heat capacity Nmm/TonneK
20	36.3	210,000	197	1.15E-5	4.45E8
300	36.7	192,000	185	1.33E-5	5.58E8
400	35.4	184,000	185	1.38E-5	6.02E8
500	33.7	175,000	185	1.44E-5	6.57E8
600	32.0	162,000	173	1.48E-5	7.44E8

Table 3.3: Temperature dependent elastic perfectly plastic parameters for P91.

T °C	Conductivity mmTonne/s <sup>3</sup> K	Youngs Modulus MPa	Yield Stress MPa	Coefficient of thermal expansion K <sup>-1</sup>	Specific heat capacity Nmm/TonneK
20	22.5	213,000	394	1.15E-5	4.40E8
300	26.2	198,791	377	1.33E-5	5.10E8
400	27.7	183,938	358	1.38E-5	6.00E8
500	27.7	165,882	306	1.44E-5	6.85E8

Table 3.4: Temperature dependent elastic perfectly plastic parameters for IN740H.

T °C	Conductivity mmTonne/s <sup>3</sup> K	Youngs Modulus MPa	Yield Stress MPa	Coefficient of thermal expansion K <sup>-1</sup>	Specific heat capacity Nmm/TonneK
20	10.2	221,000	742	1.24E-5	4.49E8
300	14.5	206,000	742	1.35E-5	4.85E8
400	15.7	200,000	742	1.39E-5	4.98E8
500	17.1	193,000	742	1.43E-5	5.13E8

The headers designed each incorporate a tube welded onto their exterior surfaces. The finalized dimensions of the headers are outlined in Table 3.5.

Table 3.5: Finalized Wall Thickness.

Material	Header ID (mm)	Header OD (mm)	Tube ID (mm)	Tube OD (mm)
P22	387.35	565.15	32.66	50.8
P91	387.35	463.55	32.66	50.8
IN740H	387.35	418.34	32.66	50.8

Wall thicknesses for the materials were selected based on minimum requirements derived from equation 3.1 and typical schedule sizes used in industrial production. This selection led to a slight increase in the minimum wall thickness for the IN740H and P91 headers. Geometric representations of the headers are depicted in Figures 3.1, 3.2, 3.3. The tubing utilized in all headers matches that of the existing unit, so a decision was made to improve the ease with which each header could be incorporated into the existing system. Consequently, each header features a tube with a 2-inch diameter and a 0.357-inch wall thickness.

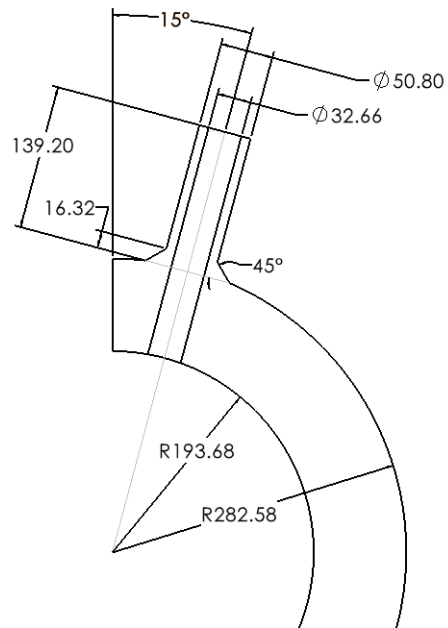


Figure 3.1: Finalized dimensions of the P22 header

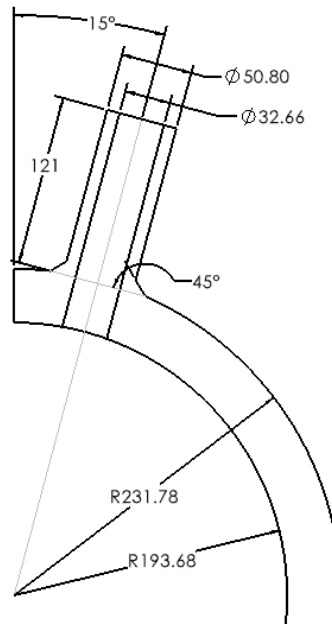


Figure 3.2: Finalized dimensions of the P91 header

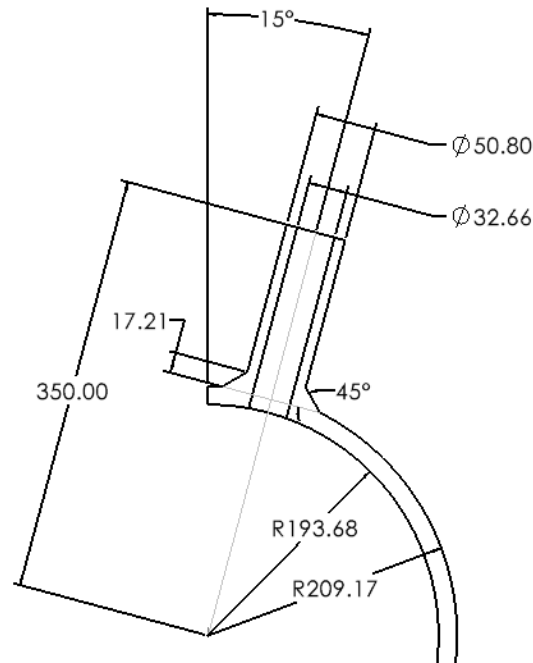


Figure 3.3: Finalized dimensions of the IN740 header

While certain manufacturing characteristics, such as the weld around the tube, are shown in the geometry, the material is uniformly represented as homogeneous across all trials. This approach aligns with the decision-making process in selecting elastic-perfectly-plastic material properties, aiming for representative comparison among the materials.

### 3.3 Design loading conditions

The company responsible for providing the service header unit also provided a dataset containing recorded temperatures and pressures taken from within the header and tube systems. The dataset includes operating data for several days. The present focuses on evaluating one of the more extreme transient cases characterized by high ramp rates and peak temperatures to assess the performance of the materials under study. This particular transient was chosen to identify which materials exhibit greater resilience under extreme conditions. Figure 3.4 illustrates the reference temperature and pressure data utilized to define this transient.

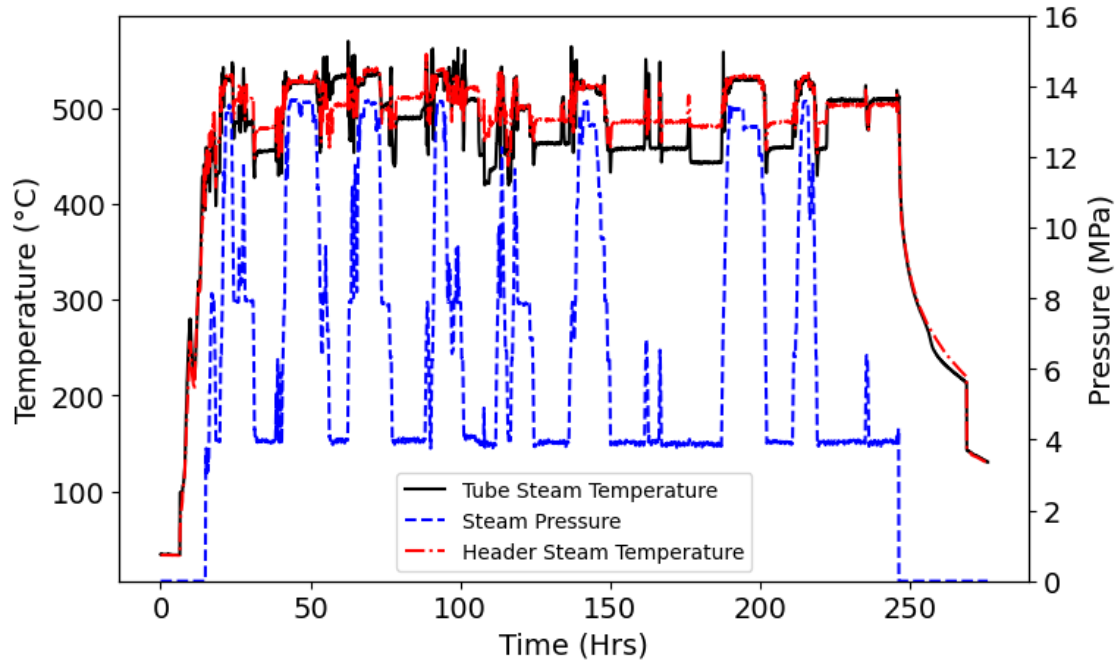


Figure 3.4: Sample of provided operating data. [6]

The transient was idealized to simplify the analysis and reduce the impact of high-frequency fluctuations, capturing the essential trend of temperature behavior. Figure 3.5 presents the modeled temperature and pressure profiles, highlighting discernible differences between the conditions within the header and those within the tube.

Notably, from Fig 3.5, it is clear that the temperature inside of the tube exhibits more pronounced fluctuations than within the header. This discrepancy arises because the header integrates multiple tube inputs, resulting in a homogenized temperature that is less prone to fluctuations. Furthermore, the observed spikes in temperature, both above and below the general transient curve, are attributed to the control mechanisms within the energy system. Initially, the system starts at approximately 450 °C, with tube transients pushing temperatures up to 565 °C, whereas temperatures within the header peak at a slightly lower 525 °C. These variances, along with the tube's temperature fluctuations, underscore the causes of the thermal stresses that can arise during transient conditions.

To simulate these conditions in our models, the temperatures are applied using

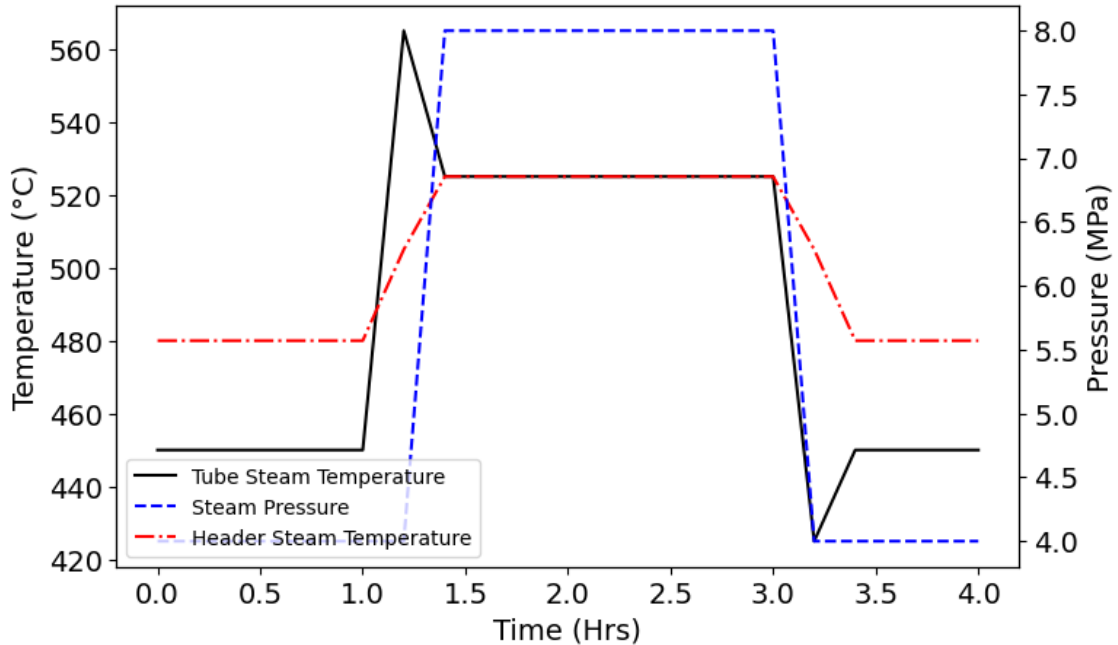


Figure 3.5: Representative transient cycle. [6]

a surface film condition within Abaqus. The exterior surfaces of the headers are represented as insulated, reflecting the energy company's intention to prevent energy loss through conduction or convection across the pipe wall. This assumption plays a critical role in the thermal stress impacts following the thermal transient.

Additionally, pressure within the system is uniformly applied to all internal surfaces. Figure 3.6 illustrates the boundary conditions employed in the model for the P91 header, illustrating the use of symmetry applied to all materials in the study. Figure 3.6 depicts how symmetry was taken advantage of in both the axial and radial directions of the header.

Symmetry is taken along these planes, with the opposite side of the header subjected to a blow-off pressure. Similarly, the tube within the header is subject to blow-off pressure to represent a closed-end condition as expressed in equation 5.1. The calculation for the blow-off pressure is detailed in Equation 3.3. The header is constrained in the y direction to prevent unrealistic movements in space, and it is applied at the lower edge of the axial symmetry plane.

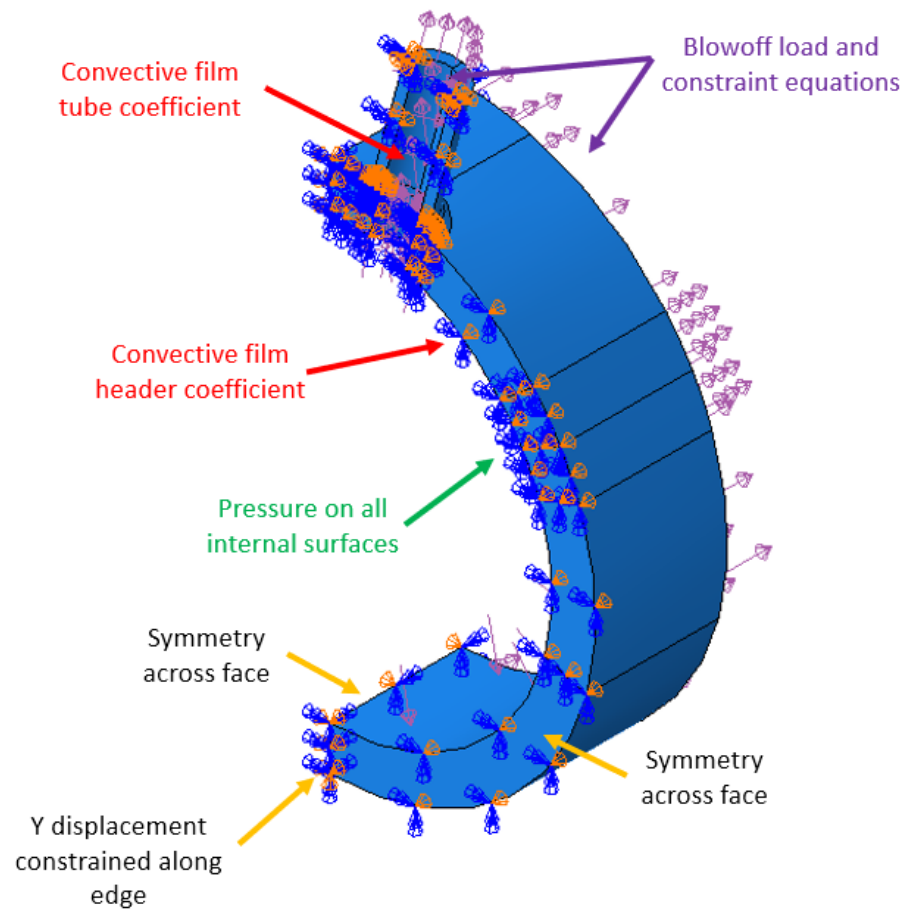


Figure 3.6: P91 boundary conditions, representative of all of the models.

$$P_{\text{tension}} = \frac{PD_i^2}{D_o^2 - D_i^2} \quad (3.3)$$

The mesh for each component was developed to strike a balance between accuracy and computational efficiency, ensuring the comparability of stress levels across models. This consideration is critical given the significant difference in wall thickness between the IN740H and P22 headers, with the IN740H being approximately one-quarter the thickness of the P22. Moreover, each model features a refined mesh around the tube-header intersection, with the mesh coarsening further away from this critical area. All models' lower section of the header has elements up to 15 mm, whereas the minimum element size is 1 mm near the tube-header intersection. This mesh sizing scheme is held constant across all models. Consequently, the number of elements in each model varies significantly, with the P22 model having 42,772 C3D20RT elements, the P91 model having 32,652 C3D20RT elements, and the IN740H model having 15,232 C3D20RT elements. The finalized meshes for the P22, P91, and IN740H models are shown in Fig. 3.7, 3.8, 3.9, respectively.

#### 3.4 Thermal-mechanical analysis

The temperature profiles on the internal surfaces of the tube and header were validated for each model to confirm the accuracy of the mesh configurations used in each model. Figures 3.10, 3.11, 3.12 illustrate the thermal convergence observed in each model relative to the applied temperatures.

Figures 3.10, 3.11, 3.12 demonstrate that there is an agreement between the applied and calculated temperatures for each of the models. Each model was subjected to thermal-mechanical loading, as outlined in the previous section. This loading was repeated several times to determine if plasticity was present and if it was to validate the material model's application further.

The results demonstrate that the location of the critical location for all of the mate-

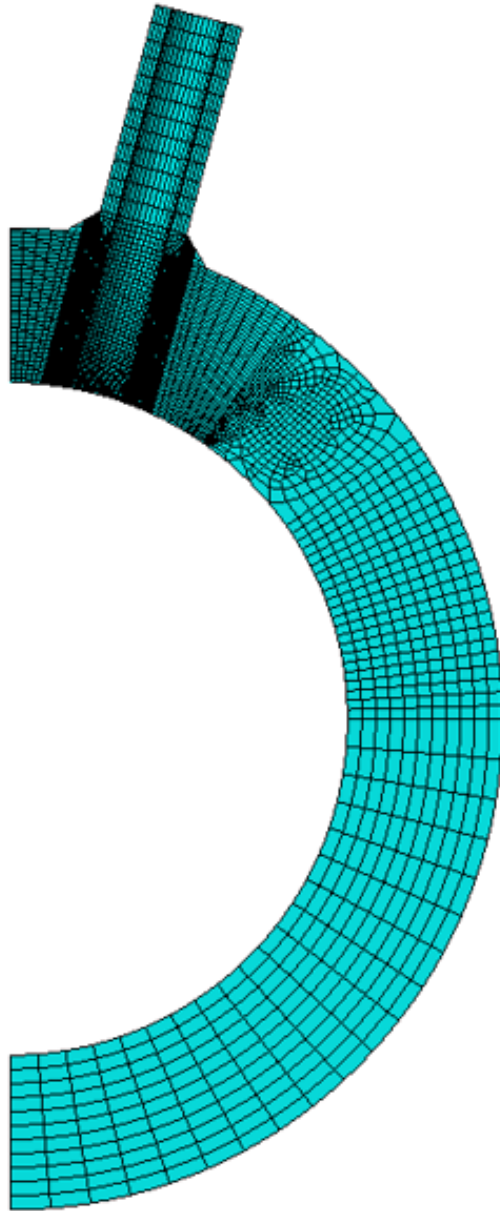


Figure 3.7: Final mesh for the P22 model 42,772 C3D20RT elements.

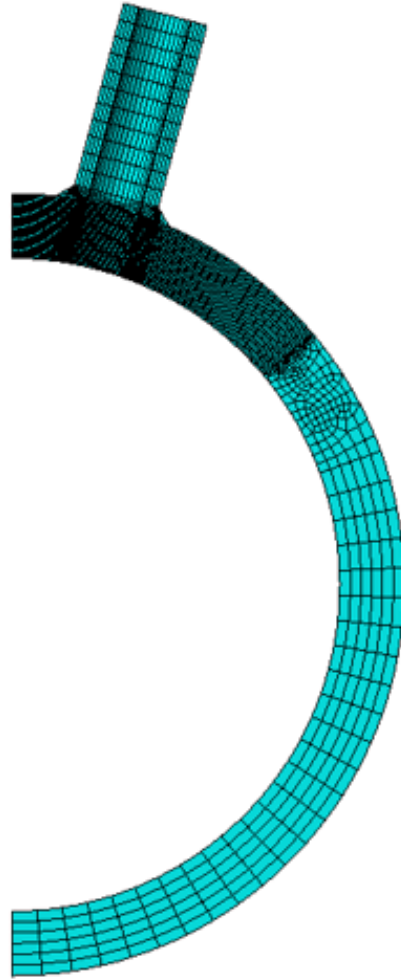


Figure 3.8: Final mesh for the P91 model 32,652 C3D20RT elements.



Figure 3.9: Final mesh for the IN740H model 15,232 C3D20RT elements.

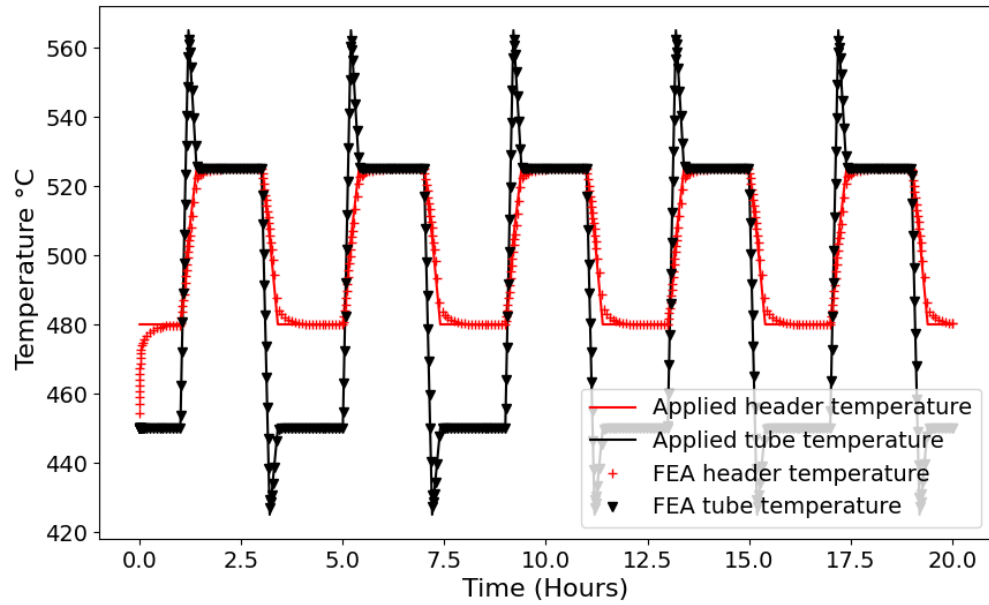


Figure 3.10: Thermal convergence of interior surfaces in P22 header.

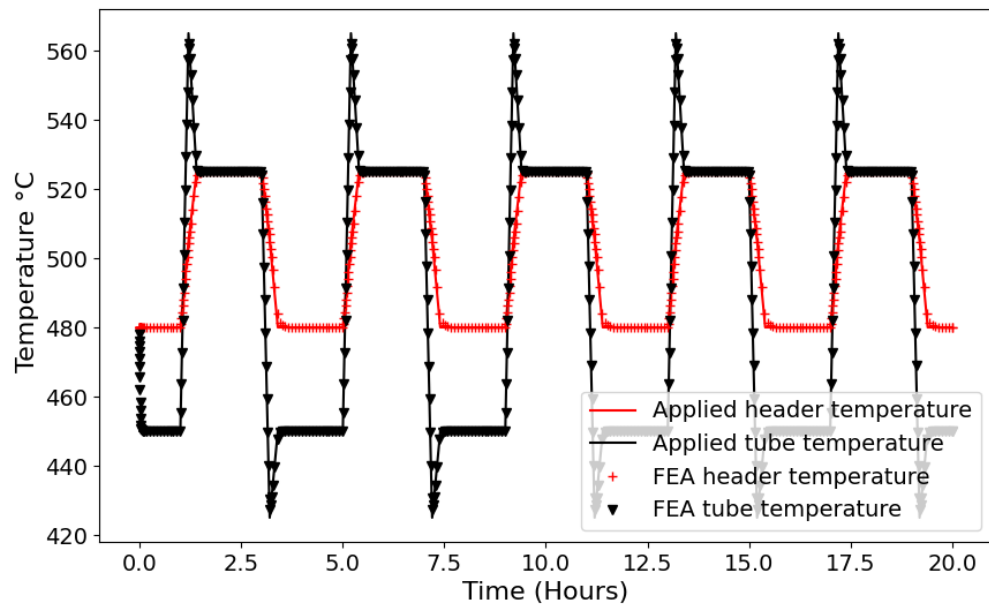


Figure 3.11: Thermal convergence of interior surfaces in P91 header.

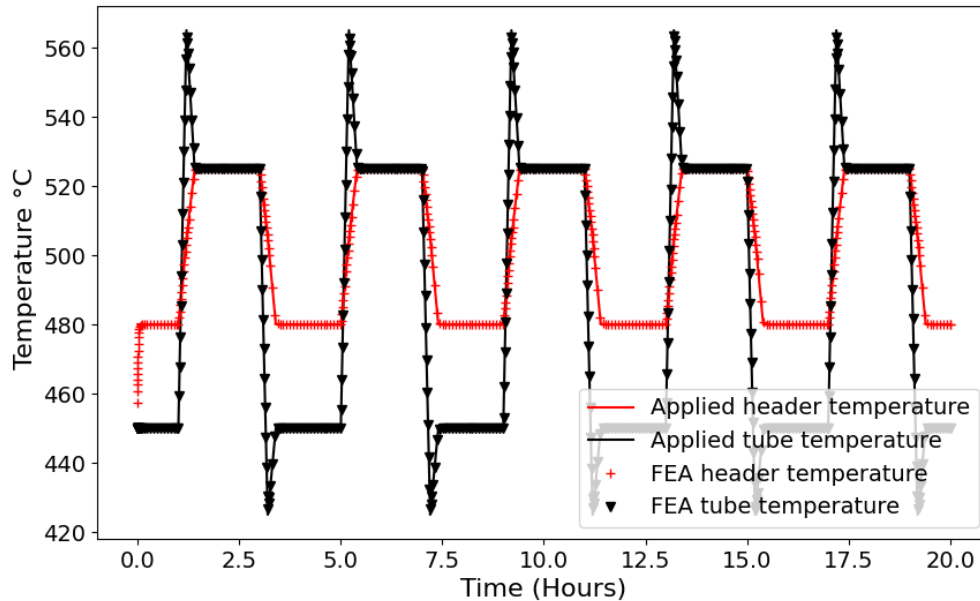


Figure 3.12: Thermal convergence of interior surfaces in IN740H header.

rials is within the through hole for the tube within the header. However, the position of the location within the ID of the tube varied for each material. The location with the highest stresses in the P22 material occurred along the axial edge approximately 40 mm from the intersection with the header, representing about halfway through the thickness of the header. While the location changed from the radial to the axial edge, the stress within the P91 header occurred at a similar location, halfway through the header at approximately 17 mm above the intersection. In contrast, the IN740H header had peak stresses occur along the axial edge of the tube header intersection. This location reflects the better thermal stability that occurs from the reduced wall thickness within the IN740H header. Nevertheless, all of the material options demonstrate that the tube header intersection is the critical location to evaluate for damage. The von Mises stress distribution and location within each of the headers are shown in Figures 3.13 through 3.15.

It follows that the critical stress component depends on the critical point's location.

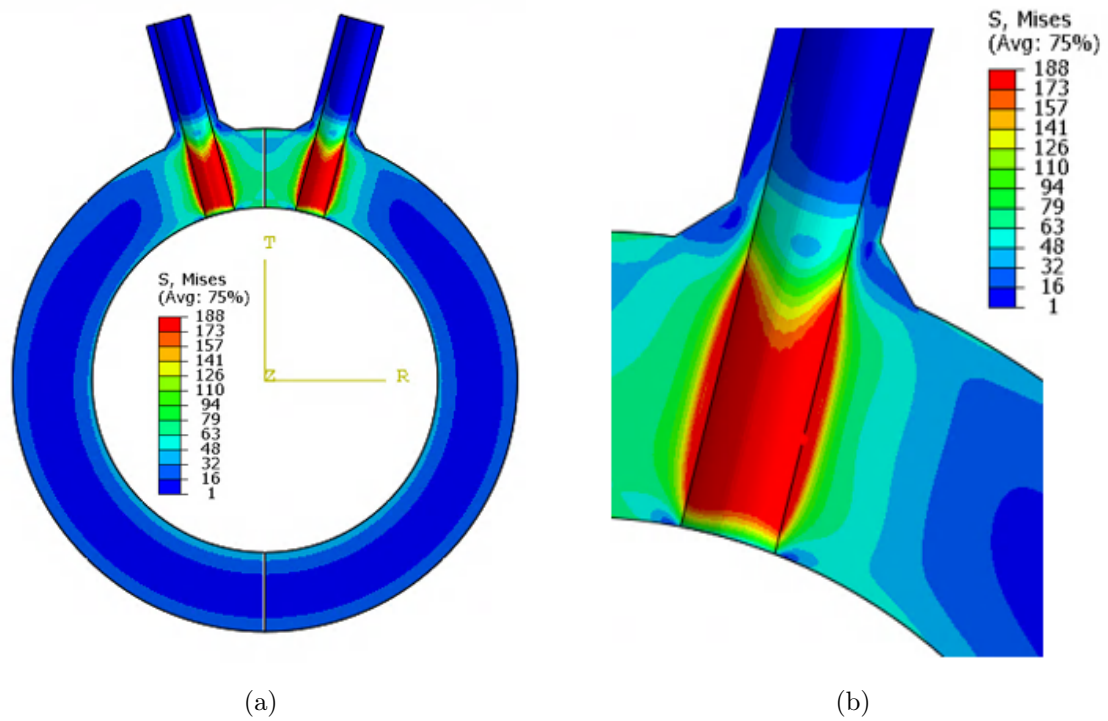


Figure 3.13: von Mises distribution and location of critical point in P22.

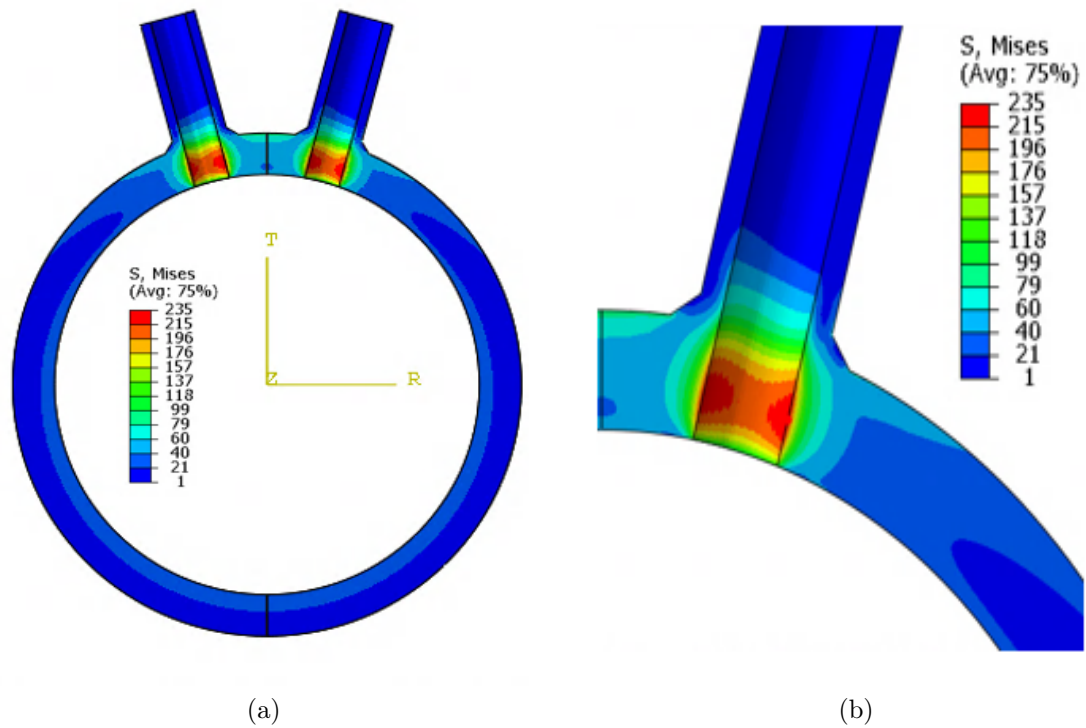


Figure 3.14: von Mises distribution and location of critical point in P91.

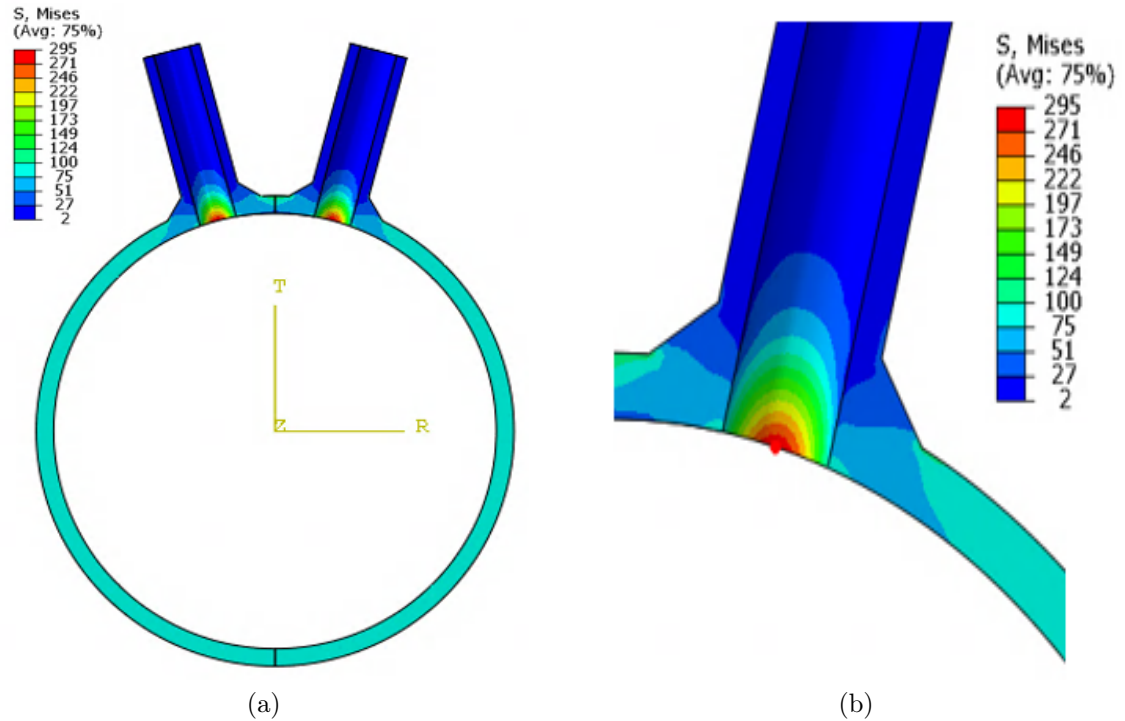


Figure 3.15: von Mises distribution and location of critical point in IN740H.

When comparing the stress at both the radial and axial locations within the materials, an interesting observation is made. Note that the similarity and difference between the peak axial stress along the radial location and the peak radial stress on the axial edge varies by material. This can be seen in Fig. 3.16 through Fig. 3.21.

For instance, comparing Fig. 3.18 to Fig. 3.19 demonstrates that the peak axial and hoop stresses within the P91 header are almost the same. In contrast, the IN740H header experiences hoop stresses that are double the axial forces within the header shown in Figures 3.21 and 3.20. In comparison, the P22 material header has an axial stress nearly triple the stress despite the additional thickness. This highlights the influence of the thermal stresses that occur from the increased thickness within the material. By evaluating the stress over time compared to the thermal transient, it is possible to evaluate which section of the transient influences the stress behavior of the material. Fig. 3.22 through 3.24 represent the stress response of the material compared to time, providing the thermal transient within the tube and header for

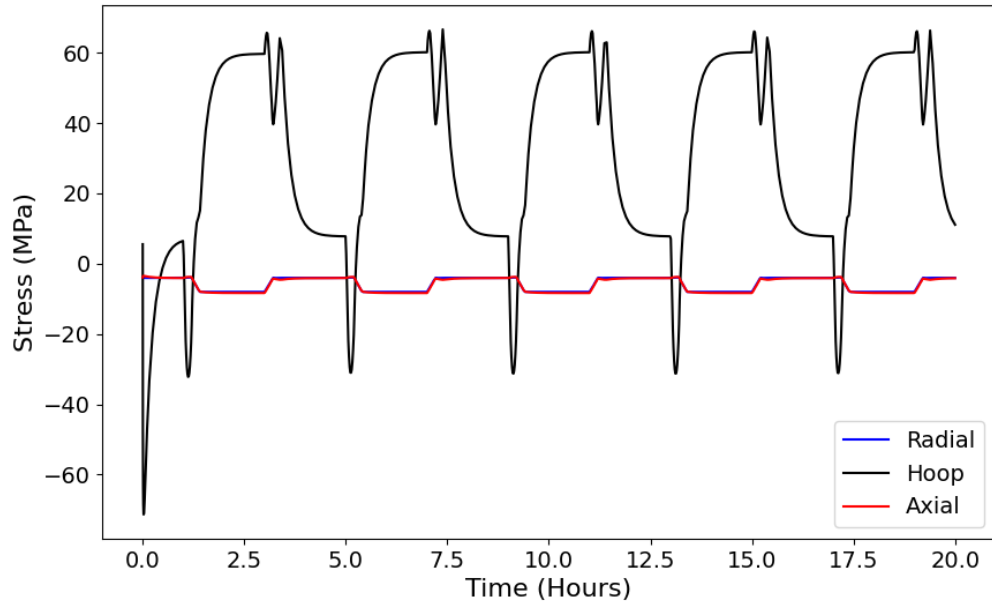


Figure 3.16: Decomposed stress component response of the P22 header taken at the peak axial location.

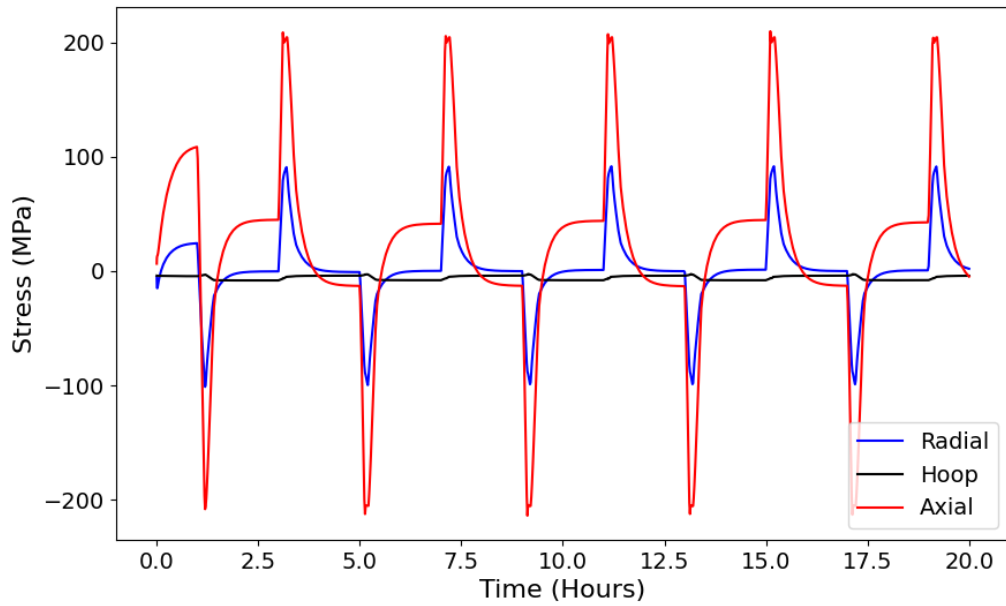


Figure 3.17: Decomposed stress component response of the P22 header taken at the peak radial location.

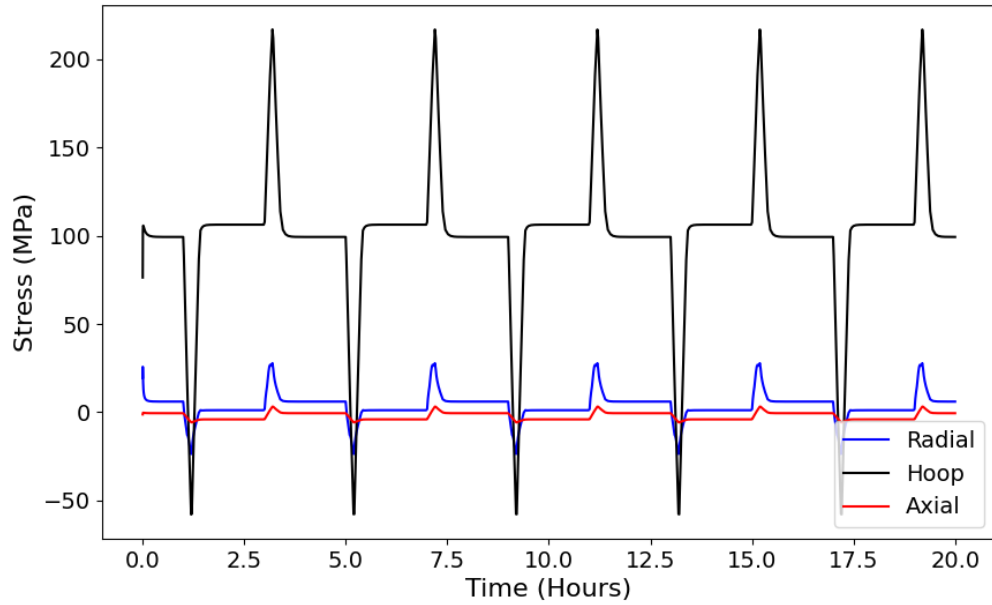


Figure 3.18: Decomposed stress component response of the P91 header taken at the peak axial location.

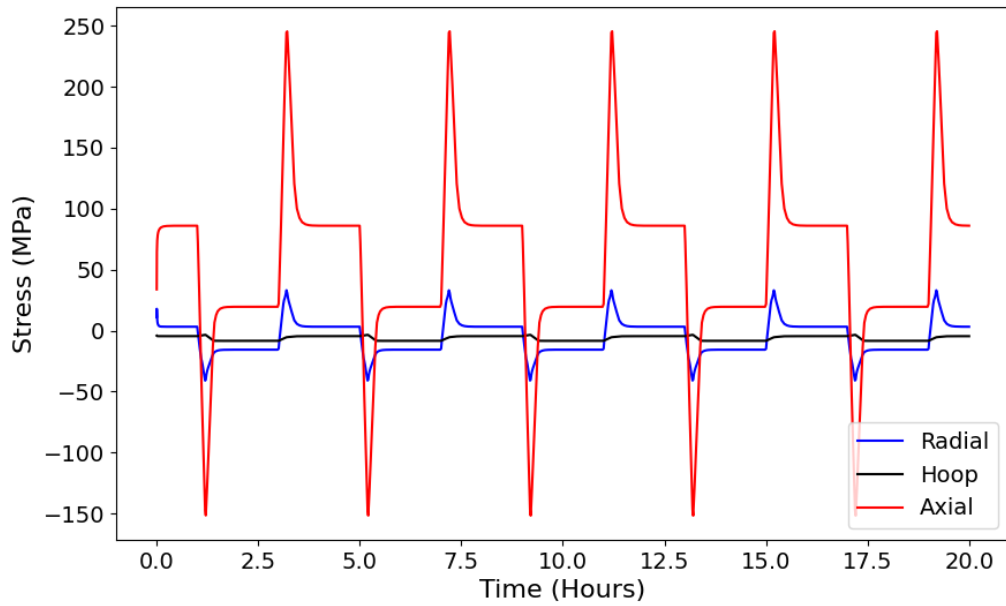


Figure 3.19: Decomposed stress component response of the P91 header taken at the peak radial location.

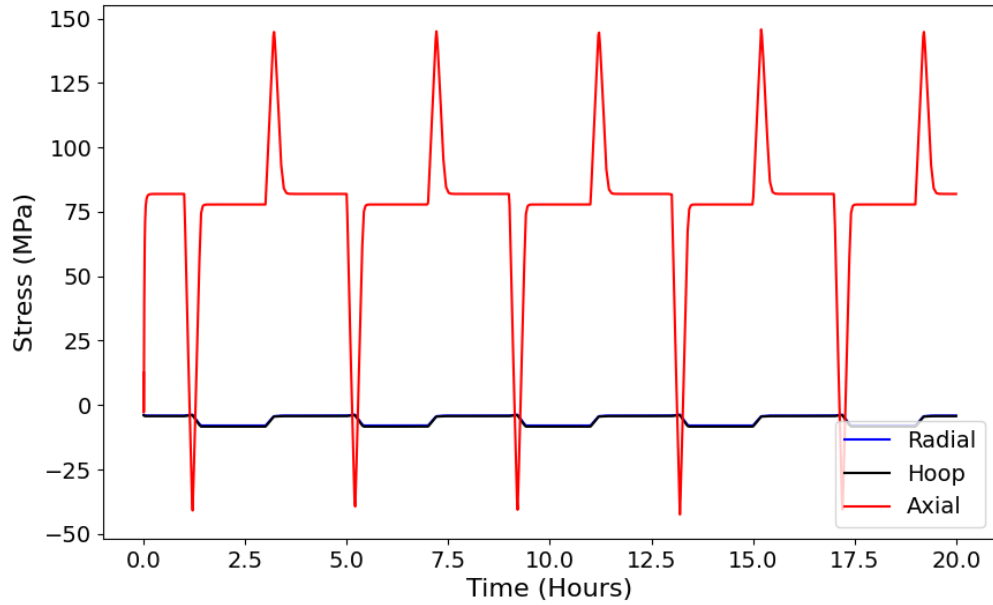


Figure 3.20: Decomposed stress component response of the IN740H header taken at the peak radial location.

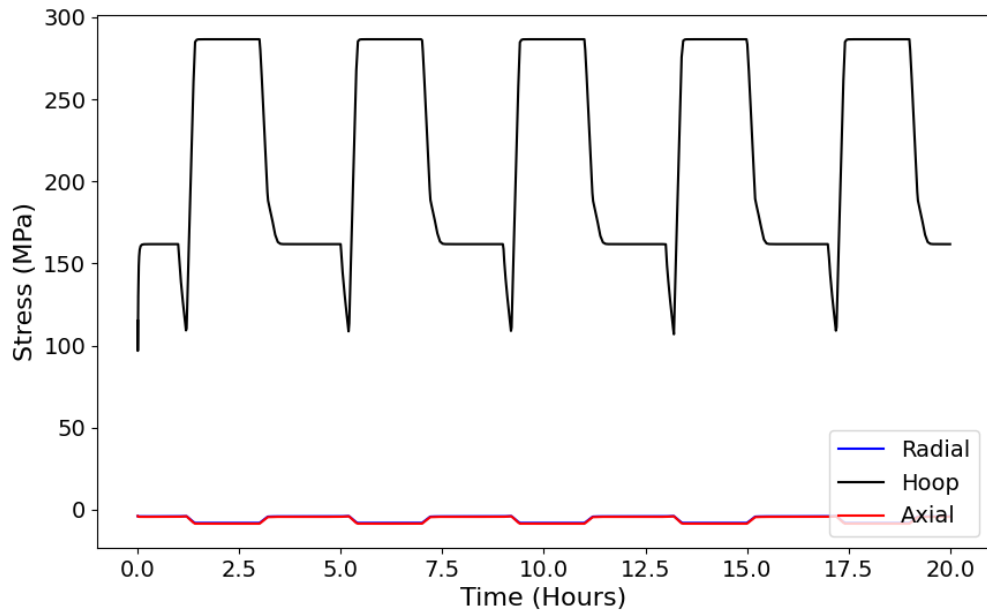


Figure 3.21: Decomposed stress component response of the IN740H header taken at the peak axial location.

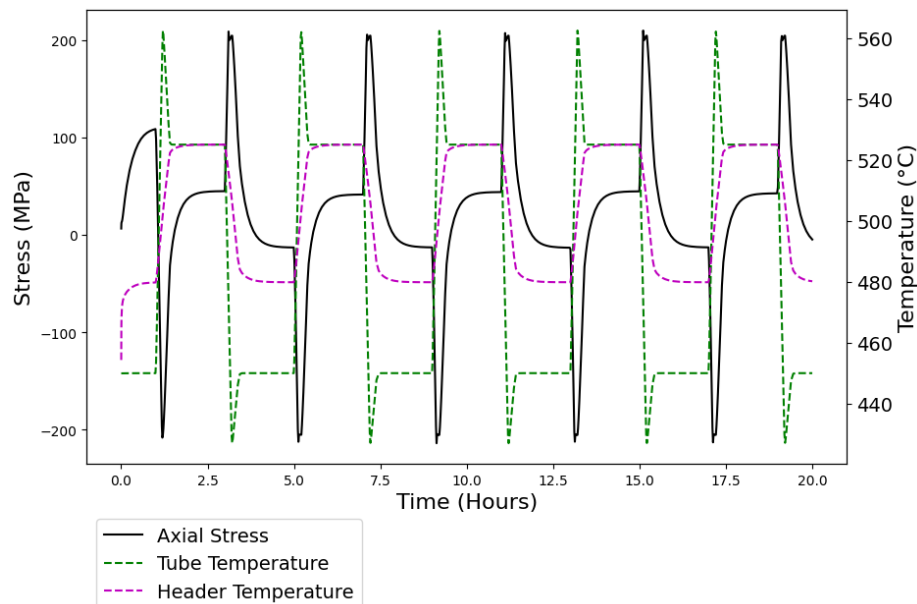


Figure 3.22: Stress in comparison to temperature and time for the P22 header taken at the peak radial location.

comparison.

It is clear from the analysis that significant stress increases occur in both the P22 and P91 headers during rapid temperature changes within the system. This is represented by the rapid spikes in stress following the change in the tube temperature of the system. This is an important observation, given that cooling transients may stem from operational anomalies within the system, potentially leading to more rapid cooling rates than those typically associated with increasing temperature scenarios. Such cooling events lead to material contraction while the bulk of the material remains hot, creating thermal gradients that increase stress across the header's thickness. Similar phenomena are observed during temperature increases, though the stress on internal surfaces may shift from tensile to compressive. In contrast, however, Fig. 3.24 demonstrates that the stress within the IN740H header does not fluctuate with the temperature. This can be attributed to the notably thinner walls that are used within the header. This example demonstrates one benefit of using a stronger material, resulting in lower minimum wall thickness. These figures demonstrate the interaction

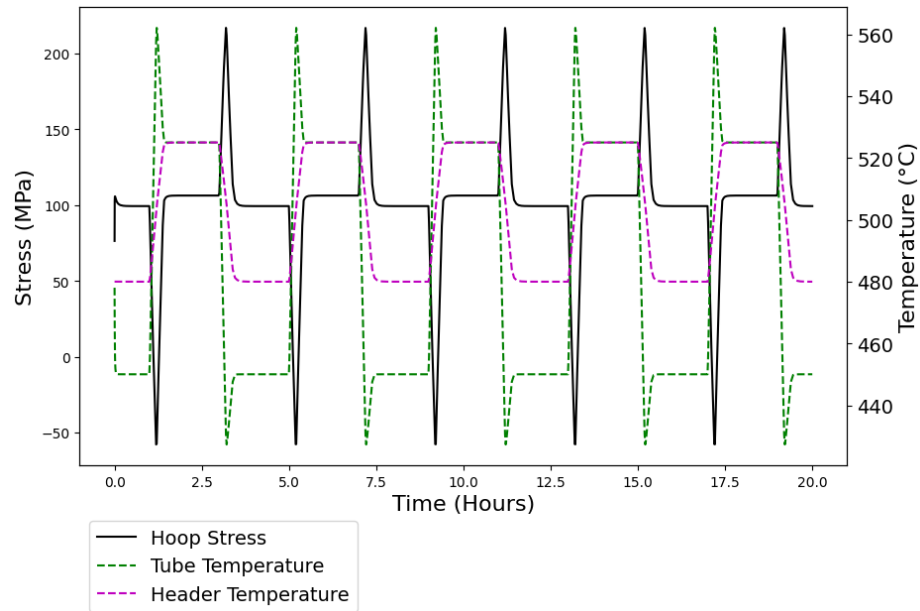


Figure 3.23: Stress in comparison to temperature and time for the P91 header taken at the peak axial location.

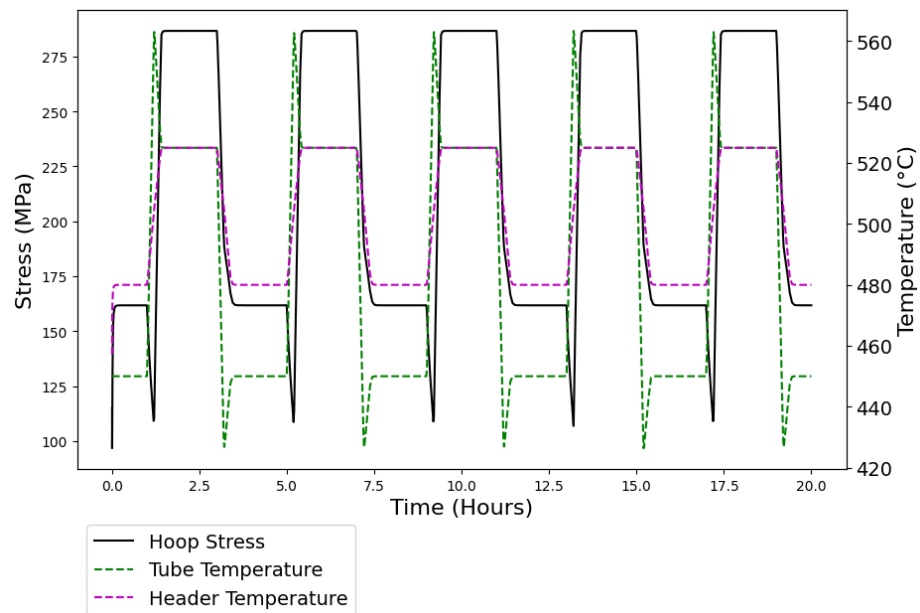


Figure 3.24: Stress in comparison to temperature and time for the IN740H header taken at the peak axial location.

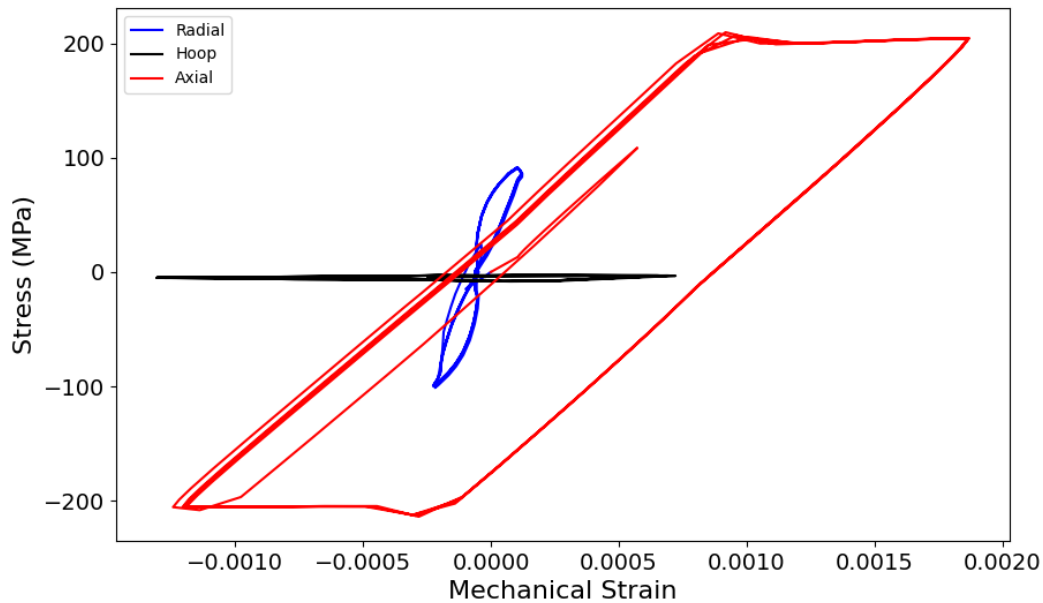


Figure 3.25: Stress-strain response of the P22 header taken at the peak radial location.

of thermal transients and material stress responses, highlighting the need to evaluate a thermal transient during operation.

### 3.5 Fatigue life predictions

Evaluating the stress-strain response of the material can highlight significant contributions to fatigue. Figures 3.25 through 3.30 represent the decomposed stress-strain responses of each of the materials stemming from the transient, taken from the location correlating to the highest stresses along the radial and axial directions.

These figures show that the axial stress is the most influential as it reaches the highest stresses. These figures also highlight the robustness of the material choices chosen as the chosen alternatives experience stresses far exceeding the yield strength of the P22 header without incurring damage. For instance, the highest stress within the P91 header is 234 MPa along the radial direction. Similarly, the stresses within the IN740H header were highest along the axial direction, with a peak stress of 294 MPa. Notably, the stresses for each of the alternative materials were well within the

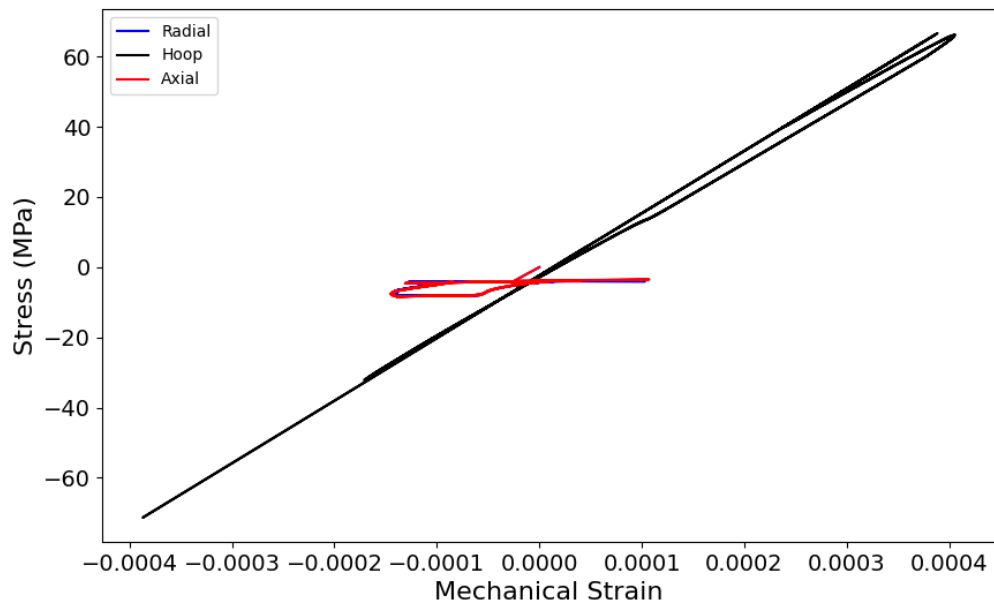


Figure 3.26: Stress-strain response of the P22 header taken at the peak axial location.

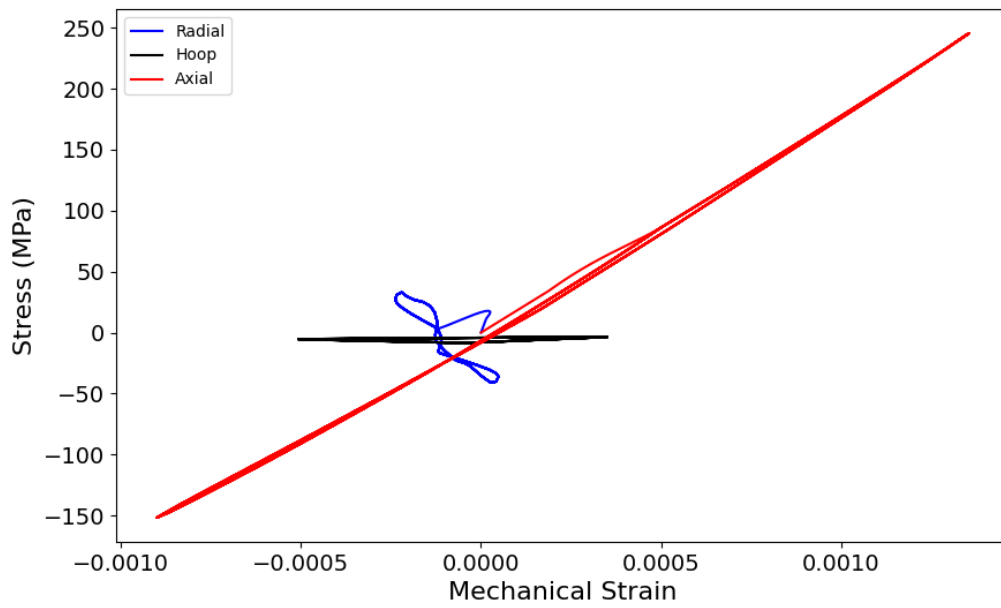


Figure 3.27: Stress-strain response of the P91 header taken at the peak radial location.

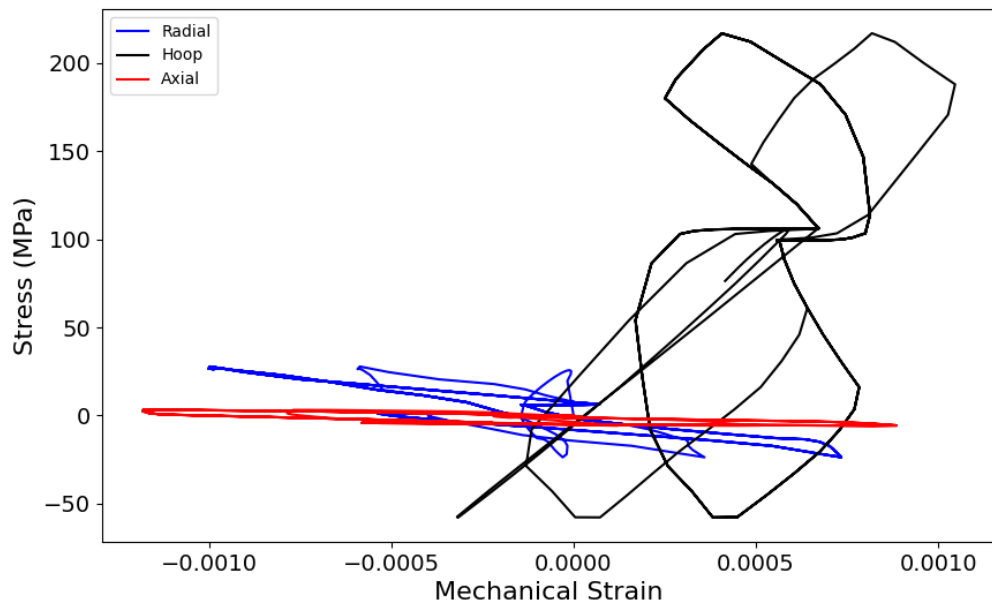


Figure 3.28: Stress-strain response of the P91 header taken at the peak axial location.

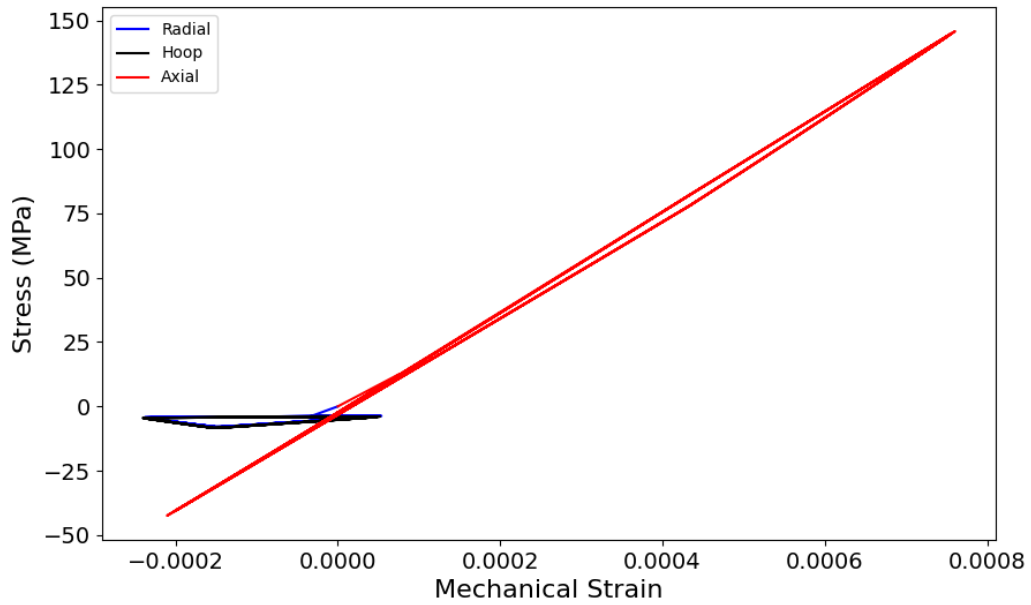


Figure 3.29: Stress-strain response of the IN740H header taken at the peak radial location.

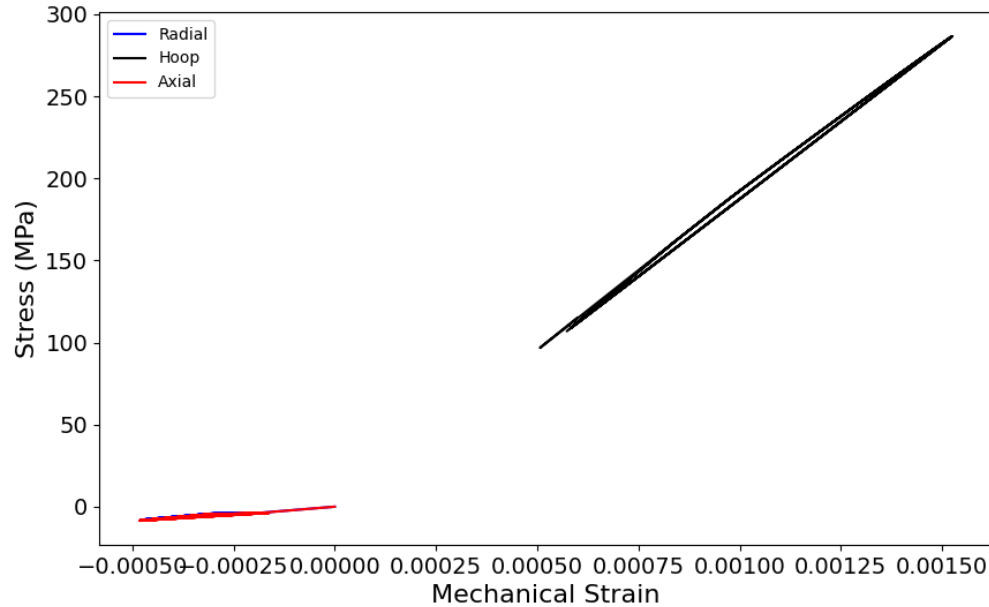


Figure 3.30: Stress-strain response of the IN740H header taken at the peak axial location.

yield stress, with the P91 material only reaching a point of 76 % of its yield stress and IN740H reaching 40 %. So, while neither of the materials experience time-independent yielding, the level of stress within P91 suggests that time-dependent factors may be influential.

It follows that only the P22 model accumulated any plasticity, which remained consistent throughout the cycles. This behavior is shown in Fig. 3.32, which presents the plastic strain over time within the headers. Additionally, Fig.3.32 shows that the IN740H and P91 header do not accumulate any plastic strain. This differentiation highlights the variation that material selection has in response to identical loading. The location of the P22 header that accumulated plastic strain is along the edge of the radial location of the tube header intersection. this location is shown in Figure 3.33(a).

The fatigue life of each material was estimated using the Ostergren damage model and critical plane approach. The Ostergren model is used to approximate the pro-

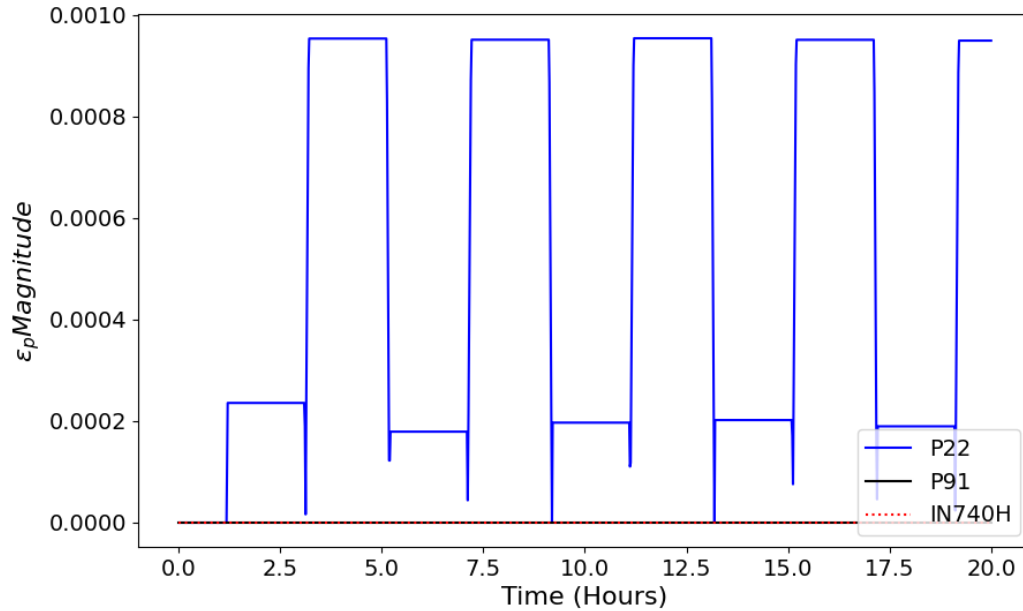


Figure 3.31: Plastic strain magnitude over time for each of the materials.

gressive fatigue of materials under cyclic loading, particularly in low cycle fatigue conditions at elevated temperatures [146]. The Ostergren model characterizes the number of cycles to failure as,

$$N_f = C(\Delta\epsilon_{in}\sigma_{max})^\beta \quad (3.4)$$

where  $\sigma_{max}$  is the peak tensile stress,  $\Delta\epsilon_{in}$  is the corresponding inelastic strain range, and  $C$  and  $\beta$  are material constants. The values of  $\beta$  and  $C$  for P22 are -1.6 and 1300, respectively [158]. Given that the P91 and IN740H models did not accumulate inelastic strain, they are not anticipated to fail from fatigue using the present model. In contrast, the peak plastic strain magnitude for the P22 header is 0.0905%. This suggests that the edge case transient could be repeated for 29,190 cycles. If the system were to experience this transient five times a day, the theoretical lifetime would be approximately 10 years. This starkly contrasts the P91 and IN740H materials, which did not show signs of fatigue from the present study.

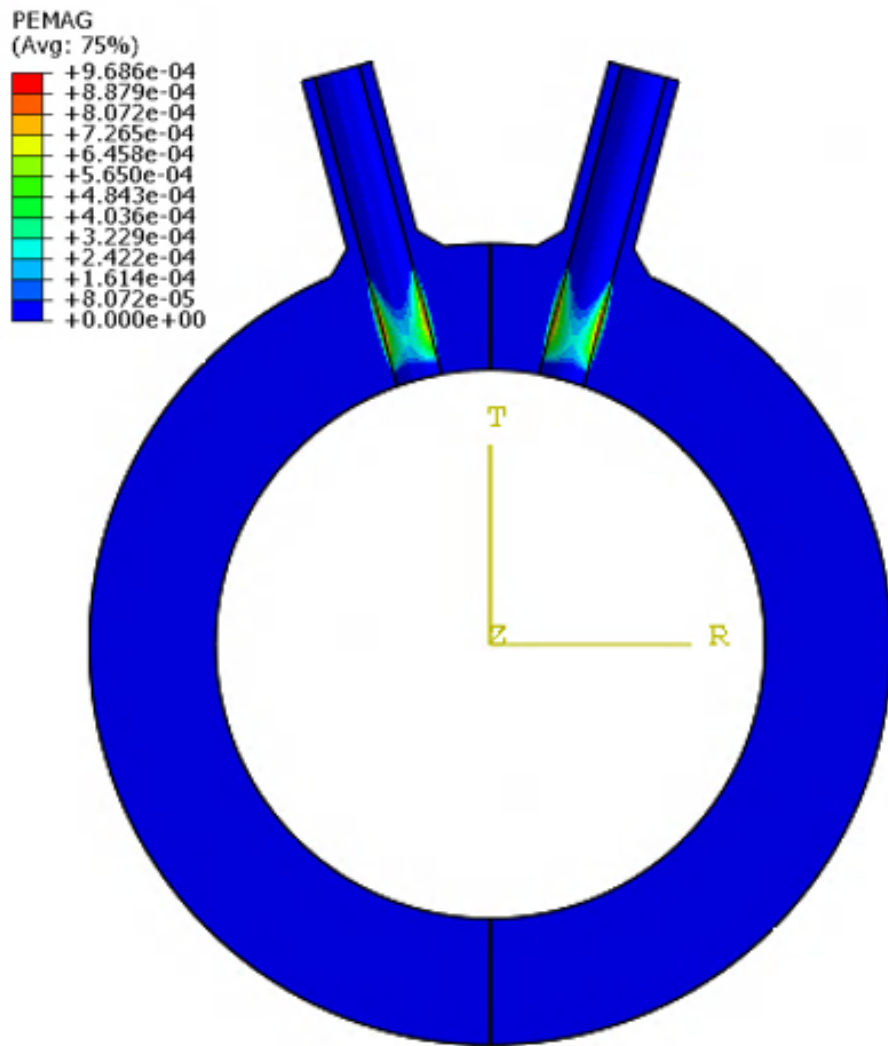


Figure 3.32: Plastic strain magnitude distribution in the P22 header.

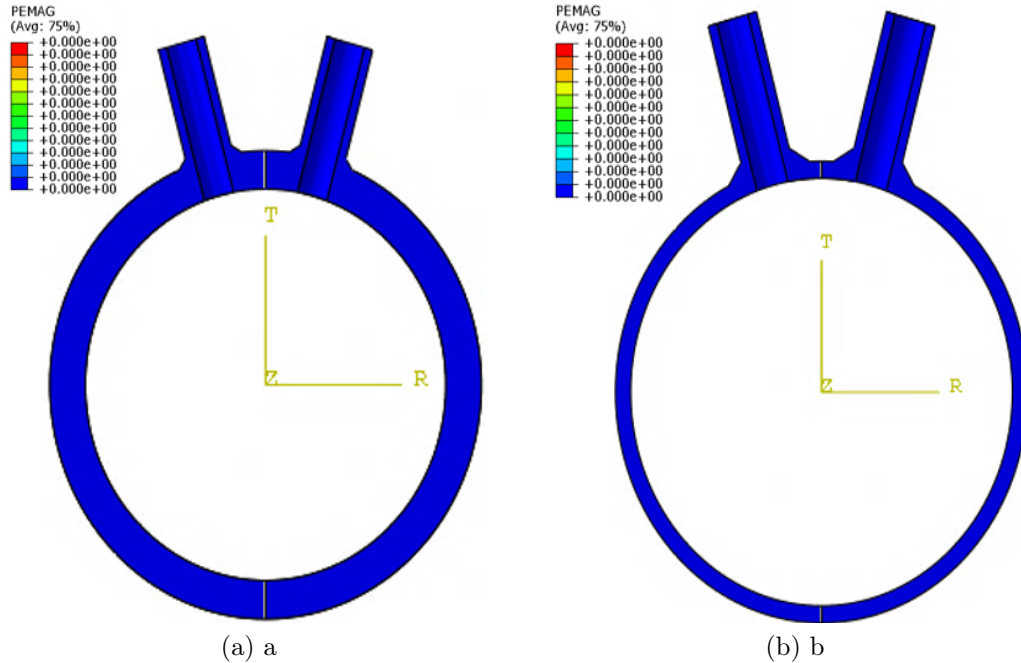


Figure 3.33: Plastic strain magnitude distribution in each of the (a) P91 (b) IN740H headers.

### 3.6 Conclusion

The analysis suggests that a header made of P22 alloy could possibly experience fatigue failure within 10 years. Under the same loading conditions, the headers designed with P91 and IN740H alloys demonstrate improved durability, with no significant accumulation of damage suggesting fatigue failure. These results highlight their improved performance over the 2.25Cr-1Mo material.

However, material costs play a significant role in the decision-making process when considering the cost-benefit analysis. Market estimates for generalized seamless pipe were used to establish the price of each header. The breakdown of the cost is shown in Table 3.6 [159]. While the costs will likely fluctuate for the actual header, the market pricing for standardized seamless pipe will serve as the comparison.

The data presented in Table 3.6 highlights the substantial cost associated with the IN740H alloy. Despite its considerably lower weight compared to the P22 header, the IN740H variant incurs more than twice the expense of either alternative. Conse-

Table 3.6: Cost Estimate.

Material	USD Per Ton	USD Per Pound	Weight (Pound)	Final Cost USD
P22	1,580	0.79	17,679	13,967
P91	5,110	2.56	6,697	17,145
IN740H	44,000	22	2,670	58,737

quently, for the purposes of this project, the IN740H header is deemed economically unfeasible. In contrast, the P91 header presents only a 22% cost increase over the P22 header, making it a competitive alternative.

The expected rise in operational fluctuations further supports the selection of P91. Additionally, accounting for time-dependent effects, which were not included in this analysis, suggests that prolonged exposure to high temperatures could accelerate damage in the P22 header more so than in the P91 header. Despite the initial 20% cost premium for P91, the diminished need for future repairs indicates that the additional upfront investment could be recuperated within two decades.

In conclusion, choosing between P22 and P91 depends on weighing the immediate costs against long-term system performance. If the operational environment evolves to include more frequent and severe transients over the next 10 years, P91 serves as the primary option. Conversely, if operational demands are expected to stabilize or diminish, the P22 header may offer better cost efficiency, particularly when considering the potential for extended service life beyond 10 years when factoring in repair costs. This analysis demonstrates the importance of considering a comprehensive view when evaluating a material for performance and economic considerations.

## CHAPTER 4: Service exposure effects on 2.25Cr-1Mo steam header service life

### 4.1 Introduction

This section evaluates the service exposure effects on the service life of a 2.25Cr-1Mo header, adapted from the work by Zimnoch et al. [6]. Therefore, the material presented in this section directly links to the framework of the published work. The validity of FEA models is significantly dependent on the precision of the applied material properties and the suitability of the material model. This understanding surfaced after noting discrepancies in the predicted lifespans of an outlet header. As a result, specimens were obtained from a decommissioned steam header, which had previously operated for more than 200,000 hours at temperatures around 538 °C. The Electric Power Research Institute completed the fabrication and testing of the service-exposed samples [6]. Characterizing the aged samples involved uni-axial incremental triangular strain testing consisting of cycles of repetitive strain blocks. Each block contained fifty cycles at specified strain ranges and temperatures, with the strain increments set at 0.1%, 0.25%, 0.4%, 0.5%, 0.75%, returning to 0.5%, and then 0.25%. This sequence was repeated six times per sample, resulting in a total of 2100 cycles. The illustration of this strain application is shown in Figure 4.1. This testing scheme was performed at temperatures of 20 °C, 300 °C, and 500 °C, intended to mirror the range of thermal and mechanical conditions likely encountered by the header. The material's full stress-strain behavior at each temperature is detailed in Figs. 4.2, 4.3, and 4.4 provided, with the reported stress and strain values representing the stable reaction of the samples across the various strain intervals [6].

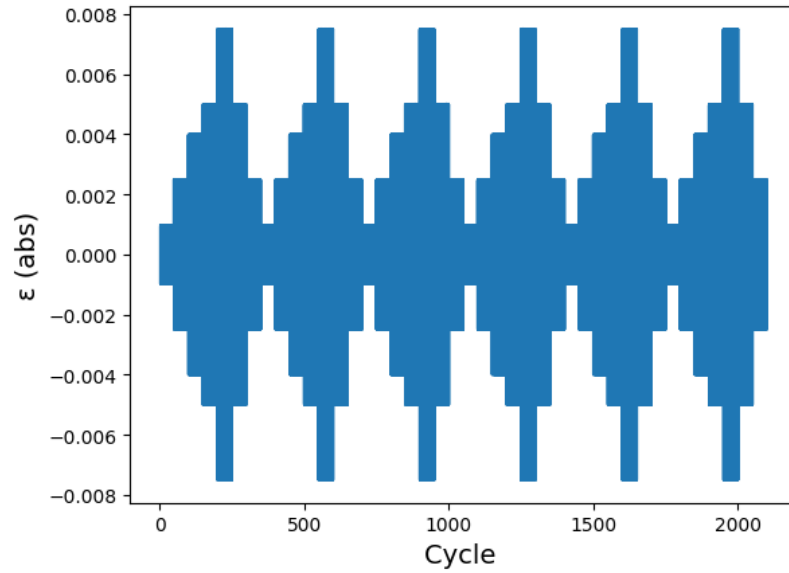


Figure 4.1: Complete strain history of service exposed test sample at 20 °C. [6]

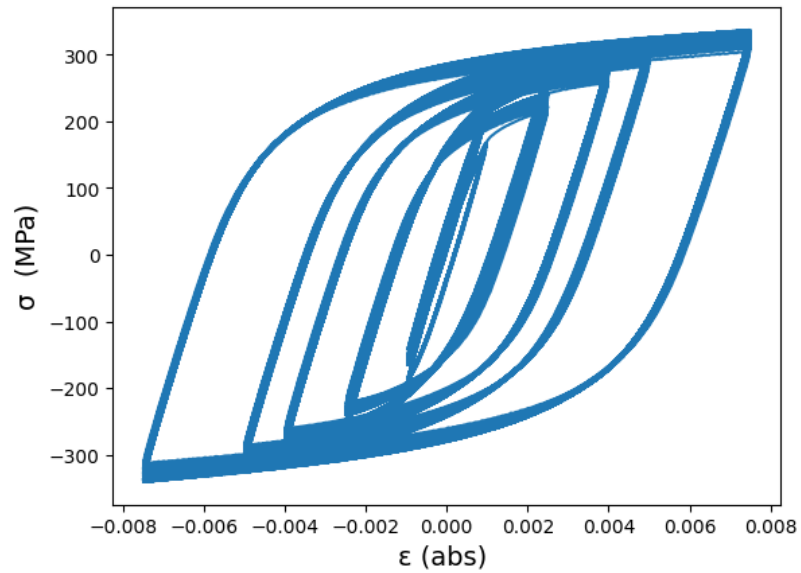


Figure 4.2: Complete hysteresis history of service exposed test sample at 20 °C. [6]

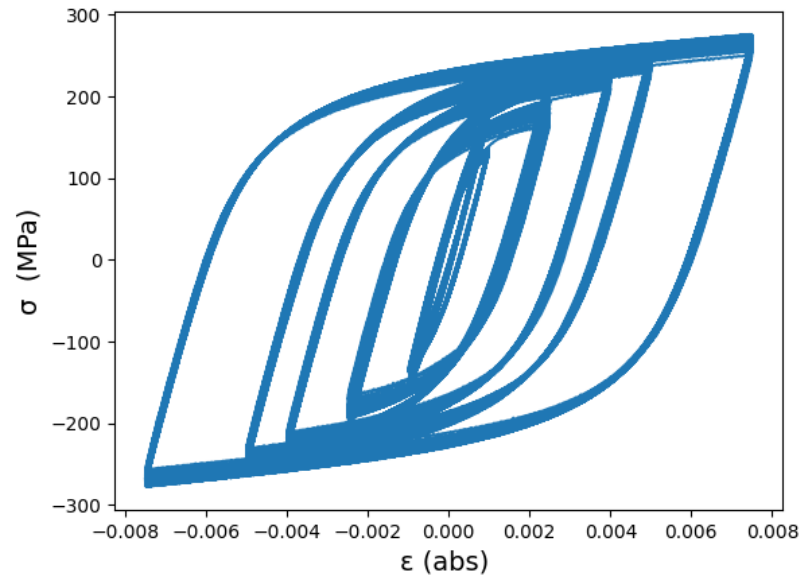


Figure 4.3: Complete hysteresis history of service exposed test sample at 300 °C. [6]

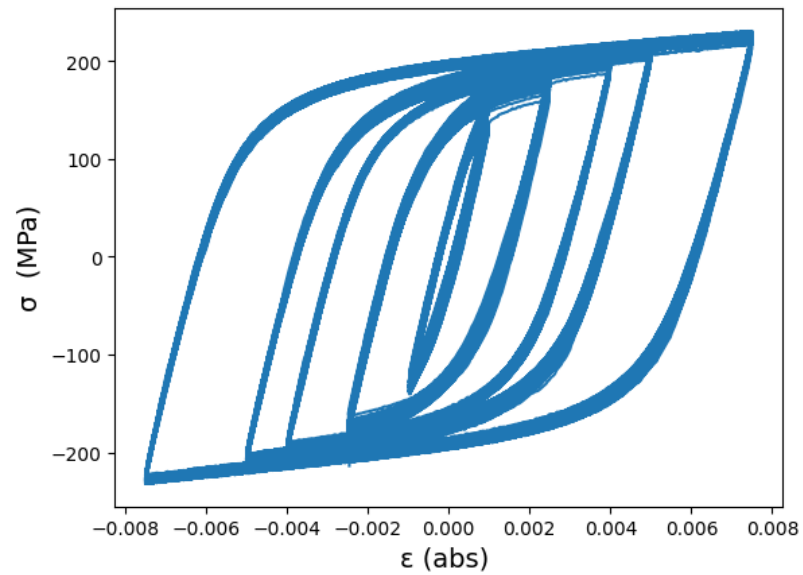


Figure 4.4: Complete hysteresis history of service exposed test sample at 500 °C. [6]

## 4.2 Experimental Characterization

### 4.2.1 Experimental results

Considering the previous operational history of the header, a complete record of the strain history of the material samples was unavailable. Consequently, acquiring the Isotropic hardening parameters was unfeasible, leading to the decision to solely utilize the kinematic hardening variables to represent the material. Notably, due to the testing sequence endured by the specimens, any potential impact of Isotropic hardening would have dissipated. Furthermore, although minor inaccuracies might arise during the initial hardening response of the header, the present work only evaluates the stabilized outcome when gauging the remaining lifespan [160]. Hence, the use of kinematic hardening was deemed appropriate.

The material data for the virgin samples is sourced from the NIMS online material database [161]. The mechanical properties of the virgin samples are outlined in Table 4.4. All of the materials comply with the requirements of ASME BPVC for SA335-P22. The virgin samples were tested using constant amplitude strain cycles using a strain rate of  $10^{-3}\text{s}^{-1}$ . The reported amplitudes are from the half-life of the samples, where failure is defined as a 25% decrease in the maximum tensile load of the stable condition.

Figures 4.5, 4.6, and 4.7 illustrate the stable hysteresis loop of the materials after service exposure in comparison to the virgin samples at temperatures of  $20^{\circ}\text{C}$ ,  $300^{\circ}\text{C}$ , and  $500^{\circ}\text{C}$ , respectively. It is clear from these figures that the service-exposed material exhibits a significantly lower stable cyclic stress-strain response compared to the virgin material. For example, in Fig. 4.6, the service-exposed sample demonstrates a peak stress of 214 MPa at 0.25% strain, while the virgin sample exhibits a peak stress of 294 MPa. This is a result of the yield stress of the service-exposed sample being lower than that of the virgin material.

Evaluating the plastic strain range of a complete hysteresis loop between the two

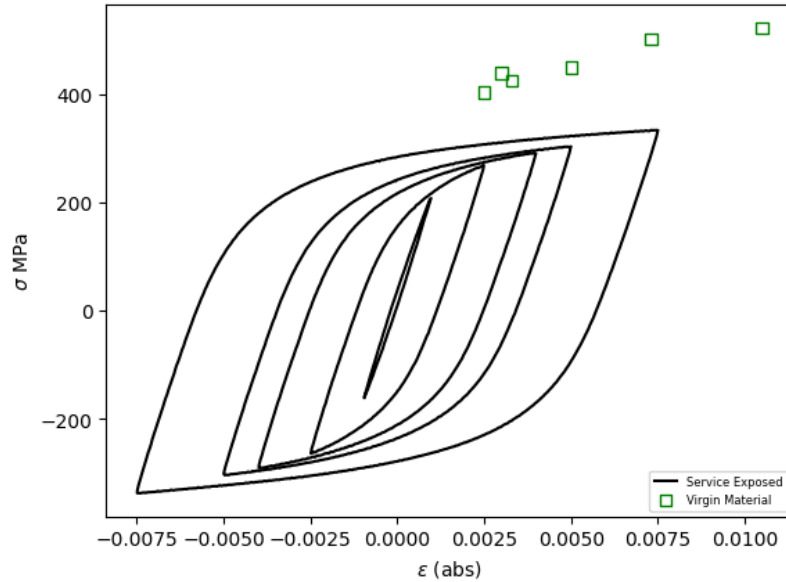


Figure 4.5: Stable hysteresis response of virgin and service exposed material at 20 °C. [6]

materials elucidates the variation in their responses. For instance, the inelastic strain range of the 0.5% hysteresis loop of the virgin and service-exposed material at 300Å°C is 0.00638 and 0.0075, respectively. This indicates that the service-exposed material would accumulate approximately 19% more strain than the virgin material in this condition.

These findings align well with previous investigations of service-exposed material. For instance, Okazaki compared the stable cyclic stress-strain response of 2.25Cr-1Mo material extracted from boiler tubes exposed to around 100,000 hours of service [34]. Their study reported an approximate 20% reduction in the stress of the stable CSS response, a reduction also observed in control samples solely exposed to thermal aging. A number of studies attribute this strength reduction to carbide evolution in P22, leading to coarser carbides and alterations in the matrix composition [54]. Consequently, the material experiences a decrease in strength, rendering it more vulnerable to thermal fatigue [34].

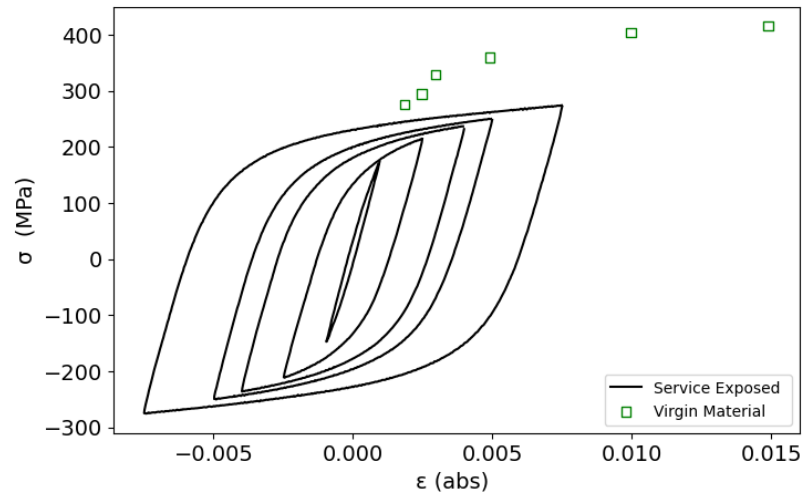


Figure 4.6: Stable hysteresis response of virgin and service exposed material at 300 °C. [6]

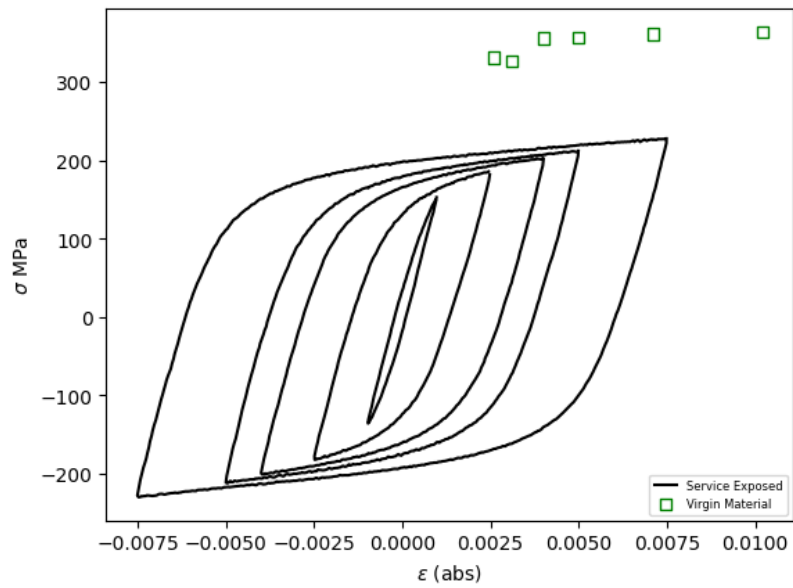


Figure 4.7: Stable hysteresis response of virgin and service exposed material at 500 °C. [6]

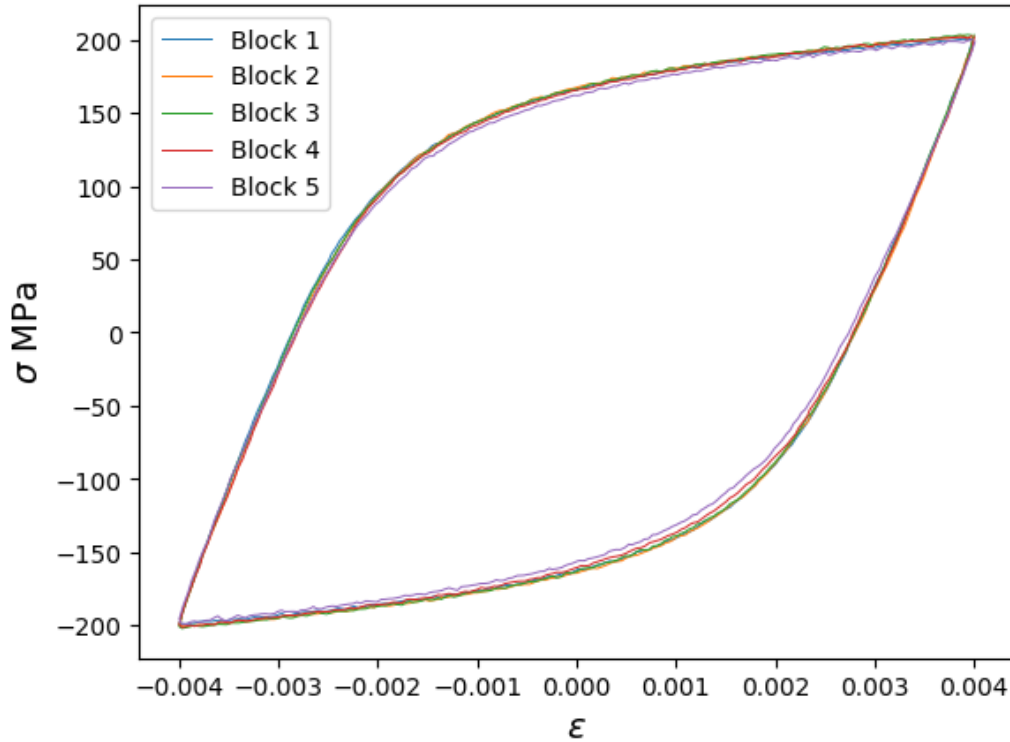


Figure 4.8: Stable hysteresis loop for service exposed material at 500 °C. [6]

## 4.2.2 Identification of Parameters

### 4.2.2.1 Service Exposed Material

Determining the material parameters for service-exposed materials involves applying the Chaboche NLKH model to the samples' mechanical behavior. The initial step in this process involves analyzing the experimental data to capture the material's stabilized response, as illustrated in Figs. 4.2–4.4. The stable response can be used to directly determine the values for  $\sigma_a$ ,  $\epsilon_a$ ,  $k$ , and  $\epsilon_p$ . According to theory, the value of  $k$  signifies the initial departure from a straight-line response. However, the exact value for this departure, particularly the plastic strain value, is left open to interpretation. Yet, many have suggested it may be less than the 0.2% typically used for the yield point [110,162]. In the current work, the onset of non-linearity is defined as a plastic

strain ( $\epsilon_p$ ) of  $10^{-5}$ . This choice reflects the inherent variability in interpreting these measurements, further illustrated by the variation seen in the stable hysteresis loops of the service-exposed material. For instance, Fig. 4.8 illustrates a difference of 20 MPa in the value of  $k$ , depending on the chosen stable hysteresis curve for evaluation. This approach emphasizes the inherent difficulties in firmly establishing a set of material parameters by highlighting the variability and interpretive challenges found while evaluating the service-exposed material's response. Hence, to ensure uniformity between the materials, the value of  $k$  was calculated using the Ramberg-Osgood formula defined as,

$$\frac{\Delta\sigma}{2} = k' \left( \frac{\Delta\epsilon_p}{2} \right)^{n'} \quad (4.1)$$

where  $n'$  and  $k'$  are material constants. Figure 4.9 demonstrates how the material model corresponds with the test data. The coefficients obtained are outlined in Table 4.3. Once the values of  $n'$  and  $k'$  are established, it is possible to calculate the yield stress  $k$  required for the Chaboche NLKH model by assuming a small plastic strain and substituting  $k$  for the equation's left side.

The process used to establish the Chaboche NLKH coefficients is dependent on the number of back-stresses selected. Figure 4.10 demonstrates how two sets of the Chaboche NLKH parameters can be used to fit the virgin material experimental data at 400 Å°C. The process starts by selecting initial values for the parameters  $\gamma_i$  and  $C_i$  and graphing the stress response over a hypothetical strain range. The parameters are then adjusted to establish an accurate representation of the material behavior using their sum. Figure 4.10 illustrates how the two segments representing  $i = 1$  and  $i = 2$  are chosen so that they target separate regions of the stress-strain response. This is demonstrated by the initial steep rise of the curve representing  $i = 1$ , which then stabilizes, shifting the influence of larger strains to the parameter choice for  $i = 2$ . The strain range that is selected for optimizing coefficients should also be considered. For instance, the present study assumes minimal plastic deformation. Therefore, it

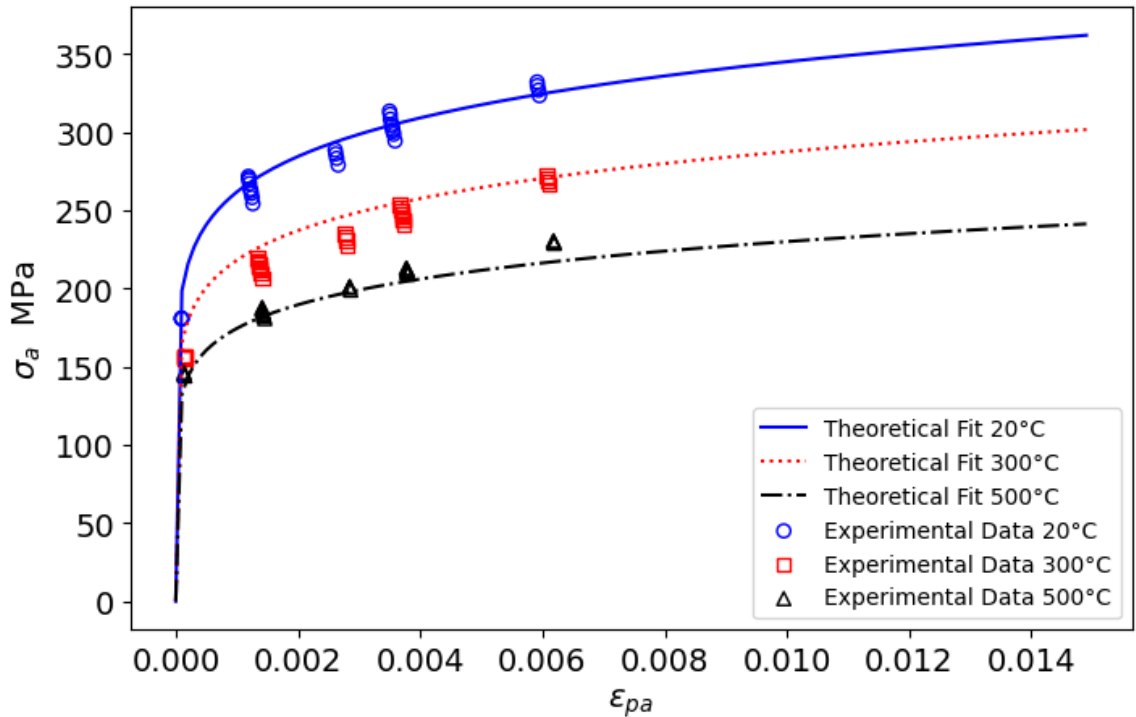


Figure 4.9: Fitment of  $k'$  and  $n'$  coefficients for Service-Exposed material. [6]

is beneficial for the model's alignment to favor the lower strain range region. While in an ideal case, the model would be selected to represent the entirety of the strain range, as Fig. 4.10, this is not always feasible. The finalized coefficients for the service exposed Chaboche NLKH model are documented in Table 4.1.

Table 4.1: Temperature dependent Chaboche NLKH parameters for service exposed P22.

Temperature (°C)	K MPa	$C_1$	$\gamma_1$	$C_2$	$\gamma_2$
20	150	200,000	2,300	22,000	200
300	125	150,000	2,300	19,000	200
500	100	150,000	2,300	15,000	200

#### 4.2.2.2 Virgin Material

The process of obtaining material parameters for the virgin material follows similar steps, requiring the Chaboche NLKH model to be fit to the mechanical response of the samples. However, a complete strain history is not available for the virgin

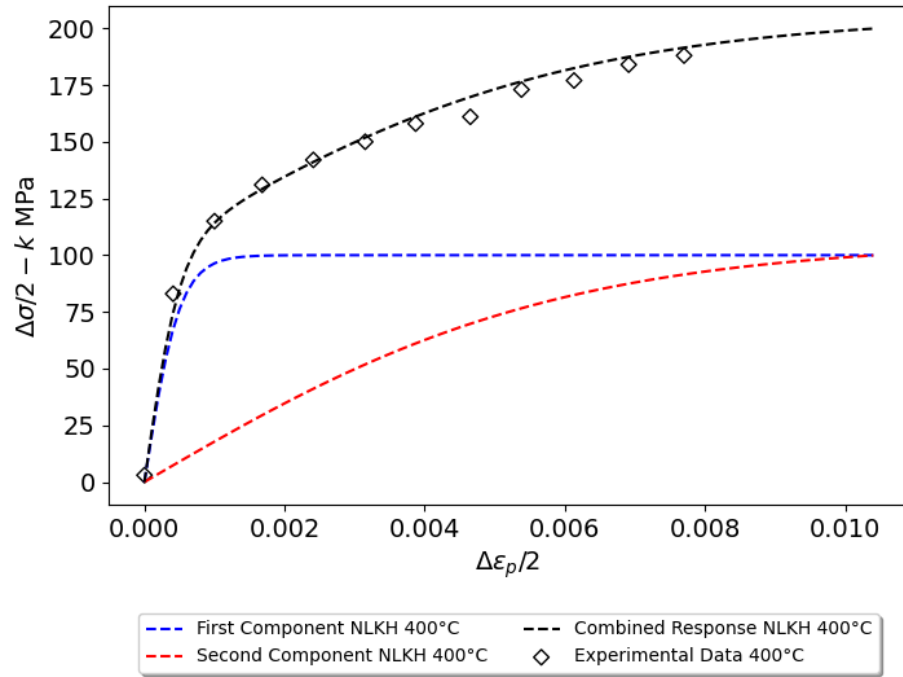


Figure 4.10: Chaboche NLKH data vs. data for service exposed material. [6]

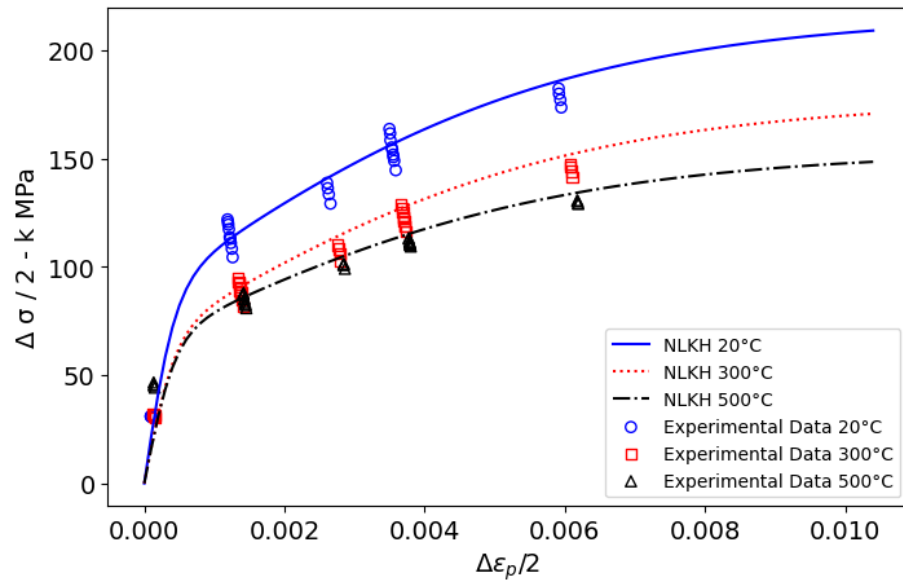


Figure 4.11: Chaboche NLKH data versus experimental data for service exposed material. [6]

material. Consequently, the process also begins by finding  $n'$  and  $k'$ . The fit of the coefficients selected is shown in Figure 4.12. The  $k'$  and  $n'$  coefficients for both materials are shown in Table 4.3. Comparing the material response between the virgin in service exposed materials, as shown in Fig.4.12 and Fig. 4.9, respectively, highlights the decrease in material strength over time. For example, the yield stress of the room-temperature virgin material is approximately 100 MPa higher than that of the service-exposed material. The process of determining the Chaboche NLKH model coefficients is the same as that described for the service-exposed material. The response of the virgin material using the established NLKH coefficients is shown in Figure 4.13. The Chaboche NLKH coefficients for the virgin material are shown in Table 4.4.

Material properties such as Young's modulus and thermal conductivity are assumed to be constant between the two materials. These characteristics stem from the composition and structure of the material and, therefore, do not change with time or inelastic deformation. Table 4.2 outlines the temperature-dependent properties that are applied to both of the materials.

Table 4.2: Temperature dependent parameters for both P22 models.

Temperature °C	Conductivity $\frac{mmTonne}{s^2K}$	Density $\frac{Tonne}{mm^3}$	Modulus MPa	CTE $\frac{1}{K}$	Specific heat capacity $\frac{Nmm}{TonneK}$
20	36.3	7.75E-9	210,000	1.15E-5	4.45E8
300	36.7	7.75E-9	192,000	1.33E-5	5.58E8
400	35.4	7.75 E-9	184,000	1.38E-5	6.02E8
500	33.7	7.75E-9	175,000	1.44E-5	6.57E8
600	32.0	7.75E-9	162,000	1.48E-5	7.44E8

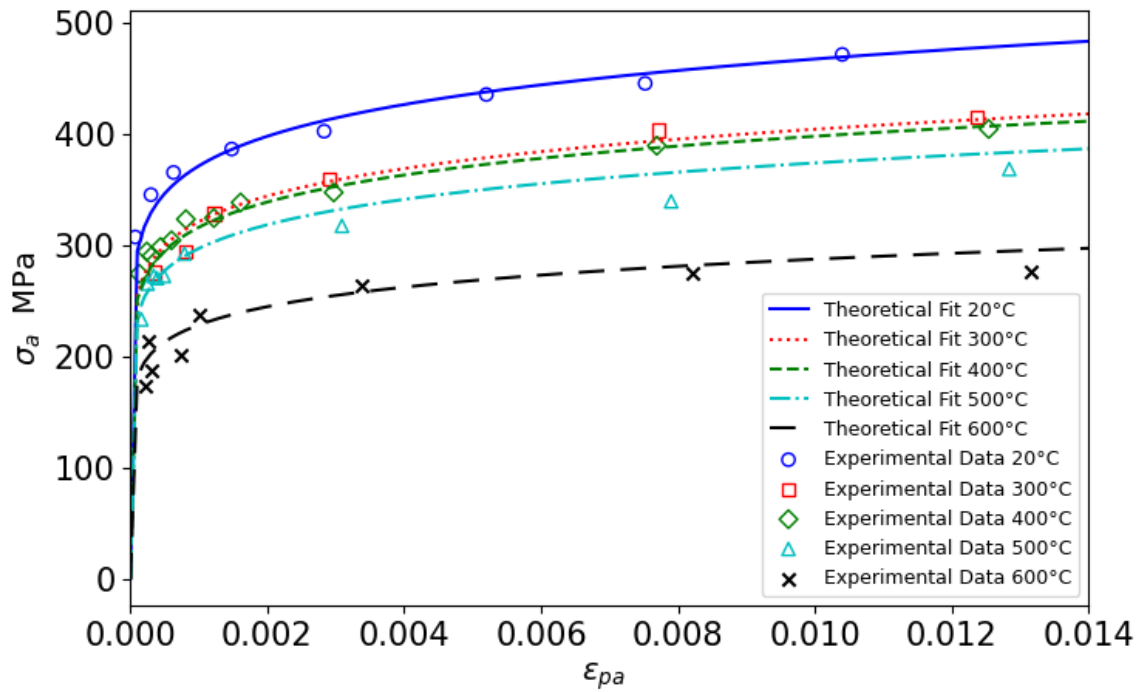


Figure 4.12: Fitment of  $k'$  and  $n'$  coefficients for Virgin material. [6]

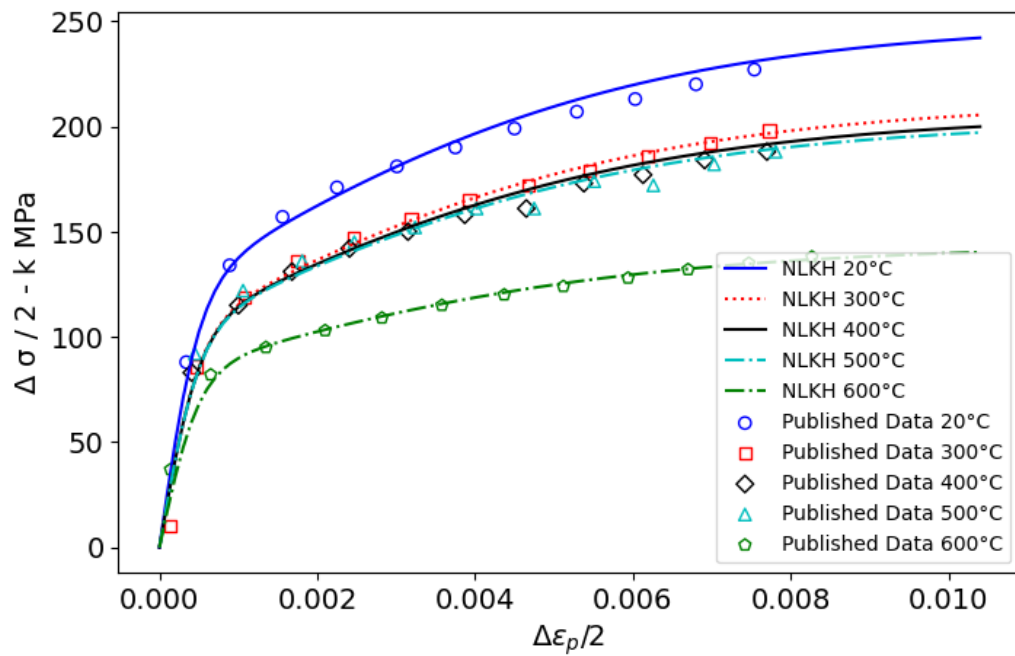


Figure 4.13: Chaboche NLKH data versus experimental data for virgin material. [6]

Table 4.3: Comparison of  $k'$  and  $n'$  values at different temperatures for virgin and service-exposed materials.

Temperature °C	Virgin		Service Exposed	
	$n'$	$k'$	$n'$	$k'$
20	0.1	740	0.12	600
300	0.1	640	0.12	500
400	0.1	630	N/A	N/A
500	0.1	592	0.12	400
600	0.1	455	N/A	N/A

Table 4.4: Temperature dependent Chaboche NLKH parameters for virgin P22.

Temperature (°C)	K MPa	$C_1$	$\gamma_1$	$C_2$	$\gamma_2$
20	234	240,000	2,000	21,000	170
300	202	200,000	2,000	19,000	170
400	199	200,000	2,000	18,000	170
500	187	200,000	2,000	17,500	170
600	144	165,000	2,000	10,400	170

Determining the Chaboche NLKH parameters for a material based on the stress-strain response is a process that can be summarized in the following:

1. **Hysteresis Loop Construction:** Construct the stress-strain hysteresis loops for the provided data set.
  - (a) If multiple strain ranges are provided, partition the data to evaluate each strain range block separately.
2. **Identify Stable Response:** Determine which cycle(s) represent the stable response and isolate the hysteresis loop.
3. **Characterize Response:** Calculate the values for  $\Delta\sigma$ ,  $\Delta\epsilon_p$  from the stable response.
  - (a)  $\Delta\epsilon_p$  is taken as the width of the hysteresis loop when  $\sigma = 0$ .
4. **Determine  $k$ :** Determine the deviation from linearity of the hysteresis loop

- (a) If the stress-strain response history is available,  $k$  is found from the deviation from linearity of the hysteresis loop
    - i. Proceed to step 6
  - (b) If complete hysteresis loops are not provided, continue with step 5
5. **Calculate  $k'$  and  $n'$ :** Using the amplitudes from the hysteresis loop, calculate  $k'$  and  $n'$
- (a) The values for  $k'$  and  $n'$  can be found using the relationship  $\sigma_a = k' \left(\frac{\Delta\epsilon_p}{2}\right)^{n'}$
  - (b) Approximate the deviation from linearity as a small plastic strain, e.g 1E-5
    - i. Therefore  $k$  is theoretically represented as  $k'(1E-5)^{n'}$
6. **Strain Iteration:** Repeat Steps 2 through 4 for each strain range in consideration.
7. **Data Comparison:** Create a plot comparing the measured values for  $\Delta\sigma/2 - k$  vs.  $\Delta\epsilon_p/2$ .
8. **Literature Review:** Optional: Review the literature to see if there are  $C_i$  and  $\gamma_i$  values that can be used as initial estimates.
9. **Initiate NLKH Coefficients:** Determine how many back-stress terms you need  $i = (2, 3)$ .
- (a) If  $i = 1$ , the model will predict ratcheting under non-zero mean stress
  - (b) Typically, the values for  $C_i$  are in the tens of thousands, and  $\gamma_i$  falls within the hundreds.
10. **Establish Trial Data:** Create a trial set of data using independent strain data and equation 2.27 to plot the predicted stress amplitude in comparison to the experimental data.

(a) Reference Fig.4.10

11. **Error Minimization:** Minimize the error by adjusting  $C_i$  and  $\gamma_i$  as needed.
12. **Temperature Dependency:** Repeat steps 1-8 for each temperature in consideration.

### 4.3 Fatigue life predictions

There are many ways to model fatigue failure within materials. One model developed to evaluate fatigue at elevated temperatures is the Ostergren damage model [146]. This model approximates the hysteretic strain energy in low-cycle fatigue by correlating the largest tensile stress and plastic strain to the number of cycles to failure. This damage function representation is taken along the plane, which maximizes the damage in multi-dimensional fatigue [146]. The cycle that is evaluated for the fatigue response is the stable response, which will represent the behavior of the material for the majority of the fatigue life. Notably, if the process is used to evaluate a variable load history, each minor cycle should be evaluated using a rain flow cycle counting technique after a stable response has been achieved. The number of cycles to failure is defined by the Ostergren model as,

$$N_f = C(\Delta\epsilon_{in}\sigma_{max})^\beta \quad (4.2)$$

where  $C$  and  $\beta$  are material constants. Fitting the damage function to the number of cycles allows the constants  $C$  and  $\beta$  to be determined. This is done by plotting the cycles until failure versus the damage function on a log-log axis. Figures 4.14 through 4.18 illustrate the relationship between the damage function and the virgin material at various temperatures. The values for  $C$  and  $\beta$  were selected so that they biased low cycle fatigue, thereby enforcing the accuracy of the model in this region.

The values of  $C$  and  $\beta$  are shown in Table 4.5. The parameters for the Ostergren model were established by fitting data taken from the virgin material at various tem-

Table 4.5: Comparison of C and ( $\beta$ ) values at different temperatures.

Temperature °C	(Constant C)	(Exponent $\beta$ )
20	5500	-1.4
300	4500	-1.8
400	2000	-1.8
500	1300	-1.6
600	1000	-1.5

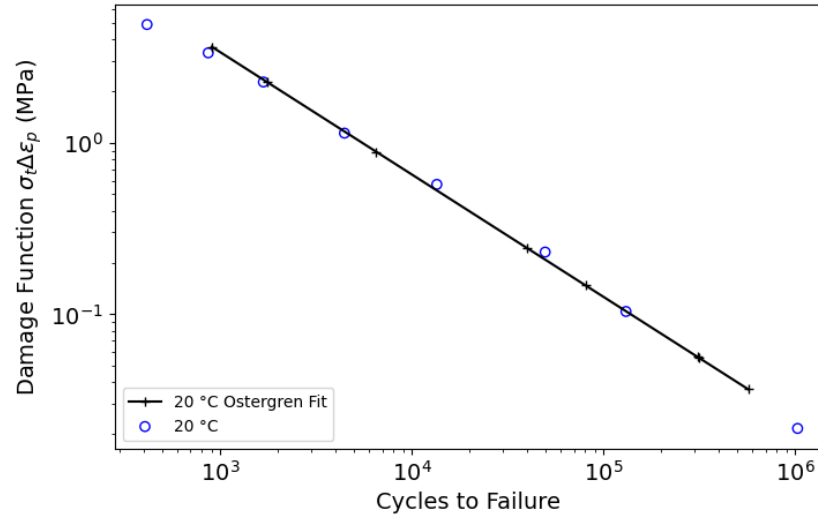


Figure 4.14: Correlation of virgin material data with damage function at 20 ° C.

peratures. Unfortunately, test data was not available for the service-exposed material to provide a comparison. As a result, the service life of both materials is approximated from the virgin material fatigue properties. Additionally, the properties used to evaluate the material response of the headers were taken as 600 ° C. The adjustment was made to ensure conservative life estimations. Although slight discrepancies may exist between the average cycle temperature and the curve representation applied, the curve closely aligns with the temperature range, minimizing potential errors to negligible levels.

#### 4.4 Boundary Conditions

The models were subjected to sequential thermal-mechanical loading to represent the operating conditions that the ex-service unit was subjected to. Figure 4.19 illus-

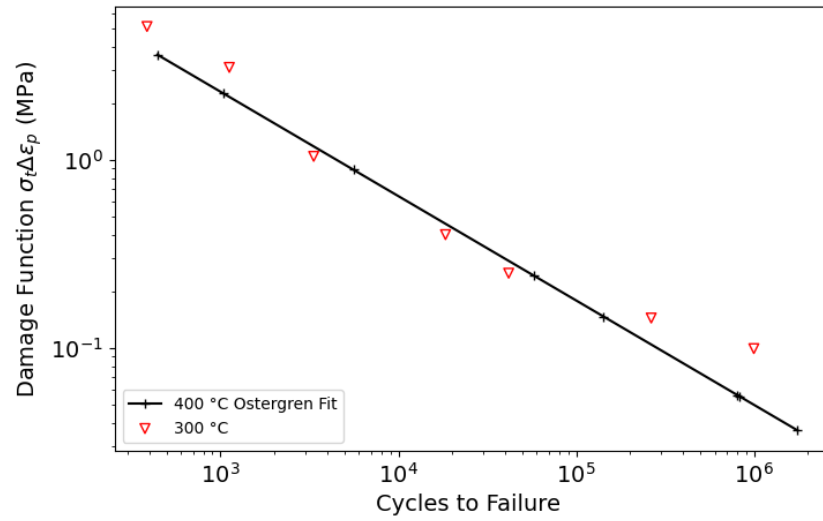


Figure 4.15: Correlation of virgin material data with damage function at 300 ° C.

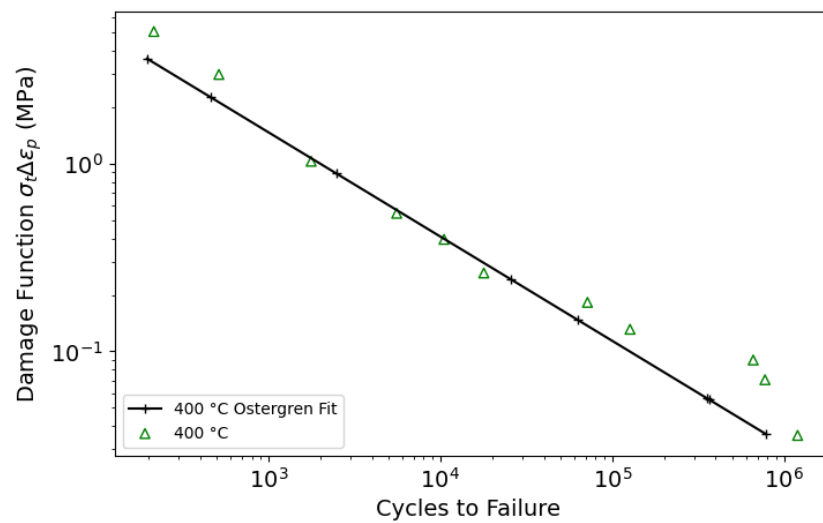


Figure 4.16: Correlation of virgin material data with damage function at 400 ° C.

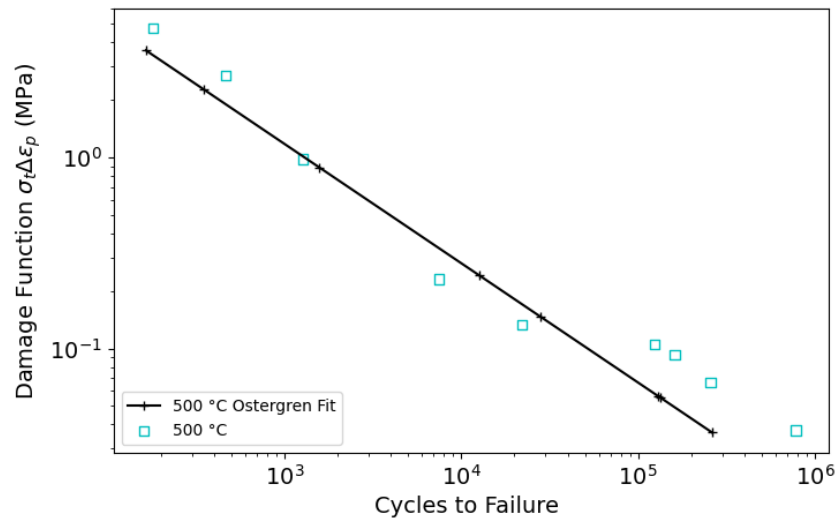


Figure 4.17: Correlation of virgin material data with damage function at 500 ° C.

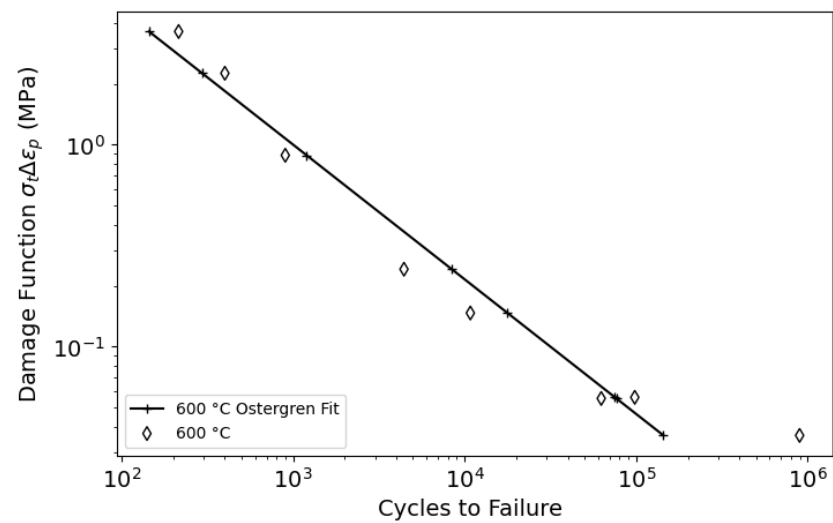


Figure 4.18: Correlation of virgin material data with damage function at 600 ° C.

trates the temperature and pressures found in a representative ten-day operational period. Based on this, three transients were developed to capture the primary patterns of the data and disregard high-frequency fluctuations. This approach allows the identification of the header's response to different characteristics of the ten-day response. The first transient represents a typical startup and shutdown procedure shown in Fig. 4.23. This transition is intended to represent the global response of the system under normal operating conditions. The other transients are designed to represent the temperature fluctuations that can occur at different tube header connections. The transients are separated in a common and limit case transient shown in Fig 4.21 and 4.22, respectively. These transients represent the variation of temperature changes that can occur across different tubes. In many cases it is not uncommon for the temperature of the tube to exceed the target temperature for a short period of time prior to adjusting to the final temperature. This is represented in the limit case transient. However, this does not reflect every tube that joins to the header, and the more common cases are represented in Figure 4.21. This correlates well with industrial experience in the case that failures often occur at individual tubes, not collectively across the system. The idealized transient for the common loading is shown in comparison to normal operating data in Figure 4.20, where it is clear that the rate of temperature change is captured.

Given the periodicity and symmetry of the header, only one-quarter of the model is used to evaluate the header's response. A pressure load is applied across the interior surfaces of the header and tube. Also, a closed-end condition is applied to the end of the header such that a proportional pressure is applied to the end surfaces. Symmetry is implemented by setting the displacement normal to the symmetry face to zero. An equation-type constraint is also added to the header's face to ensure uniform deformation. The model is constrained in the  $Y$ -direction by setting the  $u_Z$  displacement of the bottom edge of the header to zero. The temperature is controlled

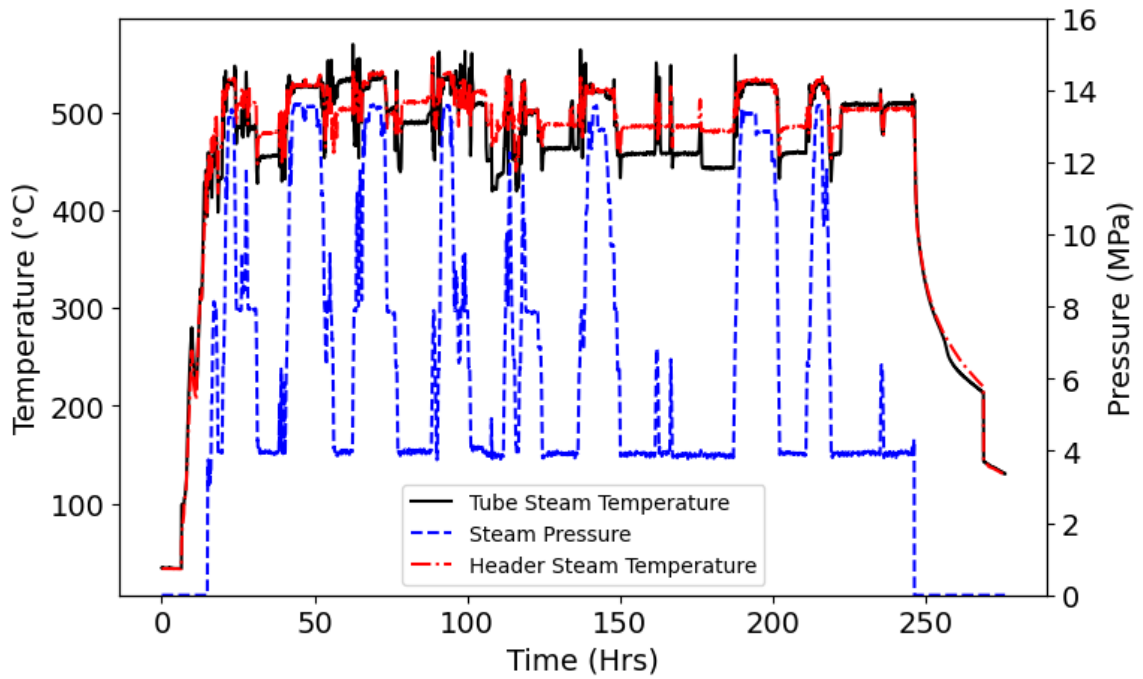


Figure 4.19: Sample of provided operating data. [6]

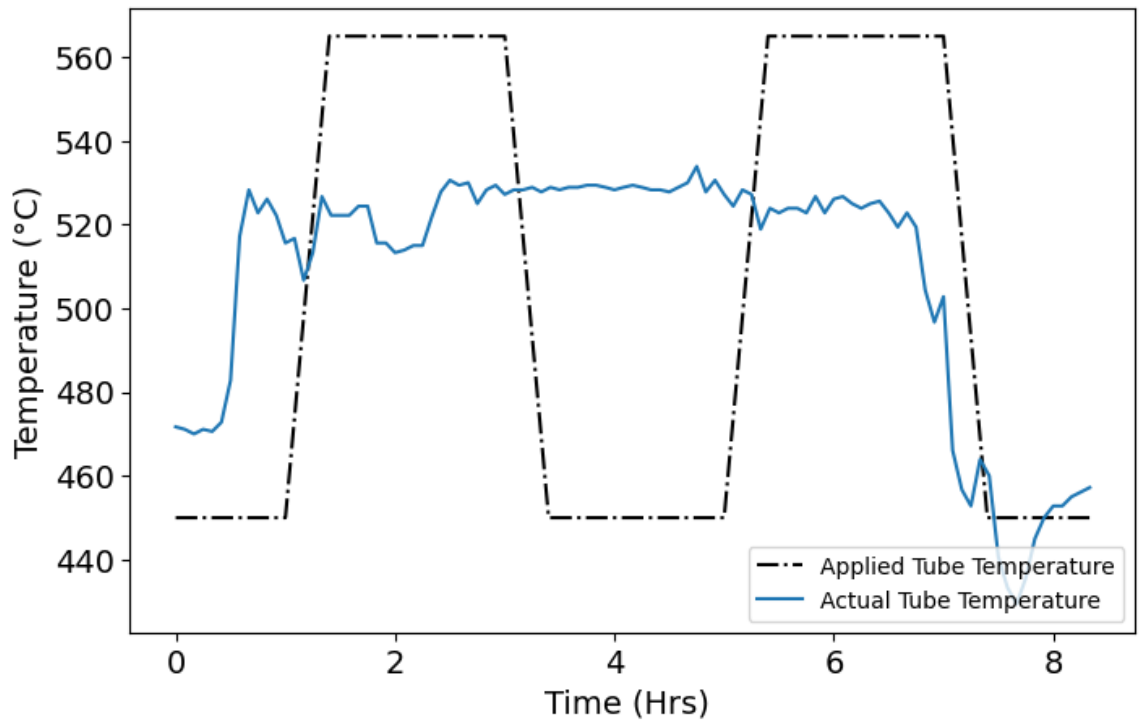


Figure 4.20: Tube temperature comparison for the slow cycle. [6]

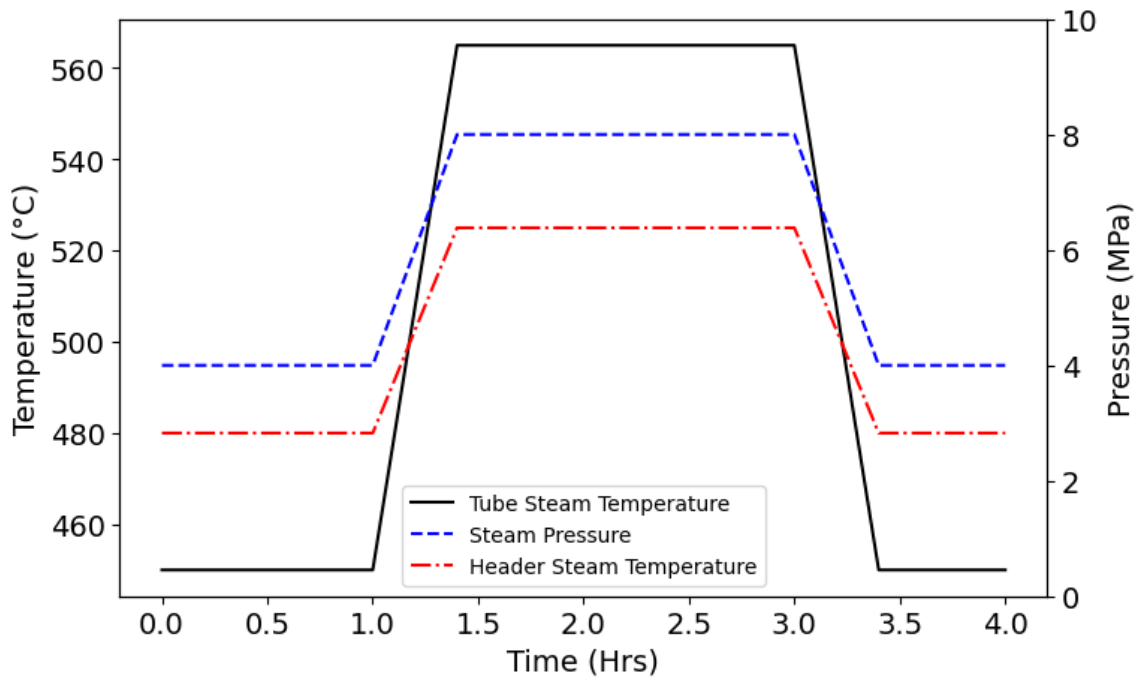


Figure 4.21: Representative slow transient cycle. [6]

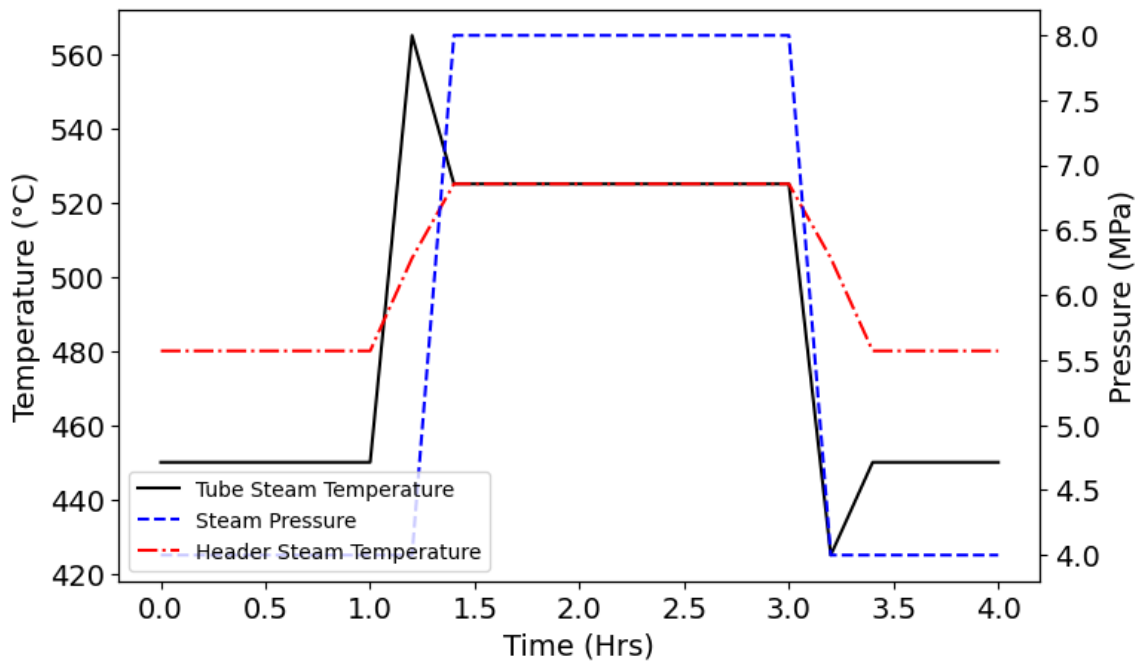


Figure 4.22: Representative rapid-case transient cycle. [6]

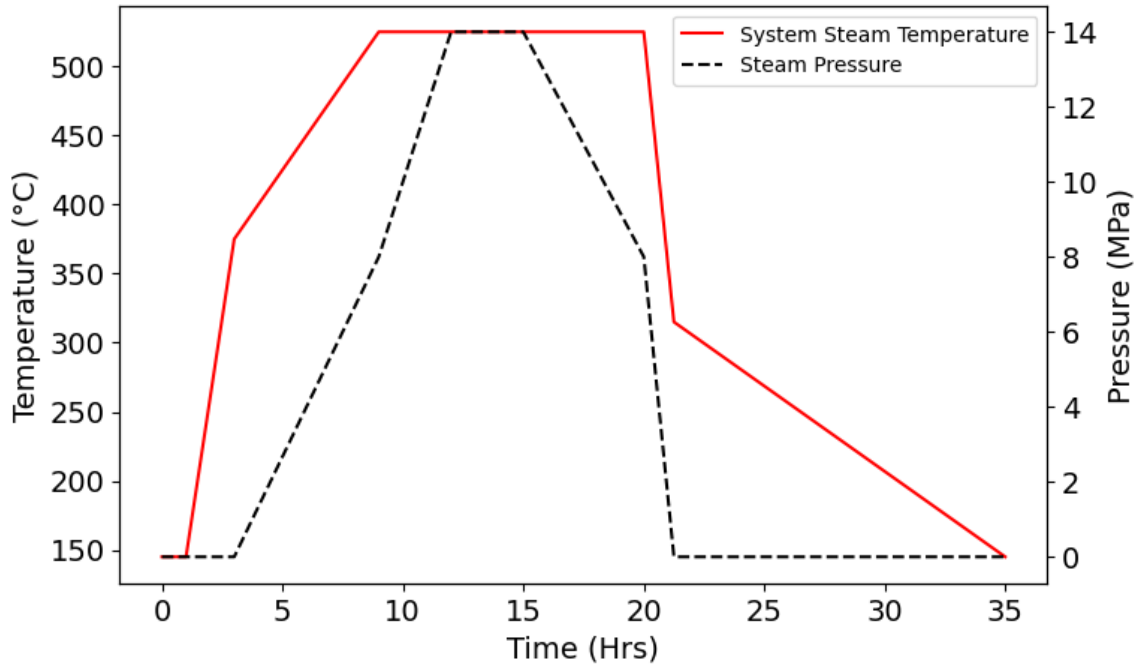


Figure 4.23: Representative startup and shutdown cycle. [6]

by applying a convective film condition to the internal surfaces of the header. Separate sink temperatures are used for the header and tube surfaces. Figure 4.24 illustrates the boundary conditions for further clarification.

The header mesh is optimized to reduce the total number of elements used in the simulation. This is represented in mesh, detailing how the mesh is refined in the region where the tube intersects the header. This region experiences the highest stresses during operation and is the area of interest for the present study. The mesh in the regions surrounding the tube is refined to a minimum size of 0.5 mm and gradually transitioned to larger elements along the lower region of the header of 25 mm. The final mesh consisted of 48,736 C3D20RT elements and 213,396 nodes.

#### 4.5 Results and Discussion

To verify the accuracy of the boundary conditions, we compare the stresses obtained from the finite element model when the header is subjected to internal pressure with those derived from the closed-form solution for thick-walled pressured vessels [163].

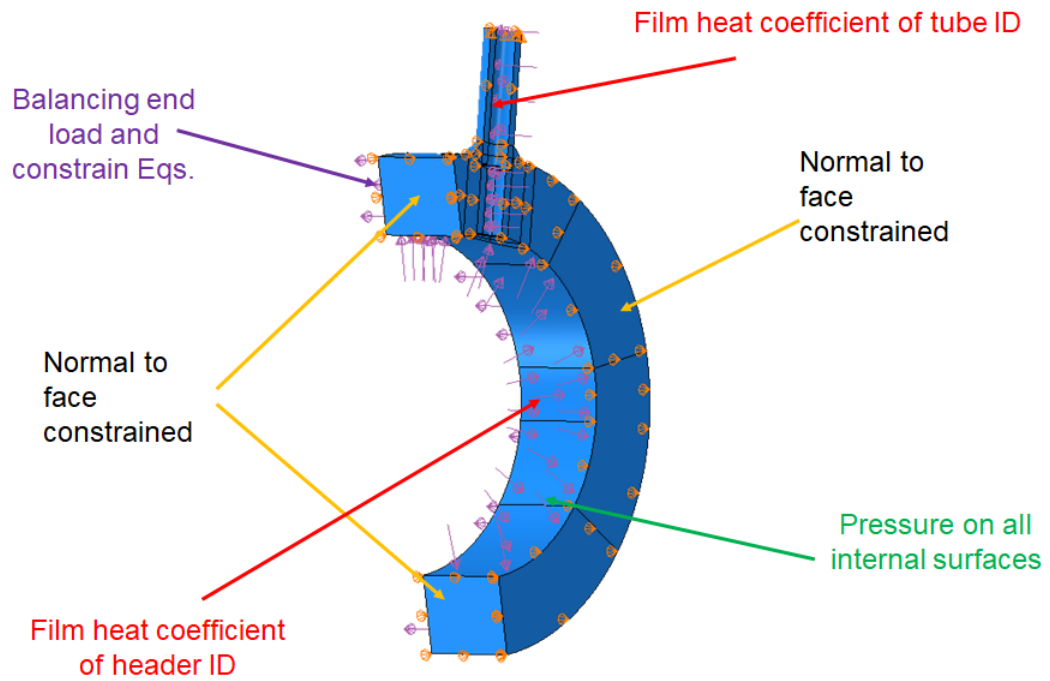


Figure 4.24: Model boundary conditions. [6]

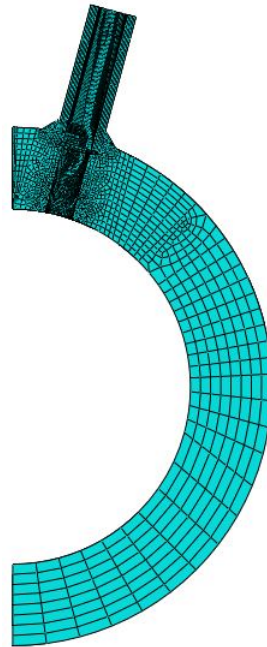


Figure 4.25: 3D meshed header with 48,736 C3D20RT elements. [6]

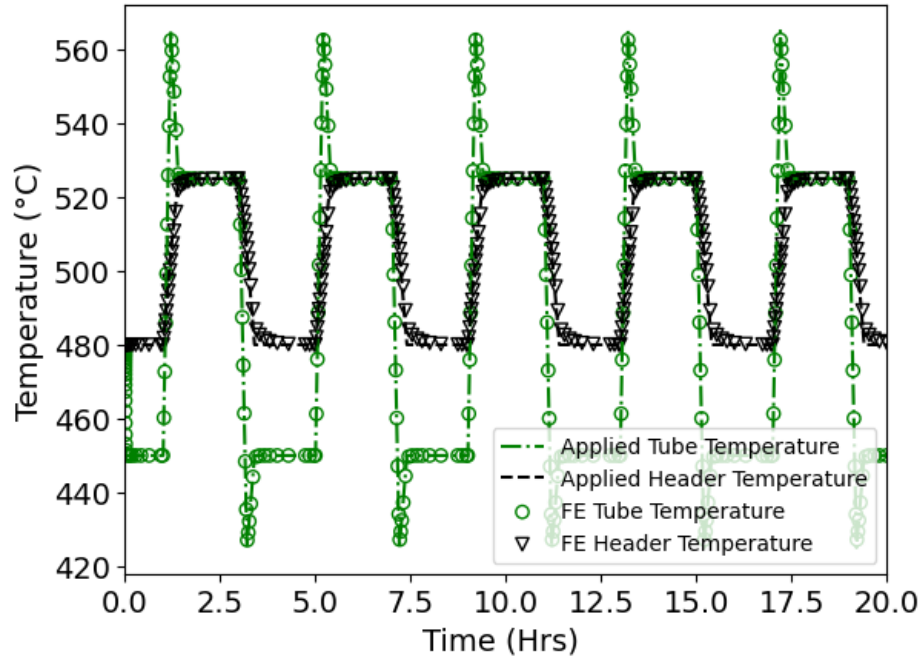


Figure 4.26: Temperature Profile Validation. [6]

The finite element outcomes align well with the closed-form solutions, confirming their validity. Furthermore, the model is checked for thermal convergence. The thermal evaluation involves evaluating the sink temperature of the model relative to the temperature applied to the surface. Figure 4.26 compares the model's thermal profile and the applied temperature profile. The results demonstrate a close match between the thermal profile of the model and the applied temperature profile.

Each model compares the expected service life using the previously mentioned idealized temperature and pressure profiles. The loading undergoes multiple cycles to confirm a stable cyclic state, signifying that the material's hardening behavior no longer influences strain accumulation. The stable cyclic state can be identified from the convergence of the plastic strain magnitude. While the present work evaluates three separate transients, all cases are found to shake down within the initial cycles. This is illustrated by the stabilization of the material in response to the rapid transient illustrated in Fig. 4.27. Figure 4.27 demonstrates that the magnitude of plastic strain is more significant for the service-exposed material header than the virgin material

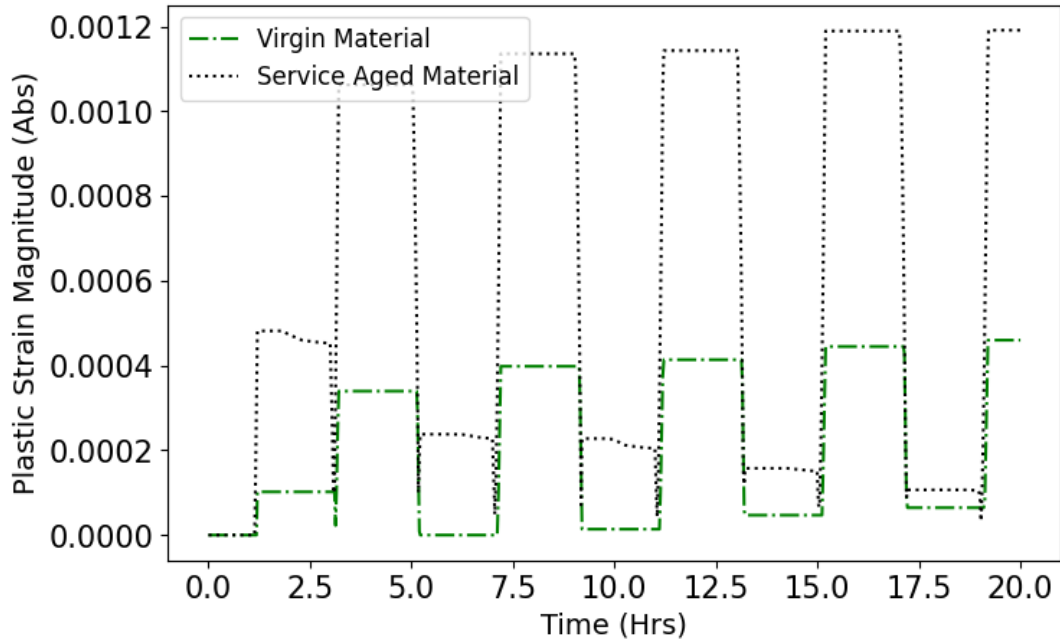


Figure 4.27: Accumulated plastic strain vs. time for rapid-case transient. [6]

header. This accumulation occurs at the location shown in Fig 4.34b.

While the service life primarily depends on plastic strain, assessing stress distribution within the structure can aid in identifying vulnerable locations susceptible to plastic strain due to ongoing degradation or rapid transients. Figures 4.28 through 4.33 show the contours of the peak von Mises stress within the headers modeled with virgin or service-exposed material model under startup and shutdown, slow transient, and rapid-case transients.

When examining the stress contour for various loading profiles, it becomes evident that the rapid-case transient induces the highest stress levels midway through the cylinder bore. Conversely, during the startup-shutdown cycle, peak stress levels occur at the intersection of the tube and bore. This observation confirms that the location with the highest peak stress, and subsequently inelastic strain, varies depending on the temperature and pressure profile applied. For instance, the region where the through hole intersects the inner diameter of the header has the largest stress concentration

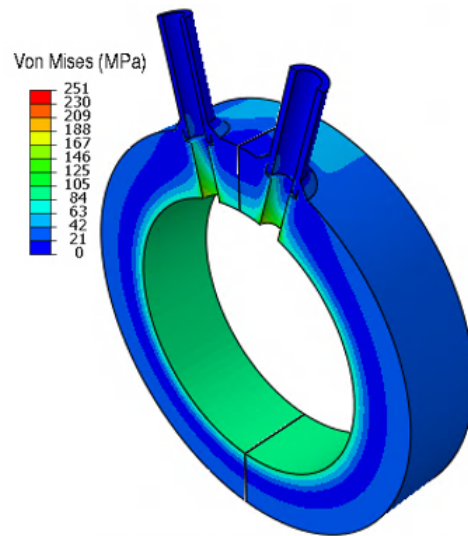


Figure 4.28: Virgin material peak von Mises response to the startup and shutdown transient loading profile. [6]

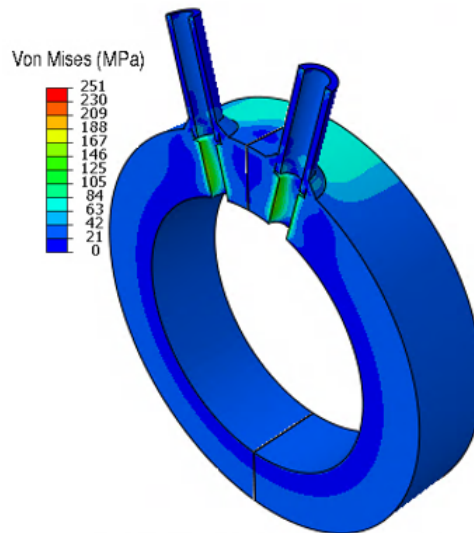


Figure 4.29: Virgin material peak von Mises response to the slow transient loading profile. [6]

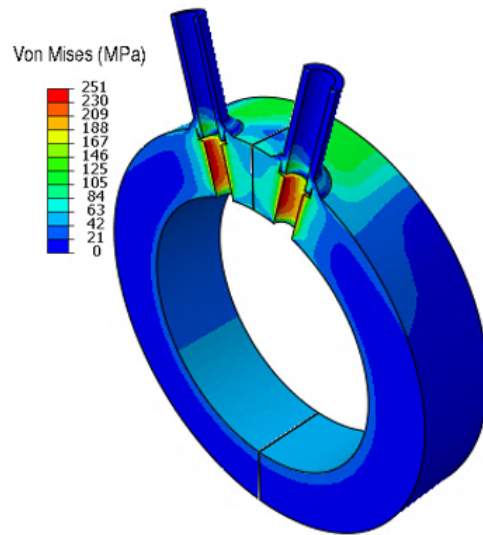


Figure 4.30: Virgin material peak von Mises response to the rapid-case transient loading profile. [6]

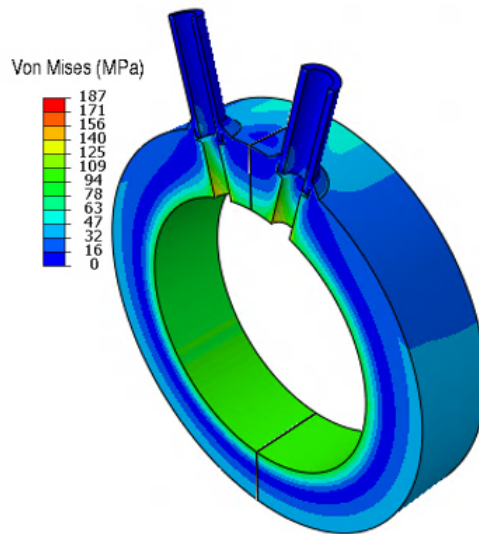


Figure 4.31: Service exposed material peak von Mises response to the startup and shutdown transient loading profile. [6]

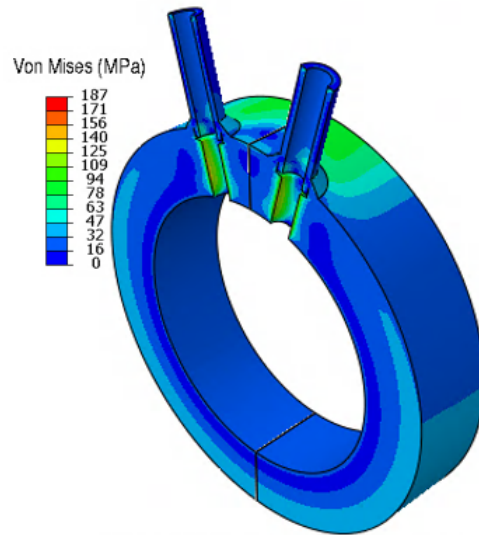


Figure 4.32: Service exposed material peak von Mises response to the slow transient loading profile. [6]

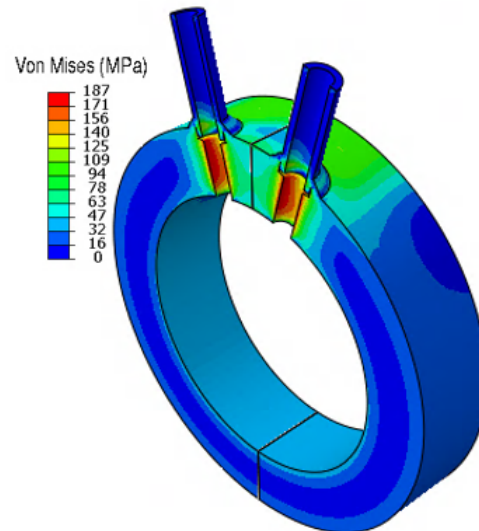


Figure 4.33: Service exposed material peak von Mises response to the rapid-case transient loading profile. [6]

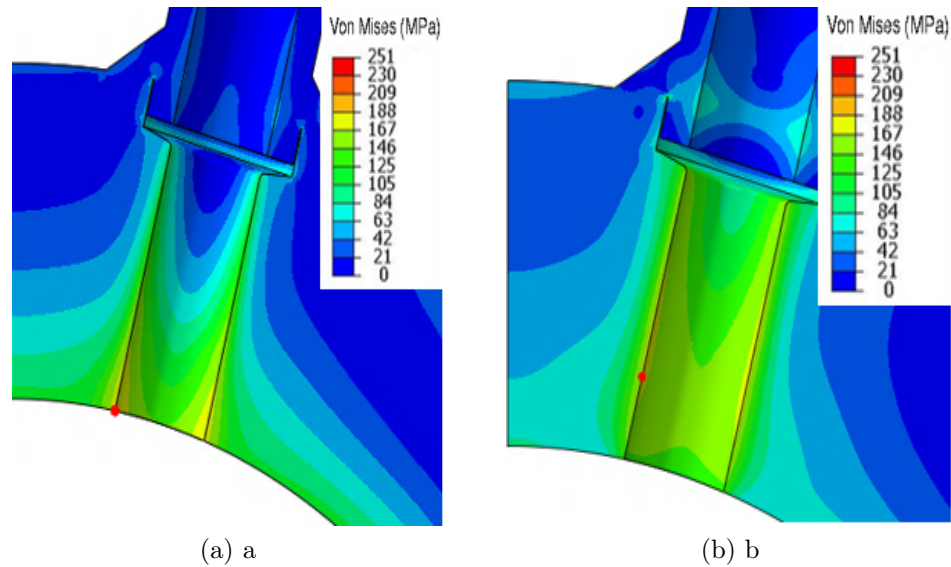


Figure 4.34: Location of peak stress in response to (a) startup and shutdown (b) common/rapid transient loading profiles. [6]

during the startup and shutdown loading. For clarity, the location of the peak stress is highlighted in red in 4.34a.

The stress-strain response obtained from the models with the virgin and service-exposed material models is shown in Fig. 4.35 and Fig. 4.36, respectively. These graphs show that the largest stress component is in the axial direction. Also, as shown in Fig. 4.35, no plastic strain is accumulated in the Virgin material in response to the startup and shutdown cycles. Therefore, it follows that there is no change in the response across five cycles. In response to the startup and shutdown loading, the peak stable von Mises stress reaches a magnitude of 161 MPa for the virgin material and 128 MPa for the service-exposed material. However, due to the increased strength of the virgin material, its higher stress does not result in plastic strain accumulation. Although this region has the highest stress levels for the startup and shutdown loading, no plastic strain accumulated in either material. Therefore, neither material is predicted to accumulate fatigue damage from the startup and shutdown loading profile.

Conversely, the application of the transient loading profiles depicted in Fig. 4.21

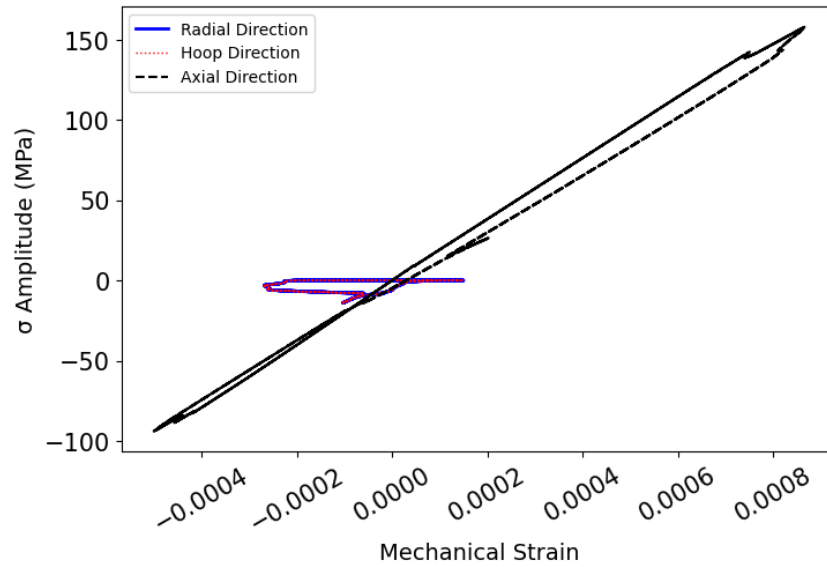


Figure 4.35: Stress-strain response of the header to a startup and shutdown loading when virgin material is used. [6]

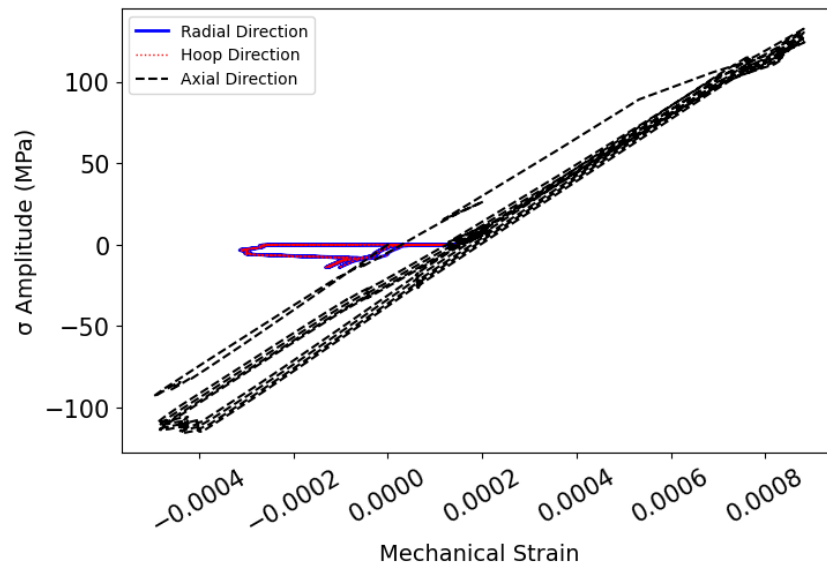


Figure 4.36: Stress-strain response of the header to a startup and shutdown loading when service exposed material is used. [6]

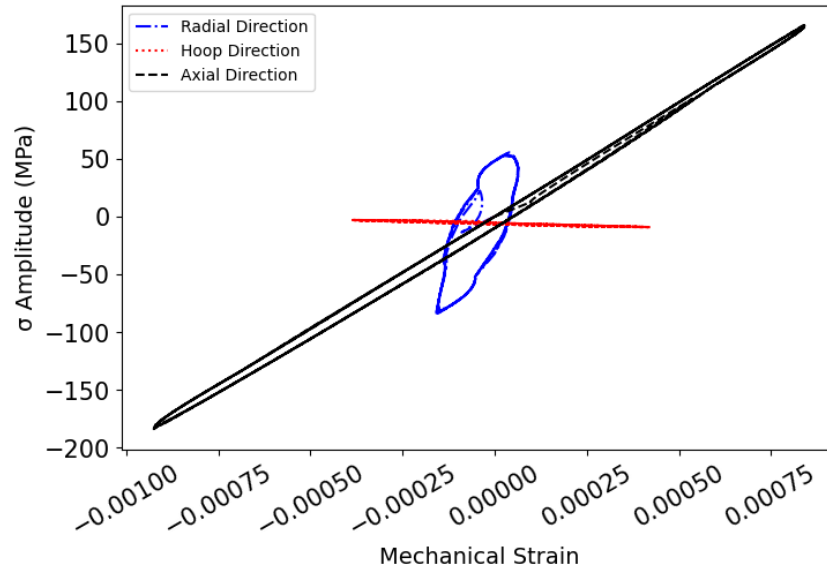


Figure 4.37: Stress-strain response of the header to slow transition loading when the virgin material model is used. [6]

and Fig. 4.22 results in elevated peak stresses, consequently causing the accumulation of plastic strain. Additionally, the location of peak stress, and as a result, plastic strain accumulation, shifted, as illustrated in Fig. 4.34b, where both transients cause the peak stress to occur along the circumferential edge, 30-50 mm into the through-hole within the header. While the peak stress location remains consistent across various materials, the magnitude of the inelastic strain differs. This divergence becomes evident when examining the stress-strain response for the two models under slow transients, as depicted in 4.37 and 4.38. These figures highlight that the axial and radial stress components significantly contribute to material fatigue. The width of the hysteresis loop for each component represents the influence of each strain component on the fatigue of the material. Due to the larger inelastic strains in the axial and radial direction, the service-exposed material model shows substantially more plastic strain accumulation. The slow transient results in the service-exposed header having a peak plastic strain magnitude of 0.023%, whereas the virgin material header does not accumulate any plastic strain.

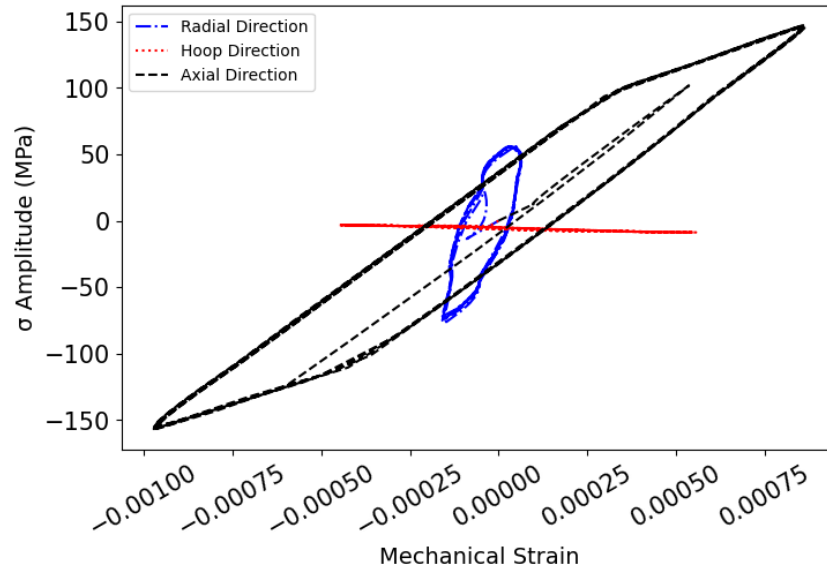


Figure 4.38: Stress-strain response of the header to slow loading when the service exposed material is used. [6]

The difference between the two materials implies that fatigue failure would not occur in virgin material header during normal transients. On the other hand, the service-exposed header would accumulate a limited amount of fatigue as a result of the common transient. This discrepancy highlights the significance that incorporating representative material properties can have on remaining service life estimates. Moreover, the findings suggest that continued degradation may occur, leading to accelerated fatigue over time.

Both models exhibited a more pronounced LCF response when subjected to the rapid-case loading conditions. For instance, the peak plastic strain magnitude of the service-exposed material increased to 0.119% in response to the rapid-case transient. Likewise, the virgin material header, which did not accumulate plastic strain in response to the slow transient, has a peak plastic strain magnitude of 0.046%. Figures. 4.39 and 4.40 represent the decomposed stress-strain response observed at the critical location of the headers under rapid transient loading.

The primary stress contribution occurs along the axial edge in the three transients

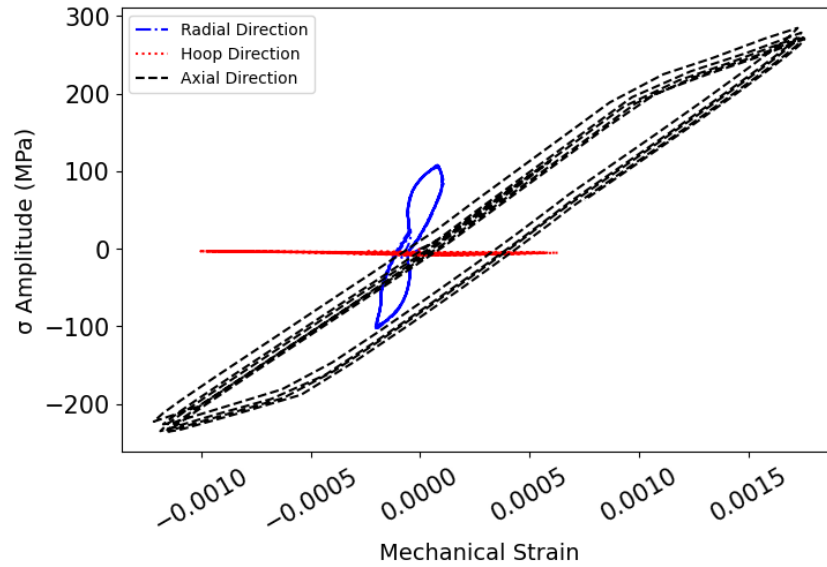


Figure 4.39: Stress-strain response of the header to rapid-case loading when virgin material is used. [6]

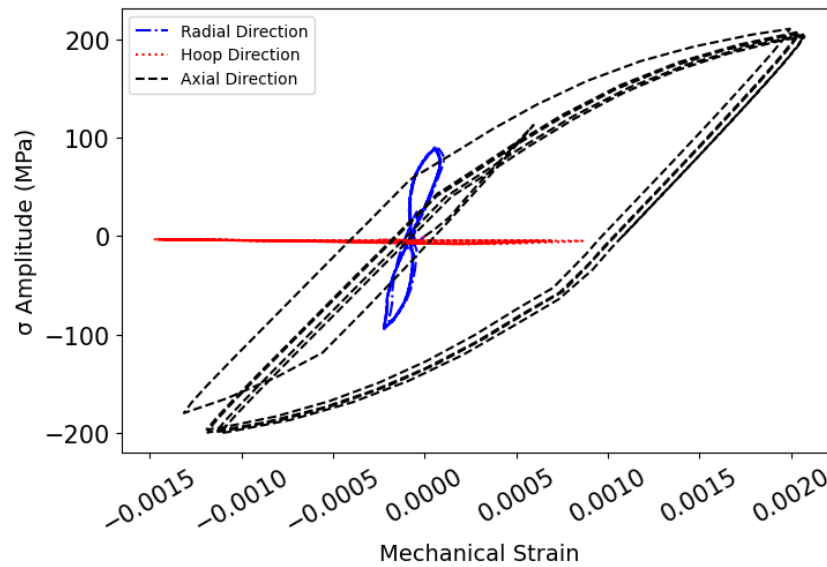


Figure 4.40: Stress-strain response of the header to rapid-case loading when service exposed material is used. [6]

considered. However, the global response of the material following a typical startup and shutdown procedure does not appear to damage the header. Conversely, the rapid case transient is found to cause damage regardless of the service exposure history for the material. The influence of prior service exposure, as the remaining service estimate for the service-exposed material is a third of the virgin material. Furthermore, the study demonstrates how the threshold for damage is also lowered. This is demonstrated by the response of the materials due to the common transient, where the lifespan of the service-exposed material is expected to accumulate a small amount of fatigue damage compared to virgin materials, which are unharmed. The finalized results are shown in Table 4.6.

Table 4.6: Predicted Lifetime of Header.

Material	Startup and Shutdown YTF	Slow Transient YTF	Rapid Transient YTF
Virgin	N/A	N/A	15
Service Exposed	N/A	85	5

## 4.6 Conclusion

The present work demonstrates how the Chaboche NLKH material model parameters could be obtained using the experimental data. The material parameters were acquired for a pristine P22 sample and a sample that has been in service within a steam header for 20 years. The material properties were employed in a finite element model to forecast the life expectancy of a steam header, illustrating how prior service exposure influences the estimated remaining lifespan of a component. The findings illustrated that the material exposed to service accumulates inelastic strain under loading conditions that would not affect a virgin material. This suggests that the threshold for damage accumulation of a header with significant service exposure is lower than that of a newly replaced component. Therefore, it would be possible to overestimate the remaining service life of a header if the prior service exposure of the material is not considered.

Furthermore, this variation suggests that the threshold for the service-exposed material to experience ratcheting is also decreased. Although ratcheting was not predicted in this study, further weakening of the service-exposed material could potentially result in accelerated failure. Therefore, conducting additional studies to comprehend the rate at which the material deteriorates would be beneficial in determining if the header may reach a point of accelerated failure.

This variation also suggests that the threshold for the service-exposed material to experience ratcheting is lowered. While ratcheting was not predicted in the current work, further weakening of the service-exposed material could lead to accelerated failure. Therefore, it would be beneficial to complete additional studies to understand the rate at which the material deteriorates to determine if the header reaching a point of accelerated failure is possible.

While the present work demonstrates that the virgin material is less prone to thermal fatigue, it does not imply that a newly implemented header would accumulate

inelastic strains at rates similar to the original unit. As mentioned, the demand for combined cycle systems is gradually transitioning to a lesser role in energy generation. Therefore, the prolonged periods of use that the former unit experienced, slowly degrading the strength of the material, are less likely to occur. Consequently, the rate of material degradation due to micro-structural changes will likely be impeded. As a result, locations that do not experience rapid-case transients would likely not develop time-independent inelastic strains and not fail due to LCF.

In contrast, the regions that do experience the rapid-case transients would be subjected to a larger number of transients in a shorter amount of time than the previous unit. The increased frequency of these transients suggests that these regions within a newly implemented header could begin to fail in less time than the outgoing unit. These factors, among many others, should be considered when evaluating the replacement of an existing component.

## CHAPTER 5: Comparison of Crack Propagation Methods in a 2.25Cr-1Mo steam header

### 5.1 Introduction

This section evaluates the quasi-static crack growth of a postulated SECC in a 2.25Cr-1Mo header, adapted from the work by Zimnoch et al. [7]. Therefore, the material presented in this section directly links to the framework of the published work. Fatigue crack growth is a critical design engineering phenomenon that characterizes a material's progressive failure under cyclic loading. Understanding the crack growth process is fundamental to approximating the lifespan of components subjected to cyclic stresses. In the present work, two methods are compared to evaluate the predicted growth of an SECC in a P22 outlet header. The first method is an iterative interpolation of the SIF found in Abaqus using the seam crack methodology. The second method incorporates the recently incorporated \*Fatigue methodology in Abaqus that uses Paris law crack growth to propagate a crack through an XFEM domain [164]. The methodology and results obtained from each method are presented.

### 5.2 Material Properties and Boundary Conditions

#### 5.2.1 Material Properties

The selection of 2.25Cr-1Mo steel, designated as P22 within ASTM classification, for the header material, aligns with the reference header used to provide the operating data. The material properties used in the linear elastic analysis are shown in Table 5.1. The focus on LEFM in the present work excludes plasticity from the analysis. This simplification allows for a more focused review of the process developed to grow a

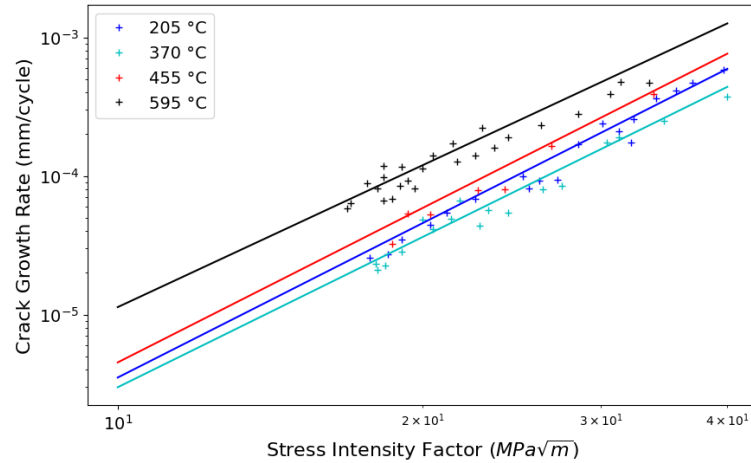


Figure 5.1: Influence of temperature on crack growth rate and Paris Law fit.

seam crack within the Abaqus framework.

The fracture properties for the material were adapted from the Grade 22 Handbook presented by EPRI [165] and are shown in table 5.2. The temperature-dependent Paris law coefficients used to represent crack growth are found by curve-fitting trial data to test data on a log-log plot. The coefficients are adjusted to minimize the error between test and trial data. An illustration of the coefficients to the trial data is represented in Figure 5.1. The finalized coefficients are provided in Table 5.2. Notably, the analysis demonstrates a significant increase in crack growth rates when exposed to elevated temperatures, highlighting the need for incorporating temperature-dependent coefficients in fracture mechanics studies. Although some margin of error may exist within the coefficients used in the present study, their application for the present work is assumed reasonable, as minor inaccuracies regarding the rate at which the crack grows are incidental to the premise of automating crack growth. Furthermore, initial results demonstrate that the range of SIF obtained in the analysis is well below the lower bound  $K_{IC}$  of the material of  $K_{IC} = 3160 MPa\sqrt{mm}$  such that the behavior of the crack growth would not significantly change due to any minor error [166].

Table 5.1: Temperature dependent material properties models.

Temperature °C	Conductivity $\frac{mmTonne}{s^3K}$	Density $\frac{Tonne}{mm^3}$	Modulus MPa	CTE $\frac{1}{K}$	Specific heat capacity $\frac{Nmm}{TonneK}$
20	36.3	7.75E-9	210,000	1.15E-5	4.45E8
300	36.7	7.75E-9	192,000	1.33E-5	5.58E8
400	35.4	7.75 E-9	184,000	1.38E-5	6.02E8
500	33.7	7.75E-9	175,000	1.44E-5	6.57E8
600	32.0	7.75E-9	162,000	1.48E-5	7.44E8

Table 5.2: Temperature-dependent Paris law parameters.

Temperature °C	C $\frac{mm/cycle}{MPa\sqrt{m}^n}$	n
20	1.7E-08	2.9
205	7.0E-10	3.7
300	7.5E-10	3.6
455	9.0E-10	3.7
595	4.5E-09	3.4

## 5.2.2 Boundary Conditions

In the pursuit of validating the automated crack growth algorithm, the boundary conditions applied to the model are based on real operational data acquired during service. The boundary conditions incorporate the steam temperature and pressure data reflecting a 24-hour cycle within the power plant. Figure 5.2 illustrates the temperature and pressure fluctuations throughout the day, distinguishing between the temperatures found in the tube and those within the header. This is a result of multiple tubes with various temperatures feeding into the header, resulting in a lower homogenized temperature with reduced fluctuations.

However, to improve the model's efficiency and focus on the more critical trends, the data is simplified by removing high-frequency temperature fluctuations. The comparison of the reference temperature to what is applied to the model is demonstrated in Figures 5.3 and 5.5. This approach is key to reducing computational costs while capturing the overarching trend influencing crack growth predictions. Figure 5.5 illustrates the simplified boundary temperature and pressure boundary conditions

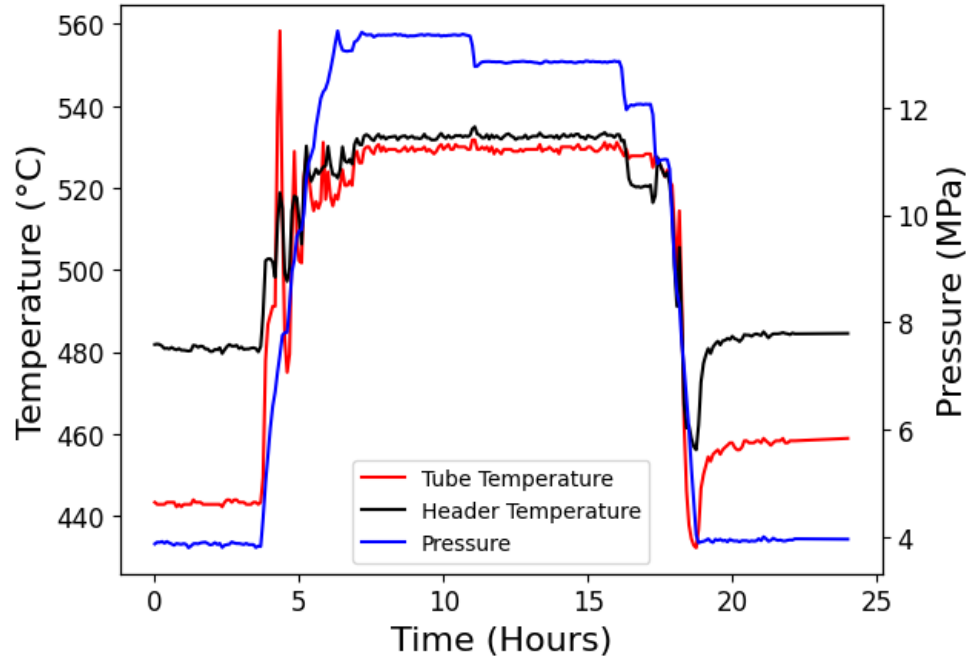


Figure 5.2: Reference temperature and pressure data for a 24-hour cycle. [7]

applied to the model.

The steam temperature is represented in the model through the use of convection on the internal surfaces. The external surfaces of the header and tube are assumed to be insulated and do not have convection applied to their surfaces. Similarly, the pressure is applied to all of the internal surfaces to simulate the operational conditions. Taking advantage of the symmetry found in the header, only a segment of the header is represented, resulting in a singular tube within the global model. The axial surface of the header opposite the symmetry plane and the top surface of the tube is subjected to blow-off pressures to simulate closed-end conditions as shown in equation 5.1.

$$P_{\text{tension}} = \frac{PD_i^2}{D_o^2 - D_i^2} \quad (5.1)$$

As a result, the lower edge of the symmetric model is restrained along the vertical direction to prevent unrealistic movement. A detailed illustration of the boundary conditions applied to the global model is represented in Figure 5.6.

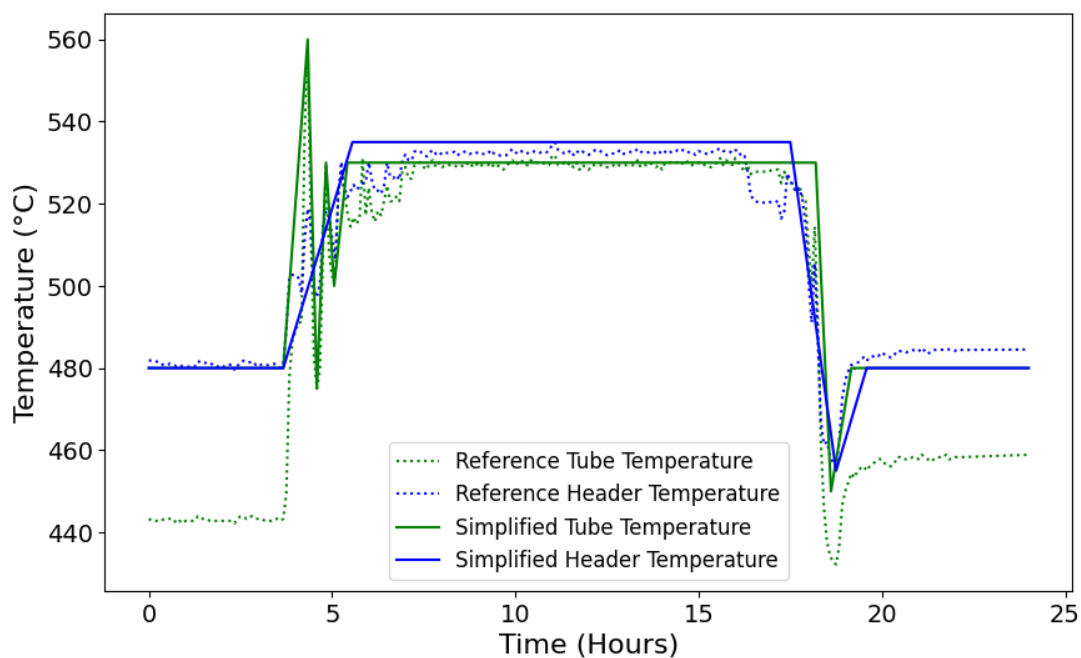


Figure 5.3: Simplified temperature compared to reference data. [7]

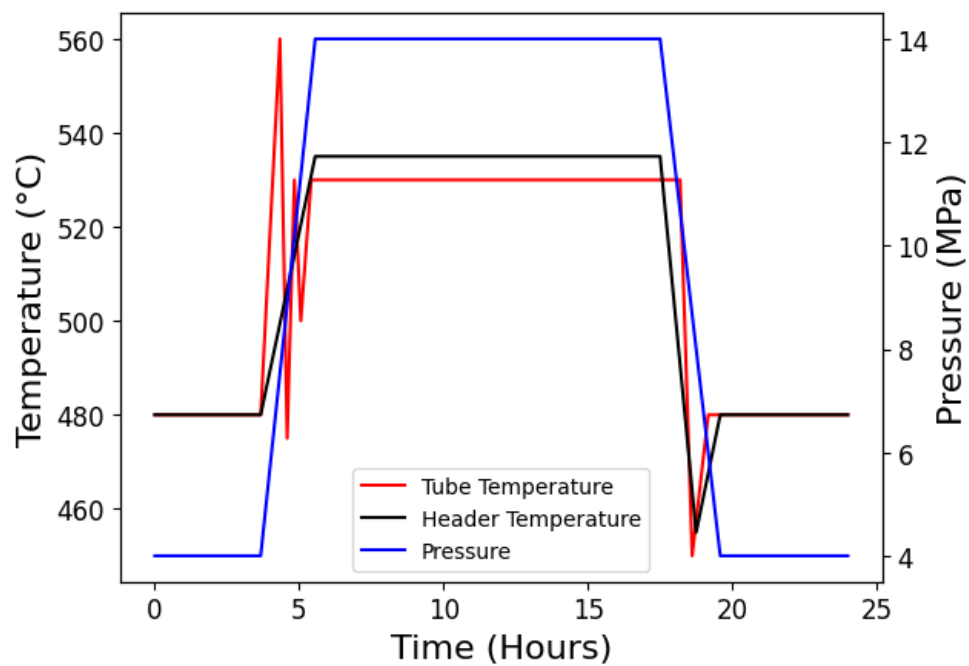


Figure 5.4: Simplified temperature and pressure vs time. [7]

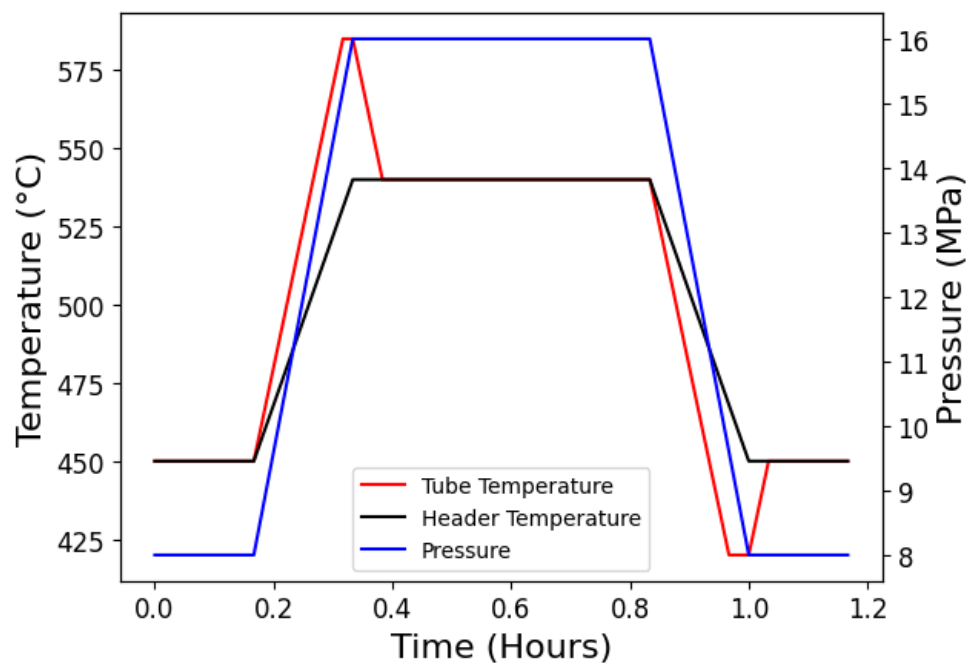


Figure 5.5: Applied temperature and pressure for crack growth vs time. [7]

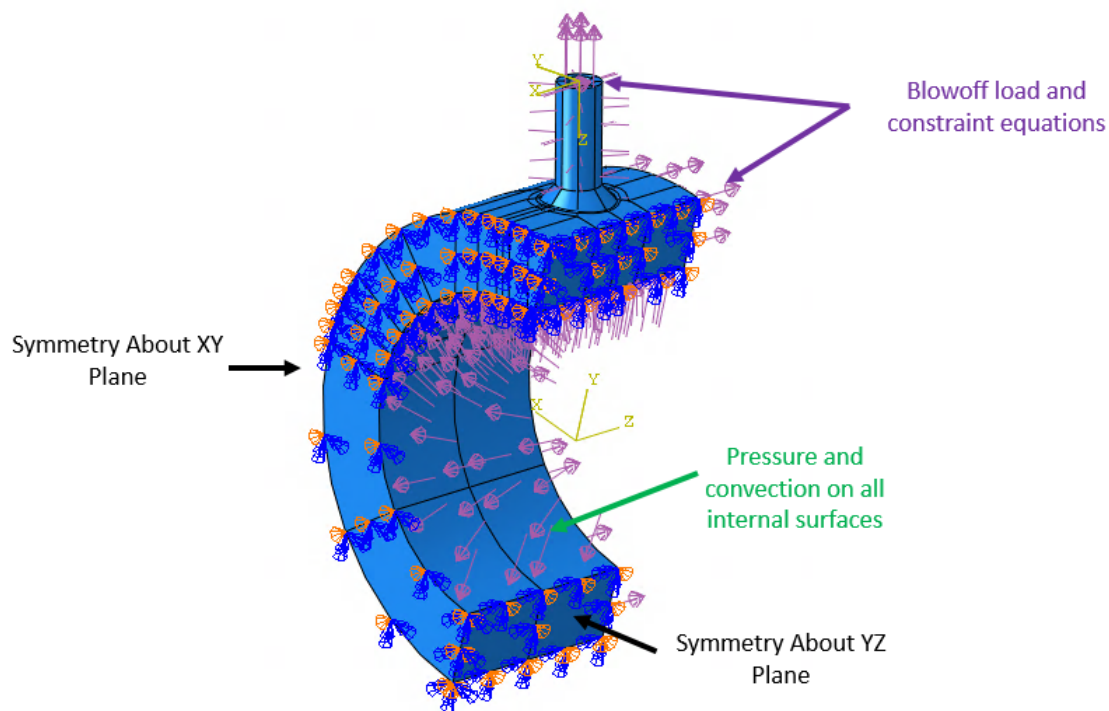


Figure 5.6: Global model boundary conditions. [7]

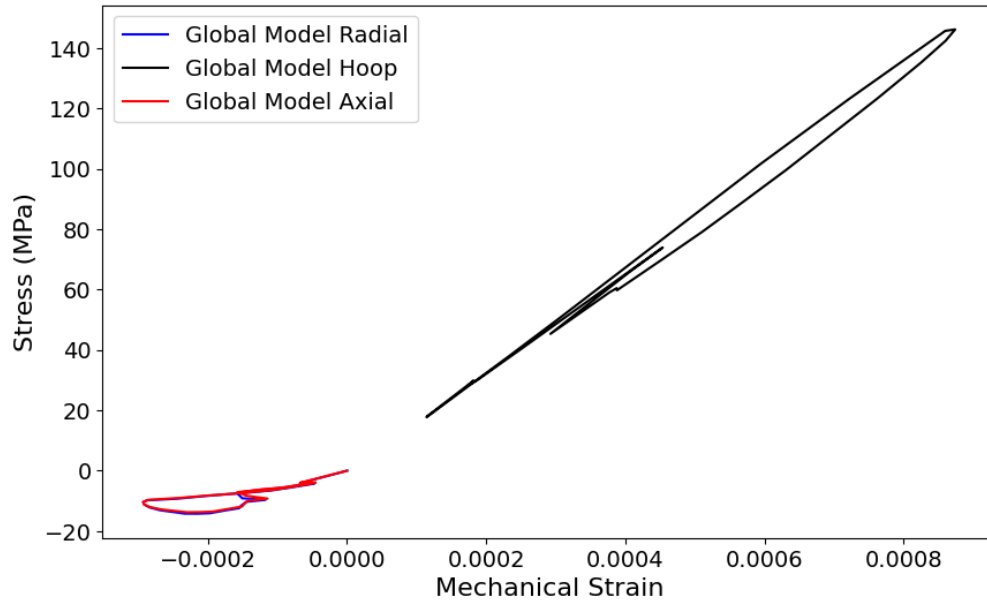


Figure 5.7: Global model stress-strain response at the critical point. [7]

Following the development of the global model, further simplifications are made to establish the sub-model tailored for the interactive process of iterative crack growth. The refinement begins by evaluating the stress response of the global model, which is used to determine the location of the zone with the highest stress and, likely, the most prone to crack initiation and propagation. As illustrated in Fig. 5.7, the axial section of the tube header intersection experiences significantly higher stresses during the 24-hour cycle. Furthermore, as Fig. 5.7 presents, the hoop stress is the predominant stress component. Suggesting that a crack in this region would experience high levels of Mode I loading, which is immensely relevant for crack growth.

### 5.3 Automated Iterative Method

#### 5.3.1 Theory

The contour integral represents a robust method for establishing the strength of the crack-tip field surrounding the crack tip. This method establishes several contours around the node representing the crack tip and creates a ring from one face of the crack front to the other. The output is a ring surrounding each node along the crack front. The SIF is interpreted from the J-integral, which is used to define the energy released associated with the advancement of a crack front. The J-integral is defined in equation 5.2.

$$J = \int_A \lambda(s) \mathbf{n} \cdot \mathbf{H} \cdot \mathbf{q} dA \quad (5.2)$$

where  $dA$  is the surface element,  $\mathbf{n}$  is the outward normal perpendicular to the crack surface,  $\mathbf{q}$  is the direction of virtual crack extension, and  $\mathbf{H}$  is defined as,

$$\mathbf{H} = \left( WI - \sigma \cdot \frac{\partial u}{\partial x} \right) \quad (5.3)$$

where  $W$  represents the strain energy found in an elastic material. In the case of LEFM for homogeneous isotropic materials, the stress intensity factors are related to the J-integral through the relationship,

$$J = \frac{1}{\bar{E}} (K_I^2 + K_{II}^2) + \frac{1}{2G} K_{III}^2 \quad (5.4)$$

where  $\bar{E} = E$  for plane stress and  $\bar{E} = \frac{E}{1-\nu^2}$  for plane strain. In Abaqus, the J-integral is found by creating rings of elements around the nodes representing the crack front. An illustration of the contour regions is shown in Figure 5.8. Given the path independence of the J-integral, multiple contours are defined to establish convergence of the J-integral around the crack tip. To improve the accuracy of the J-integral within Abaqus, the elements along the front of the crack front are specified

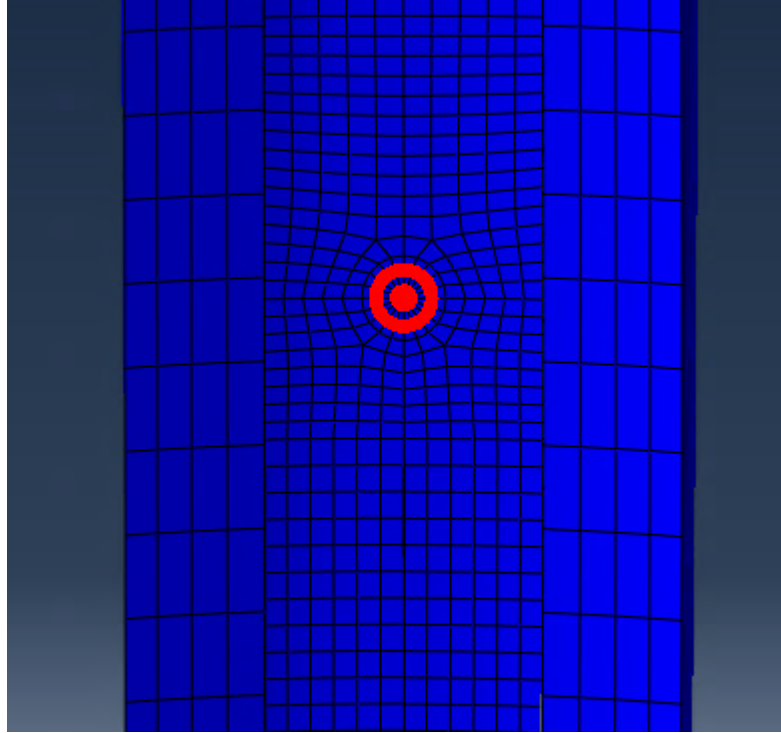


Figure 5.8: Nodes used in a stress contour around the crack front.

as collapsed node wedge elements. Through the collapse of the nodes along the crack front, the quadrilateral elements are represented with a wedge shape.

Given that the problem being evaluated assumes elastic behavior. The crack front was modeled using collapsed C3D20R elements, with the mid-side nodes moving to the quarter points. The quarter-point is identified as the position located at a distance equivalent to one-fourth of the element's length, measured along its uncollapsed edge from the crack edge. This change results in a stress singularity that can be represented as  $1/\sqrt{r}$  [167]. This stress distribution allows Abaqus to closely match the stress field as,

$$\begin{aligned}
 \sigma_{ij} = & \frac{K_I}{\sqrt{2\pi r}} f_{ij}^I(\theta) + \frac{K_{II}}{\sqrt{2\pi r}} f_{ij}^{II}(\theta) + \frac{K_{III}}{\sqrt{2\pi r}} f_{ij}^{III}(\theta) \\
 & + T\delta_{1i}\delta_{1j} + t_1^0\delta_{1i}\delta_{2j} + t_2^0\delta_{2i}\delta_{2j} + t_3^0\delta_{2i}\delta_{3j} \\
 & + \sigma_{13}^0\delta_{1i}\delta_{3j} + (\nu T + E\epsilon_{33})\delta_{3i}\delta_{3j} + O(r^{0.5})
 \end{aligned} \tag{5.5}$$

where  $r$  and  $\theta$  are the in-plane polar coordinates around the crack tip,  $\delta$  is the Kro-necker delta, and  $f_{ij}$  are known functions of  $\theta$ . The indices 1,2,3 represent the direc-tion along the crack surface perpendicular to the crack front, the direction normal to the crack surface, and the direction tangential to the crack front, respectively. The superscripts  $I$ ,  $II$ , and  $III$  correspond to the loading mode.  $T$  represents the stress and is a representation of the likelihood of a crack to kink. The terms containing  $K_i$  represent the stress component using the following relationships.

$$\lim_{r \rightarrow 0} \sigma_{ij}^I = \frac{K_I}{\sqrt{2\pi r}} f_{ij}^I \theta \quad (5.6)$$

$$\lim_{r \rightarrow 0} \sigma_{ij}^{II} = \frac{K_{II}}{\sqrt{2\pi r}} f_{ij}^{II} \theta \quad (5.7)$$

$$\lim_{r \rightarrow 0} \sigma_{ij}^{III} = \frac{K_{III}}{\sqrt{2\pi r}} f_{ij}^{III} \theta \quad (5.8)$$

$$\sigma_{ij} = \sigma_{ij}^I + \sigma_{ij}^{II} + \sigma_{ij}^{III} \quad (5.9)$$

However, in the case of LEFM, the range of  $K$  is considered. In a uni-axial cyclic analysis, the stress intensity factor will vary over some range defined as,

$$\Delta K = K_{max} - K_{min} \quad (5.10)$$

where  $\Delta K$  is the stress intensity factor range. Hence, the rate at which the crack propagates can be represented using the relationship established by Paris and Erdogan [168]. Their relationship describes the linear region of crack growth as,

$$\frac{da}{dN} = C \Delta K^m \quad (5.11)$$

where  $C$  and  $m$  are material constants, and  $\frac{da}{dN}$  is the crack growth per cycle. This relationship has been expanded for mixed mode loading through the use of an effective SIF defined as,

$$\frac{da}{dN} = C \Delta K_{eff}^m \quad (5.12)$$

where  $K_{eff}$  is the effective SIF defined as,

$$\Delta K_{eff} = \sqrt{\Delta K_I^2 + \Delta K_{II}^2 + \Delta K_{III}^2} \quad (5.13)$$

In real-world applications, components are often subjected to complex stress states, where the combination of multiple modes of fracture becomes relevant. Therefore, the SIF used to evaluate the crack growth increment is taken as  $K_{eff}$  throughout the analysis. This provides the ability to capture crack growth behavior more accurately over a larger range of loading conditions. Additionally, the SIF range is evaluated by excluding the effects due to compressive stresses. The present work focuses on evaluating crack propagation within LEFM. Within the framework of LEFM, cracks do not amplify the stress concentration under compression, such that the influence of negative SIF is minimal. This approach, however, differs when accounting for plasticity, where the load ratio is relevant due to the influence of the mean stress on the crack growth rate.

### 5.3.2 Automation Methodology

The sub-model is created by incorporating the tube-header intersection along the axial direction of the header. The size of the sub-model is chosen to balance the computational efficiency and accuracy required to propagate the postulated crack. The sub-model incorporates the global model's boundary conditions, with the addition of the sub-model-specific boundary condition along the surfaces corresponding to the global model, as represented in Figure 5.9.

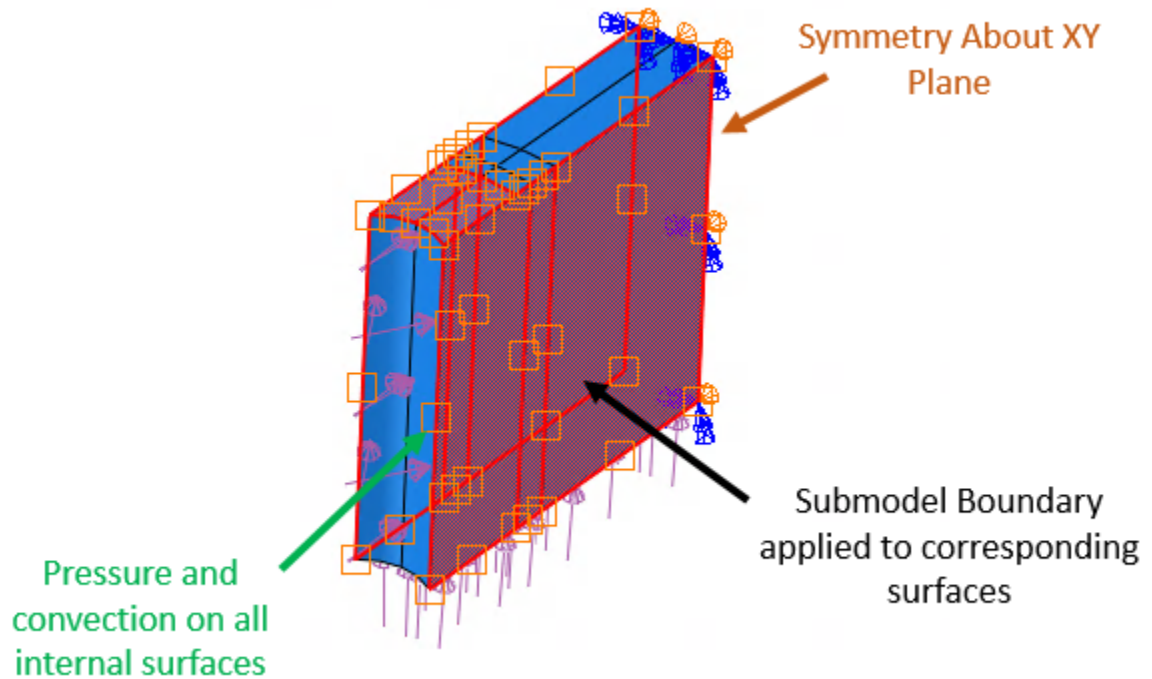


Figure 5.9: Sub-model boundary conditions. [7]

In most cases, a single sub-model provides a level of fidelity adequate for a crack analysis to be completed within Abaqus. However, the present work necessitates the use of a separate cracked mesh sub-model due to restrictions within Abaqus and mesh continuity considerations unique to the innovative approach applied. As a result, the cracked region is represented as a distinct sub-model, integrated into the broader sub-model through tie constraints. The distinction between the two regions is shown in Figure 5.10. This setup allows for the iterative propagation of the crack surfaces and mesh partitions while adhering to the sub-model boundary condition restrictions. Hence, the outer region of the sub-model is configured to preserve the stability of the sub-model boundary condition concerning the global model, while the tied constraint facilitates the movement of the crack front. This methodology enables the iterative propagation of an SECC within the constraints of a sub-model, overcoming Abaqus's limitations regarding the movement of faces associated with

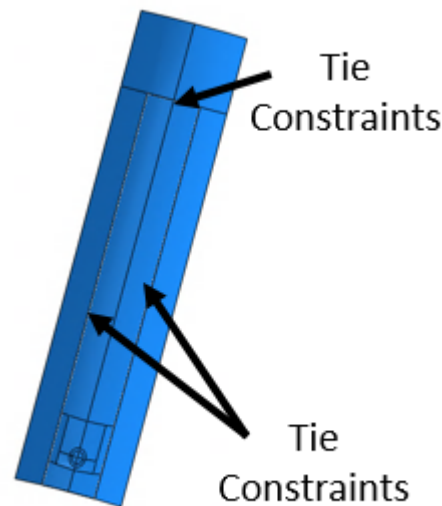


Figure 5.10: Automated cracked region sub-model tie constraints. [7]

sub-model boundary conditions. This approach ensures that the region surrounding the crack front maintains high fidelity across multiple iterations while maximizing computational efficiency.

The present work incorporates the automated growth of an SECC located in the corner of an outlet header. This process is based on iterative quasi-static analysis where the user can specify the number of increments to iterate, the size of the initial defect, the boundary conditions for the cycle, and the ending condition. This iterative approach allows for a more detailed analysis of crack growth behavior under variable conditions, providing valuable insight into the behavior of the crack as it grows over time. By enabling users to specify parameters such as the size of the initial defect and the number of increments to grow the crack between analyses, the present work offers a customizable framework for investigating multiple cases of SECC. Moreover, the flexibility in defining the boundary and exit conditions allows the user to efficiently evaluate multiple scenarios. Through this novel approach, we aim to streamline the assessment procedure for SECC in headers, offering a practical tool to help others assess the risk of failure. The incorporation of the automated growth represents

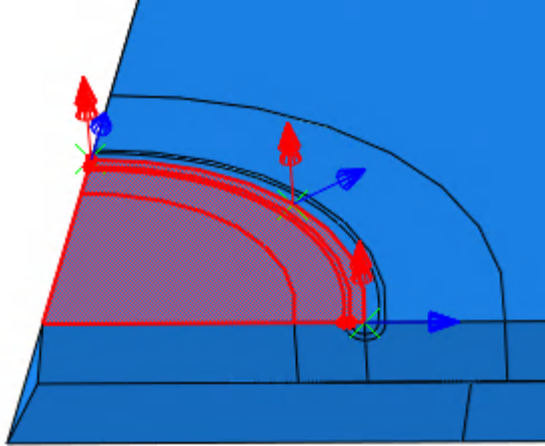


Figure 5.11: Boundary describing the initial seam crack and the virtual extension directions. [7]

a significant advancement in quasi-static LFM analysis, providing a more robust foundation for evaluating SECC propagation behavior in realistic loading scenarios.

The automation process starts with the definition of the model's basic aspects. This includes defining the material properties required to analyze the mechanical response, such as Young's modulus, thermal conductivity, and fracture toughness. At the same time, the geometry of the header is established by defining the inner and outer diameters of the outlet header and tubes. The initial boundary conditions are also established, defining the operational pressure and temperature cycles that will be evaluated in the subsequent analyses. To minimize computational costs during the crack growth process, the thermal boundary conditions on the cracked models will be imported from an initial global model. Therefore, the first trial that is processed is the heat transfer step, solving for the convective thermal transients on the internal surfaces of the header. After completion, the code automates the importation of the boundary condition, switching the model to the mechanical step. The mechanical step is responsible for establishing the displacement field used to serve as the basis for the sub-model. After the global mechanical response is finalized, the sub-model

is established, which serves as the region used for crack growth automation. The use of a refined sub-model minimizes computational costs while maintaining mesh fidelity during growth. The creation of the cracked sub-model involves defining the crack path through the use of surface sweep partitioning. This process also prepares the output of the model by defining the seam crack region and crack normal for the analysis.

With the sub-model established, the model begins quasi-static simulation to evaluate the crack's growth. This process involves submitting the cracked sub-model for analysis, interpreting the results to determine the effective SIF along the crack front, and updating the crack path based on Paris law. This iterative approach is repeated until the predefined end condition is met. After the analysis is complete, the user can evaluate the data exported during the simulation to accurately evaluate the crack's progression through the material.

A detailed explanation of the steps that occur during the automated method is outlined in Figure 5.12.

### 5.3.3 Calibration of finite element model

The accuracy and computational efficiency correlate significantly with the quality of the underlying mesh. To strike a balance between accuracy and costs, the present work refines the mesh in the region around the tube header intersection while coarsening the mesh in the regions outside the area of interest. The smallest elements within the global header are 3.5 mm, while the larger elements have edge lengths over 50 mm. This approach maintains accuracy in the region of interest while minimizing the computational costs. The finalized mesh for the global model consists of 30,960 C3D20R elements, represented by Figure 5.13.

Similarly, the size of the outer regions of the sub-model mesh is selected to correlate with the global model in the region of the tube header intersection. The initial size of the outer layer of the sub-model is selected as 3.5 mm to optimize the con-

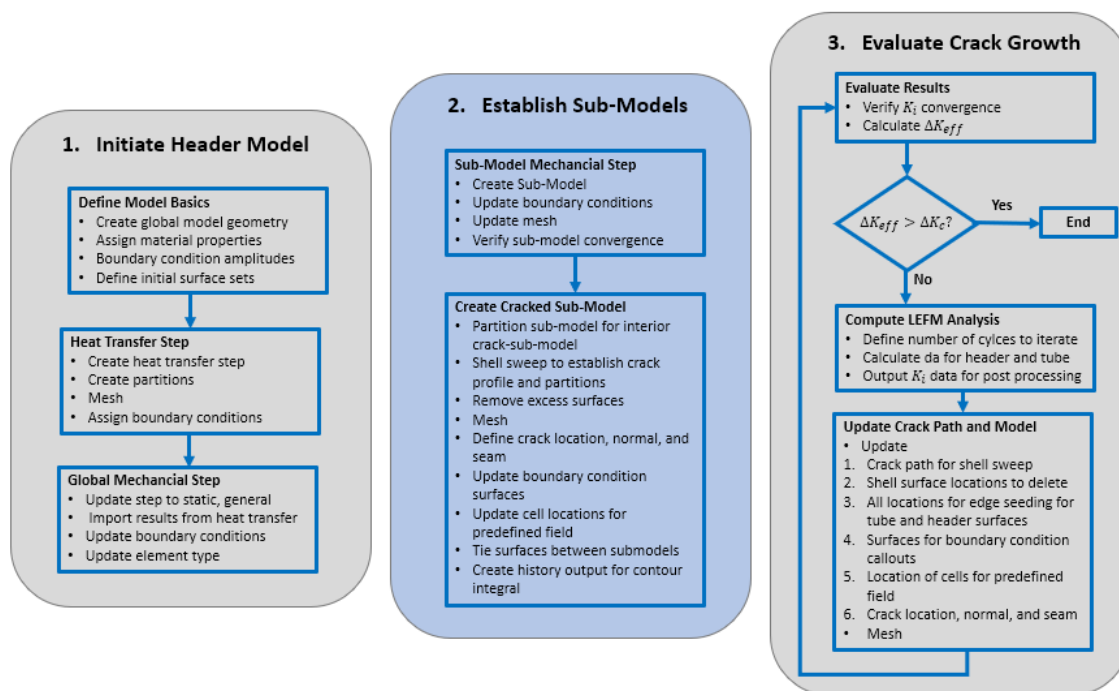


Figure 5.12: Summary of crack growth modeling procedure.

tinuity between the sub-model boundary condition faces. Figure 5.14 represents the initial sub-model mesh comprising 3,564 C3D20R elements. Before incorporating the cracked region within the sub-model, the sub-model's accuracy is evaluated by comparing the stress response with that from the global model. The response is taken at the point with the highest stress found at the axial point of the tube header intersection, as shown in Figure 5.15.

The stress-strain response of each normal stress component for both models is shown in Figure 5.16. Figure 5.16 demonstrates the convergence of the models as each stress component maintains within 2% similarity throughout the cycle.

The sub-model containing the cracked region is also evaluated for accuracy prior to applying the seam crack to the model. This is done by evaluating the automated mesh with the partitions for the cracked region in comparison to the previous models. As Fig. 5.17 illustrates, the stress response at the critical point is consistent for each model. As Fig. 5.17 demonstrates the hoop stress is the most critical component.

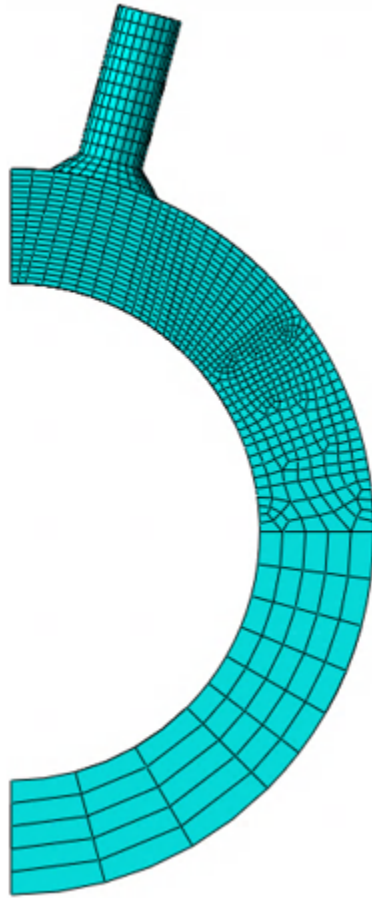


Figure 5.13: 3D meshed header with 30,960 C3D20R elements. [7]

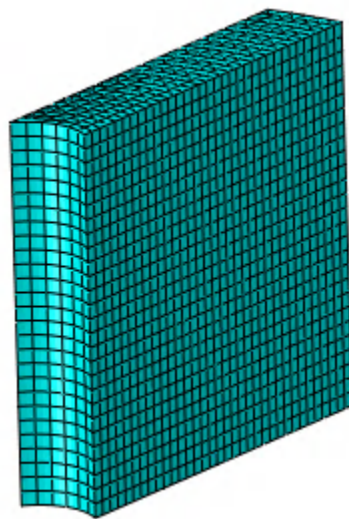


Figure 5.14: Meshed sub-model with 3,564 C3D20R elements. [7]

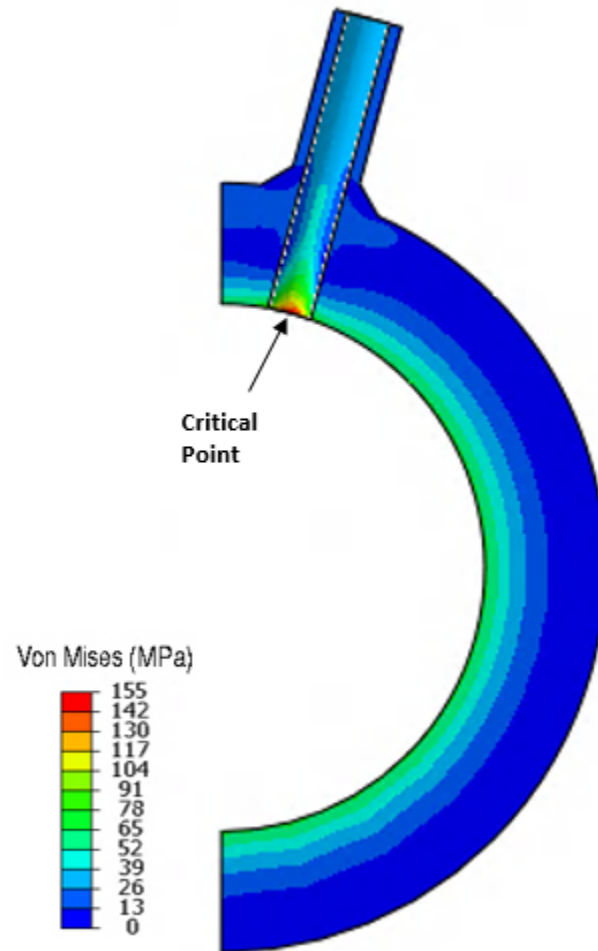


Figure 5.15: Location of critical point. [7]

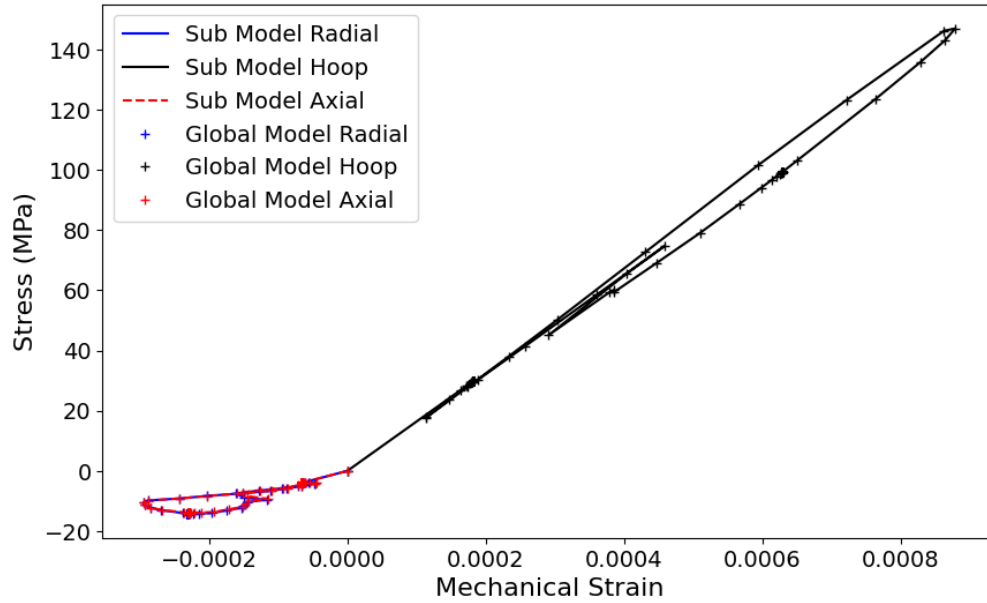


Figure 5.16: Stress-strain response of sub-model compared to global model at critical point. [7]

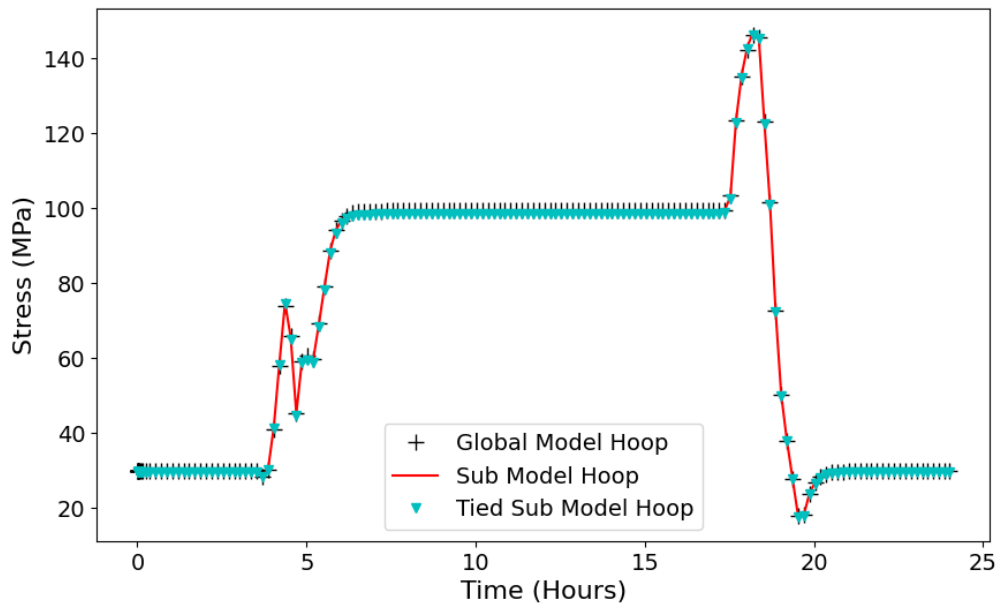


Figure 5.17: Stress-strain response of sub-models compared to global model at critical point. [7]

The process of meshing a seam crack in Abaqus requires a unique meshing technique. The most visible requirement is the use of wedge elements surrounding the crack front. This type of meshing scheme is often referred to as a spider-web mesh and is used to represent the  $1/\sqrt{r}$  stress distribution surrounding the crack front of an elastic material. As a result, the mesh region surrounding the cracked front maintains a high degree of fidelity, with the wedge elements having a long side of 1 mm and the elements in the surrounding region having a size of 0.7 mm. While this approach adds significant computational costs to the analysis, it provides a level of robustness to the present work. As the cracked region is automatically propagated throughout the material, it is imperative that each mesh maintains the same level of refinement. Therefore, the mesh of the initial sub-model contains significantly more elements than the prior sub-model, with 43,674 C3D20R elements. Through this refinement level, the mesh can iterate automatically without the need for further partitioning. Examples of the initial cracked mesh at one-quarter wall thickness and the mesh as the crack has reached one-half wall thickness are shown in Figure 5.18.

In contrast to the non-damaged models, the iterative crack model is validated through the examination of the contour-internal surrounding the crack front. The convergence of the crack front at the locations where the crack intersects the tube and the header are shown in Fig 5.20 and Fig.5.19, respectively.

Figures 5.20 and 5.19 demonstrate that the SIF is converged within the first five contours surrounding the crack front. This validation authenticates the model's accuracy, bolstering the choice to use similar levels of refinement through the crack propagation process.

The model is evaluated individually for the influence of pressure and temperature effects prior to evaluating crack growth. Figure 5.21 illustrates the relationship between the SIF  $K_I$  and the angular position along the crack front after five years. Figure 5.21 highlights that the relationship of the SIF is consistent as the pressure

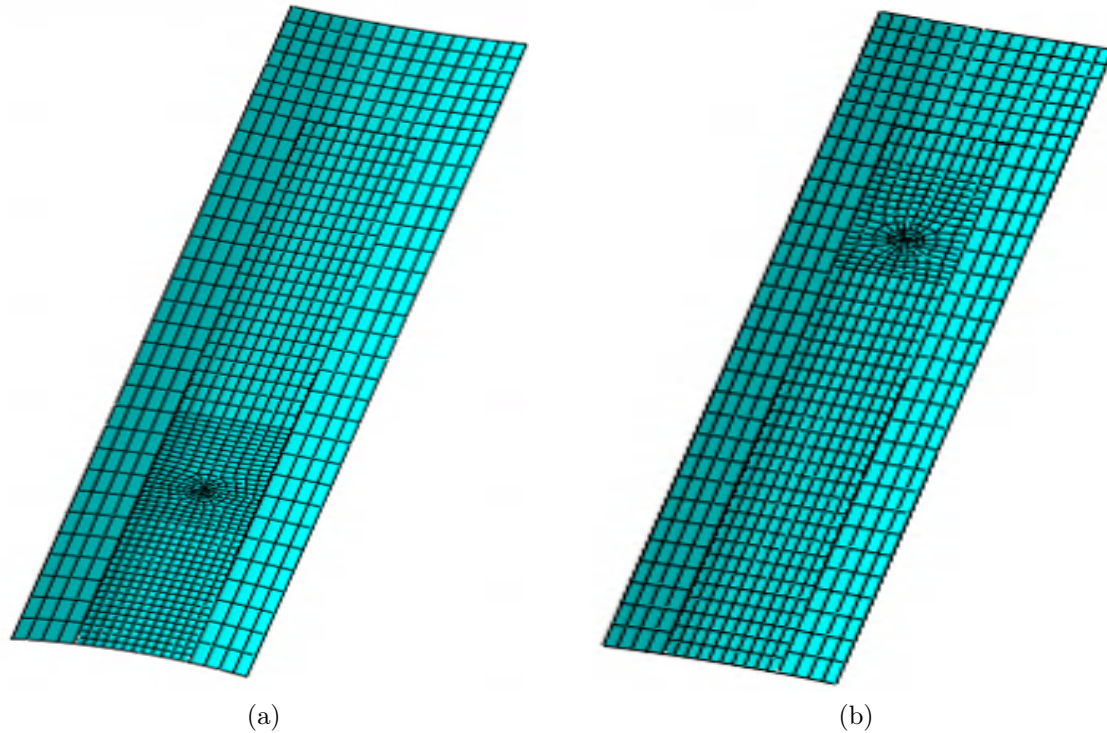


Figure 5.18: Meshed crack sub-model at (a) initial state (b) after cycling for thirty-five years. [7]

increases, demonstrating a linear relationship between pressure and SIF along the crack front.

Similarly, Figure 5.22 presents the influence of pressure on  $K_I$  at the critical points of the tube and header intersection. As expected, the relationship is linear at both locations, with the rate of increase in  $K_I$  at the tube location being significantly higher than at the header intersection. This relationship suggests that the influence of the pressure on the SIF at a constant temperature can be approximated for the entire pressure range. Pressure plays a critical role in the influence of crack propagation. At the peak operating pressure in the present work, the crack-header intersection experiences a  $K_I$  of  $5.3 \text{ MPa}\sqrt{\text{m}}$  which increases to  $8.3 \text{ MPa}\sqrt{\text{m}}$  at the intersection of the tube. These values account for nearly half of the SIF found along the crack front, highlighting the influence of pressure on the stress state of the crack.

The influence of the thermal transient is also evaluated individually to review their

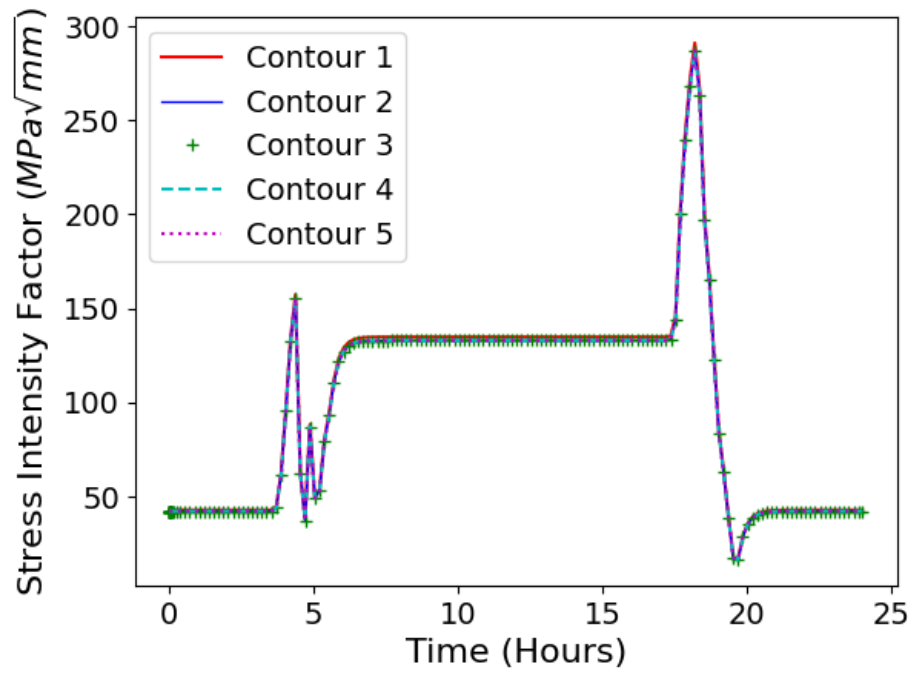


Figure 5.19: Stress intensity factor vs time for first five contours at crack header intersection. [7]

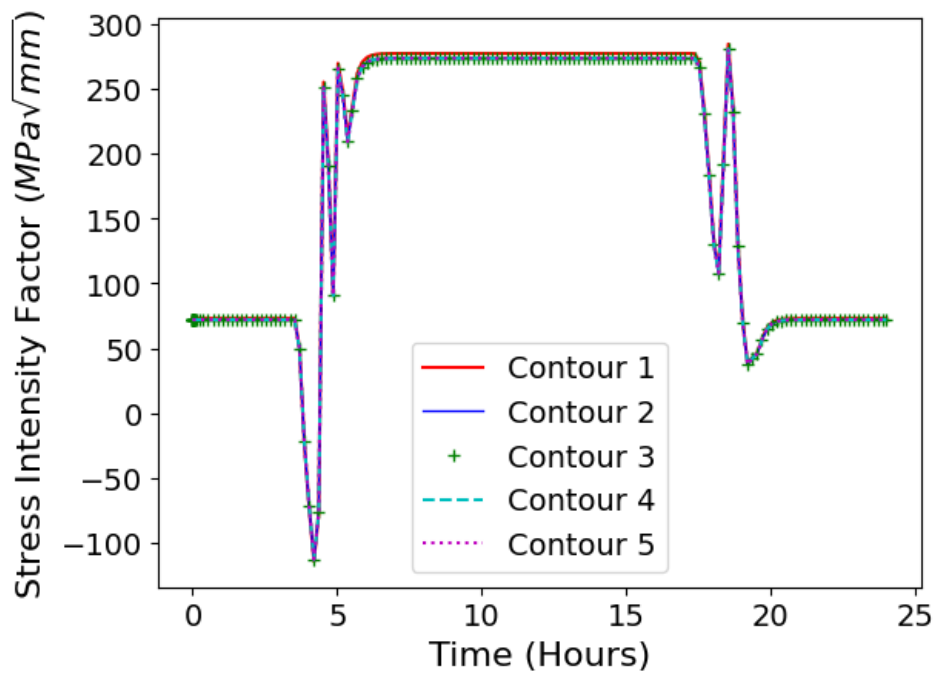


Figure 5.20: Stress intensity factor vs time for first five contours at crack tube intersection. [7]

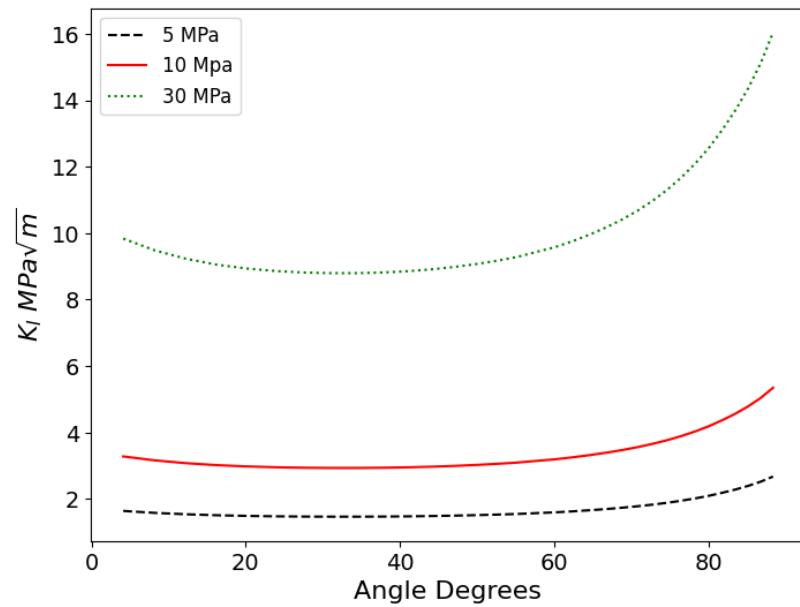


Figure 5.21: Stress intensity factor  $K_I$  vs angular position for the crack at five years response to pressure. [7]

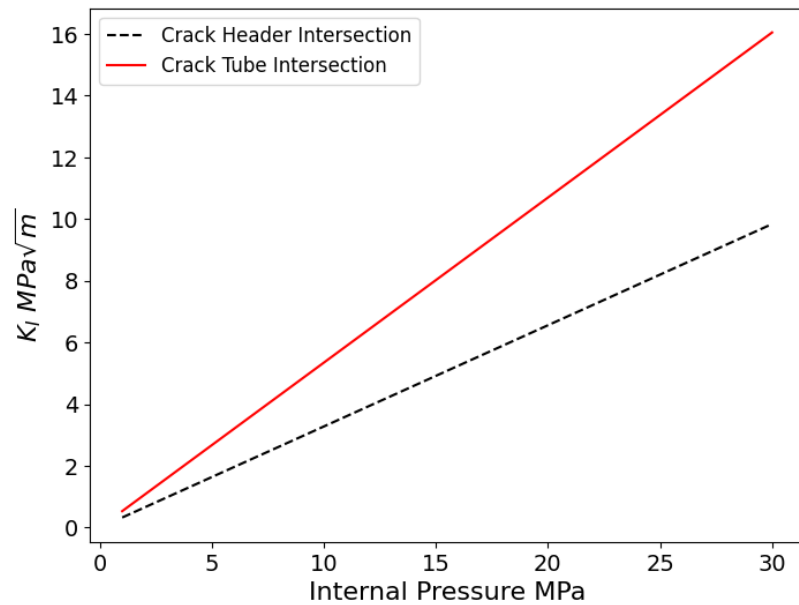


Figure 5.22: Influence of pressure on  $K_I$  at surface crack locations at five years. [7]

impact on the crack growth behavior. Figures 5.23 and Fig. 5.24 illustrate the SIF in response to the thermal response. These figures show that the magnitude of the SIF is significantly smaller than the trials evaluating pressure. Also notable is that the influence of  $K_I$  is dominant at both locations and during both transients.

As 5.23 demonstrates, the influence of the thermal transient alone influences the crack at the intersection of the header and tube differently. Near the intersection of the header, the SIF experiences a peak at the start of the transient that subsides as the temperature homogenizes. This results in the crack in the region near the header experiencing a positive SIF during the initial ramp and compressive forces during the subsequent cooling transient.

In contrast, the SIF near the tube is initially compressive during the initial transient before quickly transitioning to positive during the thermal correction. This is followed by a period where the SIF increases during the cool-down and experiences a negative spike during the thermal correction. This pattern suggests that the thermal ramp-up may influence crack propagation along the header, whereas the cooling transient may have more influence over the thermal contribution to stress within the tube. Moreover, this indicates that the thermal response of the SIF along the crack is out-of-phase with respect to the  $K_I$  behavior. This phenomenon can be associated with the differences in the thermal traits that the regions experience.

Figures 5.27 through Fig. 5.35 illustrate the contribution of each SIF component over time at the locations where the crack intersects the tube and the header. The variation in  $K_I$  over time elucidates how the structure reacts to combined primary and secondary forces; for instance, the pressure develops a positive  $K_I$  prior to the presence of thermal stresses. However, when there is a spike in temperature, the system experiences compressive strains on the internal surfaces. Therefore, despite an increase in operating pressure, the  $K_I$  initially decreases during the start of the transient.

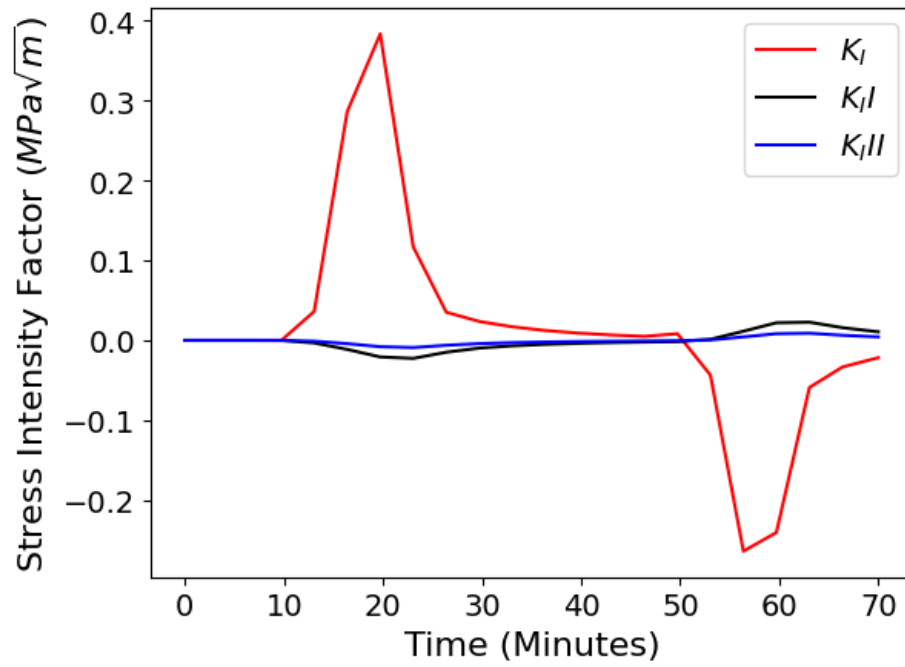


Figure 5.23: Thermal response of SIF at crack header intersection. [7]

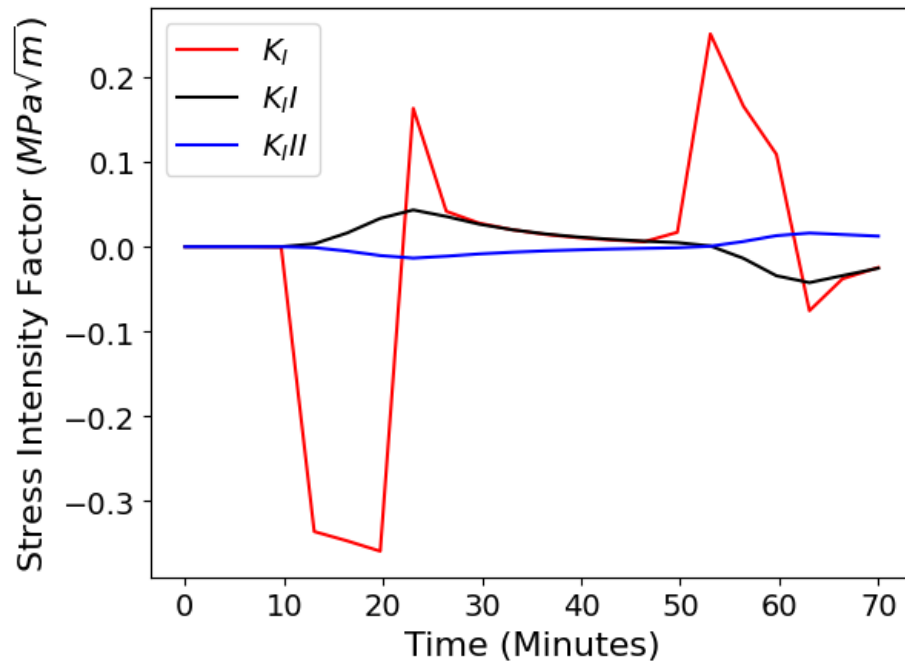


Figure 5.24: Thermal response of SIF at crack tube intersection. [7]

Conversely, when the temperature experiences a cooling transient, the interior surfaces of the system undergo higher tensile forces. Hence, the magnitude of  $K_I$  reaches higher values than either of the individual cycles. Interestingly, these phenomena are diminished as the crack propagates with time. The reduction in peak stresses as the crack grows can be attributed to the reduction in the stress profile surrounding the stress riser of the tube-header intersection.

Throughout the propagation, the  $K_I$  is highest at the location that intersects the tube. This is a result of the additional stress applied by the blow-off pressure on the face of the tube and the higher thermal gradients that occur within the tube. The influence of the minimized thermal transient resulting from the homogenized steam is demonstrated in Fig. 5.23. As Fig. 5.23 demonstrates, the rate of change of the  $K_I$  within the header is significantly slower than that within the tube.

#### 5.4 Crack growth analysis

The present work propagates the crack through the thickness of an outlet header, tracking the crack's progression through the wall of the sub-model. Assuming periodic inspections and taking into consideration the calculated growth rate, we simulate the crack growing steadily over five-year intervals. Figures 5.27 through Fig. 5.35 represent the crack growing steadily over the five-year intervals. The responses at each interval align with the patterns found from analyzing the individual responses and reflect their interaction.

Therefore, by examining an entire cycle to determine  $K_I$ , we gain a more robust understanding of how the crack may propagate with time. These phenomena are exacerbated by the temperature difference between tube and header surfaces. Ultimately, the high hoop stress, combined with the internal pressure reaction, results in a  $K_I$  high enough for crack growth. Notably, the magnitude of  $K_I$  from the mechanical and thermal loading combination exceeds their individual contributions.

The peak  $K_I$  for the tube and the header both occur during the cooling transient.

However, there is a slight delay between the peak stress resulting from the variation in thermal transient. Figures 5.36 through Fig. 5.44 illustrate the behavior of  $K_I$  along the crack front at each of these times. In these figures, the angle is taken along the axial direction of the header such that 0 degrees represents the crack intersection with the header, and 90 degrees represents the intersection with the tube.

Each of the figures, Fig. 5.36 through Fig. 5.44 illustrate how  $K_I$  changes along the crack front. This variation is a result of the crack's orientation with respect to the loading direction and depth. In each case,  $K_I$  is higher at the intersection with the tube and lower within the header, whereas the minimum  $K_I$  occurs in the middle of the crack. The variation of  $K_I$  between the times that  $K_I$  is maximized at the crack intersection with the tube and header illustrates the influence of the thermal gradient on the tube intersection is greater. So, although the SIF increases within the tube, it is lowered within the header. Furthermore, this variation presents a critical oversight of the SECC method. As  $K_I$  varies along the crack front, so would the crack growth over time. As Fig. 5.36 illustrates, this variation on the initial crack is already on the order of  $8 MPa\sqrt{m}$ , and the rate of change is biased to increase rapidly as it approaches the tube. Evaluating Fig. 5.42 demonstrates how this behavior is exaggerated as the crack grows, where the variation along the front is more abrupt, exceeding a variation of  $10 MPa\sqrt{m}$  along the crack front. This change further suggests that the shape of the crack front should change with time. However, with the restriction of an SECC, this variation is impossible to represent. Therefore, these figures represent a significant limitation to the use of SECC for crack propagation.

Figure 5.25 demonstrates the growth of the crack over time. From this figure, it is clear how the crack propagates more along the region of the tube than within the header. Additionally, Fig. 5.25 presents how the distance with respect to the intersection of the tube with the header increases the overall stress and crack growth between cycles. The tube's growth slows significantly as the crack propagates away

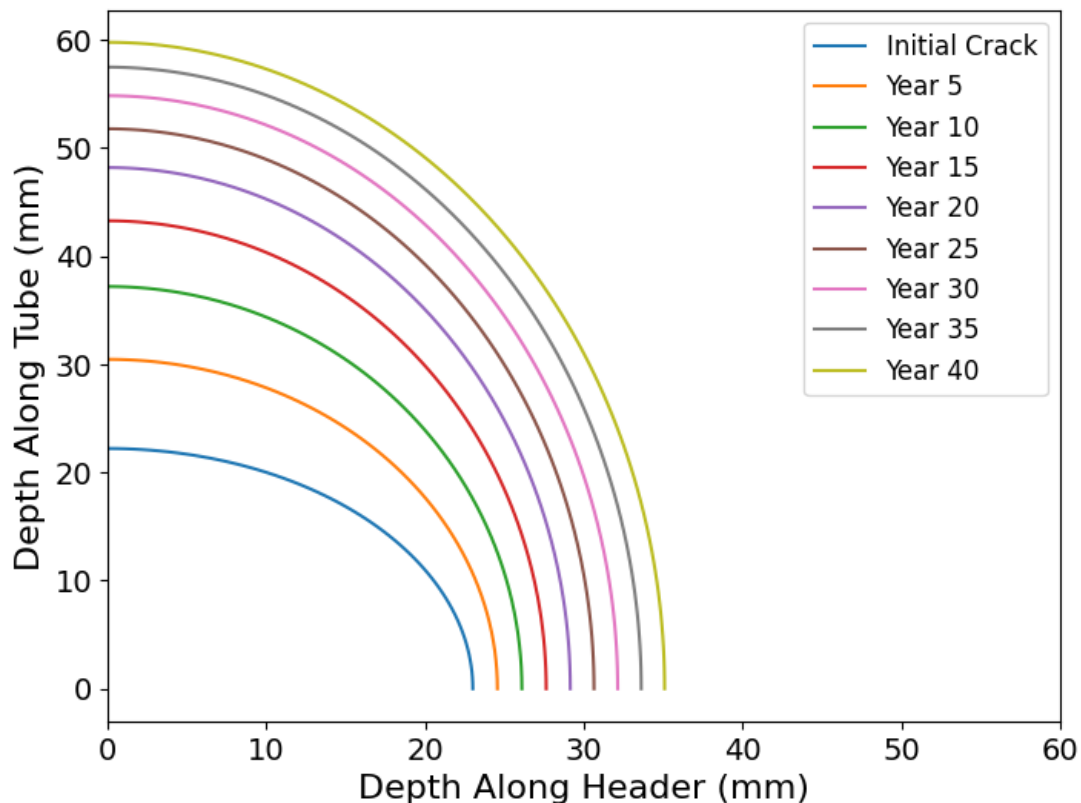


Figure 5.25: Evolution of crack front over time. [7]

from the stress concentration. Figure 5.26 shows each increment between cycles. Figure 5.26 demonstrates the clear slowing of the propagation of the crack-front within the tube. The crack begins by growing at a rate of over 8 mm a year before slowing to a rate of about 2 mm every five years along the tube. However, throughout the entire process, the growth rate along the header remains fairly consistent, with the initial increment being 1.5 mm and the final increment being 1.54 mm. The slow growth of the crack within the header and within the tube at later times demonstrates the robustness of the initial design, such that an exaggerated transient has minimal damaging effects.

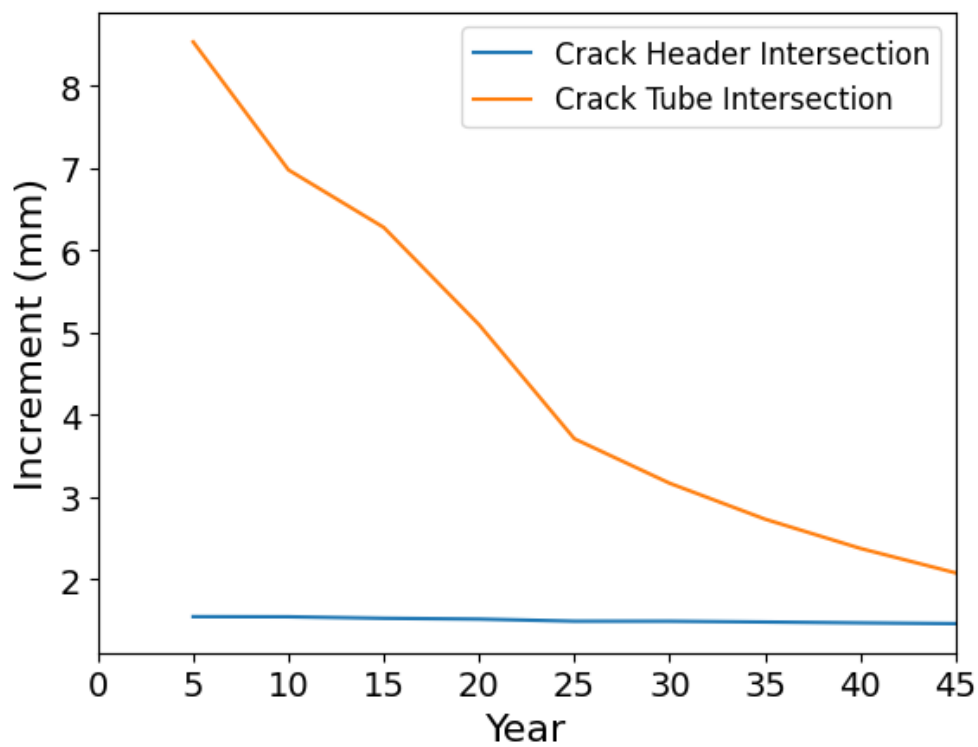


Figure 5.26: Incremental crack growth over time. [7]

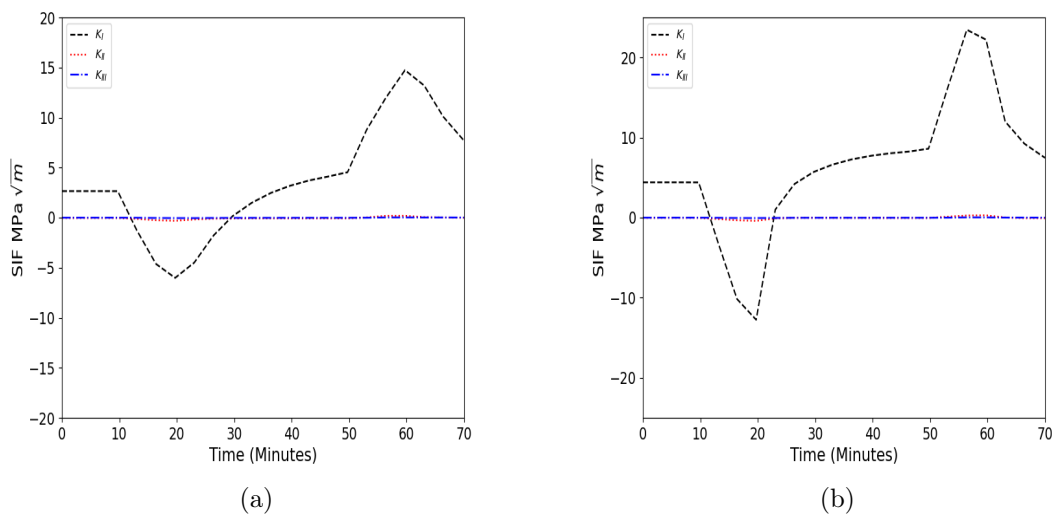


Figure 5.27: Time-dependent response of  $K_I$ ,  $K_{II}$ , and  $K_{III}$  at the intersection of the crack and the (a) header (b) tube. [7]

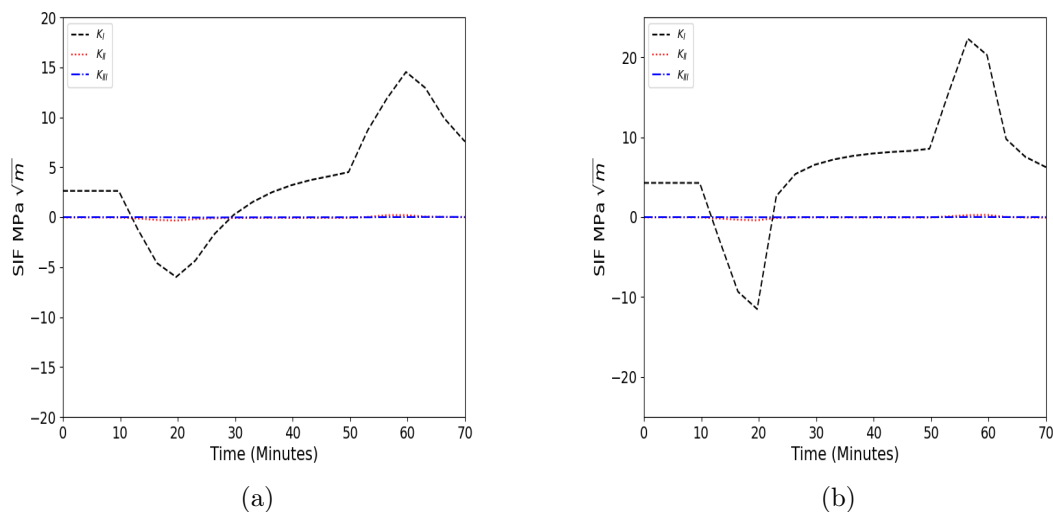


Figure 5.28: Time-dependent response of  $K_I$ ,  $K_{II}$ , and  $K_{III}$  at year 5 at the intersection of the crack and the (a) header (b) tube. [7]

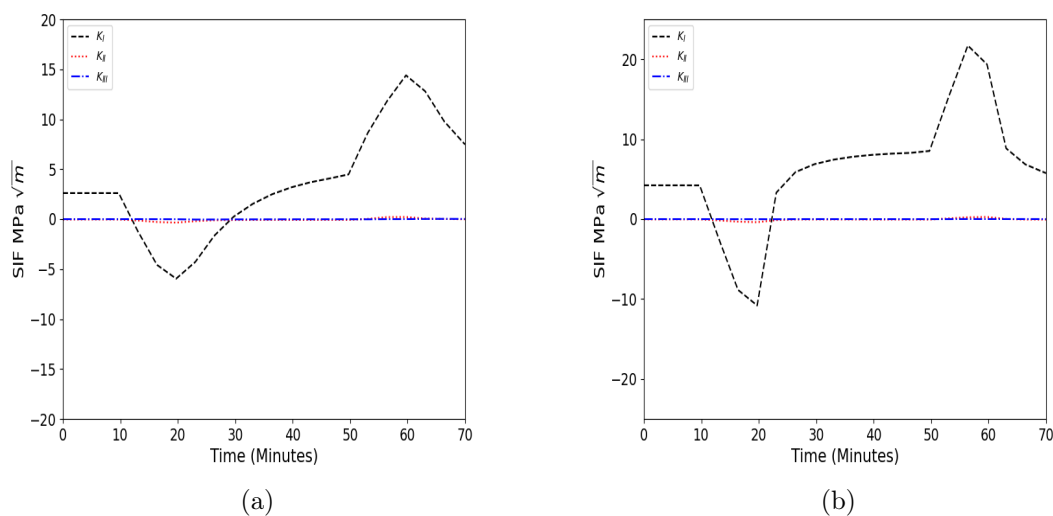
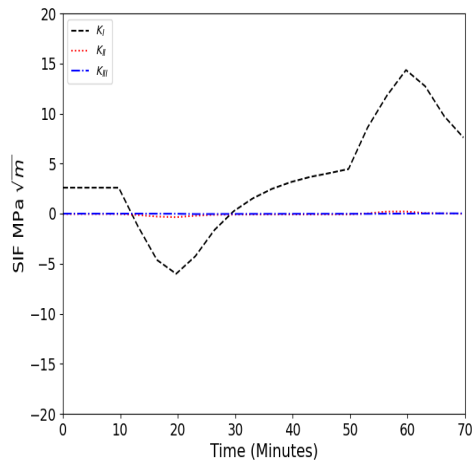
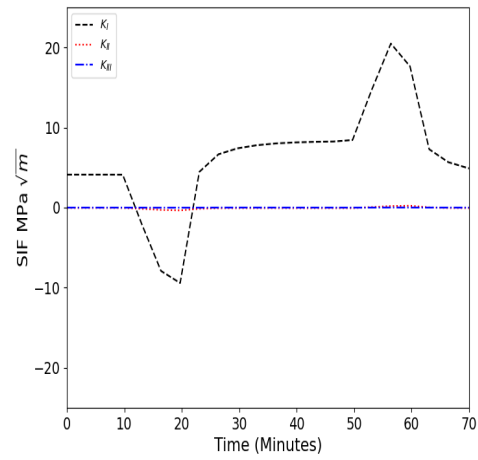


Figure 5.29: Time-dependent response of  $K_I$ ,  $K_{II}$ , and  $K_{III}$  at year 10 at the intersection of the crack and the (a) header (b) tube. [7]

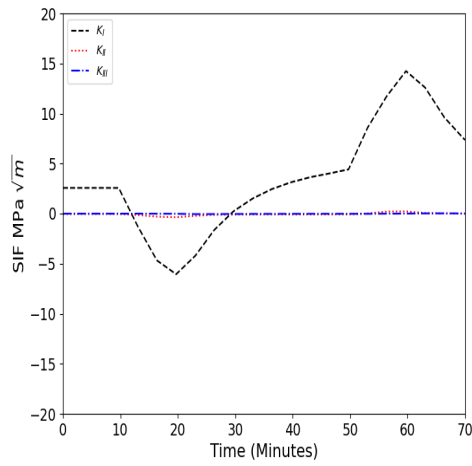


(a)

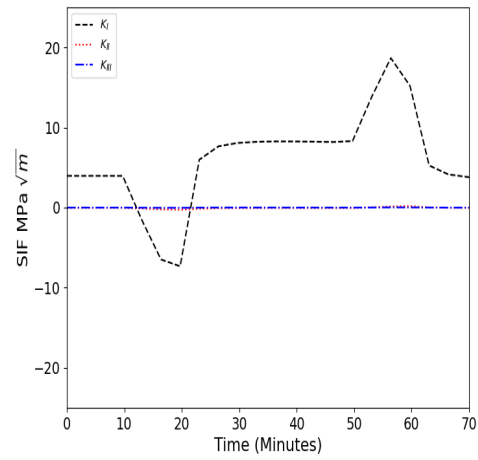


(b)

Figure 5.30: Time-dependent response of  $K_I$ ,  $K_{II}$ , and  $K_{III}$  at year 15 at the intersection of the crack and the (a) header (b) tube. [7]

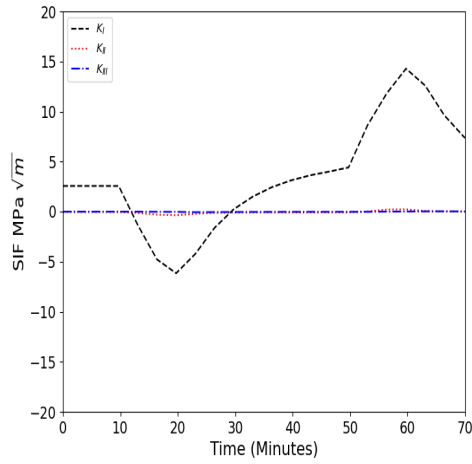


(a)

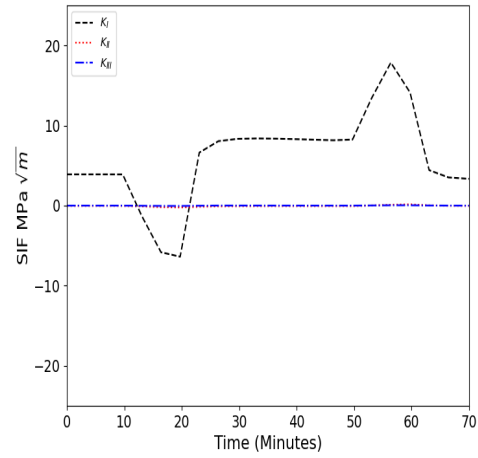


(b)

Figure 5.31: Time-dependent response of  $K_I$ ,  $K_{II}$ , and  $K_{III}$  at year 20 at the intersection of the crack and the (a) header (b) tube. [7]

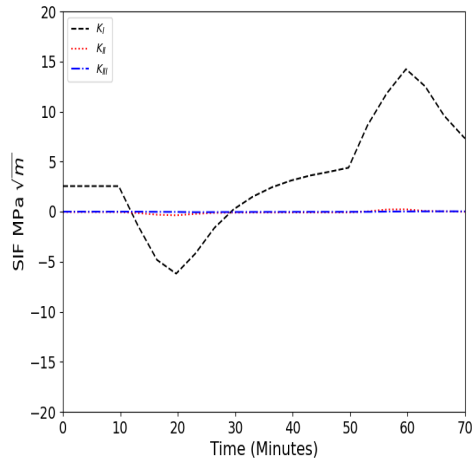


(a)

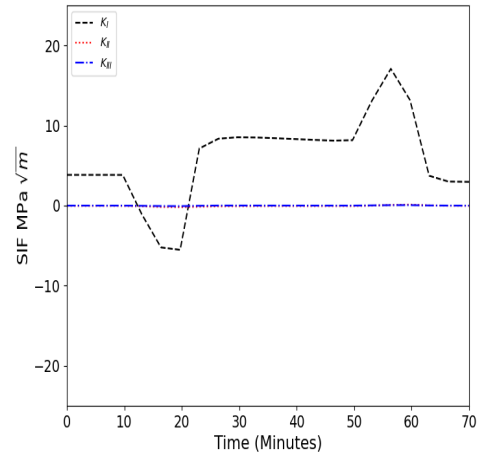


(b)

Figure 5.32: Time-dependent response of  $K_I$ ,  $K_{II}$ , and  $K_{III}$  at year 25 at the intersection of the crack and the (a) header (b) tube. [7]

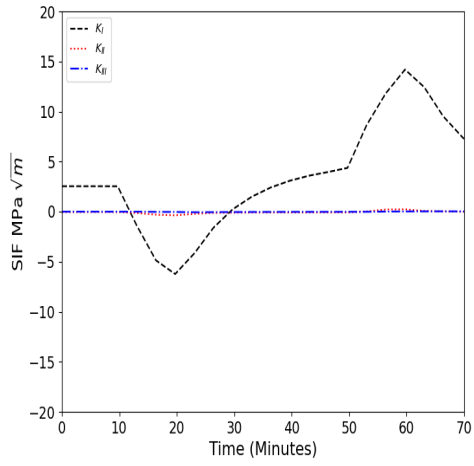


(a)

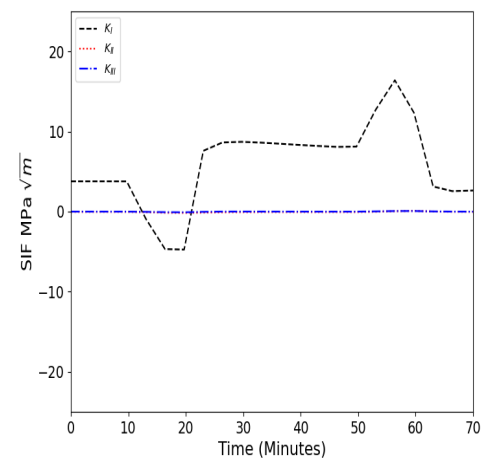


(b)

Figure 5.33: Time-dependent response of  $K_I$ ,  $K_{II}$ , and  $K_{III}$  at year 30 at the intersection of the crack and the (a) header (b) tube. [7]

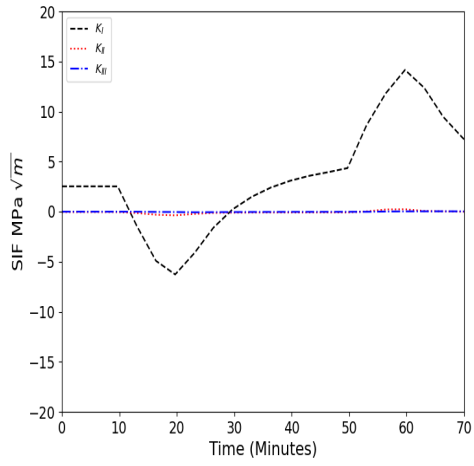


(a)

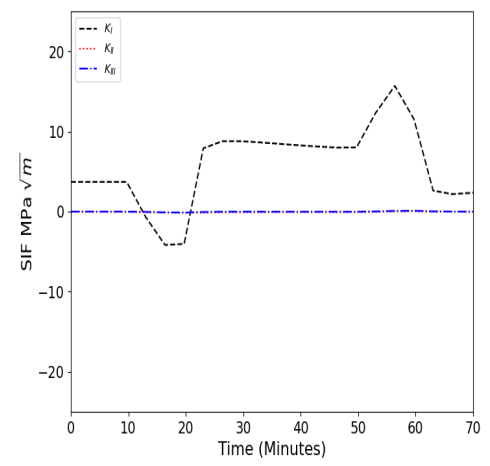


(b)

Figure 5.34: Time-dependent response of  $K_I$ ,  $K_{II}$ , and  $K_{III}$  at year 35 at the intersection of the crack and the (a) header (b) tube. [7]



(a)



(b)

Figure 5.35: Time-dependent response of  $K_I$ ,  $K_{II}$ , and  $K_{III}$  at year 40 at the intersection of the crack and the (a) header (b) tube. [7]

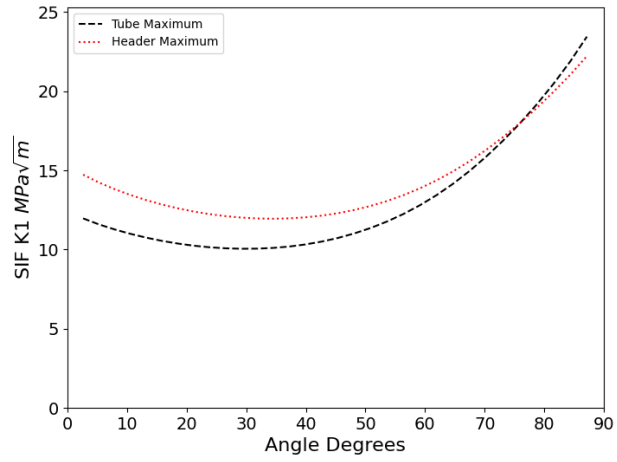


Figure 5.36:  $K_I$  along the crack front for the time representing the highest value for the location intersecting the header and tube for the initial crack. [7]

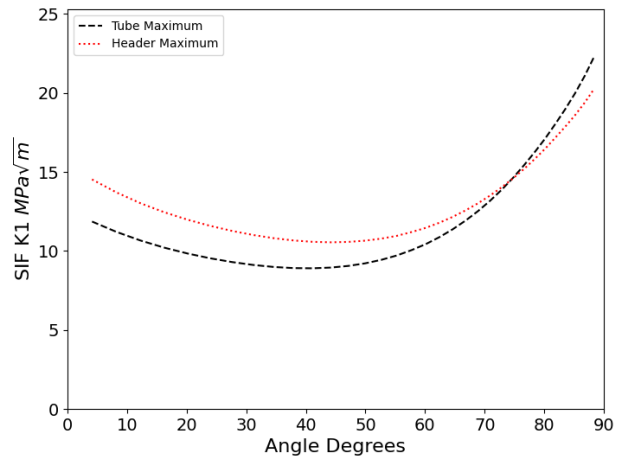


Figure 5.37:  $K_I$  along the crack front for the time representing the highest value for the location intersecting the header and tube for the crack at five years. [7]

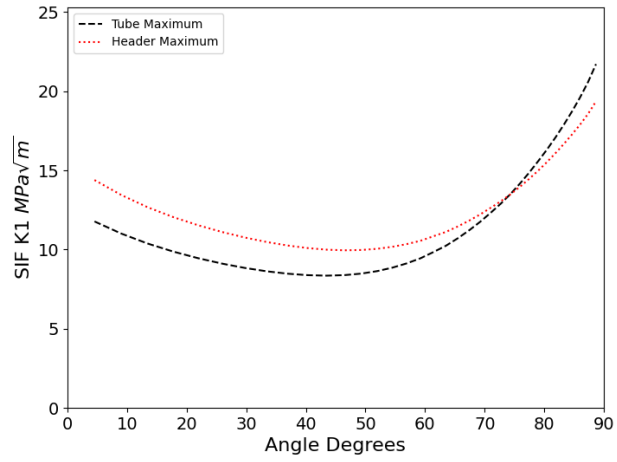


Figure 5.38:  $K_I$  along the crack front for the time representing the highest value for the location intersecting the header and tube for the crack at ten years. [7]

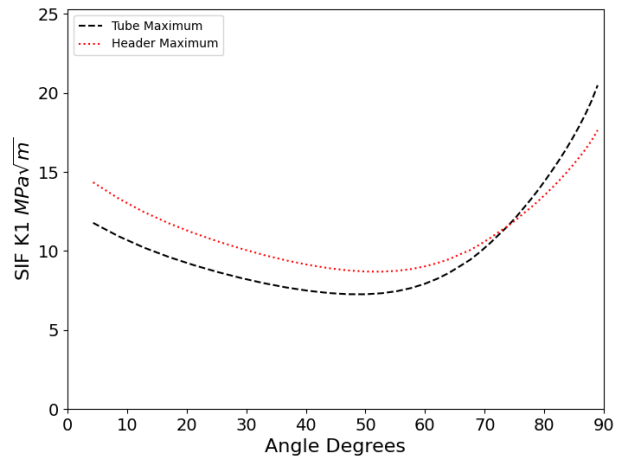


Figure 5.39:  $K_I$  along the crack front for the time representing the highest value for the location intersecting the header and tube for the crack at fifteen years. [7]

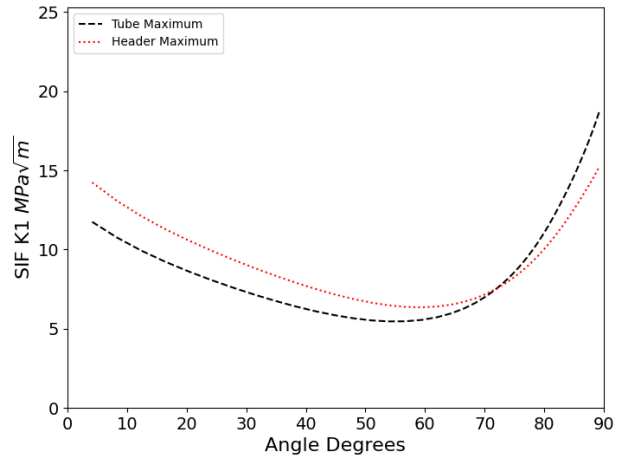


Figure 5.40:  $K_I$  along the crack front for the time representing the highest value for the location intersecting the header and tube for the crack at twenty years. [7]

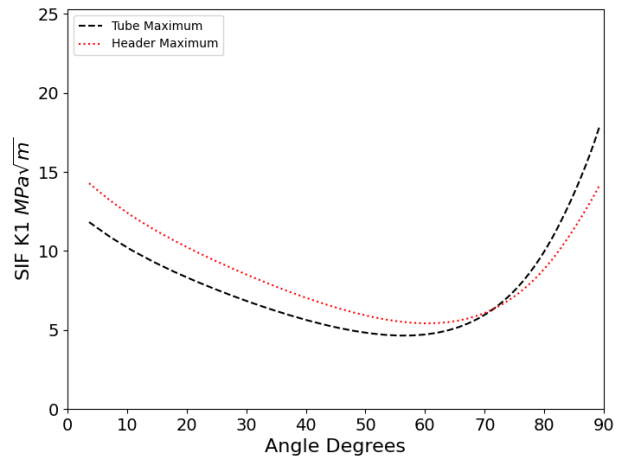


Figure 5.41:  $K_I$  along the crack front for the time representing the highest value for the location intersecting the header and tube for the crack at twenty-five years. [7]

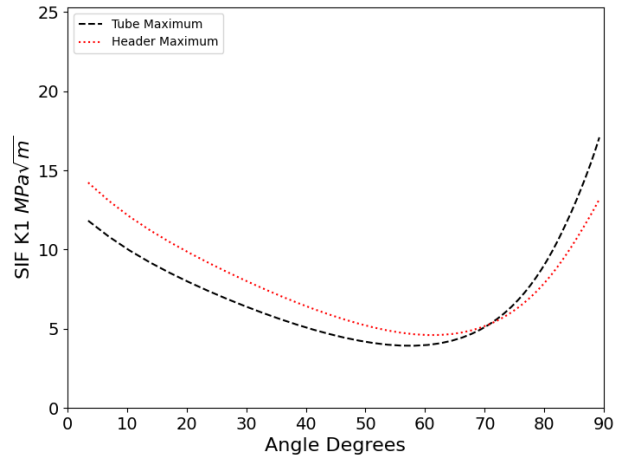


Figure 5.42:  $K_I$  along the crack front for the time representing the highest value for the location intersecting the header and tube for the crack at thirty years. [7]

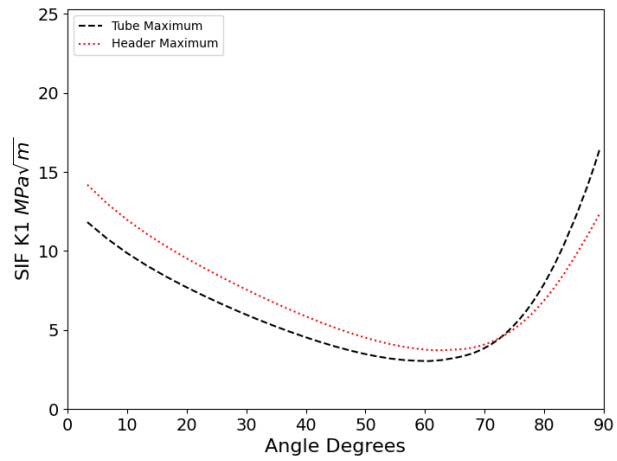


Figure 5.43:  $K_I$  along the crack front for the time representing the highest value for the location intersecting the header and tube for the crack at thirty-five years. [7]

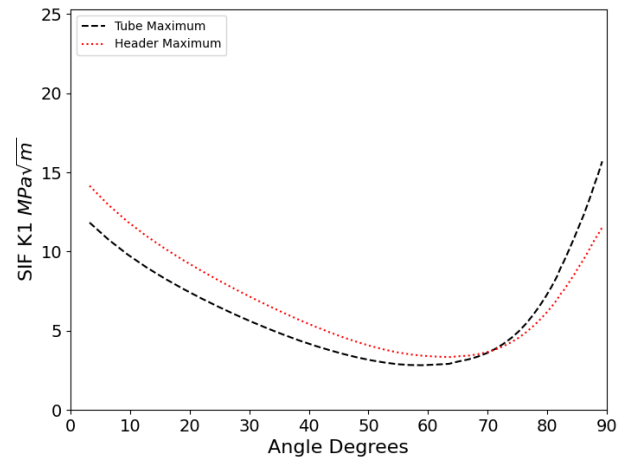


Figure 5.44:  $K_I$  along the crack front for the time representing the highest value for the location intersecting the header and tube for the crack at forty years. [7]

## 5.5 XFEM Fatigue Analysis

### 5.5.1 Background

Conventional finite element methods cannot model discontinuities with standard polynomial functions. Alternative approaches, such as seam cracks, have been established to help capture the behavior. However, these methods require special meshing refinement techniques, leading to a significant dependence on the mesh structure. One method developed to try and alleviate these restrictions is the extended finite element method, XFEM. Unlike other methods, XFEM allows crack growth to occur by enriching the elements and allowing for nodal separation. The method was proposed in the late 1990s by Belytschko and Black concurrently with Moes et al. [169,170]. The method works by adding a heavy side function and near-tip enriched functionality to the continuous displacement of the displacement field shown as,

$$\mathbf{u}(\mathbf{x}, t) = \sum_{I=1}^n N_I(\mathbf{x}) \mathbf{u}_I(t) + \sum_{J=1}^n N_J(\mathbf{x}) H(\mathbf{x}) \mathbf{b}_J(t) + \sum_{K=1}^n N_K(\mathbf{x}) \sum_{L=1}^4 F_L(\mathbf{x}) c_k(t) \quad (5.14)$$

where  $N_I$  are typical finite element interpolation functions,  $n$  is the number of nodes,  $u_I$  is the displacement,  $H$  represents the Heavyside step function,  $\mathbf{b}_J$  represents the additional degrees of freedom from the Heavyside step function,  $F_L$  is a set of enrichment functions relating to the crack tip, and  $c_k$  is the corresponding degrees of freedom. The two additional functions  $H$  and  $F_L$  are used to represent the jump across the fractured elements and describe the asymptotic behavior near the crack tip.

$$F_L(x) = \left[ \sqrt{r} \sin \frac{\theta}{2}, \sqrt{r} \cos \frac{\theta}{2}, \sqrt{r} \sin \theta \sin \frac{\theta}{2}, \sqrt{r} \sin \theta \cos \frac{\theta}{2} \right] \quad (5.15)$$

where  $r$  represents the position from the crack tip, and  $\theta$  represents the angular position with  $\theta = 0$  defined as tangent to the crack tip. While the displacement

function is applied to all nodes in the domain, the Heavyside function enrichment,  $H$ , is only applied to elements that are cut by the crack front. Similarly,  $F_L$  is only applied to elements that are cut by the crack tip. The direction of crack propagation in XFEM is based on the work by Erdogan and Sih, defining the extension direction as the direction of maximum tangential stress [171],

$$\theta = \cos^{-1} \left( \frac{3K_{II}^2 + \sqrt{K_I^4 + 8K_I^2 K_{II}^2}}{K_I^2 + 9K_{II}^2} \right) \quad (5.16)$$

Incorporating the use of Abaqus \*Fatigue significantly improves the ability to evaluate crack growth in materials. In the current work, this technique is combined with LEFM and Paris law to determine the crack growth of an SECC. Similar to the prior work, an effective stress intensity factor is found to quantify the growth that would occur over a given cycle. The effective stress intensity factor found for a given load cycle is defined as,

$$\Delta K_{eff} = \sqrt{A\Delta K_I^2 + B\Delta K_{II}^2 + \frac{C}{1-\nu}\Delta K_{III}^2} \quad (5.17)$$

where A, B, and C are material constants [172]. During the \*Fatigue simulation, the user specifies the minimum and maximum cycles that can be incremented between analyses. This specification is used along with damage tolerances to control the number of cycles between measurements until the total number of cycles has been completed. At the end of each completed cycle increment, Abaqus evaluates the stress state of each node along the crack front, which is used to determine the damage. Abaqus combines the known nodal spacing along with the current damage and Paris law to establish the number of cycles to crack each element along the crack tip. The analysis is set to fail at least one element per increment, where the element with the lowest remaining number of cycles is used until failure is established to establish the number of cycles used to extrapolate forward. Additional elements may also

accumulate damage and be deleted if they are anticipated to fail within the number of cycles incremented forward. The damage at the next increment is evaluated as,

$$D_{N+\Delta N} = D_N + \frac{\frac{da}{dN} \Delta N_{min}}{a_N} \quad (5.18)$$

where  $D_N$  is the damage at the end of the cycle and  $a_N$  is the characteristic length of the element ahead of the crack tip. Using this damage function, elements are removed when  $D = 1$ . In cases where  $0 \leq \Delta D \leq 1$ , the elements can be partially released, and the effective length is updated and incorporated into the subsequent Paris law calculation. The effective length is defined as,

$$\Delta a_n^{eff} = (1 - D) \Delta a_N \quad (5.19)$$

Elements ahead of the crack tip can accumulate partial damage when the following relationship is met.

$$\frac{\text{Log} \Delta N_j - \text{Log} \Delta N_{min}}{\text{Log} \Delta N_{min}} \leq \Delta D_{Ntol} \quad (5.20)$$

where,  $\Delta D_{Ntol}$  is a user specified tolerance. Other work has demonstrated that a  $\Delta D_{Ntol} = 0.25$  provides a balance between accuracy and computational costs [173]. With this criterion, elements ahead of the crack tip that meet the criterion of  $D \geq 0.75$  are partially released.

### 5.5.2 Modeling Approach

Following the work of the automated iterative approach, symmetry is applied to reduce and simplify the response of the header. Similar boundary conditions are applied through internal pressure and symmetry; however, an additional layer is taken along the XY plane. Figure 5.45 illustrates the boundary conditions that were applied to the model.

The initial crack front is applied by cutting the model with a shell surface. The

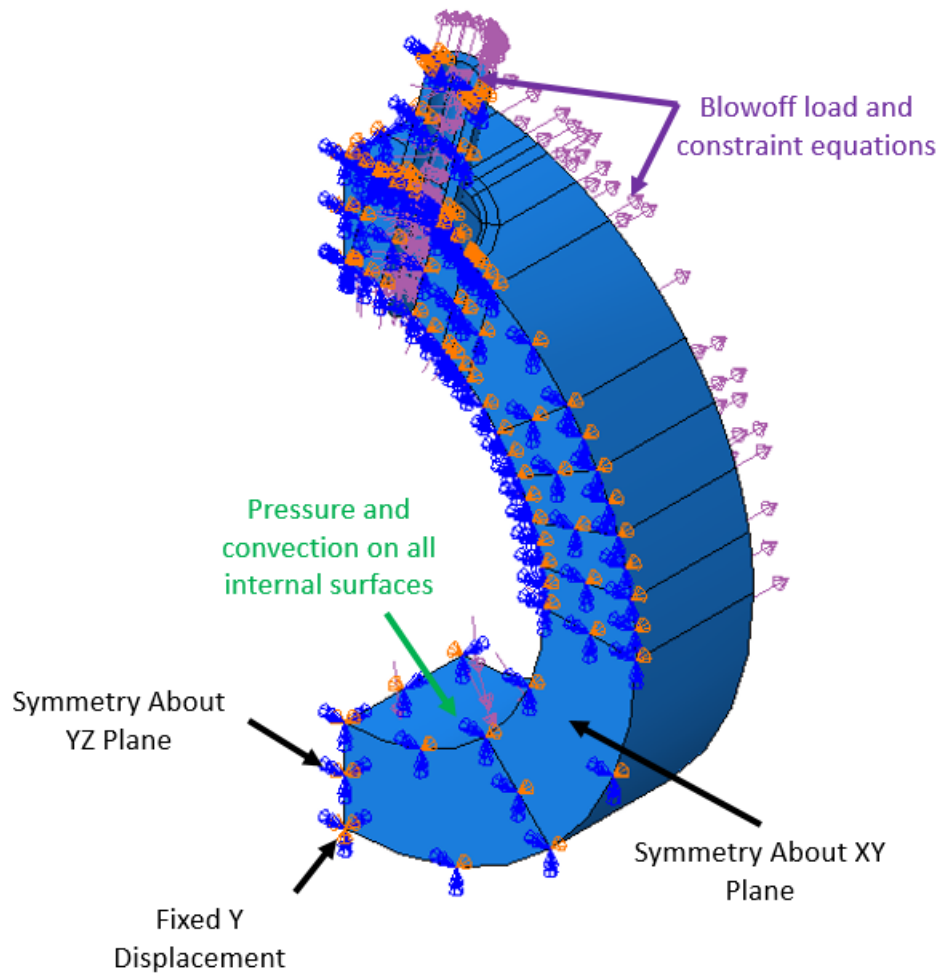


Figure 5.45: Boundary conditions used in XFEM model. [7]

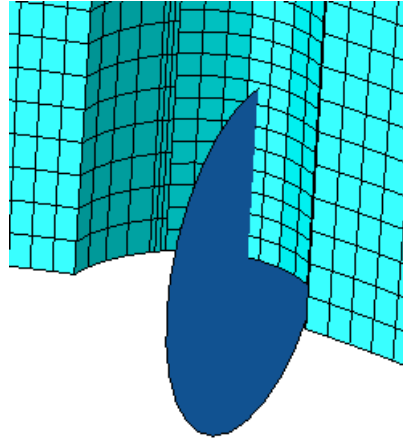


Figure 5.46: Surface used to define initial crack front in XFEM. [7]

initial crack matches the profile postulated in the seam crack analysis, and its application to the XFEM model is shown in Figure 5.46.

Also, a feature unique to XFEM is that it requires a specified enrichment region. Therefore, the sub-model region used in the iterative crack growth process is selected to define the region available for crack propagation. This region will be evaluated using two mesh distributions. The first mesh is selected to balance accuracy and computation costs. The elements within the region have edge lengths of 2 - 3 mm. The total number of elements is 23,084 C3D8R elements. To validate the results, a refined mesh consisting of uniform 1 mm elements is also developed, resulting in 195,724 C3D8R elements is also developed. The mesh of each enriched region is shown in Figure 5.47. However, the refined mesh is only evaluated for the first two years of crack growth due to computational constraints.

To avoid unnecessary computational costs, the mesh outside the region of interest was also modified to incrementally increase the element size to 50 mm. The complete mesh used to evaluate crack growth is shown in Figure 5.48.

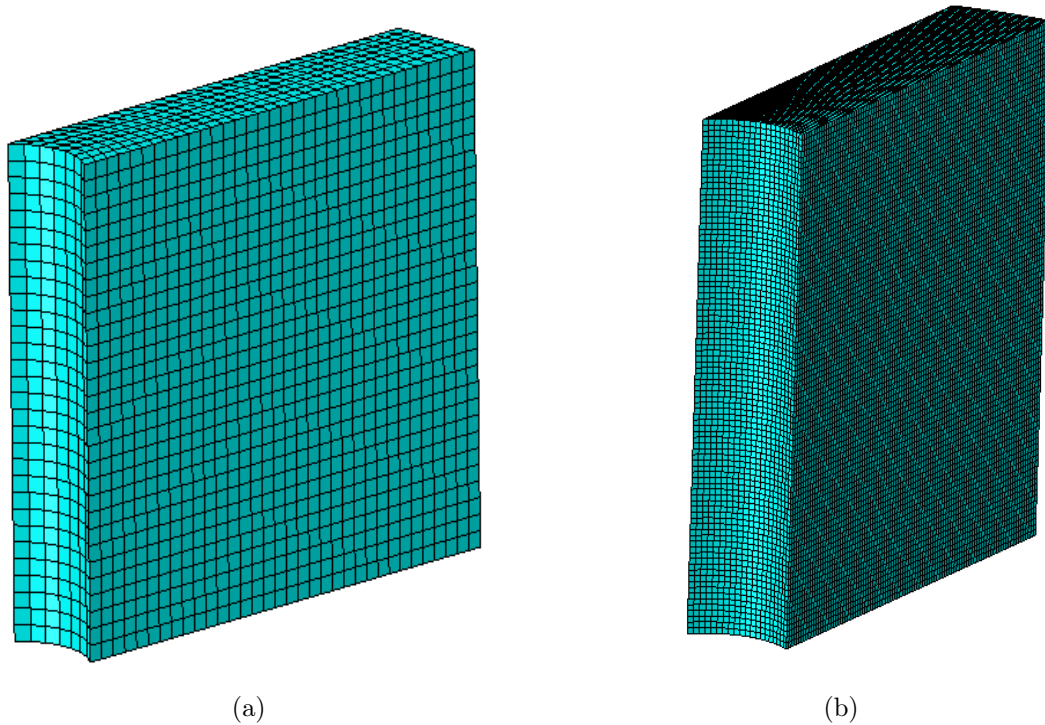


Figure 5.47: Meshed crack sub-model for (a) complete cycle (b) validation. [7]

### 5.5.3 Fatigue Analysis

The present work incorporates XFEM and Abaqus's Fatigue method to propagate an SECC through the wall of an outlet header. The results were evaluated for the influence of mesh size and the number of cycles allowed between iterations. Figure 5.49 illustrates that the mesh is fairly converged at 3 mm. The mesh dependence also appears to be independent of the maximum interval between cycle evaluations. Changing the maximum interval from sixteen months to ten years did not alter the crack growth behavior over time. Therefore, the deletion does not appear to be related to time-frame restrictions. Furthermore, the influence that the mesh size has on the shape of the crack front is also demonstrated. From Fig. 5.49, it is clear that a finer mesh is capable of capturing more of the elliptic shape of the crack front. However, this resolution comes at a significant cost. While the refined mesh consisting of structured 1 mm elements is capable of capturing the gradual growth of the crack

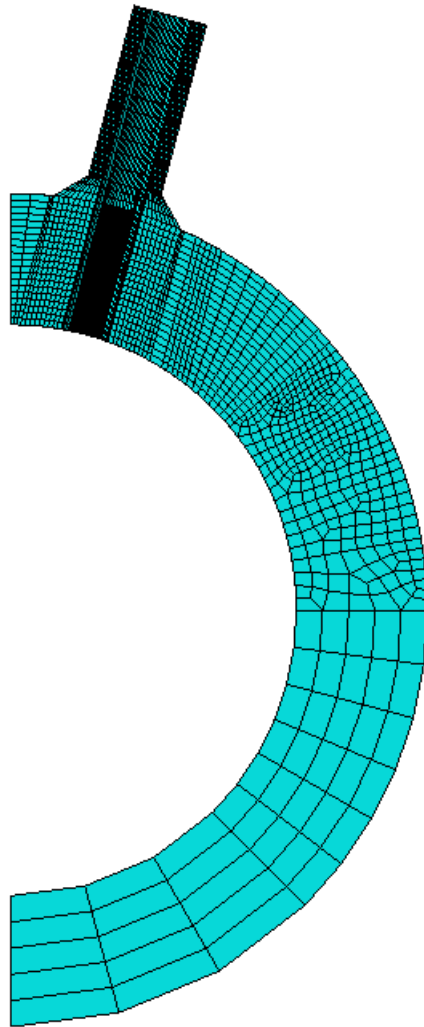


Figure 5.48: 3D meshed header for XFEM with 31,544 C3D8R elements. [7]

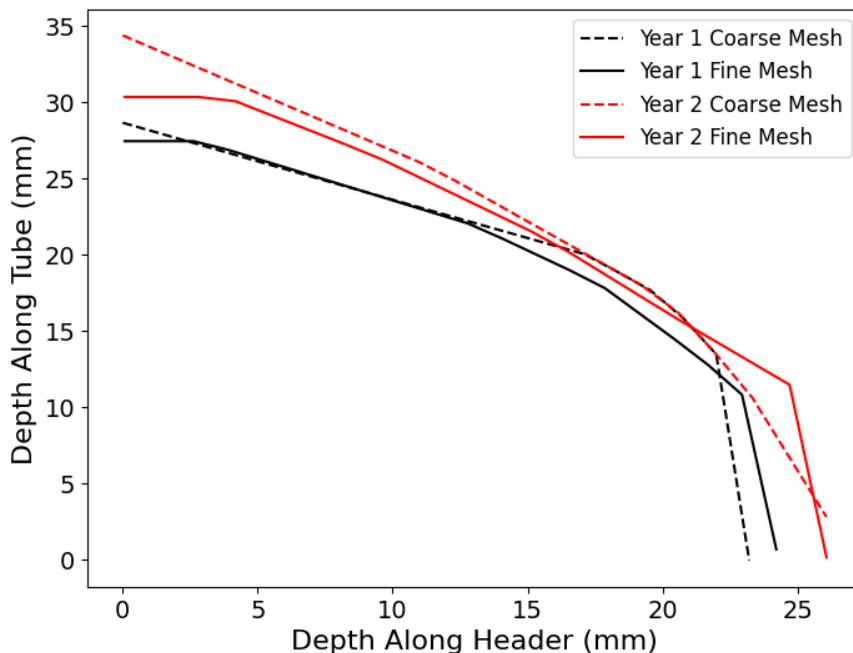


Figure 5.49: Crack front evolution with respect to mesh size. [7]

front, the computational costs are an order of magnitude larger than the coarse mesh of 2 mm x 2mm x 3mm elements. Consequently, the fine mesh was not pursued to evaluate the crack growth behavior in the current work.

Figures 5.50 and 5.51 highlight the significant variation between the rate at which the crack front extends along the tube and header. Additionally, from Figs. 5.50 and 5.51, it is clear that the crack grows along the axial direction. This is evident as there are no deviations in the crack path as the crack front advances.

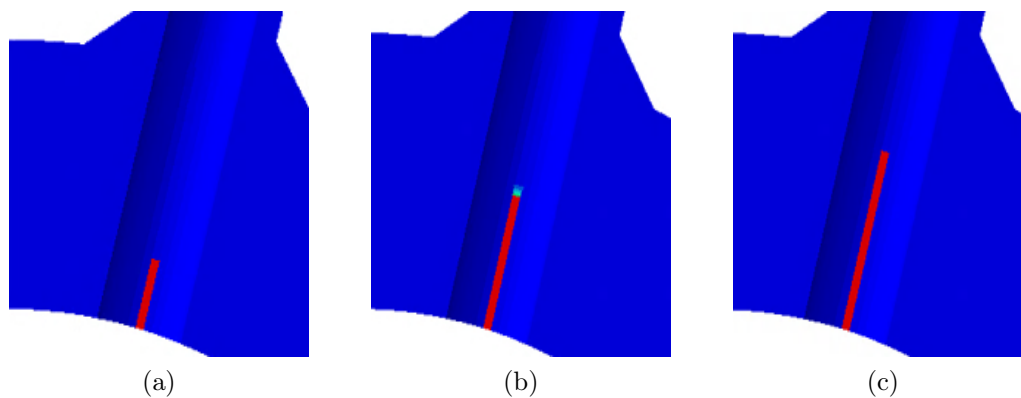


Figure 5.50: Crack propagation along tube at (a) initial (b) 5 years (c) 10 years. [7]

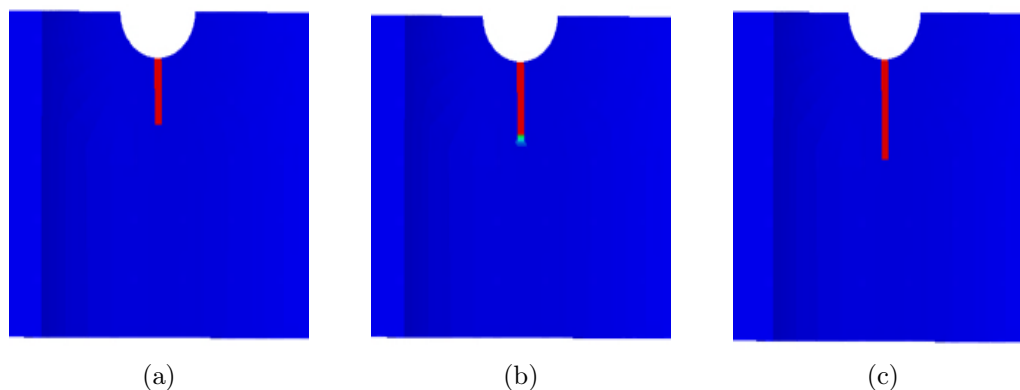


Figure 5.51: Crack propagation along header at (a) initial (b) 5 years (c) 10 years. [7]

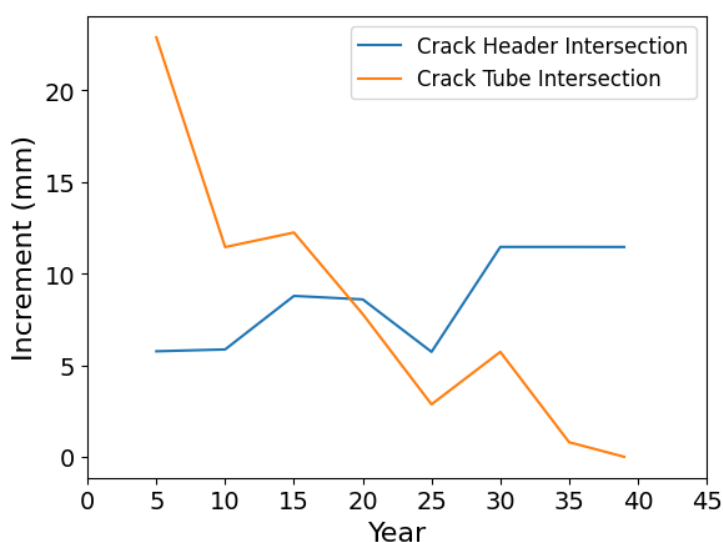


Figure 5.52: Crack growth increments over time. [7]

Moreover, as Fig. 5.52 illustrates, significant crack growth along the header does not occur until the crack growth along the tube is completed and the crack front begins to expand inwards.

Figure 5.53 illustrates the evolution of the crack front with respect to time approximated using the coarser mesh. Figure 5.53 illustrates that the crack front begins by extending through the tube at a rate significantly larger than along the header. The crack would reach the through-thickness of the tube and begin to leak within twenty years. This behavior is maintained until the crack propagates completely along the tube, at which point the crack front begins to advance rapidly along the length of the

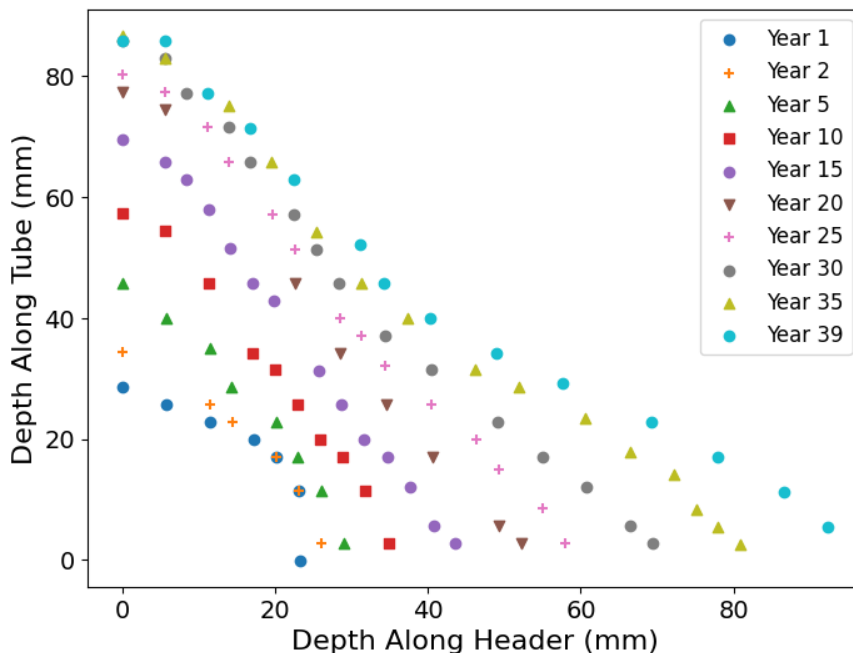


Figure 5.53: Crack front evolution over time. [7]

header.

Figure 5.52 visualizes the significant variation that occurs in the rate the crack extends with time. Although the crack initially extends primarily along the tube, the rate at which the crack extends in this direction continuously decreases with time. This is attributed to the crack moving further from the stress riser of the intersection. Additionally, Fig. 5.52 illustrates that the crack doesn't extend significantly along the header until it has extended nearly through the entire thickness of the tube. The implication is that the stress triaxiality changes after the crack has extended through the bulk of the material in one direction. As a result, the crack growth rate along the header exceeds the tube after fifteen years.

## 5.6 Method Comparison

Distinct differences were found when comparing the XFEM and contour integrals methodologies for performing a LFM fatigue analysis, although some trends remained consistent between the two approaches. Both methods were effective in cap-

turing the shape evolution of the crack front in the early stages of crack growth. The semi-elliptic shape closely matches the observed crack front evolution in XFEM, suggesting that both methods are robust at capturing the variation in stress along the crack front. The initial approximation of the crack front using an elliptic shape is reasonable, as supported by the contour similar to that of the refined mesh trials. These similarities reinforce the validity of using an elliptic shape to represent the early stages of crack growth.

However, as the crack progresses, particularly after extending throughout the header's thickness, the SECC's limitations are evident. The uneven crack growth along the header is not accurately captured by the elliptic simplification, which eliminates the evolution of the crack in this region. As a result, the SECC method does not capture the transition from concave to convex, predicted using the XFEM approach. A key factor contributing to the discrepancies is the underlying methodology incorporated in each technique. For instance, the contour integral methodology only relies on Paris law to establish the crack front and does not require periodic deletion of elements. This contrasts with the XFEM approach, where the movement through at least one element is incorporated into the fatigue process, potentially influencing the accuracy and timing of the crack progression. This highlights the additional validation required for each parameter used in an XFEM fatigue analysis.

Furthermore, while both methods demonstrate a diminishing growth rate along the tube over time, only the XFEM model is capable of capturing the increase in growth rate along the header after a period of time. Consequently, the fundamental behavior of crack growth varies significantly between the methods after a period of fifteen years. This difference highlights a potential area where the use of an elliptic crack will be inadequate in predicting the evolution of the crack front.

In summary, while both XFEM and the contour integral method provide valuable insights into the fatigue life of a component subjected to low cycle fatigue, only XFEM is

capable of accurately capturing the crack evolution. Understanding these differences is critical to selecting the appropriate method for future studies.

## 5.7 Conclusion

The present work presents a novel approach to crack growth automation using LEFM in Abaqus, focusing on semi-elliptic corner cracks. Through the use of the sub-modeling technique, we are able to use this technique on a more complex geometry. The incorporation of the sub-modeling technique demonstrates how the method could be incorporated into more complex geometries. This work is compared to a fatigue analysis that incorporates the use of XFEM and the program's fatigue functionality.

The findings substantiate that crack growth behavior within an SECC is uneven. In response to the distinctive loading within the present work, the SECC presents unique behavior where the growth slows and changes direction with time, presenting initial growth rates of eight to one within the region of the tube with respect to along the header. Within the contour integral method, the crack growth slows drastically to a ratio of two to one as the crack progresses. In contrast, the XFEM methodology captures the increase in the crack growth rate along the header after significant progression has been made along the tube. This variation is a direct consequence of the loading required to initiate crack propagation, underscoring the importance of understanding the load-induced stresses on a project prior to developing a sub-model. Furthermore, the findings illustrate the variation in crack propagation that occurs depending on the methodology selected.

Moreover, throughout the analyses, the  $K_I$  SIF consistently appeared as the most significant component in bolstering crack growth. The results demonstrate that the  $K_I$  has a linear response to the applied pressure and can fluctuate largely depending on the thermal transient. This highlights that focusing on factors that influence the Mode I loading is key to managing crack growth.

However, while evaluating the outcomes of the study, it is crucial to understand the

limitations inherent to each methodology. Specifically, the use of LEFM introduces limitations in the region around the crack tip as it omits the various considerations regarding the crack tip. Furthermore, without plasticity, the influence of the mean stress is not accurately captured in the response of the material. These omissions are noteworthy as they would play a critical role in the propagation of the crack under operational conditions. Moreover, while the methodology of a seam crack can represent the stress field around the crack tip, it falls short in scenarios where pressure could be exerted on exposed crack faces. As a result, the model cannot accurately represent the effects of such pressure on the crack's behavior. Despite these limitations, the framework established in the present work provides a robust foundation for future work. It establishes the necessary steps required to integrate the previously mentioned factors into simulations of crack growth. Therefore, while the current model may not fully capture every dynamic involved in crack propagation, it represents substantial work that can reflect crack growth behavior in materials.

## CHAPTER 6: CONCLUSIONS AND FUTURE WORK

### 6.1 Research Goals

The goal of the projects for this dissertation was to evaluate the performance of an outlet steam header through a series of evaluations. The primary goal of the first section was to develop viable alternatives to a 2.25Cr-1Mo steam header using 9Cr-1Mo-V and IN740H and evaluate them to establish a cost-benefit analysis. In order to achieve this goal, the following objectives were fulfilled:

1. Obtain ASME BPVC specifications and design headers out of P91 and IN740H to meet requirements
2. Analyze the performance of each header for durability against fatigue
3. Establish a representative transient to simplify the performance analysis
4. Analyze the cost-benefit of using each alloy

The primary goal of the second project was to characterize the material response of samples taken from an ex-service header and quantify the impact of service exposure on remaining service life estimates. In order to achieve these goals, the following objectives were fulfilled:

1. Extract material properties from uniaxial test data
2. Evaluate the performance of an outlet header using multiple load scenarios
3. Quantify the response difference that results from prior service exposure

The primary goal of the third project was to establish a method to automate the propagation of a seam crack within Abaqus and compare the results to the built-in

functionality with XFEM. In order to achieve these goals, the following objectives were fulfilled:

1. Analyze the performance of a header to establish a critical location.
2. Develop a sub-model to simplify the re-meshing process.
3. Extract crack growth properties using publicly available data.
4. Implement quasi-static crack growth using developed tools.
5. Develop a comparable model using Abaqus \*Fatigue and XFEM

## 6.2 Conclusions

The first study evaluated how the material selection between P22, P91, and IN740H affects the cost and performance of an outlet header. Three header designs were developed using the procedures outlined in ASME BPVC, and the materials were compared using FEA to examine how they reacted to representative boundary conditions found from in-service use. The study applied multiple transients, one consisting of a ten-day cycle that was evaluated using a rain flow cycle counting method. However, the results demonstrated that only the P22 model demonstrated any sign of wear and, upon further evaluation, was found to be insignificant. This prompted a reevaluation of the materials used in the second study, subsequently establishing a limit case transient. This transient was applied to the three materials, represented with perfect plasticity, to evaluate their response. The results were similar to the initial findings, where only the P22 model accumulated damage. The life expectancy of the P22 model was evaluated using the Ostergren damage model, which resulted in limited service life in response to the limit transient. Therefore, the P22 and P91 materials were selected as the primary options dependent upon future projections. The outcome of this project demonstrated that the most robust material from a technical standpoint does not always translate to the most sensible business decision. However, the study

has some gaps. For instance, the materials were represented as perfectly plastic and therefore neglected any influence that hardening, or softening, would have on the material response over time. Additionally, the material was assumed to be homogeneous throughout, neglecting any manufacturing characteristics such as welds. This was deemed admissible in the present study, given that the location under consideration for the material failure would be outside of the heat-affected zone for this feature. Furthermore, the influence of the operating environment was not considered such that the improved corrosion resistance of some of the alloys was not incorporated.

The second study investigated the effects of service exposure on the P22 header to understand how prolonged use influences the usable service life estimates. A material model was developed for the service-exposed material using the Chaboche NLKH model, which was established using test data. The material model was compared to a model representative of virgin material and evaluated in response to a ten-day representative transient. This data served as the basis for three representative transients, representing a startup and shutdown procedure, a common thermal transient, and a limit case thermal transient. The models were evaluated for remaining service life using the critical plane approach adapted from the first study. The results demonstrate that the service life from the limit case transient correlates well with observed findings. Additionally, the models highlighted the reduced strength and earlier yielding of the service-exposed material. This weakened strength made the service-exposed material susceptible to damage from transients that would not harm the virgin material. This was exemplified by a 75% reduction in cycles to failure with respect to the limit case transient. However, it's important to acknowledge the study's limitations. For instance, the analysis did not account for time-dependent effects, environmental factors that could lead to corrosion, or the impact of manufacturing details like welds on the material's performance. These are critical areas that could significantly influence the accuracy of the predictions and are excellent choices

for future investigations. In conclusion, this research adds valuable information to the body of knowledge regarding the impact of service exposure on the P22 header. Demonstrating the necessity of including service exposure considerations in material durability analyses helps provide a foundation for more accurate predictions of service life and the development of strategies to mitigate premature failure. Future research should aim to fill the gaps identified in this study, particularly by incorporating the effects of time, environmental conditions, and manufacturing processes. The project's third phase developed an innovative automation technique for iterative crack growth in the corner of an outlet header. This approach incorporates Abaqus seam crack capability in combination with the quarter-point technique to accurately represent the stress field resulting from the crack. This methodology is based on linear elastic fracture mechanics principles to evaluate static cracks within Abaqus iteratively. A Python code was specifically developed to integrate Abaqus seam crack capability with Paris Law for linear elastic crack growth, allowing the prediction of crack evolution over a number of cycles. Through the application of thermal-mechanical loading, the automated crack growth model demonstrated its capacity to iteratively update the crack front. This process incorporated automatic post-processing and re-meshing techniques, allowing the crack front to grow unevenly. The present work analyzed the odb files to establish a representative SIF range, which was subsequently used to extrapolate the progression of the crack over five-year intervals. This methodology was compared to the fatigue response of the crack established using Abaqus XFEM functionality. The results demonstrate that the crack growth was largely influenced by the stress field around the nozzle junction, resulting in the deceleration of the crack propagation as it moved further from the primary stress riser. However, when evaluating the results, it is critical to acknowledge certain limitations. It should be noted that the reliance on LEFM means the model does not account for plastic deformation at the crack tip, nor does it consider the mitigating effects of mean stress or

time-dependent changes in material properties. These are significant factors that can influence crack behavior in real-world conditions. Moreover, while the representation of the crack as a seam crack is capable of capturing the stress singularity around the crack tip, it does not provide the ability to apply pressure on exposed surfaces. Therefore, any influence that may occur as a result of additional pressure along the internal crack surfaces is not captured in the response of the crack. Yet, despite these gaps, the developed framework lays a solid foundation for future enhancements, offering a pathway for incorporating these complex behaviors into crack growth simulations. In conclusion, this research demonstrates a significant improvement in the predictive modeling of crack growth through the use of seam cracks. By demonstrating the capability of simulating the crack progression, this study lays the groundwork for future enhancements. The continued progression of development of this procedure will improve the ability to predict crack growth and, ultimately, failures within outlet headers.

### 6.3 Future Work

The present work evaluated the response to an existing outlet header. However, exploring more complex geometries presents a promising avenue for future research, expanding beyond the simplified unit required for the present work. This could allow for factors such as tube spacing and material inhomogeneities to be considered and provide a more robust evaluation. For instance, the present work did not account for welds or environmental factors. Discontinuities such as welds are a common source of failure and can play a significant role in limiting the life of a component. One avenue worth exploring would be to evaluate the influence of the weld region on crack growth following the premise of the third project. Possible examples could be to see if the weld interaction develops and propagates cracks in a similar time frame to the crack within the header. This phenomenon could be compounded by incorporating the evolution of pre-existing cracks within the header and the tube weld region. Work in this region

could incorporate the use of XFEM, taking steps to determine how the cracks interact and if they lead to a reduced lifetime. This expansion could also allow for factors such as environmental factors to be incorporated. The present work demonstrated that the material behavior changes with prior service exposure; however, similar changes occur along the crack front. Examples include the degradation of the material through oxide notching as well as the build-up of an oxide scale within the crack surface. This scale has several implications, such as reducing the effective crack opening and leading to compressive forces during unloading. Additionally, the surface of the oxide has distinct fracture properties that can lead to fracture at levels below the bulk material. Furthermore, applying material plasticity to the crack front presents several avenues for future research. This not only presents itself through the use of damage mechanics but could also be incorporated to address current shortcomings in the Abaqus software. For instance, the material's resistance to closure is not currently incorporated during unloading. This could neglect a significant amount of force in cases where the crack front is irregular, and surface friction would resist closure. Likewise, incorporating plasticity into the current work would allow crack closure pressure effects to be captured.

In a similar vein, addressing the absence of time-dependent properties in material models is another critical area for future investigations. Incorporating time-dependent properties through additional specimen testing or applying the models to fatigue scenarios could offer a deeper understanding of the impact of material degradation over time impact on structural longevity. For instance, without the incorporation of time-dependent effects, the results of the first project suggest similar performance between P91 and IN740H alloy. However, it is possible that incorporating factors such as creep into the simulation would result in decreased performance of the P91 material. Similar degradation would also likely be found in the second project if the test specimens had been evaluated for time-dependent effects. Many have documented

that the creep resistance of P22 decreases through service exposure, such that the inclusion of time-dependent effects would have likely exacerbated the variation of material lifetimes. Therefore, incorporating the influence of time-dependent creep could lead to more robust cost and remaining life estimations.

Nonetheless, incorporating the influence of time-dependent effects at elevated temperatures in combination with fatigue presents several challenges. The underlying deformation mechanisms begin to interact, and capturing their behavior in a computational model is uniquely complex. For instance, a fatigue cycle can eliminate or reset some of the dislocations that have occurred in a tensile leg of a fatigue cycle with a tensile hold. During the hold, the creep rate may have stabilized, progressing into the second stage of creep. However, during a fatigue compressive cycle, the dislocation distribution changes such that the redevelopment of primary creep would occur on the following tensile leg, accelerating the fatigue response. Likewise, compressive creep can alter the fatigue response of a crack. For instance, if a tensile overload occurs, a plastic zone will form around the crack front. It follows that the crack effectively closes when the plastic zone compresses during unloading. This generally has a beneficial influence on fatigue life as the pressure from the over-closure must be overcome before the crack can continue to propagate. However, in instances where the compressive hold is at an elevated temperature, compressive creep strains can effectively reduce the pressure required to reopen the crack. Therefore, future work could also incorporate a rain flow cycle counting method to partition individual creep-fatigue cycles and improve the accuracy of remaining life estimates. Several models have been developed to combine the effects of creep and fatigue, such as the two-layer viscoplasticity model within Abaqus. While this model demonstrates an ability to reflect test data, the underlying mechanism of partitioning forces is ultimately flawed. Therefore, the development of a model to address the interaction between dislocation movement in creep fatigue and incorporating the model presents

a significant challenge with meaningful implications.

Continued developments in this research's computational tools and methodologies also hold significant potential. For instance, while the SECC crack propagation methodology proved to be inaccurate and ultimately a poor choice for predicting crack growth, the foundation of the code presents the possibility of developing an algorithmic re-meshing tool. Throughout the process of propagating the crack, the code incorporates developing geometry and partitions, seeding individual edges, setting mesh techniques, and updating each based on interpreted results. With some refinement, it is possible that the code could be adapted to evaluate the results of a mesh quality check to then adjust or create partitions as needed. Depending on one's ambitions, the code could reach a point where the input geometry could be drastically more complex than the simplified headers used throughout the present work. If done correctly, this model could revolutionize the simulation process by introducing adaptive meshing refinement that is not currently native to Abaqus.

In summary, these proposed directions for future research aim to address the current study's limitations and push the boundaries of existing techniques. By combining advanced computational models, innovative methodologies, and a deeper exploration of material properties, these efforts could significantly contribute to developing safer, longer-lasting designs.

## REFERENCES

- [1] EPRI, *Grade 22 Low Alloy Steel Handbook: 2-1/4Cr-1Mo, 10CrMo9 10,622, STPA24*. Palo Alto, CA: 2005. 1012840.
- [2] American Society of Mechanical Engineers, *ASME Boiler and Pressure Vessel Code, Section II:Part D Properties*, 2015. New York, NY.
- [3] D. Bhattacharyya, M. Drew, S. Humphries, and W. Payten, “Characterization of deformation structures in p-22 cr–mo steel through electron backscatter diffraction and transmission electron microscopy,” *Journal of Materials Science*, vol. 58, no. 27, pp. 11286–11309, 2023.
- [4] C. Soyarslan, B. Gülçimen, S. Bargmann, and P. Hähner, “Modeling of fracture in small punch tests for small-and large-scale yielding conditions at various temperatures,” *International journal of mechanical sciences*, vol. 106, pp. 266–285, 2016.
- [5] Special Metals Corporation, “INCONEL® ALLOY 740H Data Sheet.” Available online, 2023. Chemical Composition, Applications, Metallurgy Microstructure, etc.
- [6] M. Zimnoch, I. Perrin, and A. Tabarraei, “Evaluation of the effects of service exposure on the cyclic stress strain response of a 2.25cr-1mo steam header,” *J. Pressure Vessel Technology*, Manuscript submitted for publication.
- [7] M. Zimnoch and A. Tabarraei, “Comparison of crack propagation methods in a 2.25cr-1mo outlet header,” Manuscript submitted for publication.
- [8] A. Shibli and F. Starr, “Some aspects of plant and research experience in the use of new high strength martensitic steel p91,” *International journal of pressure vessels and piping*, vol. 84, no. 1-2, pp. 114–122, 2007.
- [9] J. N. Phillips, G. S. Booras, and J. Marasigan, “The history of integrated gasification combined-cycle power plants,” *Turbo Expo: Power for Land, Sea, and Air*, vol. 50831, p. V003T03A007, 2017.
- [10] D. L. Chase, “Combined-cycle development evolution and future,” *GE Power Systems, GER-4206*, pp. 5–6, 2001.
- [11] R. Swindeman, M. Santella, P. Maziasz, B. Roberts, and K. Coleman, “Issues in replacing cr–mo steels and stainless steels with 9cr–1mo–v steel,” *International Journal of Pressure Vessels and Piping*, vol. 81, no. 6, pp. 507–512, 2004.
- [12] N. Cheruvu, “Degradation of mechanical properties of cr-mo-v and 2.25 cr-1mo steel components after long-term service at elevated temperatures,” *Metallurgical Transactions A*, vol. 20, pp. 87–97, 1989.

- [13] H. K. Yadav, L. Maddi, A. Ballal, D. Peshwe, and V. Rao, "Structural and mechanical characterization of service exposed 2.25 cr-1mo steel," *Transactions of the Indian Institute of Metals*, vol. 70, pp. 1091–1096, 2017.
- [14] R. James, S. Hesler, and J. Bistline, "Fossil fleet transition with fuel changes and large scale variable renewable integration," tech. rep., Electric Power Research Institute, Palo Alto, CA (United States), 2015.
- [15] S. Lefton, N. Kumar, D. Hilleman, and D. Agan, "The increased cost of cycling operations at combined cycle power plants," *Intertek APTECH*, November, 2012.
- [16] A. Ahmadi, M. shayegani Akmal, A. Pasha, and S. Yareie, "Failure analysis of cracked 2.25 cr-1.0 mo steel tubes of an oil refinery boiler," *Engineering Failure Analysis*, vol. 110, p. 104435, 2020.
- [17] H. Roy, D. Ghosh, P. Roy, A. Saha, A. Shukla, and J. Basu, "Failure investigation of platen superheater outlet header," *Journal for Manufacturing Science and Production*, vol. 10, no. 1, pp. 17–24, 2009.
- [18] R. Skelton and K. Challenger, "Fatigue crack growth in 214cr- 1mo steel at 525Å° ci: Effects of environment and dwell," *Materials Science and Engineering*, vol. 65, no. 2, pp. 271–281, 1984.
- [19] A. Almazrouee, R. S. Raman, K. Al-Fadhalah, M. Alardhi, and M. Alenezi, "Role of oxide notching and degraded alloy microstructure in remarkably premature failure of steam generator tubes," *Engineering Failure Analysis*, vol. 18, no. 8, pp. 2288–2295, 2011.
- [20] B. Smith, C. Erskine, R. Hartranft, and A. Marder, "High-temperature corrosion-fatigue (circumferential) cracking life evaluation procedure for low alloy (cr-mo) boiler tube steels," *Materials characterization*, vol. 34, no. 2, pp. 81–86, 1995.
- [21] Y. A. Radin and T. Kontorovich, "An analysis of the effect of protective films on the inside surface of headers and steam pipelines in combined-cycle power plants on their thermally stressed state," *Thermal Engineering*, vol. 65, pp. 698–701, 2018.
- [22] B. Smith and A. Marder, "A metallurgical mechanism for corrosion-fatigue (circumferential) crack initiation and propagation in crîž mo boiler tube steels," *Materials characterization*, vol. 33, no. 1, pp. 45–50, 1994.
- [23] B. Fournier, M. Sauzay, C. Caës, M. Noblecourt, M. Mottot, A. Bougault, V. Rabeau, and A. Pineau, "Creep-fatigue-oxidation interactions in a 9cr-1mo martensitic steel. part i: Effect of tensile holding period on fatigue lifetime," *International Journal of Fatigue*, vol. 30, no. 4, pp. 649–662, 2008.

- [24] F. Abe, M. Tabuchi, H. Semba, M. Igarashi, M. Yoshizawa, N. Komai, and A. Fujita, "Feasibility of marbn steel for application to thick section boiler components in usc power plant at 650 c," in *Proceedings of the 5th international conference on advances in materials technology for fossil power plants*, pp. 92–106, 2007.
- [25] M. Li, A. Benaarbia, A. Morris, and W. Sun, "Assessment of potential service-life performance for marbn steel power plant header under flexible thermomechanical operations," *International Journal of Fatigue*, vol. 135, p. 105565, 2020.
- [26] P. von Hartrott, S. Holmström, S. Caminada, and S. Pillot, "Life-time prediction for advanced low alloy steel p23," *Materials Science and Engineering: A*, vol. 510, pp. 175–179, 2009.
- [27] K.-F. Nilsson, F. Dolci, T. Seldis, S. Ripplinger, A. Grah, and I. Simonovski, "Assessment of thermal fatigue life for 316l and p91 pipe components at elevated temperatures," *Engineering Fracture Mechanics*, vol. 168, pp. 73–91, 2016.
- [28] M. Tan, N. Celard, K. Nikbin, and G. Webster, "Comparison of creep crack initiation and growth in four steels tested in hida," *International journal of pressure vessels and piping*, vol. 78, no. 11-12, pp. 737–747, 2001.
- [29] J.-B. Vogt, S. Argillier, J. Leon, J.-P. Massoud, and V. Prunier, "Mechanisms of cyclic plasticity of a ferrite–bainite 241cr1mo steel after long-term service at high temperature," *ISIJ international*, vol. 39, no. 11, pp. 1198–1203, 1999.
- [30] H. Shimazu, S. Konosu, Y. Tanaka, M. Yuga, H. Yamamoto, and N. Ohtsuka, "Combined effect of temper and hydrogen embrittlement on threshold for hydrogen-induced fracture in cr-mo steels," *Journal of Pressure Vessel Technology*, vol. 135, no. 2, p. 021406, 2013.
- [31] D. Ahn, P. Sofronis, and R. Dodds, "Modeling of hydrogen-assisted ductile crack propagation in metals and alloys," *International Journal of Fracture*, vol. 145, pp. 135–157, 2007.
- [32] M. T. Whittaker and B. Wilshire, "Advanced procedures for long-term creep data prediction for 2.25 chromium steels," *Metallurgical and Materials Transactions A*, vol. 44, pp. 136–153, 2013.
- [33] T. Ohba, K. Kimura, F. Abe, K. Yagi, and I. Nonaka, "Degradation in tensile and creep properties of 2.25 cr–1mo steel by long term service in plant," *Materials science and technology*, vol. 21, no. 4, pp. 476–482, 2005.
- [34] M. Okazaki, M. Hashimoto, and T. Mochizuki, "Creep-fatigue strength of long-term post-service 2· 1/4 cr-1· mo steel and remaining life estimation," 1991.
- [35] R. Sahoo, B. Jha, T. Sahoo, and S. Mantry, "Effect of microstructural degradation on solid particle erosion behavior of 2.25 cr-1mo steel," *Tribology Transactions*, vol. 57, no. 4, pp. 679–689, 2014.

- [36] C. G. Shastri, M. Mathew, P. Sreenivasan, K. Rao, G. Bandyopadhyay, and S. Mannan, "On the creep, tensile and impact properties of a 120, 000 h service-exposed 2. 25 cr-1 mo steel," *Transactions of the Indian Institute of Metals*, vol. 58, no. 2, pp. 281–285, 2005.
- [37] V. T. Paul, S. Saroja, and M. Vijayalakshmi, "Microstructural stability of modified 9cr–1mo steel during long term exposures at elevated temperatures," *Journal of Nuclear Materials*, vol. 378, no. 3, pp. 273–281, 2008.
- [38] F. Benjamin, S. Maxime, R. Alexandra, B. Françoise, and P. André, "Microstructural evolutions and cyclic softening of 9% cr martensitic steels," *Journal of Nuclear Materials*, vol. 386, pp. 71–74, 2009.
- [39] B. Fournier, M. Sauzay, C. Caës, M. Noblecourt, M. Mottot, L. Allais, I. Tournie, and A. Pineau, "Creep-fatigue interactions in a 9 pct cr-1 pct mo martensitic steel: Part i. mechanical test results," *Metallurgical and materials transactions A*, vol. 40, pp. 321–329, 2009.
- [40] B. Fournier, M. Sauzay, A. Renault-Laborne, F. Barcelo, and A. Pineau, "Microstructural evolutions and cyclic softening of 9% cr martensitic steels," *Journal of Nuclear Materials*, vol. 386, pp. 71–74, 2009.
- [41] A. Saad, W. Sun, T. Hyde, and D. Tanner, "Cyclic softening behaviour of a p91 steel under low cycle fatigue at high temperature," *Procedia Engineering*, vol. 10, pp. 1103–1108, 2011.
- [42] N. Moslemi, M. Gol Zardian, A. Ayob, N. Redzuan, and S. Rhee, "Evaluation of sensitivity and calibration of the chaboche kinematic hardening model parameters for numerical ratcheting simulation," *Applied Sciences*, vol. 9, no. 12, p. 2578, 2019.
- [43] R. Ragab, J. Parker, M. Li, T. Liu, and W. Sun, "Modelling of a grade 91 power plant pressurised header weldment under ultra super-critical creep conditions," *International Journal of Pressure Vessels and Piping*, vol. 192, p. 104389, 2021.
- [44] I. Nonaka, T. Ito, S. Ohtsuki, and Y. Takagi, "Performance of repair welds on aged 2.25 cr–1mo boiler header welds," *International journal of pressure vessels and piping*, vol. 78, no. 11-12, pp. 807–811, 2001.
- [45] B. Dogan, U. Ceyhan, and B. Petrovski, "High temperature crack initiation and defect assessment of p22 steel weldments using time dependent failure assessment method," *Engineering fracture mechanics*, vol. 74, no. 6, pp. 839–852, 2007.
- [46] A. Sedmak, M. Swei, and B. Petrovski, "Creep crack growth properties of p91 and p22 welded joints," *Fatigue & Fracture of Engineering Materials & Structures*, vol. 40, no. 8, pp. 1267–1275, 2017.

- [47] J. Zhou, R. A. Barrett, and S. B. Leen, “A physically-based method for predicting high temperature fatigue crack initiation in p91 welded steel,” *International Journal of Fatigue*, vol. 153, p. 106480, 2021.
- [48] M. Li, R. A. Barrett, S. Scully, N. M. Harrison, S. B. Leen, and P. E. O’Donoghue, “Cyclic plasticity of welded p91 material for simple and complex power plant connections,” *International Journal of Fatigue*, vol. 87, pp. 391–404, 2016.
- [49] A. Elrefaey, Y. Javadi, J. A. Francis, M. D. Callaghan, and A. J. Leonard, “Evolution of microstructure and toughness in 2.25 cr-1mo steel welds,” *International Journal of Pressure Vessels and Piping*, vol. 165, pp. 20–28, 2018.
- [50] Y. Wang, W. Zhang, Y. Wang, J. Siefert, A. Bridges, S. Kung, and Z. Feng, “Remaining lifetime assessment of 141,000-hour service-aged forge 91-pipe 91 steel header welds with novel in-situ digital image correlation,” *Materials & Design*, p. 111102, 2022.
- [51] P. Segle, L. A. Samuelson, P. Andersson, and F. Moberg, “Implementation of constitutive equations for creep damage mechanics into the abaqus finite element code-some practical cases in high temperature component design and life assessment,” tech. rep., SAQ Inspection Ltd., 1996.
- [52] X. F. Zheng, Y. J. Jiang, Y. T. Feng, Q. Wang, X. G. Niu, X. J. Hao, W. B. Li, Z. W. Li, X. X. Xu, and W. P. Li, “Failure analysis on tube socket crack of supercritical boiler water wall header,” in *Applied Mechanics and Materials*, vol. 204, pp. 4616–4619, Trans Tech Publ, 2012.
- [53] S. Holmström, J. Rantala, A. Laukkanen, K. Kolari, H. Keinänen, and O. Lehtinen, “Modeling and verification of creep strain and exhaustion in a welded steam mixer,” *Journal of pressure vessel technology*, vol. 131, no. 6, 2009.
- [54] R. Viswanathan, *Damage mechanisms and life assessment of high-temperature components*. ASM international, 1989.
- [55] R. Mittal and B. S. Sidhu, “Oil-ash corrosion resistance of dissimilar t22/t91 welded joint of super heater tubes,” *Journal of Materials Engineering and Performance*, vol. 24, no. 2, pp. 670–682, 2015.
- [56] M. Sujata, R. Bhuvana, M. Madan, M. Venkataswamy, and S. Bhaumik, “Hydrogen-assisted cracking in boiler steam drums,” *Journal of failure analysis and prevention*, vol. 9, no. 3, pp. 213–221, 2009.
- [57] K. Laha, K. Chandravathi, K. B. S. Rao, S. Mannan, and D. Sastry, “An assessment of creep deformation and fracture behavior of 2.25 cr-1mo similar and dissimilar weld joints,” *Metallurgical and Materials Transactions A*, vol. 32, pp. 115–124, 2001.

- [58] Y. Zhao, P. Fan, C. Wang, M. Liu, D. Chong, and J. Yan, "Fatigue lifetime assessment on a high-pressure heater in supercritical coal-fired power plants during transient processes of operational flexibility regulation," *Applied Thermal Engineering*, vol. 156, pp. 196–208, 2019.
- [59] R. Patil and S. Anand, "Thermo-structural fatigue analysis of shell and tube type heat exchanger," *International Journal of Pressure Vessels and Piping*, vol. 155, pp. 35–42, 2017.
- [60] J. Okrajni and M. Twardawa, "Description of the thermo-mechanical fatigue of thick-walled pressure vessels," *Procedia materials science*, vol. 3, pp. 918–923, 2014.
- [61] J. Okrajni, "Thermo-mechanical fatigue conditions of power plant components," *Journal of Achievements in Materials and Manufacturing Engineering*, vol. 33, no. 1, pp. 53–61, 2009.
- [62] O. Kwon, M. Myers, A. Karstensen, and D. Knowles, "The effect of the steam temperature fluctuations during steady state operation on the remnant life of the superheater header," *International journal of pressure vessels and piping*, vol. 83, no. 5, pp. 349–358, 2006.
- [63] X. Chen, X. Chen, D. Yu, and B. Gao, "Recent progresses in experimental investigation and finite element analysis of ratcheting in pressurized piping," *International Journal of Pressure Vessels and Piping*, vol. 101, pp. 113–142, 2013.
- [64] Z. Ma, X. Wang, H. Chen, F.-Z. Xuan, and Y. Liu, "A unified direct method for ratchet and fatigue analysis of structures subjected to arbitrary cyclic thermal-mechanical load histories," *International Journal of Mechanical Sciences*, vol. 194, p. 106190, 2021.
- [65] R. V. Selvan, P. Sathiya, K. Devakumaran, and G. Ravichandran, "The effect of ligament size on the thermal fatigue life of 9cr1mo steel boiler header under cold, warm and hot starts," *Engineering Failure Analysis*, vol. 97, pp. 727–739, 2019.
- [66] J. Rouse, P. Zacharzewski, C. Hyde, R. Jefferson-Loveday, A. Morris, and S. Kyaw, "A case study investigation into the effects of spatially dependent convection coefficients on the fatigue response of a power plant header component," *International Journal of Fatigue*, vol. 113, pp. 137–148, 2018.
- [67] T. P. Farragher, S. Scully, N. OâDowd, and S. Leen, "Development of life assessment procedures for power plant headers operated under flexible loading scenarios," *International Journal of Fatigue*, vol. 49, pp. 50–61, 2013.
- [68] M. Azamfar and M. Moshrefifar, "Moshrefifar and azamfar method, a new cycle counting method for evaluating fatigue life," *International journal of fatigue*, vol. 69, pp. 2–15, 2014.

- [69] Y. Cheng and J. Broz, "Cycle counting methods for fatigue analysis with random load histories," 1986.
- [70] S.-P. Zhu and H.-Z. Huang, "A generalized frequency separation–strain energy damage function model for low cycle fatigue–creep life prediction," *Fatigue & Fracture of Engineering Materials & Structures*, vol. 33, no. 4, pp. 227–237, 2010.
- [71] X.-W. Wang, D.-G. Shang, Y.-J. Sun, and X.-D. Liu, "Algorithms for multiaxial cycle counting method and fatigue life prediction based on the weight function critical plane under random loading," *International Journal of Damage Mechanics*, vol. 28, no. 9, pp. 1367–1392, 2019.
- [72] S. E. Moussavi Torshizi and A. Jahangiri, "Analysis of fatigue-creep crack growth in the superheater header of a power plant boilers and estimation of its remaining lifetime," *Journal of Failure Analysis and Prevention*, vol. 18, no. 1, pp. 189–198, 2018.
- [73] J.-G. Gong, F. Liu, and F.-Z. Xuan, "On fatigue design curves for 2.25 cr-1mo-v steel reactors at elevated temperature in code case 2605," *Journal of Pressure Vessel Technology*, vol. 140, no. 2, p. 021101, 2018.
- [74] F. Irmak and A. P. Gordon, "A framework for life prediction of 2.25 cr-1mo under creep and thermomechanical fatigue," in *Turbo Expo: Power for Land, Sea, and Air*, vol. 51128, p. V006T24A020, American Society of Mechanical Engineers, 2018.
- [75] B. B. Kerezsi, J. W. H. Price, and R. N. Ibrahim, "Using s–n curves to analyse cracking due to repeated thermal shock," *Journal of materials processing technology*, vol. 145, no. 1, pp. 118–125, 2004.
- [76] H. Wu, R. Pietrowski, and S. Tordonato, "Metallurgical assessment of heads containing id cracks on a secondary superheater outlet header," *Journal of failure analysis and prevention*, vol. 12, pp. 145–154, 2012.
- [77] A. Karstensen, J. Guerra, D. Knowles, and O. Kwon, "Ligament crack growth in a main steam superheater outlet header," in *ASME Pressure Vessels and Piping Conference*, vol. 47578, pp. 247–253, 2006.
- [78] O. Yasniy, Y. Pyndus, V. Iasnii, and Y. Lapusta, "Residual lifetime assessment of thermal power plant superheater header," *Engineering Failure Analysis*, vol. 82, pp. 390–403, 2017.
- [79] S. Narasimhachary and A. Saxena, "Crack growth behavior of 9cr- 1mo (p91) steel under creep–fatigue conditions," *International Journal of Fatigue*, vol. 56, pp. 106–113, 2013.

- [80] K. Kirkhope, R. Bell, and J. Kirkhope, "Stress intensity factors for single and multiple semi-elliptical surface cracks in pressurized thick-walled cylinders," *International journal of pressure vessels and piping*, vol. 47, no. 2, pp. 247–257, 1991.
- [81] H. B. Dinh and K. B. Yoon, "Numerical simulation of thermal stress and creep fatigue crack growth analysis for thick-walled tubes of header," in *Regional Conference in Mechanical Manufacturing Engineering*, pp. 837–850, Springer, 2021.
- [82] V. Gaur, V. Doquet, E. Persent, C. Mareau, E. Roguet, and J. Kittel, "Surface versus internal fatigue crack initiation in steel: Influence of mean stress," *International Journal of Fatigue*, vol. 82, pp. 437–448, 2016.
- [83] X. Sun, G. Chai, and Y. Bao, "Elastic and elastoplastic fracture analysis of a reactor pressure vessel under pressurized thermal shock loading," *European Journal of Mechanics-A/Solids*, vol. 66, pp. 69–78, 2017.
- [84] Y. Zheng, G. Wang, S. Tu, and F. Xuan, "Constraint characterization and fracture initiation analysis for semi-elliptical surface cracks in reactor pressure vessel," *International Journal of Pressure Vessels and Piping*, vol. 202, p. 104910, 2023.
- [85] Y. Lei, "Validation of contour integral functions (j and c (t)) in abaqus v6.11-v6.14 for combined mechanical and residual stresses," *Procedia Structural Integrity*, vol. 2, pp. 2566–2574, 2016.
- [86] K. Kumar, S. S. Bhadauria, and A. P. Singh, "Finite element analysis of edge and cleavage cracks in u-bend specimen using contour integral approach," *Materials Today: Proceedings*, vol. 44, pp. 865–870, 2021.
- [87] C.-H. Lee and H.-W. Chou, "Stress intensity factor assessment for reactor pressure vessel nozzles containing postulated corner cracks," *Engineering Fracture Mechanics*, vol. 275, p. 108838, 2022.
- [88] Y. Li, T. Jin, Z. Wang, and D. Wang, "Engineering critical assessment of rpv with nozzle corner cracks under pressurized thermal shocks," *Nuclear Engineering and Technology*, vol. 52, no. 11, pp. 2638–2651, 2020.
- [89] W. J. Wang and M.-S. Yim, "A fatigue crack growth prediction model for cracked specimen under variable amplitude loading," *International Journal of Fatigue*, vol. 168, p. 107387, 2023.
- [90] B. Nečemer, T. Vuherer, Z. Tonković, and S. Glodež, "Experimental and computational investigation of fatigue crack propagation using the inelastic energy approach," *Theoretical and Applied Fracture Mechanics*, vol. 119, p. 103362, 2022.

- [91] B. Nečemer, J. Klemenc, F. Zupanič, and S. Glodež, “Modelling and predicting of the lcf-behaviour of aluminium auxetic structures,” *International Journal of Fatigue*, vol. 156, p. 106673, 2022.
- [92] D. Mora, O. C. Garrido, R. Mukin, and M. Niffenegger, “Fracture mechanics analyses of a reactor pressure vessel under non-uniform cooling with a combined trace-xfem approach,” *Engineering Fracture Mechanics*, vol. 238, p. 107258, 2020.
- [93] S. El Fakkoussi, H. Moustabchir, A. Elkhalfi, and C. Pruncu, “Computation of the stress intensity factor  $k_I$  for external longitudinal semi-elliptic cracks in the pipelines by fem and xfem methods,” *International Journal on Interactive Design and Manufacturing (IJIDeM)*, vol. 13, no. 2, pp. 545–555, 2019.
- [94] L. Bouhala, Q. Shao, Y. Koutsawa, A. Younes, P. Núñez, A. Makradi, and S. Belouettar, “An xfem crack-tip enrichment for a crack terminating at a bi-material interface,” *Engineering Fracture Mechanics*, vol. 102, pp. 51–64, 2013.
- [95] G. Dominguez, M. Uddin, M. Tran, and D. J. Shim, “Natural crack growth of nozzle corner crack using extended finite element method (xfem),” in *Pressure Vessels and Piping Conference*, vol. 86175, p. V04AT06A003, American Society of Mechanical Engineers, 2022.
- [96] A. Shahani and M. A. Fasakhodi, “Finite element analysis of dynamic crack propagation using remeshing technique,” *Materials & design*, vol. 30, no. 4, pp. 1032–1041, 2009.
- [97] M. Malekan, A. Khosravi, and L. St-Pierre, “An abaqus plug-in to simulate fatigue crack growth,” *Engineering with Computers*, pp. 1–15, 2022.
- [98] K. Liu, M. Huang, J. Lin, H. Jiang, B. Wang, and H. Matsuda, “The effects of thermal stress on the crack propagation in ap1000 reactor pressure vessel,” *Theoretical and Applied Fracture Mechanics*, vol. 110, p. 102798, 2020.
- [99] ASTM Standard A335/A335M, *Standard Specification for Seamless Ferritic Alloy-Steel Pipe for High Temperature Service*. West Conshohocken, PA, 2023, DOI: 10.1520/A0335A0335M – 21A, [www.astm.org](http://www.astm.org).
- [100] S. Sirohi, A. Sauraw, A. Kumar, S. Kumar, T. Rajasekaran, P. Kumar, R. Vid-yarthi, N. Kumar, and C. Pandey, “Characterization of microstructure and mechanical properties of cr-mo grade p22/p91 steel dissimilar welds for super-critical power plant application,” *Journal of Materials Engineering and Performance*, vol. 31, no. 9, pp. 7353–7367, 2022.
- [101] EPRI, *Fossil Plant High Energy Piping Damage: Theory and Practice, Volume 1: Piping Fundamentals*. Palo Alto, CA: 2007. 1012201.

- [102] J. J. de Barbadillo, B. A. Baker, R. D. Gollihue, and S. A. McCoy, "Properties of inconel alloy 740h for high pressure steam and supercritical co2 applications," in *Pressure Technology*, vol. 40764, p. V001T01A005, American Society of Mechanical Engineers, 2018.
- [103] A. Zieliński, M. Sroka, and T. Dudziak, "Microstructure and mechanical properties of inconel 740h after long-term service," *Materials*, vol. 11, no. 11, p. 2130, 2018.
- [104] J.-L. Chaboche, "Time-independent constitutive theories for cyclic plasticity," *International Journal of plasticity*, vol. 2, no. 2, pp. 149–188, 1986.
- [105] J.-L. Chaboche and G. Rousselier, "On the plastic and viscoplastic constitutive equationsâpart i: Rules developed with internal variable concept," 1983.
- [106] W. Prager, "A new method of analyzing stresses and strains in work-hardening plastic solids," 1956.
- [107] Z. Mroz, "On the description of anisotropic workhardening," *Journal of the Mechanics and Physics of Solids*, vol. 15, no. 3, pp. 163–175, 1967.
- [108] N. Ohno and J.-D. Wang, "Kinematic hardening rules for simulation of ratcheting behavior," *European journal of mechanics. A. Solids*, vol. 13, no. 4, pp. 519–531, 1994.
- [109] P. J. Armstrong, C. Frederick, *et al.*, *A mathematical representation of the multiaxial Bauschinger effect*, vol. 731. Berkeley Nuclear Laboratories Berkeley, CA, 1966.
- [110] J.-L. Chaboche, "A review of some plasticity and viscoplasticity constitutive theories," *International journal of plasticity*, vol. 24, no. 10, pp. 1642–1693, 2008.
- [111] F. Nabarro, "Report of a conference on the strength of solids physical society," 1948.
- [112] C. Herring, "Diffusional viscosity of a polycrystalline solid," *Journal of applied physics*, vol. 21, no. 5, pp. 437–445, 1950.
- [113] R. Coble, "A model for boundary diffusion controlled creep in polycrystalline materials," *Journal of applied physics*, vol. 34, no. 6, pp. 1679–1682, 1963.
- [114] E. N. D. C. Andrade, "On the viscous flow in metals, and allied phenomena," *Proceedings of the Royal Society of London. Series A, Containing Papers of a Mathematical and Physical Character*, vol. 84, no. 567, pp. 1–12, 1910.
- [115] F. H. Norton, "The creep of steel at high temperatures," (*No Title*), 1929.
- [116] F. Garofalo and D. B. Butrymowicz, "Fundamentals of creep and creep-rupture in metals," 1966.

- [117] Y. N. Rabotnov, F. A. Leckie, and W. Prager, "Creep problems in structural members," 1970.
- [118] L. M. Kachanov, "Rupture time under creep conditions," *International journal of fracture*, vol. 97, no. 1, pp. 11–18, 1999.
- [119] R. W. Hertzberg and F. E. Hauser, "Deformation and fracture mechanics of engineering materials," 1977.
- [120] K. Tanaka and T. Mura, "A dislocation model for fatigue crack initiation," 1981.
- [121] P. Lukáš and L. Kunz, "Role of persistent slip bands in fatigue," *Philosophical magazine*, vol. 84, no. 3-5, pp. 317–330, 2004.
- [122] P. Maiya, "Considerations of crack initiation and crack propagation in low-cycle fatigue," *Scr. Metall.:(United States)*, vol. 9, no. 11, 1975.
- [123] P. Verma, N. S. Srinivas, S. Singh, and V. Singh, "Low cycle fatigue behavior of modified 9cr–1mo steel at room temperature," *Materials Science and Engineering: A*, vol. 652, pp. 30–41, 2016.
- [124] G. R. Halford, "Cumulative fatigue damage modeling—crack nucleation and early growth," *International Journal of Fatigue*, vol. 19, no. 93, pp. 253–260, 1997.
- [125] M. R. Bayoumi and A. Abdellatif, "Effect of surface finish on fatigue strength," *Engineering Fracture Mechanics*, vol. 51, no. 5, pp. 861–870, 1995.
- [126] A. Javidi, U. Rieger, and W. Eichlseder, "The effect of machining on the surface integrity and fatigue life," *International Journal of fatigue*, vol. 30, no. 10-11, pp. 2050–2055, 2008.
- [127] A. Yadollahi, M. Mahtabi, A. Khalili, H. Doude, and J. Newman Jr, "Fatigue life prediction of additively manufactured material: Effects of surface roughness, defect size, and shape," *Fatigue & Fracture of Engineering Materials & Structures*, vol. 41, no. 7, pp. 1602–1614, 2018.
- [128] P. Maiya and D. Busch, "Effect of surface roughness on low-cycle fatigue behavior of type 304 stainless steel," *Metallurgical Transactions A*, vol. 6, pp. 1761–1766, 1975.
- [129] A. Haghshenas and M. Khonsari, "On the removal of extrusions and intrusions via repolishing to improve metal fatigue life," *Theoretical and Applied Fracture Mechanics*, vol. 103, p. 102248, 2019.
- [130] L. Coffin, "Fatigue at high temperature," *Advances in research on the strength and fracture of materials*, pp. 263–292, 1978.
- [131] R. Skelton, "The prediction of crack growth rates from total endurances in high strain fatigue," *Fatigue & Fracture of Engineering Materials & Structures*, vol. 2, no. 3, pp. 305–318, 1979.

- [132] A. Batte, M. Murphy, and M. Stringer, "High-strain high-temperature fatigue properties of a 0.5Cr–Mo–V steam turbine casing steel," *Metals Technology*, vol. 5, no. 1, pp. 405–413, 1978.
- [133] R. Dawson, W. Elder, G. Hill, and A. Price, "High-strain fatigue of austenitic steels," 1967.
- [134] M. A. Miner, "Cumulative damage in fatigue," 1945.
- [135] R. Tryon and T. Cruse, "A reliability-based model to predict scatter in fatigue crack nucleation life," *Fatigue & Fracture of Engineering Materials & Structures*, vol. 21, no. 3, pp. 257–267, 1998.
- [136] S. Meyer, A. Brückner-Foit, and A. Möslang, "A stochastic simulation model for microcrack initiation in a martensitic steel," *Computational materials science*, vol. 26, pp. 102–110, 2003.
- [137] E. L. Robinson, "Effect of temperature variation on the creep strength of steels," *Transactions of the American Society of Mechanical Engineers*, vol. 60, no. 3, pp. 253–259, 1938.
- [138] R. Skelton, T. Vilhelmsen, and G. Webster, "Energy criteria and cumulative damage during fatigue crack growth," *International journal of fatigue*, vol. 20, no. 9, pp. 641–649, 1998.
- [139] J. H. Lau, S. H. Pan, and C. Chang, "A new thermal-fatigue life prediction model for wafer level chip scale package (wl CSP) solder joints," *J. Electron. Packag.*, vol. 124, no. 3, pp. 212–220, 2002.
- [140] J. Morrow, *Cyclic plastic strain energy and fatigue of metals*. ASTM International West Conshohocken, PA, 1965.
- [141] M. D. Callaghan, S. Humphries, M. Law, M. Ho, P. Bendeich, H. Li, and W. Yeung, "Energy-based approach for the evaluation of low cycle fatigue behaviour of 2.25 Cr–1Mo steel at elevated temperature," *Materials Science and Engineering: A*, vol. 527, no. 21–22, pp. 5619–5623, 2010.
- [142] C. Chang, W. Pimbley, and H. Conway, "An analysis of metal fatigue based on hysteresis energy: Main purpose of investigation is to extend halford's work on low-cycle fatigue to the medium-and high-cycle range by including the concept of an endurance limit," *Experimental Mechanics*, vol. 8, pp. 133–137, 1968.
- [143] J.-H. Hwang, Y.-J. Kim, and J.-W. Kim, "Energy-based damage model incorporating failure cycle and load ratio effects for very low cycle fatigue crack growth simulation," *International Journal of Mechanical Sciences*, vol. 221, p. 107223, 2022.
- [144] T. H. Courtney, *Mechanical behavior of materials*. Waveland Press, 2005.

- [145] J. Das and S. Sivakumar, "An evaluation of multiaxial fatigue life assessment methods for engineering components," *International Journal of Pressure Vessels and Piping*, vol. 76, no. 10, pp. 741–746, 1999.
- [146] W. Ostergren, "A damage function and associated failure equations for predicting hold time and frequency effects in elevated temperature, low cycle fatigue," *Journal of Testing and Evaluation*, vol. 4, no. 5, pp. 327–339, 1976.
- [147] C. Hu, L. Xu, L. Zhao, Y. Han, K. Song, X. Luo, and C. Li, "Investigation of low cycle fatigue crack propagation behavior of 316h steel at 550 c based on cyclic response and damage accumulation: experiment and modelling," *International Journal of Plasticity*, vol. 167, p. 103661, 2023.
- [148] R. Darveaux, "Effect of simulation methodology on solder joint crack growth correlation and fatigue life prediction," *J. Electron. Packag.*, vol. 124, no. 3, pp. 147–154, 2002.
- [149] A. Loghin and S. Ismonov, "3d fea based surrogate modeling in fatigue crack growth life assessment," *Procedia Structural Integrity*, vol. 38, pp. 331–341, 2022.
- [150] E. Wang, W. Zhou, and G. Shen, "Three-dimensional finite element analysis of crack-tip fields of clamped single-edge tension specimens—part i: Crack-tip stress fields," *Engineering Fracture Mechanics*, vol. 116, pp. 122–143, 2014.
- [151] E. Wang, W. Zhou, and G. Shen, "Three-dimensional finite element analysis of crack-tip fields of clamped single-edge tension specimens—part ii: Crack-tip constraints," *Engineering Fracture Mechanics*, vol. 116, pp. 144–157, 2014.
- [152] F. Farukh, L. Zhao, R. Jiang, P. Reed, D. Proppentner, and B. A. Shollock, "Realistic microstructure-based modelling of cyclic deformation and crack growth using crystal plasticity," *Computational Materials Science*, vol. 111, pp. 395–405, 2016.
- [153] M. Gupta, R. Alderliesten, and R. Benedictus, "A review of t-stress and its effects in fracture mechanics," *Engineering Fracture Mechanics*, vol. 134, pp. 218–241, 2015.
- [154] G. Webster and R. A. Ainsworth, *High temperature component life assessment*. Springer Science & Business Media, 1994.
- [155] J. R. Rice, "A path independent integral and the approximate analysis of strain concentration by notches and cracks," 1968.
- [156] P. C. Paris, *The growth of cracks due to variations in load*. Lehigh University, 1962.
- [157] H. C. Rhee and M. M. Salama, "Mixed-mode stress intensity factor solutions of a warped surface flaw by three-dimensional finite element analysis," *Engineering Fracture Mechanics*, vol. 28, no. 2, pp. 203–209, 1987.

- [158] M. Zimnoch, E. Haddadi, I. Perrin, and A. Tabarraei, "Effects of thermal mechanical fatigue on a 2.25 cr-1mo steam header," in *ASME International Mechanical Engineering Congress and Exposition*, vol. 87707, p. V013T15A005, American Society of Mechanical Engineers, 2023.
- [159] Aesteriron Steels, "Manufacturers and stocklist." Available online, 2023. Seamless pipe.
- [160] R. W. Smith, M. H. Hirschberg, and S. Manson, *Fatigue behavior of materials under strain cycling in low and intermediate life range*. National Aeronautics and Space Administration Washington, DC, USA, 1963.
- [161] N. Science, *Data Sheets on Long-Term, High-Temperature Low Cycle Fatigue Properties of SCMV 4 (2.25Cr-1Mo) Steel Plate for Boilers and Pressure Vessels 94*. NIMS Fatigue Data Sheet, NIMS, Tsukuba, Japan, 2004.
- [162] T. Bouchenot, B. Felemban, C. Mejia, and A. P. Gordon, "Development of noninteraction material models with cyclic hardening," *Journal of Engineering Materials and Technology*, vol. 138, no. 4, 2016.
- [163] T. A. Philpot and J. S. Thomas, *Mechanics of materials: an integrated learning system*. John Wiley & Sons, 2020.
- [164] A. user and v. . theory manuals. Dassault Systems, 2022.
- [165] D. Gandy, "The grade 22 low alloy steel handbook," *Electric Power Research Institute. Final Report*, 2005.
- [166] B. S. Institution and E. C. for Standardization, *Guide to Methods for Assessing the Acceptability of Flaws in Metallic Structures*. British standard, British Standards Institution, 2005.
- [167] T. L. Anderson, *Fracture mechanics: fundamentals and applications*. CRC press, 2017.
- [168] P. Paris and F. Erdogan, "A critical analysis of crack propagation laws," 1963.
- [169] T. Belytschko and T. Black, "Elastic crack growth in finite elements with minimal remeshing," *International Journal for Numerical Methods in Engineering*, vol. 45, pp. 601–620, June 1999.
- [170] N. Moës, J. Dolbow, and T. Belytschko, "A finite element method for crack growth without remeshing," *International Journal for Numerical Methods in Engineering*, vol. 46, no. 1, pp. 131–150, 1999.
- [171] F. Erdogan and G. Sih, "On the crack extension in plates under plane loading and transverse shear," 1963.
- [172] G. Irwin, "Linear fracture mechanics, fracture transition, and fracture control," *Engineering fracture mechanics*, vol. 1, no. 2, pp. 241–257, 1968.

- [173] R. Krueger, L. Deobald, and H. Gu, “A benchmark example for delamination growth predictions based on the single leg bending specimen under fatigue loading,” *Advanced Modeling and Simulation in Engineering Sciences*, vol. 7, pp. 1–25, 2020.